

Hiromitsu Yamagishi
Netra Prakash Bhandary *Editors*

GIS Landslide

GIS Landslide

Hiromitsu Yamagishi · Netra Prakash Bhandary
Editors

GIS Landslide

 Springer

Editors

Hirimitsu Yamagishi
Shin Engineering Consultant Co. Ltd.
Sapporo
Japan

Netra Prakash Bhandary
Ehime University
Matsuyama
Japan

ISBN 978-4-431-54390-9

ISBN 978-4-431-54391-6 (eBook)

DOI 10.1007/978-4-431-54391-6

Library of Congress Control Number: 2017935561

© Springer Japan KK 2017

This work is subject to copyright. All rights are reserved by the Publisher, whether the whole or part of the material is concerned, specifically the rights of translation, reprinting, reuse of illustrations, recitation, broadcasting, reproduction on microfilms or in any other physical way, and transmission or information storage and retrieval, electronic adaptation, computer software, or by similar or dissimilar methodology now known or hereafter developed.

The use of general descriptive names, registered names, trademarks, service marks, etc. in this publication does not imply, even in the absence of a specific statement, that such names are exempt from the relevant protective laws and regulations and therefore free for general use.

The publisher, the authors and the editors are safe to assume that the advice and information in this book are believed to be true and accurate at the date of publication. Neither the publisher nor the authors or the editors give a warranty, express or implied, with respect to the material contained herein or for any errors or omissions that may have been made. The publisher remains neutral with regard to jurisdictional claims in published maps and institutional affiliations.

Printed on acid-free paper

This Springer imprint is published by Springer Nature

The registered company is Springer Japan KK

The registered company address is: Chiyoda First Bldg. East, 3-8-1 Nishi-Kanda, Chiyoda-ku, Tokyo 101-0065, Japan

Preface

A landslide is the movement of a mass of rock, earth, or debris along a slope under the influence of gravity. Landslides are triggered by rainfall, earthquakes, volcanic eruptions, slope erosion by rivers, and human activities like slope cutting and excavation.

Several landslides include slope failures developing within, and at the margins of already existing landslides. Therefore, if landslide topography can be identified on any slopes, the potential of developing new landslides can be defined with any degree. In order to research and produce an inventory of existing landslides or landslide prone areas, topographic maps, stereo-paired aerial photographs, and satellite images such as Google Earth, can be used. During our research, we refer to the models of landslide type mentioned below. Landslides are usually classified as deep-seated landslides or shallow landslides (slope failures). Information to assess the hazards and risks on slopes is considered based on the above data.

Deep-seated landslides are usually composed of a main scarp and body or debris, while shallow landslides are composed of a scar part, a flow part, and a deposition part. In particular, deep-seated landslides have the potential to alter topography. Therefore, it is important to recognize the modification of topography in order to predict new landslides. In order to find landslide prone areas, GIS is particularly for landslide hazard mapping. These works generate a landslide inventory, and then mapping and analysing them using GIS technology process further by GIS software and related technology.

This book consists of 13 chapters dealing mostly with landslide mapping, analyses and case studies using GIS and related technology. Finally, we are grateful to all of the authors for submitting their work to this book. We also would like to show our appreciation to Ms. Taeko Sato and Mr. Thirumani Parimelazhagan, Springer for editing this book.

Sapporo, Japan
Matsuyama, Japan

Hiromitsu Yamagishi
Netra Prakash Bhandary

Contents

Part I Introduction

- 1 Identification and Mapping of Landslides 3**
Hiromitsu Yamagishi

Part II Data Analysis and Method Development

- 2 Spatial Comparison of Two High-resolution Landslide Inventory Maps Using GIS—A Case Study of the August 1961 and July 2004 Landslides Caused by Heavy Rainfalls in the Izumozaki Area, Niigata Prefecture, Japan 13**
Junko Iwahashi and Hiromitsu Yamagishi
- 3 Landslide Surface Deformation Detected by Synthetic Aperture Radar (SAR) Interferometry in Shizu Area on the Southern Foot of Mt. Gassan, Japan 31**
Hiroshi P. Sato and Akira Suzuki
- 4 Modelling a Landslide Probability Through Time as a Basis for the Landslide Hazard Forecast System 45**
Marko Komac and Mateja Jemec Auflič
- 5 Development of a GIS-Based 3D Slope Stability Analysis System for Rainfall-Induced Landslide Hazard Assessment. 71**
Cheng Qiu and Yasuhiro Mitani

Part III Mapping

- 6 Large-Scale Landslide Inventory Mapping in Lesser Himalaya of Nepal Using Geographic Information System 97**
Manita Timilsina, Netra Prakash Bhandary, Ranjan Kumar Dahal and Ryuichi Yatabe

7	A Joint Regional Slope Mass Movement Susceptibility Map	113
	Marko Komac	
8	Landslide Inventory: Challenge for Landslide Hazard Assessment in Indonesia	135
	Ngadisih, Guruh Samodra, Netra Prakash Bhandary and Ryuichi Yatabe	
Part IV Application and Case Studies		
9	Landslide Susceptibility Mapping Based on Aerial Photograph Interpretation Inventory for Tegucigalpa, Honduras: An Application of the Matrix Method.	163
	Elias Garcia-Urquia and Hiromitsu Yamagishi	
10	An Assessment of the Effective Geofactors of Landslide Susceptibility: Case Study Cibeber, Cianjur, Indonesia	183
	Yukni Arifianti and Fitriani Agustin	
11	GIS Approach to Landslide Hazard Mapping: A Case Study of Syangja District in Western Nepal	197
	Vishnu Dangol	
12	GIS Application in Landslide Susceptibility Mapping of Indian Himalayas	211
	Shantanu Sarkar and Debi Prasanna Kanungo	
13	Characteristics of the Torrential Rainfall-Induced Shallow Landslides by Typhoon Bilis, in July 2006, Using Remote Sensing and GIS	221
	Jie Dou, Hiromitsu Yamagishi, Yueren Xu, Zhongfan Zhu and Ali P. Yunus	

Part I
Introduction

Chapter 1

Identification and Mapping of Landslides

Hiromitsu Yamagishi

Abstract In order to study landslides using GIS, it is first necessary to identify landslides based on their characteristics: deep-seated landslides, such as main scarps, debris, mounds, and hollows, or shallow landslides. Deep-seated landslides are classified into rotational slide (slump), planar slide (glide), debris avalanche, or earth flows. Shallow landslides are composed of scar, flow, and deposit part. The seat is classified into planar or spoon type. After producing an inventory of landslides, an analog map should be transformed into a digital map and analyzed using GIS to obtain “landslide hazard maps” including: (1) landslide inventory maps, (2) landslide susceptibility maps, (3) landslide hazard maps, and (4) landslide risk maps. Finally, this chapter reviews on GIS landslide analyses and susceptibility mapping reviews briefly representative papers.

Keywords Landslide mapping · Landslide types · Deep-seated landslide · Shallow landslide · GIS landslide method

1.1 Landslide Identification and Type

Landslides are usually classified as deep-seated or shallow landslides (slope failures). Deep-seated landslides are of great interest for the identification of sites where additional landslides may develop, as they tend to present more threatening and plentiful instability conditions in comparison to other slope failures. Thus, they will be the focus of a more thorough description regarding their components and classification in order to support a better detection procedure. By recognizing

H. Yamagishi (✉)
Shin Engineering Consultant Co., Ltd., 2-8-30, Sakaedori, Shiroishi-ku,
Sapporo 003-0021 Japan
e-mail: hiromitsuyamagishi88@gmail.com

accurately the main features and types of landslides, it is possible to identify them using existing surface information in little time.

The following topographic characteristics are typical of deep-seated landslides: (1) main and secondary scarps, (2) cracks, (3) mounds and ridges, (4) hollows and ponds, and (5) alterations/meanders of the drainage system (streams, rivers, etc.). Scarps are significant features that form part of deep-seated landslides. The main scarp can result in variable landslide shapes: an amphitheatre shape for a rotational slump or a straight and planar failure surface for a planar slide. The landslide body and toe can present hollows or ponds, mounds, and cracks (fissures) showing various shapes and locations. In the case of a planar slide, hollows are graben shaped (depressions). Figure 1.1 shows the typical form of a rotational deep-seated landslide.

Deep-seated landslides can be classified into the following main types (Fig. 1.2): (a) Rotational Slide type, (b) Planar Slide type, (c) Debris Avalanche, and (d) Earth Flow (Highland and Bobrowsky 2008). Based on the new classification version proposed by Hungr et al. (2013), translational (Planar) slides will be referred to from now on as planar slides.

Fig. 1.1 Schematic model of typical deep-seated landslide (Highland and Bobrowsky 2008, based on Varnes 1978)

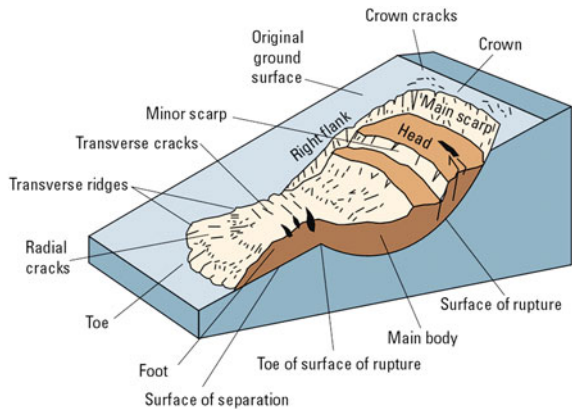
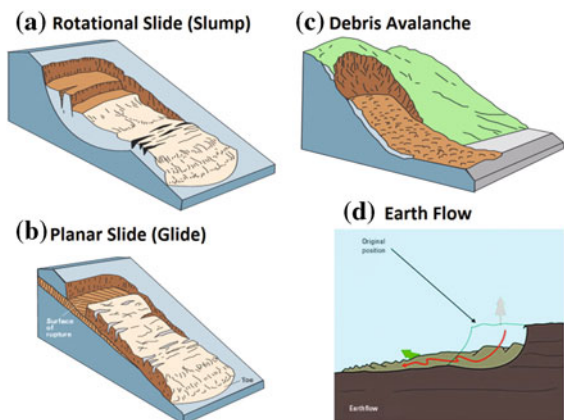


Fig. 1.2 Types of deep-seated landslides (Highland and Bobrowsky 2008, based on Varnes 1978)



Rotational type is defined as a landslide in which the rupture surface is curved upward in cross section and the movement is rotational along the axis parallel to the slope surface. The head moves vertically downward, and the displaced materials tilt backward, toward the scarp. Therefore, the portion in front of the scarp is regarded as a tensional zone; on the contrary, the marginal portion is a compression zone (Fig. 1.2a). A planar-type landslide is one that moves downward and outward, along a relatively planar surface (Fig. 1.2b). This type of slide may progress over considerable distances if the surface of rupture is sufficiently inclined, something which is in contrast to rotational slides, which tend to restore their slide equilibrium over a short distance.

Debris avalanches (Fig. 1.2c) are essentially large, extremely rapid, and often open-slope flows formed when an unstable slope collapses and the resulting fragmented debris is rapidly transported away from the slope. In some cases, snow and ice contribute to the movement if sufficient water is present. Finally, earth flows can occur on gentle to moderate slopes, generally in fine-grained soils, commonly clay or silt, but also in very weathered, clay-bearing bedrock (Fig. 1.2d). The mass in an earth flow moves as a plastic or viscous flow with strong internal deformation.

While the focus on identification of landslides has been on deep-seated types (as they can be the starting points for development of new mass movements) and shallow landslides must be considered also. Zones with numerous shallow landslides might indicate problematic conditions that can result in even more movement. An individual slope failure in a specific place can be an indicator of possible new landslides.

Shallow landslides (slope failures) tend to be triggered by heavy rainfall and high intensity earthquakes. They are characterized by a shallow depth, up to several meters, and many failures occurring at once. In addition, they are sometimes associated with mud flows and debris flows as deposit parts. Mainly, slope failures are classified into

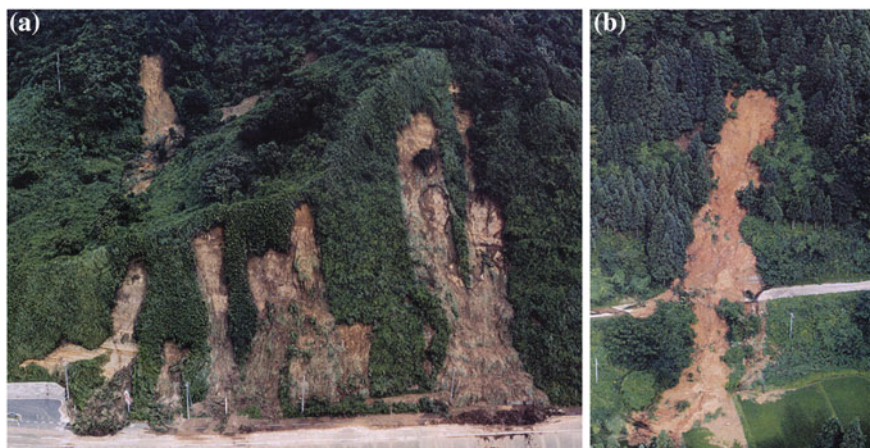


Fig. 1.3 Shallow landslides (slope failures) caused by heavy rainfalls on July 14, 2004 in Niigata, Japan. **a** Planar type and **b** spoon type

planar and concave types and are usually composed of a scarp part, a flow part, and a deposit part. They are classified into planar type, where the scar is parallel to the original slope, and spoon type, where the scar is concaved in shape (Fig. 1.3).

1.2 What Is Landslide Hazard Mapping?

Landslide maps exist in many types in terms of hazard mapping defined by the Committee on the Review of the National Landslide Hazards Mitigation Strategy, CRNLHMS (2004).

- (1) **A landslide inventory map** shows original maps of the locations and outlines of landslides. The map is a dataset representing a single event or multiple events. It is usually made by interpretation of aerial photographs, satellite images such as Google Earth or GPS measurements, etc.
- (2) **A landslide susceptibility map** shows the likelihood of a landslide occurrence on the basis of the local slope or earth conditions. Susceptibility does not consider the probability of generation, which depends on triggering factors such as rainfall or seismicity (CRNLHMS 2004).
- (3) **A landslide hazard map** indicates the potential for an occurrence giving rise to damage to human life, property, or infrastructures, etc.
- (4) **A landslide risk map** shows the expected cost of landslide damage throughout an area. Risk maps combine the probability information from a land slide hazard map with analysis of all possible consequences (property damage, casualties).

1.3 Landslide and GIS

For studying landslide mapping, many methods and techniques are developing. In particular, IT innovations, satellite imagery, and laser profiler systems have come to the fore, in addition to GIS and remote sensing.

For GIS landslide studies, it is necessary to use DEM (Digital Elevation Model). Recently, 30-m DEM has become available to download free of charge from LP DAAC Global Data Explorer: <http://gdex.cr.usgs.gov/gdex/> (see Fig. 1.4) or Alos2 of JAXA (<http://www.eorc.jaxa.jp/ALOS/en/aw3d30/data/index.htm>) for any country. A further free download is from the Geographical Survey Institute, Japan, providing 10-m DEM across Japan.

Precisely how to use GIS for landslide analyses depends on landslide type: shallow or deep-seated. In the case of shallow landslides, DEM is used for slope analyses, because shallow landslides take place along the slope, whereas deep-seated landslides are a result of slopes moving; therefore, the analysis is

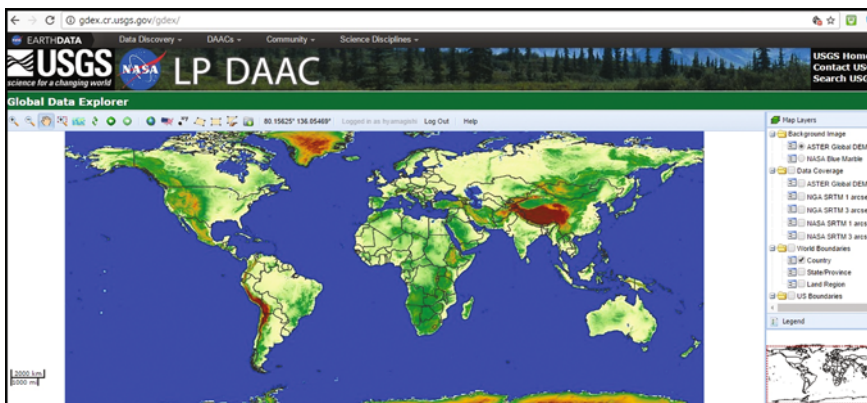


Fig. 1.4 LP DAAC global data explorer website, from which 30-m DEM is available as a free download

mostly carried out using GIS data from geological maps and vector analyses of geoprocessing and geometry functions etc.

In order to undertake landslide susceptibility mapping, many methods are used in combination with statistical software: artificial neural network (ANN; Dou et al. 2015) and logistic regression (LR: Ayalew and Yamagishi 2005).

The editors of this book decided to produce a work on GIS and landslides; therefore we called for the chapters. As a result, 13 chapters were submitted mostly from Asian, Central America and Eastern European countries. Many landslide disasters take place in these countries, so GIS technology represents significant work.

1.4 Brief Review of Studies on Landslides Using GIS and Related Technologies

There have been many papers on GIS and landslides. The keyword search for “GIS Landslide” yields more than 22,700 results on Google Scholar (April 3, 2017). Some of the most significant work is as follows.

Carrara et al. (1991) described that relevant geological and geomorphological factors were collected and processed by applying GIS technology. In particular, modules were used to both generate high-fidelity digital terrain models and automatically partition the terrain into main slope units. The results were analyzed primarily by discriminant analysis which enabled landslide hazard and risk assessment.

Van Westen and Terlien (1996) calculated average safety factors and landslide probability based on parameter maps of geology, geomorphology, and DEM. A two-dimensional hydrological model was applied to estimate groundwater levels in relation to rainfall events and a simple method for the calculation of horizontal

seismic acceleration was used for different earthquake events. The highest probability value of the various scenarios was selected for each pixel, and a final hazard map for translational landslides was constructed. The results were the first approach towards a deterministic landslide hazard analysis using GIS.

Dai and Lee (2002) analyzed the physical characteristics of landslides and the statistical relations of landslide frequency with the physical parameters on Lantau Island in Hong Kong using GIS, a database of existing digital maps, and aerial photographs. The horizontal travel length and the angle of reach, defined as the angle of the line connecting the head of the landslide source to the distal margin of the displaced mass, were used to describe the runout behavior of a landslide mass. The results indicated that the horizontal travel length of a landslide mass ranged from 5 to 785 m, with a mean value of 43 m, and the average angle of reach was 27.7°. Finally, they indicated that slope gradient, lithology, elevation, slope aspect, and land-use are statistically significant in predicting slope instability.

Ayalew and Yamagishi (2005) used a logistic regression model for regional hazard management, and multivariate statistical analysis to produce a landslide susceptibility map of central Japan. For susceptibility mapping, the use of logistic regression was found to be the best fitting function to describe the relationship between the presence or absence of landslides (dependent variable) and a set of independent parameters such as slope angle and lithology. An inventory map, as its base, of 87 landslides was used to produce the dependent variable, which took values of 0 for an absence and 1 for the presence of slope failures. Lithology, bed rock–slope relationship, lineaments, slope gradient, aspect, elevation, and road network were taken as independent parameters. The effect of each parameter on landslide occurrence was assessed from the corresponding coefficient that appeared in the logistic regression function. Among the geomorphological parameters, aspect and slope gradient had a more significant contribution than elevation. The study area was classified into five categories of landslide susceptibility: extremely low, very low, low, medium, and high.

References

- Ayalew L, Yamagishi H (2005) The application of GIS-based logistic regression for landslide susceptibility mapping in the Kakuda-Yahiko Mountains, Central Japan. *Geomorphology* 65:15–31
- Carrara A, Cardinali M, Detti R, Guzetti F, Pasqui V, Reichenbach P (1991) GIS techniques and statistical models. *Earth Surf Proc Land* 16:427–445
- Committee on the Review of the National Landslide Hazards Mitigation Strategy (2004) Partnerships for reducing landslide risks: assessment of the national landslide hazard mitigation strategy. The National Academic Press, 131 p
- Dai FC, Lee CF (2002) Landslide characteristics and slope instability modeling using GIS, Lantau Island, Hong Kong. *Geomorphology* 42:213–228
- Dou J, Yamagishi H, Pourghasemi HR, Yunus AP, Song X, Xu Y, Zhu Z (2015) An integrated artificial neural network model for the landslide susceptibility assessment of Osado Island, Japan. doi:10.1007/s11069-015-1799-2

- Hungr O, Leroueil S, Picarelli L (2013) The Varnes classification of landslide types, an update. *Landslides* 11(2):167–194
- Highland LM, Bobrowsky P (2008) *The landslide handbook-a guide to understanding Landslides*. U.S. Department of the Interior, U.S. Geological Survey, Circular 1325, 129 p
- Van Westen CJ, Terlien MJT (1996) An approach towards deterministic landslide hazard analysis in GIS: a case study from Manizales (Columbia). *Earth Surf Proc Land* 21:853–868
- Varnes DJ (1978) Slope movement types and processes. In: Schuster RL, Krizek RJ (eds) *Landslides: analyses and control special report 176*. National Academy of Sciences, Washington, D.C., pp 11–33

Part II
Data Analysis and Method Development

Chapter 2

Spatial Comparison of Two High-resolution Landslide Inventory Maps Using GIS—A Case Study of the August 1961 and July 2004 Landslides Caused by Heavy Rainfalls in the Izumozaki Area, Niigata Prefecture, Japan

Junko Iwahashi and Hiromitsu Yamagishi

Abstract The spatial distribution of shallow landslides in the Izumozaki area, Niigata, caused by the heavy rainfalls in August 1961 and July 2004 was investigated using high-resolution ortho-photoimagery and a 2-m DEM. We found that the number of the August 1961 landslides is more than twice the July 2004 landslides. More than half of the July 2004 landslides (about 70% as the number ratio and 54% as the area ratio) were primary landslides. These primary landslides seem to occur randomly regardless of the geological structure of the stratum. The large landslides which occurred in July 2004 were often expanded landslides immediately higher than the August 1961 landslides. These expanded landslides often occurred on daylighting dip slopes. Among the July 2004 landslides, the ratio of landslides along roads is very high compared to 1961 (1961: 4.2%; 2004: 16.4%).

Keywords Landslide · Ortho-photoimagery · LiDAR

2.1 Introduction

In this section, research of GIS analyses for shallow landslides caused by heavy rainfalls in Izumozaki Town, Niigata Prefecture in Japan is introduced. The authors investigated spatial distribution of shallow landslides in the Izumozaki area caused

J. Iwahashi (✉)
Geospatial Information Authority of Japan, Kitasato-1,
Tsukuba 305-0811, Ibaraki, Japan
e-mail: iwahashi-j96pz@mlit.go.jp

H. Yamagishi
Shin Engineering Consultant Co. Ltd, Hokkaido, Japan

© Springer Japan KK 2017
H. Yamagishi and N.P. Bhandary (eds.), *GIS Landslide*,
DOI 10.1007/978-4-431-54391-6_2

by heavy rainfalls in August 1961 and July 2004 using high-resolution ortho-photoimagery and a 2-m DEM from ground-based LiDAR data (Iwahashi and Yamagishi 2010).

We utilized commonly used GIS software, spreadsheet software, and statistical software. The applied skills were very simple: digitizing, overlaying, and creating graphs and tables. However, without recent advances in technology of spatial data creation such as ortho-photoimagery and high-resolution DEMs by LiDAR, the research would have not been carried out because the innovation of data creation and GIS brought enough positional accuracy of landslide inventory data. In addition, without past continuous studies of local research such as field geological surveys, referred to in the Reference, the research also would not have been carried out.

We mainly used landslide distribution data directly digitized from 50-cm digital ortho-photoimagery. Moreover, a 2-m DEM of LiDAR surveyed in November 3, 2007, was overlaid. Although the LiDAR DEM was surveyed after the July 2004 heavy rainfalls, Saito (2007) revealed that majority of landslides in the study area occurred in shallow surfaces whose thicknesses were less than 3 m. Therefore, we suppose that there is no major problem for surveying terrain attributes by the DEM. Two-meter resolution makes it possible to compare landslide polygons and topographical features of individual slopes.

2.2 Study Area

Figure 2.1 shows the location and a lithological map of the study area. The study area lies on fold mountains of sedimentary rocks and is dominated by steep slopes.

The study area lies on four sheets of 1:50,000 geological maps. We compiled four geological map sheets (Kobayashi et al. 1993; Kobayashi et al. 1995; Kobayashi et al. 2001; Takeuchi et al. 2004) referring to descriptions of the geological maps before producing GIS data of the lithology (Iwahashi and Yamagishi 2010).

The dominant lithology in the study area is sedimentary rocks of Miocene to Pleistocene: interbedded sandstone and mudstone with thick sandstone of Shiiya formation [hereinafter referred to as the Shiiya formation (interbedded sandstone and mudstone)], massive mudstone with interbedded sandstone and mudstone of Nishiyama formation [the Nishiyama formation (massive mudstone)], sandy siltstone with interbedded sandstone and mudstone of Haizume formation [the Haizume formation (sandy siltstone)], and gravel, sand, silt, and mud of Uonuma formation [the Uonuma formation (sand dominated)]. Those four groups are distributed over one km² and occupy a large portion of the mountains.

Nozaki (1994) and Nozaki (1995) reported that the Shiiya formation was of lesser intensity than the Nishiyama, Haizume, and Uonuma formations, despite the fact that the Shiiya formation is older than other formations. In the study area, many landslides are distributed in the slopes of the Shiiya formation.

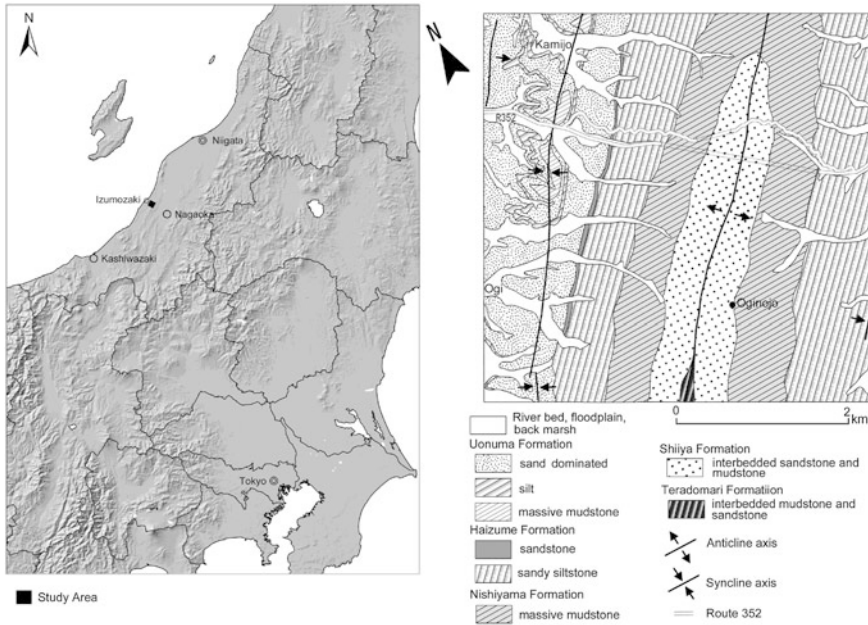


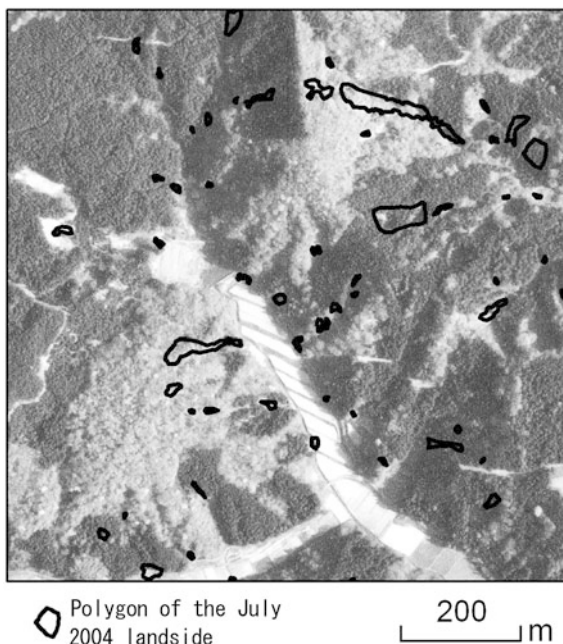
Fig. 2.1 Study area and its lithological map. The lithological map is compiled from 1:50,000 geological maps of Kobayashi et al. (1993), Kobayashi et al. (1995, 2001), Takeuchi et al. (2004)

In the study area, cedar plantations and broad-leaved deciduous forests are widely distributed. Vegetation of the study area is well controlled by humans. According to the observation of air-photographs, a considerable portion of the study area was logged in the 1940s. After the 1960s, the study area is covered by forest and there has been no bare land (Fig. 2.2). The distribution of cedar plantation has been changed widely every 10–20 years due to logging. There is no concrete evidence that vegetation influences the development of landslides. Therefore, the vegetation was not considered as a predisposition in this study area.

2.3 Details of the August 1961 and July 2004 Heavy Rainfalls in the Study Area

The Izumozaki area has suffered several disasters caused by heavy rainfalls in the last several decades. Many landslides occurred in the study area, in particular due to the 5 and 20 August 1961 heavy rainfalls caused by a typhoon and the 13 June 2004 heavy rainfalls caused by a rainy season front (Yamagishi et al. 2008). This study focuses on landslides caused by the two events.

Fig. 2.2 Landslides induced by the July 2004 rainstorms plotted on the monochrome air-photograph taken in 2001 by GSI. *Dark parts* correspond to artificial forests of cedars, and *gray parts* to broad-leaved deciduous forests



According to reports of the meteorological observatory, daily precipitation of the 5 August 1961 heavy rainfall in the study area was estimated as 250 mm. Maximum hourly precipitation in the study area was unknown; however, it was 40 mm in Nagaoka which is located 10 km east of Izumozaki. Half of the residential buildings in the Izumozaki area suffered damage and 14 people were lost because of landslides (Tokyo District Meteorological Observatory 1961). Two weeks later, heavy rainfalls came again. On August 20, 1961, middle of Niigata Prefecture suffered concentrated heavy rains. Daily precipitation of the study area was 126 mm (Society of Agricultural Meteorology of Niigata Prefecture 1961). According to Tokyo District Meteorological Observatory (1961), most of the damage of Izumozaki was caused by the 5th August heavy rainfall, however, Saito (2007) reported that many landslides occurred in the eastern slopes of Oginjo on 20th August.

The 13 July 2004 heavy rainfalls were caused by a rainy season front. The greatest damage came from an overflow of the Kariyata River on the plains. In the Izumozaki area, many landslides occurred and one person was lost. Kawashima et al. (2005) reported detailed data of precipitation. In the town office of Izumozaki and Mishima, which are close to the study area, the daily precipitation was approximately 350–370 mm. The maximum hourly precipitation in the Izumozaki area was approximately 50 mm (Yamagishi et al. 2008).

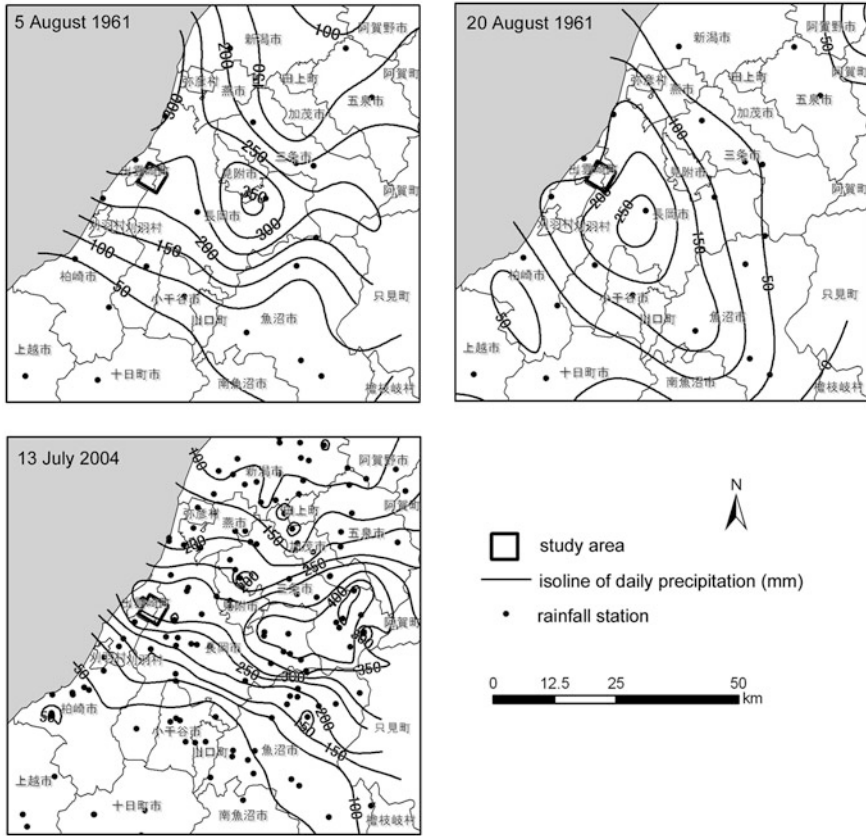


Fig. 2.3 Distribution maps of daily precipitation of the August 1961 heavy rainfalls (*upper-right* and *upper-left*) and July 2004 heavy rainfalls (*lower-left*). Precipitation data are from Society of Agricultural Meteorology of Niigata Prefecture (1961), Kawashima et al. (2005). Isolines of daily precipitations were interpolated by spline interpolation from the data of rainfall stations

As described above, the two events were different in their rainfall processes. The August 1961 heavy rainfalls occurred twice in two weeks. The June 2004 heavy rainfalls were all at once, however, it rained harder than the August 1961 heavy rainfalls (Fig. 2.3).

2.4 Preparation of GIS Data

2.4.1 Preparation of Landslide Inventory Data

Positional accuracy of landslide distributions is the key for this study. We made an effort to digitize accurate landslide polygons. At first, photographic papers of aerial photographs of 1961 and 2004 were used to grasp rough locations of landslides by a three-dimensional view. 1:20,000 scaled monochrome aerial photographs taken by GSI on May 20, 1962, were used for the landslides caused by the August 1961 heavy rainfalls (hereinafter referred to as the August 1961 landslides). These photographs were taken nine months after the heavy rainfalls; however, disaster-relief work had not been done and locations of the landslides were easily identified. 1:25,000 scaled color aerial photographs taken by GSI on the July 24, 2004, were used for the landslides caused by the 13 July 2004 heavy rainfalls (hereinafter referred to as the July 2004 landslides). In this study, we digitized landslide polygons on 50-cm resolution ortho-photoimagery. The ortho-photoimagery was created by ERDAS Imagine (Hexagon Geospatial) using 1200 dpi scanned films of aerial photographs. We digitized landslide polygons using ArcGIS (ESRI). By enlarging the ortho-photoimagery on a PC monitor, small landslides with a width of several meters were identified and accurate polygons were digitized.

For terrain data, we used a 2-m DEM derived from LiDAR data surveyed on the November 3, 2007. The study area experienced the 2004 Niigata Prefecture Chuetsu Earthquake (M 6.8) on the October 23, 2004. However, the earthquake brought on a few landslides in the study area (Iwahashi et al. 2008). Compared with the 24 July 2004 aerial photographs, we found almost no new landslides on the digital aerial photographs taken at the same time with LiDAR.

Lithology, positional relationships with roads, positional relationships with the 1961 landslides (for the July 2004 landslides only) were inputs as attributes of landslide polygons. Areas of landslides were calculated using the GIS software.

We used a compiled and simplified 1:50,000 geological map (Fig. 2.1) as the basis for lithological data. A 1:50,000 map scale is too small compared with the resolution of the DEM. Therefore, we modified the attributes of landslide polygons manually, especially in the case that the location of alluvium (inferred from the shaded relief image of LiDAR DEM) was overlaid in the polygons of mountainous rocks in the GIS data of lithology.

We have classified positional relationships between the landslides and the roads, as landslides in natural slopes and landslides in road slopes. Road slopes were certified using the shaded relief image created by the 2-m DEM. We also defined the new or widened roads that were not shown in the 20 May 1962 aerial photographs, as newly constructed roads after 1962.

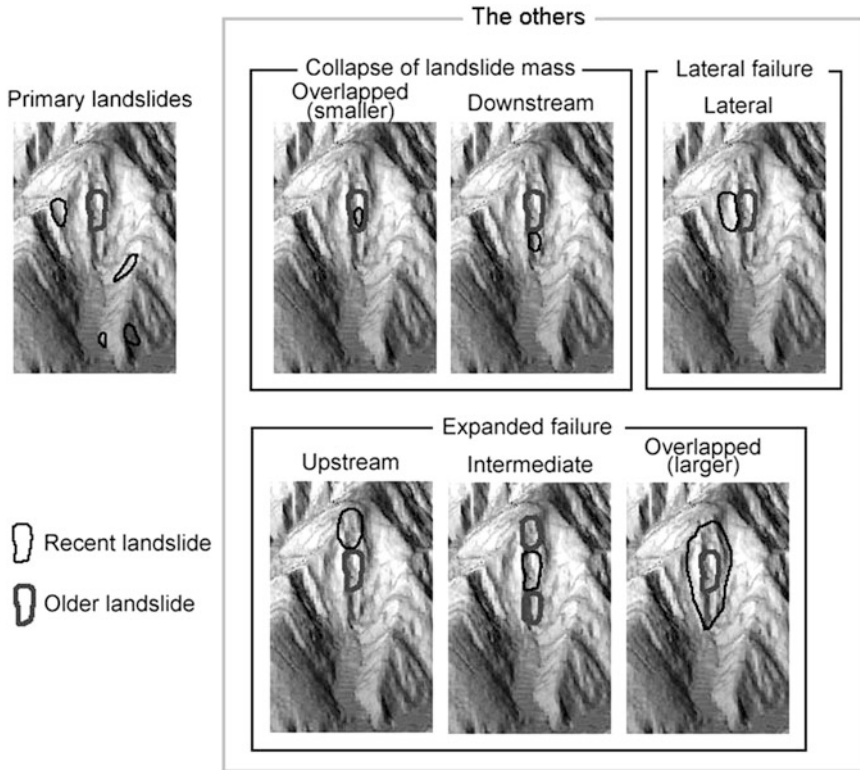


Fig. 2.4 Images showing frame formats of positional relations between new and old landslides. In this figure, gray polygons and black ones indicate 1961 landslides and 2004 landslides, respectively

The July 2004 landslides can be classified into primary landslides, meaning those without any relationship to the August 1961 landslides in the same valley side slope, and other landslides with the August 1961 landslides in the same valley side slope. Moreover, we re-classified the other landslides as follows. Figure 2.4 shows schematic images of the descriptions.

- Overlapped (smaller): small landslide occurred on the 1961 landslide*
- Downstream: landslide occurred in a downstream valley of the 1961 landslide*
- Lateral: landslide occurred in a close lateral valley of the 1961 landslide*
- Upstream: landslide occurred in an upstream valley of the 1961 landslide*
- Intermediate: landslide occurred between the two 1961 landslides*
- Overlapped (larger): large landslide occurred on and around the small 1961 landslide*

horizontal dip	daylighting dip	parallel dip	hangnail dip	vertical dip	infacing dip
	outfacing dip				
$\gamma = 0^\circ$	$0^\circ < \gamma < \theta$	$\gamma = \theta$	$\theta < \gamma < 90^\circ$	$\gamma = 90^\circ$	$90^\circ < \gamma < 180^\circ$
stable	extremely unstable	stable to unstable	stable	stable to rather unstable	stable

Fig. 2.5 Classification of the structure of stratum defined by relational inclination between surface slope gradient (θ) and slope gradient of geological discontinuity planes (γ) such as planes of stratification or joint face (Suzuki 2000)

2.4.2 Preparation of the Data for Structure of Stratum

We created the data for the inner structure of stratum for each geological formation using the slope gradient and the slope orientation calculated from the 2-m DEM, and strike and dip data digitized from the 1:50,000 geological maps (Kobayashi et al. 1993; Kobayashi et al. 1995, 2001) adding 13 point data measured at the foot of mountains from Yamagishi et al. (2005). The data show the area of classified groups for the structure of stratum according to Suzuki (2000) (Fig. 2.5).

Since the data of dip and strike are based on descriptions in the 1:50,000 geological maps, positional accuracy of the data is not commensurate with the 2-m DEM. However, since the orientations of strata are broadly constant between fold axes, we thought the problem would not have a significant effect on the results. Meanwhile, the resolution of DEM will cause a significant problem for preparing the data of the structure of stratum. A high-resolution DEM was needed to prepare surface slope orientation data which express the real situation of slopes. The method of preparation of the data is described in Fig. 2.6.

In the classification, we omitted the slopes where the geological surface was in a direction perpendicular to the ground surface (approximately 26% in the mountain slope), because we cannot determine if those slopes are infacing or outfacing. We classified infacing dips into two categories: those in which the dip is greater or less than 40°. In the case of outfacing dips, the dip degrees were already taken into account when classifying daylighting dip, parallel dip, and hangnail dip (Fig. 2.5). There are no vertical dip slopes in the study area.

2.4.2.1 Slope Angles of Mountains for Each Geological Structure of Stratum

The average slope angles for each geological structure type of stratum calculated by the 2-m DEM are shown in Table 2.1. The average slope gradients in Table 2.1 are the values for the all mountain slopes including landslides.

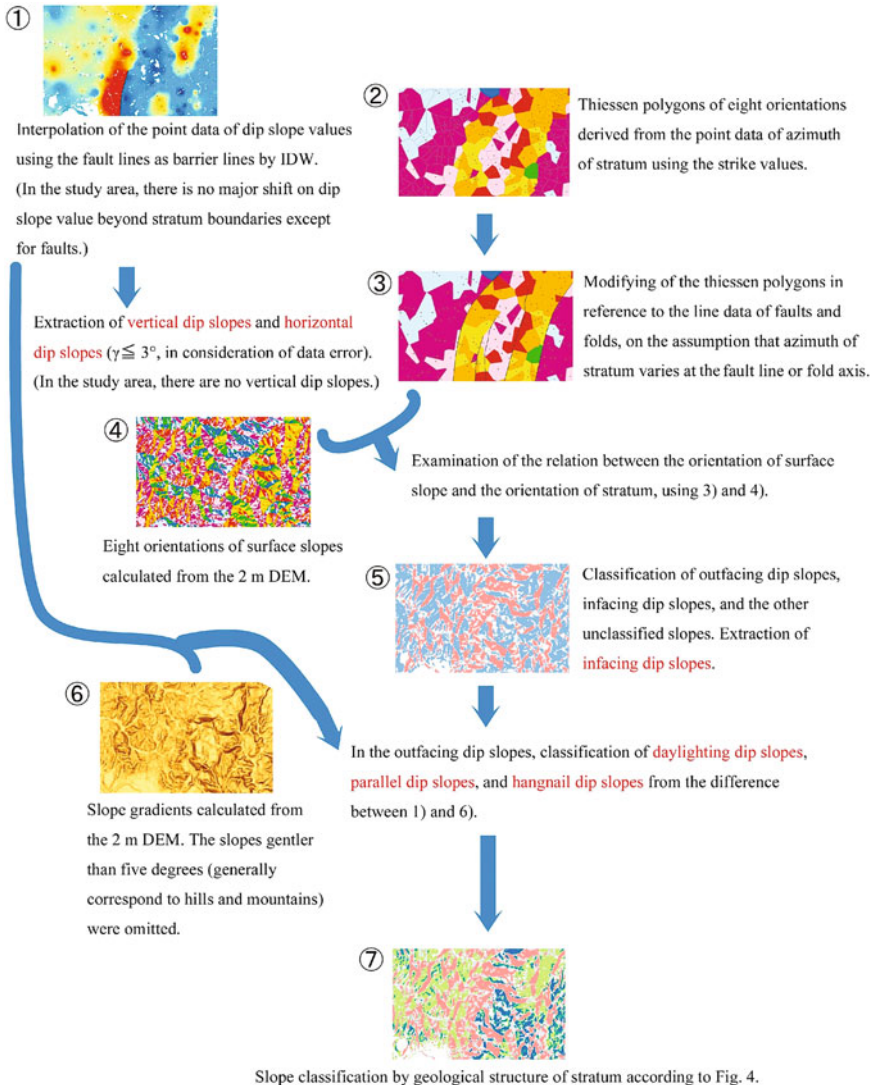







Fig. 2.6 Method of preparation of the data for structure of stratum using GIS

It is estimated that steep slopes are mainly distributed in hangnail dips in the Uonuma formation (sand dominated) and the Haizume formation (sandy siltstone), and parallel and hangnail dips in the Nishiyama formation (massive mudstone) and the Shiiya formation (sandstone dominated). Around the study area, especially hangnail dip slopes are stable (Suzuki 2000), and it is known there were few occurrences of slope failure in the Chuetsu Earthquake (Sasaki et al. 2006). The presence of many steep slopes does not always mean the area is unstable in high-resolution observation.

Table 2.1 Geological structures for stratum and the average slope gradient (°) according to the formations

	Uonuma formation (sand dominated)	Haizume formation (sandy siltstone)	Nishiyama formation (massive mudstone)	Shiia formation (interbedded sandstone and mudstone)
Daylighting dip 	18.4	23.9	29.0	27.8
Parallel dip 	18.9	27.7	38.8	42.1
Hangnail dip 	29.2	36.2	39.0	43.2
Infacing dip (dip < 40) 	23.0	28.2	27.4	33.8
Infacing dip (dip > 40) 	22.5	31.1	32.9	29.6

To determine average slope gradients, the slopes less than 5° calculated in 5 by 5 cell windows, which coincided with valley bottoms or plains, were omitted

In the Uonuma formation (sand dominated), the Haizume formation (sandy siltstone), and the Shiia formation (interbedded sandstone and mudstone), infacing dip slopes are steeper than daylighting dip slopes or parallel dip slopes. On the contrary, the Nishiyama formation (massive mudstone) shows no concrete tendency.

2.5 Results

2.5.1 Comparison of the Densities of the August 1961 and July 2004 Landslides

Table 2.2 shows the number of landslides for each lithological unit. Landslide numbers and areas for the July 2004 landslides were 1/2–1/3 of those in the August 1961 landslides. In both disasters, landslides occurred most frequently on the slopes

Table 2.2 Number of landslides for each lithological unit

	August 1961	July 2004	A/B	Average value of slope gradient (°)
	Number of landslides/km ² (A)	Number of landslides/km ² (B)		
Uonuma formation (sand dominated)	134.4	47.8	2.8	21.4
Haizume formation (sandy siltstone)	152.1	56.2	2.7	26.5
Nishiyama formation (massive mudstone)	184.3	74.2	2.5	29.9
Shiia formation (interbedded sandstone and mudstone)	88.6	43.3	2.0	28.4

Table 2.3 Number of landslides for each category of geological structure of stratum

	August 1961		July 2004	
	Number of landslides	%	Number of landslides	%
Daylighting dip	776	29.7	375	36.5
Parallel dip	21	0.8	7	0.7
Hangnail dip	206	7.9	95	9.3
Infacing dip (dip < 40°)	218	8.3	109	10.6
Infacing dip (dip > 40°)	680	26.0	173	16.8
Not categorized	710	27.2	268	26.1

of the Nishiyama formation (massive mudstone) and less frequently on the slopes of the Shiiya formation (interbedded sandstone and mudstone), although average slope angle is the largest in the Shiiya formation.

Table 2.3 shows landslide densities for each geological structure type of stratum. In the infacing dip slopes whose dip is steeper than 40°, number densities of landslides in the August 1961 landslides are 10% larger than those in the July 2004 landslides. In the daylighting dip slopes, the number is 5% less than those in the July 2004 landslides. Differences of other values are less than a few percentage points; the overall trends observed in Table 2.3 are similar in the two disasters.

However, different characteristics were observed in the frequency of the structure of stratum of the two categories of the July 2004 landslides: isolated landslides which occurred in the different slopes of the August 1961 landslides (primary landslides) and landslides which occurred in the same side slope of the August 1961 landslides. We describe this in the next section.

2.5.2 Position of the July 2004 Landslides in Relation to the August 1961 Landslides

Among the July 2004 landslides, 70% of landslides in number and 54% of landslides in area are regarded as primary landslides, and the other landslides occurred in the same valley side slopes (Table 2.4).

As can be inferred from the median values of the area of landslides, *Upstream*, *Intermediate*, and *Overlapped (larger)* types are mainly large landslides and indicated to be expanded failures of older ones. Most of these expanded type landslides are the *Upstream* type.

The sum of the numbers of *Overlapped (smaller)* and *Downstream* types is approximately half of the July 2004 landslides which occurred in the same valley side slope of the August 1961 landslides. Among these, especially the *Overlapped (smaller)* type is dominant. *Overlapped (smaller)* and *Downstream* types are inferred to be collapses of landslide masses of the August 1961 landslides. *Lateral* type landslides are also small. The median values of the area of those small landslides are close to the value of primary landslides (83 m²).

Table 2.4 Position of the July 2004 landslides in relation to the August 1961 landslides

Type of the July 2004 landslides	Number of landslides	%	Total area of landslides (ha)	%	Median area of landslides (m ²)
Primary	724	70.5	13.54	54.0	83
Overlapped (smaller)	125	9.8	1.78	7.1	60
Downstream	31	2.4	0.76	3.0	92
Lateral	59	5.7	1.27	5.1	93
Upstream	69	5.4	4.28	17.1	307
Intermediate	5	0.4	0.22	0.9	525
Overlapped (larger)	14	1.1	3.21	12.8	1874

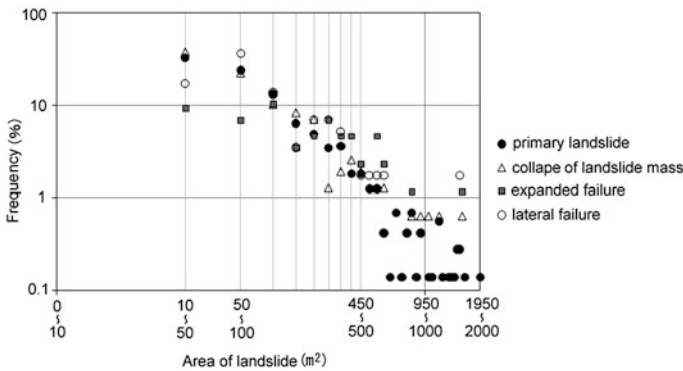


Fig. 2.7 Frequency distribution of landslides. Landslides larger than 2000 m² are not included in this figure. Axes of the graph are in logarithmic scale

Figure 2.7 shows the size-frequency distribution of the July 2004 landslides, for the primary landslides and the other landslides. The sizes were calculated by GIS using landslide polygons. The size distribution of the primary landslides is close to a power-law distribution. There are many *Lateral* type landslides in a range between 50 and 100 m². The slope of the graph of the expanded failures is significantly different from that of the primary landslides.

Figure 2.8 shows pie charts of the geological structure of stratum in relation to the types of the July 2004 landslides. The pie charts of “all mountain slope” indicate a standard of ratio of geological structure for each lithological unit. All charts of the primary landslides are similar to the charts of all mountain slopes. This fact indicates that the influence of geological structure on the occurrence of primary landslides is small. In contrast, except for the Nishiyama formation (massive mudstone), expanded type landslides include a larger ratio of daylighting dip slopes than the original percentage shown in the pie charts of “all mountain slope.” In the case of sandstone slopes, it can be estimated from the pie charts that collapse of landslide masses and lateral landslides mainly occurred in the infacing dip slopes.

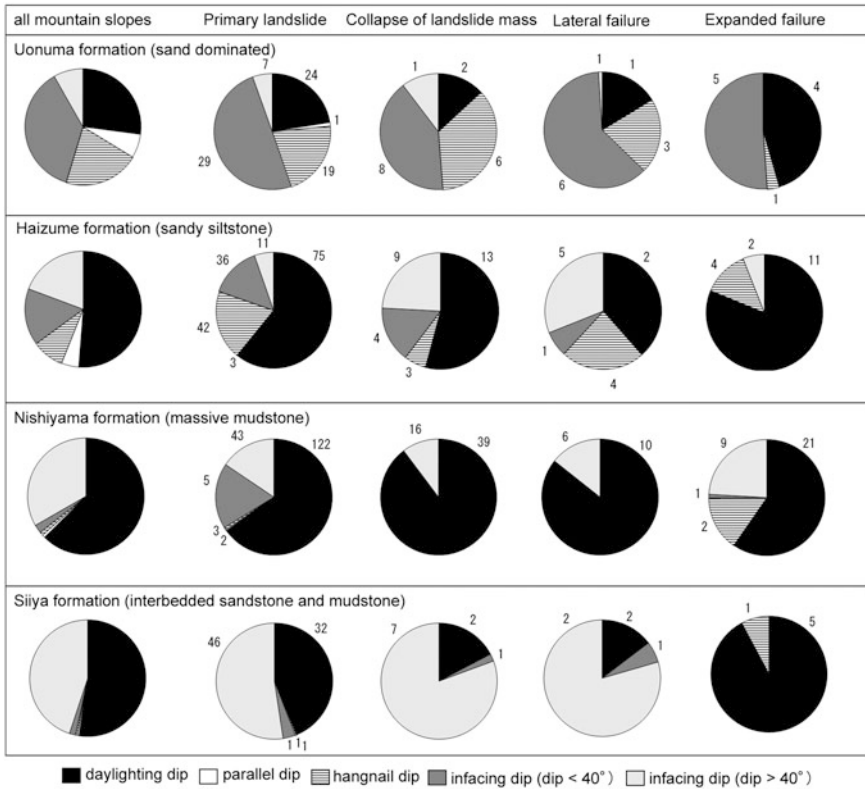


Fig. 2.8 Pie charts showing positional relations between geological structures in the July 2004 landslides and the August 1961 landslides. Angles of pie charts indicate the area ratio. *Subscripts* are numbers of landslides. The *leftmost pie* chart shows the area ratio in all mountain slopes

2.5.3 Landslides Along the Roads

Observing the landslide distributions (Fig. 2.9), there is a significant difference between the spatial distributions of the August 1961 and July 2004 landslides separate from geology. Though the July 2004 landslides were considerably less than the August 1961 landslides, the July 2004 landslides are prominent in that there were many landslides in artificial slopes around roads. Before 1961, the only road which had been constructed by cutting the hillside slopes was Route 352; most roads were constructed along the lines of the feet or ridges of mountains. In 1962–2004, many forest roads were constructed by cutting or filling. In the study area, most of the artificial slopes of the new roads are covered by wire mesh and grass seed spraying; shotcrete or mold blocks are seldom used for slope protection.

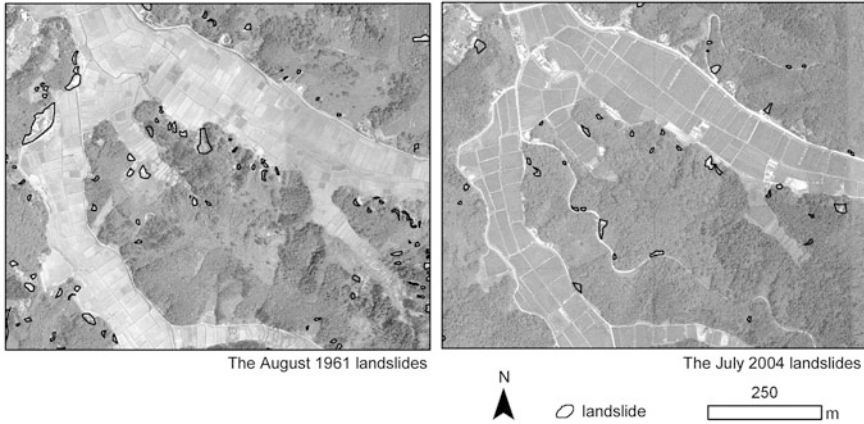


Fig. 2.9 August 1961 landslides (*left* the background air-photograph was shot by GSI in 1962) and the June 2004 landslides (*right* the background air-photograph was shot by GSI at shortly after the heavy rainfalls) around Kamijo in Izumozaki town

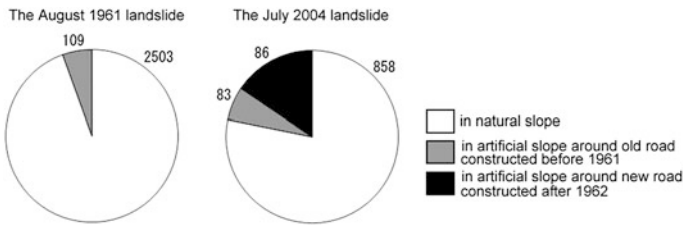


Fig. 2.10 Pie charts showing the comparison between the August 1961 landslides and the July 2004 landslides along roads. Angles of pie charts indicate the area ratio. *Subscripts* are numbers of landslides

Figure 2.10 shows the pie charts which show the areas of landslides in natural slopes, in artificial slopes around old roads constructed before 1961, and in artificial slopes around new roads constructed after 1962. Landslides that occurred in artificial slopes around roads are only 4.2% (109 per 2612 in number) of the August 1961 landslides, however, are 16.4% (169 per 1028 in number) of the July 2004 landslides. It is clear from the charts that the increase of landslides occurring in artificial slopes comes from the landslides around new roads.

Positional relationship between the type of landslide based on Fig. 2.4 and roads are shown in Fig. 2.11. Figure 2.11 reveals the following. In the sandstone slopes, most of the landslides around the new roads constructed after 1962 were primary landslides. In contrast, large expanded landslides significantly occurred around the new roads in massive mudstone slopes.

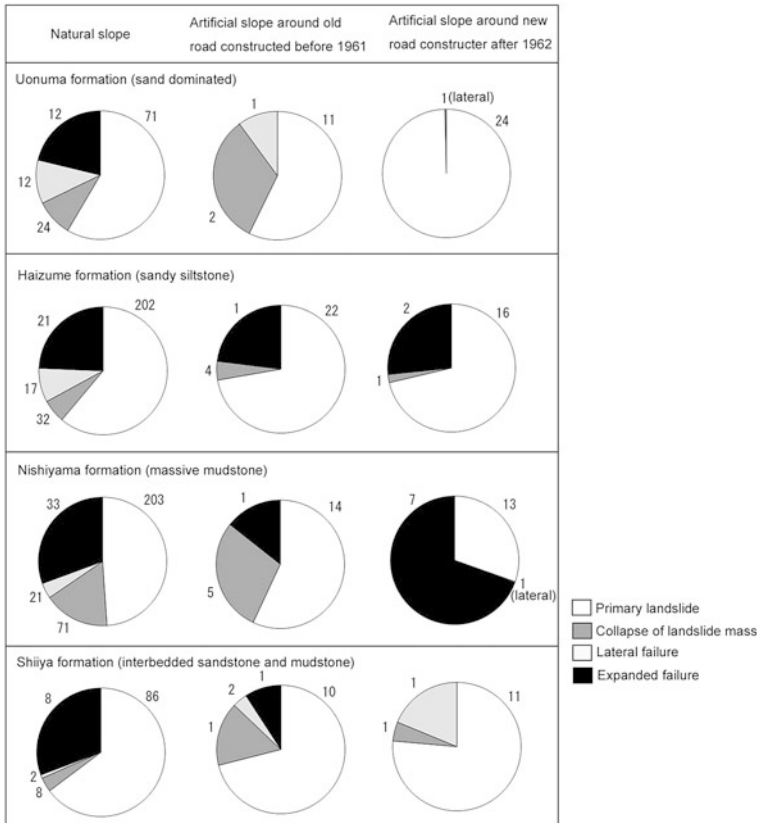


Fig. 2.11 Pie charts showing classifications of the July 2004 landslides on the basis of Fig. 2.4 for each lithological unit, and positional relation with roads. Angles of pie charts indicate the area ratio. *Subscripts* are numbers of landslides

2.6 Discussion and Conclusion

The August 1961 heavy rainfalls were twice in two weeks. The June 2004 heavy rainfalls were all at once, however, in 2004 it rained harder than the August 1961 heavy rainfalls according to the daily precipitation in the study area (Fig. 2.3). Those different rainfall processes are probably related to the landslide densities per lithological unit (Table 2.2).

Seventy percent (in number) of the July 2004 landslides were small primary landslides which occurred in valley side slopes not affected by the August 1961 landslides. On any lithological unit, the pie charts of the types of geological structure for primary landslides (Fig. 2.7) are similar to those of all mountain slopes. This indicates that primary landslides occurred randomly. Therefore, even a

simple method using topographical attributes such as slope gradient and convexity will be able to bring a valuable hazard evaluation for primary shallow landslides in the slopes without old landslides.

The other landslides which occurred in the same valley side slopes of the August 1961 landslides can be classified into (1) collapse of landslide mass of the August 1961 landslide, (2) expanded failure of the August 1961 landslide, and (3) landslide occurred in a close lateral valley of the August 1961 landslide. Though Type 1 is the largest in the number of landslides, Type 2 should be noticed, because Type 2 landslides are the largest in scale and they significantly affect human society. After our analyses using GIS, most of the expanded failures (Type 2) are slope failures of upstream slopes of the August 1961 landslides. Except for the slopes of the Nishiyama formation (massive mudstone), expanded failures (Type 2) often occurred in daylighting dip slopes (Fig. 2.5). Therefore, daylighting dip slopes of sedimentary rocks, which have a clear layered structure and an old landslide in their downstream, should be noted. For the slopes which have a history of slope movement in the last several decades, extensive mapping of landslide distribution and information of the geological structure of stratum are more important than topography.

Artificial steep slopes cut along new forest roads cannot be disregarded because they are outstanding origins of recent landslides. In the July 2004 landslides, differences of landslide type (Fig. 2.4) are observed according to the geological structure of stratum (Fig. 2.11). In the sandstone slopes (the Uonuma and Shiya formation), most of the landslides around the new roads constructed after 1962 were primary landslides. In contrast, large expanded failures significantly occurred around the new roads in massive mudstone slopes (the Nishiyama formation).

References

- Iwahashi J, Yamagishi H (2010) A reinvestigation on spatial distribution of shallow landslides induced by the August 1961 and the July 2004 heavy-rainfalls in Izumozaki area, Niigata—GIS analyses using high resolution ortho images and a 2-m DEM. *J Jpn Landslide Soc* 5 (47):274–282 (in Japanese with English abstract). https://www.jstage.jst.go.jp/article/jls/47/5/47_5_274/_pdf. Accessed 18 Feb 2013
- Iwahashi J, Yamagishi H, Kamiya I, Sato HP (2008) Discriminant analysis for landslides caused by the 2004 Niigata heavy rainfall in July and the Mid Niigata prefecture earthquake in October. *J Jpn Landslide Soc* 45(1):1–12 (in Japanese with English abstract and figures). https://www.jstage.jst.go.jp/article/jls/45/1/45_1_1/_pdf. Accessed 18 Feb 2013
- Kawashima K, Izumi K, Iyobe T (2005) Outline of climate and detailed precipitation in 2004, July at the Niigata-Fukushima heavy rainfall disasters. Report of grants-in-aid for scientific research (No. 16800001), pp 23–39 (in Japanese)
- Kobayashi I, Tateishi M, Uemura T (1993) Geology of the Izumozaki district. Quadrangle series, scale 1:50,000. Geological Survey of Japan, 91p (1 sheet)
- Kobayashi I, Tateishi M, Yoshimura T, Ueda T, Kato H (1995) Geology of the Kashiwazaki district. Quadrangle series, scale 1:50,000. Geological Survey of Japan, 101p (1 sheet)
- Kobayashi I, Tateishi M, Komatsubara T (2001) Geology of the Sanjo district. Quadrangle series, scale 1:50,000. Geological Survey of Japan, 98p (1 sheet)

- Nozaki T (1994) Mechanical properties of landslide-mother-rocks in Niigata Prefecture (I)—laboratory test of intact rocks. *J Jpn Landslide Soc* 2(31):17–23 (in Japanese with English abstract and figures). https://www.jstage.jst.go.jp/article/jls1964/31/2/31_2_17/_pdf. Accessed 18 Feb 2013
- Nozaki T (1995) Mechanical properties of landslide-mother-rocks in Niigata Prefecture (II)—laboratory test of intact rocks. *J Jpn Landslide Soc* 2(32):17–25 (in Japanese with English abstract and figures). https://www.jstage.jst.go.jp/article/jls1964/32/2/32_2_17/_pdf. Accessed 18 Feb 2013
- Saito M (2007) Landslides induced by the 2004 July 13 heavy rainfalls in the Izumozaki area—investigation of topographical and geological causes. Research report of in 2006 fiscal year. Graduate School of Science and Technology, Niigata University, 119p (in Japanese with English abstract)
- Sasaki Y, Shiomi T, Anan S (2006) Landform and geology, in report on damage to infrastructures by the 2004 Mid Niigata prefecture earthquake. Research report of public works research institute no. 203. National Institute for Land and Infrastructure Management, 24p (in Japanese). <http://www.nilim.go.jp/lab/bcg/siryou/rpn/rpn0027.htm>. Accessed 18 Feb 2013
- Society of Agricultural Meteorology of Niigata Prefecture (1961) Nourin kisyo (Agricultural meteorology), vol 9, No. 8, 17p (in Japanese)
- Suzuki T (2000) Introduction to map reading for civil engineers, vol 3. Terrace Hills and Mountain. Kokon-shoin, 942p (in Japanese)
- Takeuchi K, Yanagisawa Y, Miyazaki J, Ozaki M (2004) 1:50,000 Digital geological map of the Unuma region, Niigata prefecture (ver. 1). Open-file report. Geological Survey of Japan, No. 412, 9p (1 CD-ROM)
- Tokyo District Meteorological Observatory (1961) Tokyo kanku ijo kisho hokoku (Report of abnormal climate in Tokyo district), July–Sept 1961, vol 2, No. 3, pp 15–23 (in Japanese)
- Yamagishi H, Ayalew L, Watanabe N, Marui H, Kawabe H (2005) Landslides induced by the July 13, 2004 heavy rainfall in Mid Niigata Region. Report of grants-in-aid for scientific research (No. 16800001), pp 84–93 (in Japanese)
- Yamagishi H, Saito M, Iwahashi J (2008) The characteristics of the heavy rainfall-induced landslides in Izumozaki area, Niigata, Japan—GIS using comparison between 2004 July failures and the past ones. *J Jpn Landslide Soc* 45(1):57–63 (in Japanese with English abstract and figures) https://www.jstage.jst.go.jp/article/jls/45/1/45_1_57/_pdf. Accessed 18 Feb 2013

Chapter 3

Landslide Surface Deformation Detected by Synthetic Aperture Radar (SAR) Interferometry in Shizu Area on the Southern Foot of Mt. Gassan, Japan

Hiroshi P. Sato and Akira Suzuki

Abstract L-band (22.36 cm in wavelength) radars such as ALOS (Advanced Land Observing Satellite)/PALSAR (Phased Array type L-band Synthetic Aperture Radar) are suitable for observing landslide surface deformation in Japan. In this study, we produced InSAR (SAR interferometry) images using PALSAR data and observed the fringes produced; after subtracting orbital and topographic fringes, the resulted fringe indicated a 2×1 km landslide surface deformation on the southern foot of Mt. Gassan (stratovolcano, 1,994 m in elevation) in Japan; this landslide is actually a reactivated old landslide. According to a previous study, slide surfaces can be identified both in the deposits and in the underlying mudstone, which has a maximum depth of 160 m from the ground surface. The InSAR image indicated surface deformation at more than half of the L-band wavelength along the LoS (line of sight). Because of the good coherence (0.4–0.6) of the obtained InSAR image, we unwrapped the phase of the InSAR image and obtained a continuous phase. We found that the detected landslide deformation could be separated into two sections: a fluvial erosion-affected section and an upper slope section. In the former section, repeated surface deformation between 0 and 7 cm along the LoS implies the deformation by many sub-slide surfaces. In the latter section, surface deformation along LoS uniformly increased from 2.5 cm at the upper scarp to 13.5 cm at the foot of the slopes; this implies that one large rigid landslide block controls surface deformation. An on-site GPS survey of the fluvial erosion-affected section revealed the landslide's surface deformation, and the measurement results from the GPS survey show good agreement with the InSAR results.

Keywords Landslide · SAR · GPS · InSAR

H.P. Sato (✉)

Department of Geography, College of Humanities and Sciences, Nihon University,
3-25-40 Sakura-Josui, Setagaya Ward, 156-8550 Tokyo, Japan
e-mail: satou.hiroshi37@nihon-u.ac.jp

A. Suzuki

Geospatial Information Authority of Japan (GSI), 1 Kitasato, 305-0811 Tsukuba, Japan

© Springer Japan KK 2017

H. Yamagishi and N.P. Bhandary (eds.), *GIS Landslide*,

DOI 10.1007/978-4-431-54391-6_3

3.1 Introduction

A synthetic aperture radar (SAR) is an active microwave imaging system used to monitor Earth's surface, and it has cloud-penetrating as well as day/night operational capabilities. This remote sensing technique has been developed for acquiring digital elevation models (DEM) or crustal dynamics deformations since the 1970s, facilitated by the development of specific data processing techniques such as Zebker and Goldstein (1986) or Massonnet et al. (1993).

SAR interferometry (InSAR) has piqued maximum interest among researchers concerned with landslides. L-band InSAR applications have already been reported in landslide studies. Kimura and Yamaguchi (2000) measured landslide deformation on the slope near the Itaya abandoned mine, Yamagata Prefecture, Japan, using InSAR images from JERS-1 (Japanese Earth Resources Satellite-1, launched by the Japan Aerospace Exploration Agency < JAXA >)/SAR (L-band, 22.36 cm in wavelength) data. Catani et al. (2005) also measured ca. 4 cm landslide deformation per 44 days along line of sight (LoS: line through the satellite above the ground and target on the ground) on the slope of Mt. Rasciesa, close to Bolzano in the Italian Alps using JERS-1/SAR data. However, these studies do not consider the ground truth data to evaluate the measurement result. Payret et al. (2008) measured landslide deformation at the Kahrod landslide in the Alboz range (Iran) using InSAR images from ENVISAT (Environmental Satellite)/ASAR (Advanced SAR) data (C-band: wavelength is 5.66 cm). They reported that on-site GPS survey's results had good consistency with the 35-day InSAR measurement result. They also reported that coherence, that is explained in Sect. 3.3.3, is good for the 35-day InSAR image because the landslide area is free of any significant vegetation.

However, the humid climate in Japan induces rapid and dense vegetation growth, and a C-band microwave is reflected by the top layer of the canopy; two SAR observations do not give better coherence in an InSAR image. In contrast, an L-band microwave can penetrate through vegetation. Therefore, an L-band radar such as ALOS (Advanced Land Observing Satellite, launched by JAXA)/PALSAR (Phased Array type L-band SAR) is more suitable for observing landslide deformation in Japan. In this study, we show landslide measurement results using InSAR images derived from ALOS/PALSAR data, and we will evaluate InSAR measurement results using on-site GPS survey's results for the study area.

3.2 Study Area

This study focused on the Shizu area (Figs. 3.1a, 3.1b; 38.491232°N, 140.001°E) in Nishikawa Town, Yamagata Prefecture, Japan, on the southern foot of Mt. Gassan (elevation: 1,984 m). Mt. Gassan is a stratovolcano, and its volcanic activity began in the late Pleistocene (ca. 88,000 years ago) and ceased ca. 36,000 years ago or later (Nakazato et al. 1996). Pre-Neogene granite and Neogene volcanic rocks, tuff,

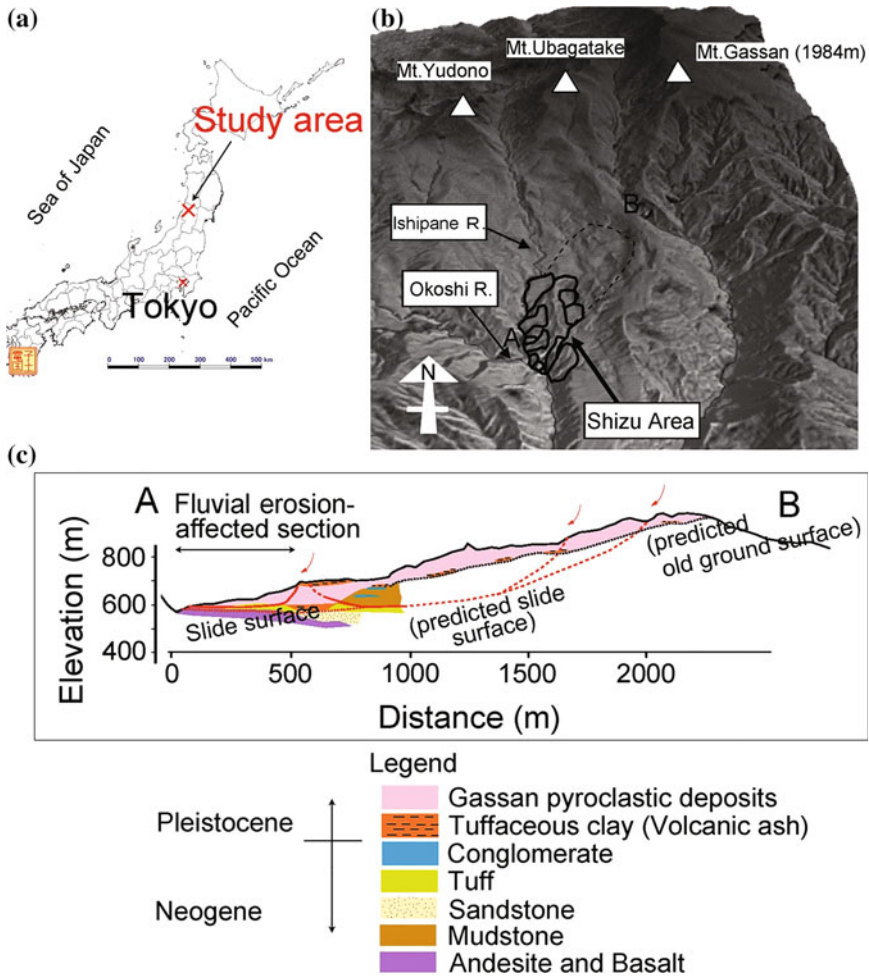


Fig. 3.1 Study area on the southern foot of Mt. Gassan (Hanaoka et al. 2011, revised). **a** An index map, **b** a bird's eye view of the study area, and **c** the geologic cross section (A–B, the location is shown in **b**)

and mudstone (Yamagata Prefecture 1974) are overlaid by the Gassan's lava, pyroclastic flow deposits, and pyroclastic debris from an avalanche that occurred at the time of the later volcanic activity (Nakazato et al. 1996). In Shizu area, a thick debris avalanche deposit stratum covers the Neogene stratum as shown in geologic section A–B (Fig. 3.1c, location of the A–B is shown in Fig. 3.1b), and an unconformity exists between both strata; the presence of partial tuffaceous clay (volcanic ash) that contains sharp thin lacustrine deposit layers complicates the geologic stratum (Hanaoka et al. 2011).

The active landslide block extends into the area 2 km along the slope length and 1 km along both the Okoshi River and its branch, the Ishipane River (Fig. 3.1b). In Fig. 3.1b, current-activated landslide blocks (section affected by fluvial erosion of Ishipane River) are delineated by a black solid line, and the old landslide area is delineated by a dashed line. The slide surface is estimated to lie in Pleistocene debris avalanche deposits and Neogene sediments, and the maximum depth of the slide surface in the Neogene sediments is ca. 160 m below the ground surface. Many slickensides and striae are confirmed by boring into the tuff and mudstone layer that is a few tens of meters in thickness. This data supports the conclusion that these landslides were sequentially activated (Hanaoka et al. 2011).

3.3 Method

3.3.1 SAR Geometry and Data Used in This Study

As shown in Fig. 3.2, our study used InSAR images that covered a swath of ca. 70 km on the ground. In order to produce InSAR image, InSAR needs to observe a given location twice. However, because satellites do not move along a fixed track, but have orbits that can vary slightly in the space, the first observation may not be in full agreement with the second; i.e., the observations reflect the differences in the orbital tracks. The index of the difference between the positions is B_{PERP} (Fig. 3.2)—the vertical component of the length from the position of the second observation satellite to the LoS of the first observation. Further, Fig. 3.2 shows that as ALOS moves along the descending (southward) orbit, the azimuth (along-track) direction is southward. The range (cross-track) direction is westward and downward; this is the condition under which microwaves are transmitted from the radar. ALOS/PALSAR, 695 km above the ground, observes the study area from an oblique LoS.

Fig. 3.2 Geometry of InSAR observations (descending orbit)

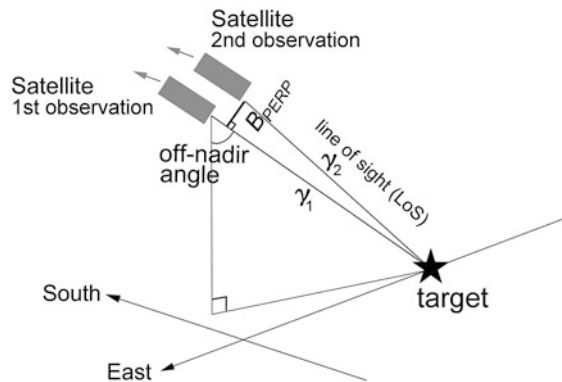


Table 3.1 Specifications of ALOS/PALSAR data

Master	Slave	Orbit	Path	Frame	B_{PERP}	Off-nadir angle
September 12, 2006	September 17, 2008	Descending	58	2840	+104 m	34.3°

The first and second images obtained by SAR are called the master and the slave images, respectively. In this study, we used the SAR images observed from a descending orbit as shown in Table 3.1. In Table 3.1, B_{PERP} is also described; for InSAR processing, the longer the B_{PERP} , the weaker is the coherence. Therefore, in this study, we selected a combination of images whose B_{PERP} was less than 1500 m and hence yielded good coherence for accurately estimating surface deformation.

InSAR images, the phase and amplitude (intensity of backscattering on the ground) are stored as a complex number. A slope away from the radar transmission with an angle that is steeper than the off-nadir angle (Fig. 3.2) provokes radar shadows (European Space Agency 2000). Resolution of an ALOS/PALSAR image is ca. 10 m on the ground at the center of swath; however, since this study adapts two-look processing to reduce phase noise, resolution is ca. 20 m on the ground because the real part and the imaginary part of the complex number are added, respectively, between master and slave SAR images.

In principle, InSAR deformation measurement precision is on the order of millimeters (Geospatial Information Authority of Japan 2004). However, owing to various errors caused by meteorological, ionospheric, and temporal changes in the scatters as well as due to different looking-angles from the satellites and other conditions, precision of each InSAR image with respect to deformation measurement is different. Such errors caused by observational conditions are relatively easy to remove, but it is difficult to fully remove errors caused by meteorological or ionospheric conditions. In the 1992 Landers earthquake's case, precision of InSAR measurement result of deformation was 3.4 cm in root mean square errors, as checking up the result of geodetic survey on the nine control points (Massonet et al. 1993). Therefore, centimetric surface deformation (Ferretti et al. 2000) more than ca. 3 cm along LoS can be measured. For understanding in detail, the InSAR processing method refer to previous reports such those of Tobita et al. (1998) and Colesanti and Wasowski (2006).

3.3.2 SAR Data Processing

In this study, the main processes considered include (1) interferometric processing, (2) orbit and topographic phase removing, (3) filtering for reduction of phase noise, (4) phase unwrapping, and (5) conversion of the unwrapped phase to the LoS distance (slant range) change.

1. Interferometric processing

Until recently, the phase of a SAR image was not tended to consider since it is uniformly distributed in the interval $[-\pi, \pi]$ for rough surfaces (single look complex) (Wegmüller et al. 2000). However, in situations where two SAR images are acquired from almost the same orbit, the phase difference φ is related to the LoS distance change Eq. (3.1)

$$\varphi = -\frac{4\pi}{\lambda}(|\gamma_1| - |\gamma_2|), \quad (3.1)$$

where λ is microwave wavelength, $|\gamma_1|$ and $|\gamma_2|$ are the distance from the satellite to the target on the ground along the LoS for the first observation and that for the second observation, respectively. The phase difference φ results in a fringe pattern, also called an interferogram.

2. Orbital and topographic phase term removing

Since an orbital phase can be simulated using the two measurements of satellite positions, γ_1 and γ_2 , the orbital phase was removed from the InSAR image to obtain a flattened InSAR image. The topographic phase contained in the InSAR image was also removed using a simulated topographic phase, which was subtracted from the InSAR image to obtain the residual phase; here, we used a 50-m-resolution Digital Elevation Model (DEM) from a contour map published by the Geospatial Information Authority of Japan.

3. Filtering for reduction of phase noise

Phase noise was reduced by the adaptive filtering method, which reflects variable low-band pass characteristics derived directly from the power spectrum of the fringes in the InSAR image (Goldstein and Werner 1998). Finally, the SAR image was obtained.

4. Phase unwrapping

The obtained phase in the InSAR image is limited only in one cycle $[-\pi, \pi]$; however, the continuous whole phase at each point needs to be recovered to describe real surface deformation. Therefore, phase unwrapping, which decides the correct integer of the phase cycle that should be added to the original phase, was applied to the final InSAR image using the method of Goldstein et al. (1988). The phase unwrapping is often difficult to resolve for low coherence areas, especially in rugged terrain (Wegmüller et al. 2000).

5. Conversion of the unwrapped phase to LoS distance change

After the phase unwrapping, the continual phase was simply recalculated into LoS distance change by using half of the microwave length. Using only half of the wavelength allows for the removal of duplication of the change in LoS distance; this change is actually observed by considering the distance covered from the satellite to the target on the ground and back. In this study, e.g., $22.36/2 \times 1 = 11.18$ cm, $22.36/2 \times 2 = 22.36$ cm, and $22.36/2 \times 3 = 33.54$ cm correspond to π , 2π , and 3π ; However, the InSAR image obtained from the orbit gives only a one-dimensional LoS distance change.

3.3.3 Coherence

There are many phase noise contributions, as previously mentioned; an example of temporal change appears on the scatters in areas of thick snow coverage or sandy dunes. Since conditions of snow or sand surfaces tend to scatter microwave changes after a few milliseconds, the coherence is low. The exposed rocks or urban areas remain stable even after years, and the coherence in these areas is high.

Coherence is estimated by an index of phase stability such as the normalized correlation coefficient, which will be calculated using corresponding complex values from the two SAR images. Definition and calculation method of the coherence can be seen in Tobita et al. (1998). The coherence value ranges from 0 (the interferometric phase is just noise, low coherence) up to 1 (absence of phase noise, high coherence).

3.3.4 GPS Survey

To compare the LoS distance change by InSAR with the measurement result by on-site GPS, we used the GPS survey's result obtained by the Shinjo River Office, Ministry of Land, Infrastructure, Transport, and Tourism. That office surveyed the deformation using a GPS receiver at a control point. A GPS receiver was also installed at a reference point outside the landslide where no deformation was expected. The baseline between the control point and the reference point was 5 km in length. The survey was performed by the static method and the observation period was more than one hour each day. GPS survey's measurement error is estimated as 5 mm (offset) + 1 ppm \times 5 km (baseline length) = 1 cm in planimetry and 5 mm + 2 ppm \times 5 km = 1.5 cm in elevation (Tsuchiya and Tsuji 1997). GPS survey's measurement error is considered as $1/\sqrt{2} = \pm 0.7$ cm, $1/\sqrt{2} = \pm 0.7$ cm, and ± 1.5 cm for northing, easting, and up component, respectively. The GPS survey was not daily but periodically performed. Therefore, we selected the GPS survey's result that was observed at the dates close to the master and slave SAR images observation date. Figure 3.3 depicts GPS survey at the GPS control point "GPS-G3," location of which will be explained in Sect. 3.4.2.

Since the LoS distance change by InSAR is one-dimensional, we projected the GPS-surveyed 3-D (northing, easting, up) deformation change into a one-dimensional LoS distance change, i.e., as shown in Table 3.2, we calculated the inner product of GPS-surveyed 3-D deformation change and 3-D unit vector along the LoS, (0.11, -0.62, -0.78) (positive sign for westward and downward). The calculation yielded the LoS distance change by GPS; then, we compared LoS distance change by InSAR with the change by GPS. The 3-D GPS survey's measurement error was also projected into one-dimensional LoS distance by calculating inner product using the unit vector.

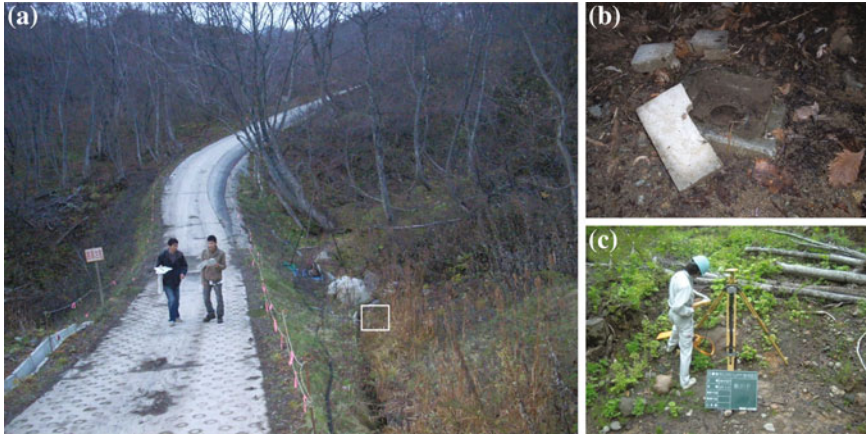


Fig. 3.3 GPS survey at the control point “GPS-G3.” **a** Topography around the control point (white rectangle shows the location of the point), **b** the control point, **c** GPS survey. Photographs in (a) and (b) were taken by the authors on November 10, 2009, and (c) was taken by the Shinjo River Office on August 5, 2008

Table 3.2 GPS-surveyed 3-D deformation at the location GPS-G1

Period	Overlapped days	ΔN (m)	ΔE (m)	ΔH (m)	Inner product (cm)
1. October 29, 2008–August 11, 2006	736	−0.075	−0.022	0.016	−0.7
2. October 29, 2008–October 19, 2006	699	−0.074	−0.021	−0.002	0.6
3. August 5, 2008–October 19, 2006	656	−0.073	−0.032	−0.024	3.1
4. August 5, 2008–August 11, 2006	693	−0.074	−0.033	−0.006	1.7

Note 1 unit vector along LoS (westward and downward: plus) is (0.11, −0.62, −0.78) at the center of the InSAR image

Note 2 InSAR measurement period is September 17, 2008–September 12, 2006 (736 days), as mentioned in Table 3.1

3.4 Result

3.4.1 InSAR Image, Coherence, and LoS Distance Change

Figure 3.4 shows the finally obtained InSAR image. As shown in the figure, the outer rim of the phase-changed area (color changed area from blue to red to yellow and then back to blue) limits the surface deformation area; it shows the surface deformation at more than half of the wavelength along LoS that includes any

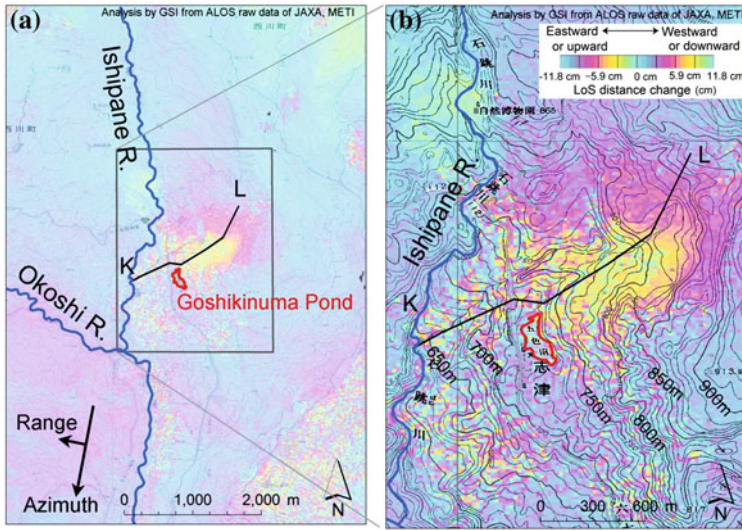


Fig. 3.4 InSAR image. Back image is 1/50,000 map image published by Geospatial Information Authority of Japan

current active landslides in the fluvial-erosion-affected section (Fig. 3.1c). It was found that at the upper end of the deformation-detected area corresponds with the unclear scarp just below the range (Fig. 3.1b, dashed line near B).

Figure 3.5a shows LoS distance change, which is calculated from the continuous phase after phase unwrapping, shown in Fig. 3.4. Figure 3.5b shows the coherence that is near 1.0 along the Ishipane River, the paved road and the artificial building arrangement near Goshikinuma Pond (Figs. 3.4 and 3.5b), where there is a comparable depression zone in the head of the fluvial-erosion-affected section, and some partial slope surfaces. Coherence near 0.0 also appears on the other partial slope surfaces and bottoms of small tributaries; however, generally speaking, Fig. 3.5b shows that coherence is 0.4–0.6. Referring back to our experience, this coherence is not so bad; therefore, the phase-unwrapped result of Fig. 3.5a is thought to show landslide surface deformation well between the twice SAR observation.

Drawing the profile K-L of LoS distance change (Fig. 3.5c), which nearly corresponds to the section A–B in Fig. 3.1c, allows for a more detailed spatial analysis of LoS distance changes. Profile K–L longitudinally samples the LoS distance change between K, in the bottom escarpment undercut by Ishipane River, and L, on the old landslide block (just below the ridge).

In Fig. 3.5c, profile K–L shows discontinuity of -1.0 – 13.5 cm at 710–860 m from K. Further, at 860–1800 m from K, the LoS distance change decreases gradually from 860 m to 1800 m toward L, until the upper-part of the old landslide, where LoS distance change returns to ca. 2.5 cm. These LoS distance change implies that the old landslide is reactivated and slides as one rigid large block.

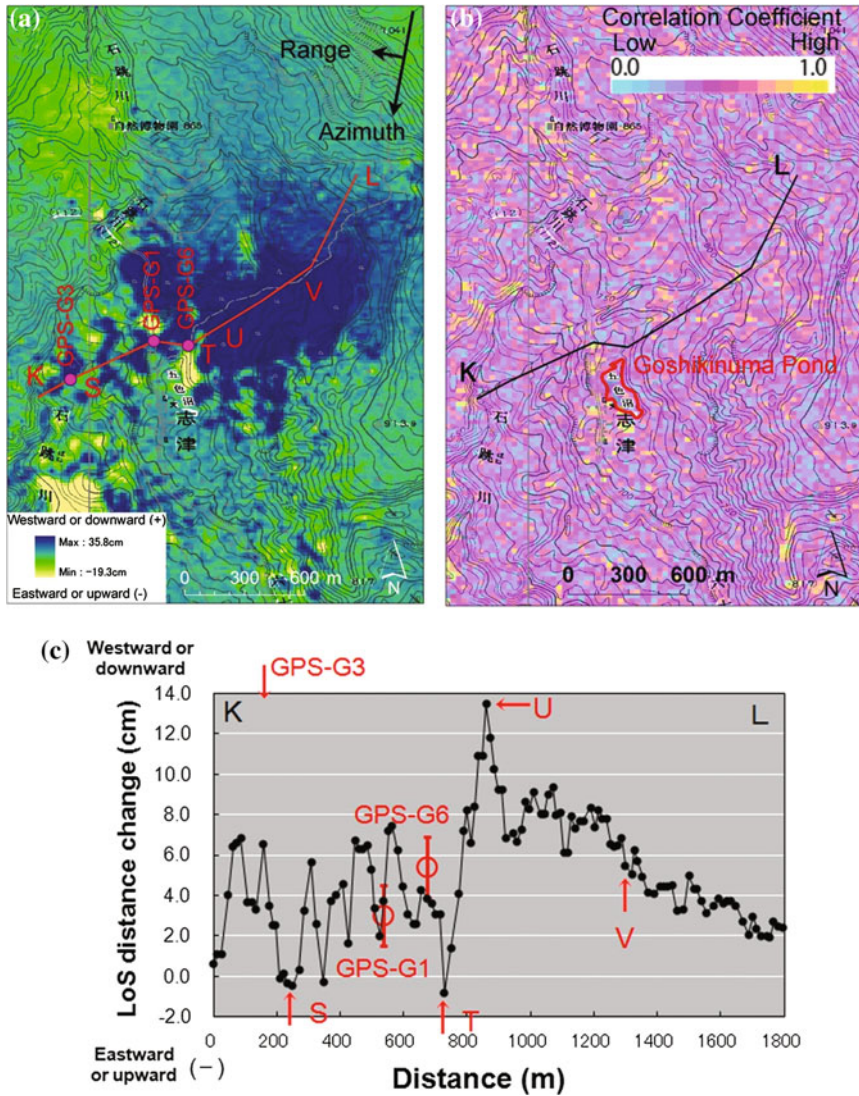


Fig. 3.5 Comparison of one-dimensional (along LoS) landslide surface deformation by InSAR image and GPS. **a** An unwrapped phase image (September 12, 2006–September 17, 2008), **b** a coherent image (1.0: high, 0.0: low), and **c** landslide surface deformation between K and L through GPS-G1, -G3, and -G6. Back image is 1/50,000 map image published by Geospatial Information Authority of Japan

At 0–710 m from K in Fig. 3.5c, the LoS distance remarkably changes in the range 0–7 cm, which implies that small landslide blocks separately move westward or downward. However, at 220 and 710 m from K, the LoS distance change becomes negative, measured as -0.3 and -1.0 cm, respectively. This finding means

that partial landslide blocks are occasionally uplifting or moving eastward, and it implies that landslides in this section move intricately as directly affected by Shipane river erosion, different from 860 to 1800 m from K (Fig. 3.4c).

3.4.2 Comparison Between GPS Survey and InSAR Measurements

The location of the GPS control point is shown as “GPS-G1” in Fig. 3.5a. The deformation surveyed by GPS is also shown in Table 3.2, and since the GPS survey is not performed just at the acquisition date of the SAR master and slave images; four GPS survey periods overlap with the InSAR measurement interval. GPS period 1 in Table 3.2 means that the InSAR measurement interval is fully covered by the GPS survey; however, both October 29, 2008, and August 11, 2006, is out of the InSAR measurement interval. Therefore, the deformation that occurred at a date close to October 29, 2008 or August 11, 2006, is not reflected in the LoS distance change revealed by InSAR. GPS period 3 in Table 3.2 indicates the shortest overlapped days among the four GPS periods; however, at least the GPS period 3 does not include the deformation that occurred at the dates out of the InSAR measurement interval, therefore, we selected the GPS period 3 and plotted the inner product at the red dot (GPS-G1) in Fig. 3.5c. This shows good harmony of deformation results between InSAR measurement and GPS survey. Error bar shows ± 1.5 cm that is GPS survey’s measurement error along the LoS calculated by the inner product using the unit vector. Figure 3.5c shows S, T, U, and V, and these locations are also depicted in Fig. 3.5a.

The location and the surveyed deformation at the GPS control points “GPS-G3” and “GPS-G6” are also shown in Fig. 3.5a and Table 3.3, respectively. As observation period in these points is different from the period 3 in Table 3.2, we selected the observation periods that is close to the period 3, as shown in Table 3.3. As shown in Fig. 3.5c, InSAR measurement result is within the measurement error bar of GPS-G6; however, as shown in Table 3.3, result of GPS survey at the point of GPS-G3 shows remarkable deformation, 88.0 cm along the LoS and the result is

Table 3.3 GPS-surveyed 3-D deformation at the locations GPS-G3 and -G6

Point	Period	ΔN (m)	ΔE (m)	ΔH (m)	Inner product (cm)
GPS-G3	August 5, 2008–November 25, 2006	-0.795	-1.569	0.003	88.0
GPS-G6	August 5, 2008–December 7, 2007	-0.024	-0.034	-0.046	5.4

Note 1 unit vector along LoS (westward and downward: plus) is (0.11, -0.62, -0.78) at the center of the InSAR image

Note 2 InSAR measurement period is September 17, 2008–September 12, 2006, as mentioned in Table 3.1

not shown in Fig. 3.5c (only position of GPS-G3 is shown in Fig. 3.5c). This is because InSAR cannot detect local steep gradient of deformation (coherence is locally depressed), and this measurement limitation causes the discrepancy of deformation results between InSAR measurement and GPS survey at the point of GPS-G3.

3.5 Discussion

Referring to the geologic cross section (Hanaoka et al. 2011, revised) in Fig. 3.1c, the predicted slide surface of the landslide in the upper slope section is thought to correspond with the slide surface of the old landslide. Contrary to the landslide in the fluvial erosion-affected section, the landslide in this section is thought to move as a rigid block, judging from the LoS distance change shown in Fig. 3.5c. Therefore, it is estimated that not so many sub-slide surfaces developed in this section. The GPS-G6 is near this section, and the InSAR measurement along LoS was in acceptable error range with the GPS survey's result.

In the fluvial erosion-affected section, the surface of the landslide moves in a complicated fashion, judging from the LoS distance change shown in Fig. 3.5c. In other words, many sub-slide surfaces develop in this section, many blocks are separated, and each block's movement creates its own deformation. It is thought that some blocks move at the remarkable deformation amount of up to 7 cm along the LoS for two years, and the other blocks move at either a moderate amount or not at all. On the one hand, the GPS-G1 is located in this section, and the InSAR measurement along LoS was consistent with the GPS survey's result. On the other hand, the GPS-G3 is also located in this section and deformation 88.0 cm along LoS was surveyed by GPS; however, InSAR could not detect such the deformation that may have local steep gradient of deformation. If many GPS receivers would be installed along the profile K-L shown in Fig. 3.5c, such a remarkable-moderate surface deformation pattern and local steep gradient of deformation could be clearly evaluated.

Both the upper slope section and the fluvial erosion-affected section face westward, and direction of LoS is westward. The average slope angle is 10° in both sections, which have also locally steep slopes at the angle of 20° – 30° and more that correspond with the sub scarp at the head of sub-blocks of the landslide. On the middle and bottom of these sub scarps, shadow would occur and preclude continuity of phase. Such phase discontinuities would yield some partial unwrapping errors, as can be seen in Fig. 3.5a. However, because such sub scarps exists with uniformity in both sections, and because the coherence shown in Fig. 3.5b is relatively high, we think the deformation result along the LoS was correctly obtained, that the remarkable-moderate deformation sequence was in the fluvial erosion-affected section, and that the continuous deformation was in the upper slope section.

3.6 Conclusion

The two-year-interval InSAR images have revealed landslide surface deformation in the Shizu area, Yamagata Prefecture, Japan. Deformation of the landslides in the fluvial erosion-affected section was already known from the findings of an in situ GPS survey; however, the InSAR images revealed that the deformation area extends not only into the fluvial erosion-affected area but also to the upper slope up to the ridge. On the one hand, the landslide surface spatially repeated the remarkable deformation and moderate deformation in the fluvial erosion-affected section, and the LoS distance change was at most ca. 7 cm westward and downward. On the other hand, in the upper slope section, the landslide moved as rigid block. The LoS distance change was ca. 2 cm at the unclear scarp next to the ridge and 14 cm at the end of the landslide block near Goshikinuma pond. Phase unwrapping of the InSAR image gave a one-dimensional LoS distance change for the two years, and it was found that the LoS distance change detected by InSAR indicated good consistence with the change measured by in situ GPS static survey.

ALOS has been operated for over five years, which was its target life and well beyond its design life of three years; due to a power generation anomaly, JAXA decided to complete operations of ALOS on May 12, 2011 (JAXA 2011). However, space-borne InSAR technique is fruitful for monitoring landslide surface deformation across a wide area, and therefore it will be helpful for the landslide management office to arrange for a GPS survey in landslide areas. From this viewpoint, we think future monitoring and reporting on landslide surface deformation will be conducted using InSAR.

Acknowledgements The PALSAR data used in this study were provided by JAXA. The Ministry of Economy, Trade and Industry (METI) and JAXA retain the ownership of the original SAR data. The Shinjo River Office provided in situ GPS survey result and the photograph. Prof. Hiroshi Yagi (Yamagata Univ., Japan) guided geological and geomorphologic characteristics in the field and showed overview of the recent landslide deformation there. We are thankful for them.

References

- Catani F, Farina P, Moretti S, Giovanni N, Strozzi T (2005) On the application of SAR interferometry to geomorphological studies: estimation of landform attributes and mass movements. *Geomorphology* 66:119–131
- Colesanti C, Wasowski J (2006) Investigating landslides with space-borne synthetic aperture radar (SAR) interferometry. *Eng Geol* 88:173–199
- European Space Agency (2000) Independence of solar illumination. <https://earth.esa.int/web/guest/missions/esa-operational-eo-missions/ers/instruments/sar/applications/radar-courses/course-3/>. Accessed 30 Nov 2016
- Ferretti A, Prati C, Rocca F (2000) Measuring subsidence with SAR interferometry: applications of the permanent scatters technique. *Proc Sixth Int Symp Land Subsidence* 2:67–79
- Geospatial Information Authority of Japan (2004) InSAR Q&A. <http://vldb.gsi.go.jp/sokuchi/sar/qanda/qanda-e.html>. Accessed 30 Nov 2016

- Goldstein RM, Werner CL (1998) Radar interferogram filtering for geophysical applications. *Geophys Res Lett* 25:4035–4038
- Goldstein RM, Zebker HA, Werner CL (1988) Satellite radar interferometry: two-dimensional phase unwrapping. *Radio Sci* 23:713–720
- Hanaoka M, Abe T, Yanaba K, Tsunaki R, Muraoka H, Higaki T, Hayashi S, Abe S (2011): Study on Mt. Gassan volcanic activity by Shizu area investigation in Mt. Gassan. In: Proceedings of 2011 annual meeting of Japan society of erosion control engineering, pp 160–161 (in Japanese)
- JAXA (2011) DAICHI (ALOS) operation completion. http://www.jaxa.jp/press/2011/05/20110512_daichi_e.html. Accessed 29 Oct 2012
- Kimura H, Yamaguchi Y (2000) Detection of landslide areas using radar interferometry. *Photogram Eng Remote Sensing* 66:337–344
- Massonnet D, Rossi M, Carmona C, Adragna C, Peltzer G, Feigl K, Rabaue T (1993) The displacement field of the Landers earthquake mapped by radar interferometry. *Nature* 364:138–142
- Nakazato H, Oba T, Itaya T (1996) The geology and K-Ar ages of the Gassan volcano, northeast Japan. *J Mineral Petrol Econ Geol* 91(1):1–10 (in Japanese with English abstract)
- Peyret M, Djamour Y, Rizza M, Ritz J-F, Hurtrez J-E, Goudarzi MA, Nankali H, Chery J, Dortz KL, Uri F (2008) Monitoring of the large slow Kahrod landslide in Alborz mountain range (Iran) by GPS and SAR interferometry. *Eng Geol* 100:131–141
- Tobita M, Fujiwara S, Ozawa S, Rosen PA, Fielding EJ, Werner CL, Murakami M, Nakagawa H, Nitta K, Murakami M (1998) Deformation of the 1995 North Sakhalin earthquake detected by JERS-1/SAR interferometry. *Earth Planet Space* 50:313–325
- Tsuchiya J, Tsuji H (1997): Easy-to-understand GPS survey. *Japan Association of Surveyors*, p 455 (in Japanese)
- Wegmüller U, Stozzi T, Tosi L (2000) Differential SAR interferometry for land subsidence monitoring: methodology and examples. *Proc Sixth Int Symp Land Subsidence* 2:93–105
- Yamagata Prefecture (1974) 1:50,000 Geologic sheet map “Gassan” and the guidebook (in Japanese)
- Zebker HA, Goldstein RM (1986) Topographic mapping from interferometric synthetic aperture radar observations. *J Geophys Res* 91:4993–4999

Chapter 4

Modelling a Landslide Probability Through Time as a Basis for the Landslide Hazard Forecast System

Marko Komac and Mateja Jemec Auffer

Abstract In the past 20 years, intense short- and long-duration rainfall has triggered numerous shallow landslides worldwide, caused extensive material damage to buildings, infrastructure, and roads, and unfortunately also caused loss of human life. Slovenia was no exception in this regard. But these landslide-related problems could be identified and minimised if the knowledge of the landslide occurrence would be upgraded with the more in-depth knowledge of the relationship between the triggering factors (rainfalls) and landslides. In the frame of the national project *Masprem*, we aim to develop an automated, online tool for predicting landslide hazard forecast at the national level. This tool will provide an early warning system for landslide events in Slovenia, a regional country that is highly vulnerable to extreme meteorological events and to landslides. A system for landslide hazard forecast will be based on the real-time rainfall data, rainfall thresholds for landslide triggering, and the landslide susceptibility map. The proposed system will inform inhabitants of an increased landslide hazard as a consequence of heavy precipitation that would exceed the landslide triggering values.

Keywords Landslide hazard · Early warning system · Real-time rainfall · Slovenia

4.1 Introduction

Landslide is one of the most common world disasters that pose the threat to population and property and often also claim lives. In the last decade, over 7500 people died worldwide due to extreme rainfall events that trigger landslides (IDD 2009).

M. Komac (✉)

Faculty of Civil and Geodetic Engineering, University of Ljubljana,
Jamova c. 2, p.p. 3422, 1000 Ljubljana, Slovenia
e-mail: mkomac@fgg.uni-lj.si; m.komac@telemach.net

M.J. Auffer

Geological Survey of Slovenia, Dimičeva ulica 14, 1000 Ljubljana, Slovenia

© Springer Japan KK 2017

H. Yamagishi and N.P. Bhandary (eds.), *GIS Landslide*,
DOI 10.1007/978-4-431-54391-6_4

Hence, gathering of the knowledge about these dangerous phenomena and the urgency to understand them is a necessity. Society strives towards self-protection and self-preservation, or at least mitigation of the consequences if they cannot be prevented. To manage the hazards associated with shallow landslides, an accurate predictive warning system for rainfall-induced slope failures is needed.

Spatial and temporal landslide occurrences are associated with many factors, divided into two groups. Precondition factors are generally naturally induced, which over longer period govern the stability conditions of slopes (rock characteristics, slope inclination, slope curvature, slope orientation, altitude, distance from geological boundaries, distance from structural elements, distance from surface water net, surface water flow length, and type of land use). The second group consists of triggers that can result from human activity, or natural phenomena. These are divided into preparatory (logging of the forest, slope cuts) and triggering factors (intensive and prolonged rainfall, soil erosion, and seismic activity).

Rainfall influence on the occurrences of slope mass movements is the subject of research of many researchers worldwide. First analysis of the impact of rainfall focused only on the cumulative value of the daily precipitation (Crozier and Eyles 1980; Terlien 1998; Crozier 1999; Wilson 2000), but the latter research proved strong effect of antecedent rainfall that triggers slope failures (Kim et al. 1992; Glade et al. 2000; Aleotti 2004; Zezere et al. 2005; Jemec Aufferl and Komac 2011). Intensity and period of rainfall that trigger landslides play an important role when assessing triggering thresholds values. In general, two major thresholds can be defined: minimum threshold and maximum threshold, which identify the lower and upper boundaries of the threshold's probability range (White et al. 1996). The minimum threshold defines the lowest level, below which a landslide does not occur. The maximum threshold is defined as the level above which a landslide almost certainly occurs. A relatively short but high-intensity rainfall (i.e. less than 1-h rainfall) may result in a high surface run-off. This situation often results in the saturation of soils, the development of perched aquifers, and a rapid rise in groundwater levels. The temporary creation of perched aquifers, and high pore-water pressure reduces the soil strength, which can lead to slope failure. Likewise, low-intensity, lengthy storms, lasting a few days, may increase deep groundwater levels, and high pore-water pressure can reduce the soil strength, again. However, not every rainfall occurrence triggers a slope failure. In fact, groundwater conditions in soil-covered hillslopes are controlled by water infiltration from the surface (Buchanan and Savigny 1990). Despite a large amount of rainfall, there can be insufficient pore pressure within near-surface soils to trigger shallow landslides. In general, mechanical hydraulic and soil characteristics, soil thickness, geology, vegetation cover and its contribution to soil strength, and local seepage conditions are particular to a geographical site and may induce variable instability conditions in response to rainfall (Crosta 1998).

In a few places of the world, rainfall thresholds are a part of the operational landslide warning systems, in which real-time rainfall measurements are compared with established thresholds, and when pre-established values are exceeded, alarm messages are issued. A detailed review of the literature reveals that one of the first

real-time systems for issuing a warning of the landslide during intensive precipitation was designed for San Francisco Bay Region (California) (Keefer et al. 1987). The early warning system accurately predicted the times of actual debris flow and was used by local governments as a basis for planning an emergency response for recommending temporary evacuation of hazardous areas. The developed warning system used empirical and analytical relations between rainfall and landslide initiation, real-time regional monitoring of rainfall data from telemeter rain gauges, National Weather Service precipitation forecasts, and delineation of debris flow hazard areas. In the Hong Kong, where landslides often occur after intense short rainfall period, the Government Landslide Warning System has been in operation since 1984. One of the most sophisticated landslide prediction systems has Japan. Landslide disaster prediction support system LAPSUS is software used by the National Research Institute for Earth Science and Disaster Prevention (NIED) to provide information about the potential shallow landslides and the evaluation of landslide risk (Fukuzono et al. 2004). The information is open to the public. This system is organised into three sections: observation, analyses, and management. Rainfall is measured by rain gauges, and the information is sent to a local station where it is analysed using the standard rainfall programs based on the static slope stability model. To improve the accuracy of rainfall prediction, combinations of radar rain gauge systems (MP-X) and telemetering are used in order to analyse data in real time. In China, a regional warning system to monitor landslides and mudslides was built up and extended along the upper reaches of the Yangtze River in 1991 (Xiaoping et al. 1996). The network protected a population of 300,000 people and had forecasted 217 landslides avoiding estimated economic losses of US\$27 million. A system for warning against landslide occurrence in Rio de Janeiro has been installed 1996 by the Rio de Janeiro Geotechnical Engineering Office (GeoRio) and was based on weather forecast, an automated rain gauge network, and records of landslides. Alarm is triggered when the rain gauge network software indicates that the hourly or daily rainfall threshold levels were reached at least at three rain gauges, and the short-term weather forecast predicts heavy rainfall in the successive hours. Once these conditions are reached, GeoRio contacts the Civil Defence Board of the Rio Government to assess the situation and implement action (Ortigao 2000). In New Zealand, experts developed a system for the real-time prediction of the occurrence of shallow landslides triggered by rains, based on the weather forecasts, generated by global and regional models. The Water Center for the Humid Tropics of Latin America and the Caribbean (CATHALAC 2012) has recently developed an automated, online tool for predicting landslide hazards in Mesoamerica, the first effort of its kind at the regional level. The tool will provide early warning for landslide events in Mesoamerica, a region exposed to the flooding and landslides.

With respect to numerous landslide occurrences, the landslide early warning systems in a real-time mode have been developed also in several countries in the Europe (systems ILEWS, AlpEWAS, INCA, DORIS). However, the main drawback of these systems is each system uses its own (and different) hazard maps, rainfall threshold, rainfall scenarios, and forecasts at different scales on the local and

regional levels. These differences represent a continuous challenge for the experts and institutions dealing with natural hazards in Europe and hamper larger benefits to end-users and stakeholders in the future.

The role of rainfall in landslide activity in Slovenia has been previously discussed and analysed by Komac (2005). Komac (2005) evaluated the thresholds above which significant numbers of landslides occur in 24-h and 48-h periods. The rainfall values range from 100 to 150 mm for a 24-h period and between 130 and 180 mm for a 48-h period. Jemec Auflič and Komac (2011) introduced the impact of antecedent rainfall on landslide occurrence for the Škofjeloško-Cerkljansko area where landslides occur very frequently. An analysis of antecedent rainfall and the rainfall total on the given day revealed that landsliding is seen to be generally related to the amount of rainfall in a certain period over which accumulated rainfall initiates a slope failure. Therefore, when daily rainfall exceeds the antecedent rainfall, more than 150 mm of antecedent rainfall is required to initiate landslides and 200 mm when at least 7 days of antecedent rainfall is considered.

Slovenia has a highly diverse landscape and climate due to its position between the Alps, the Mediterranean Sea, the Dinarides, and the Pannonian Basin. According to Komac and Ribičič (2006), a quarter of Slovenian territory is exposed to landslides. In the past 20 years, intense short- and long-duration rainfall has triggered numerous shallow landslides, caused extensive material damage to buildings, infrastructure, and roads, and unfortunately also caused death of human life. These events could be identified and to some extent also minimised if better knowledge of the relation between landslides and rainfall would be available. A near real-time system for landslide hazard forecast would provide vital information on this issue. The objective of this paper is to present a plan for the landslide hazard forecast system and the modelling landslide probability through time using a real-time forecast at the regional level. When operational the system will inform inhabitants of an increased landslide hazard as a consequence of heavy precipitation that would exceed the landslide triggering values.

4.2 Brief Overview of Geology

Geomorphology, geology, and climate conditions play the most important role in the preparatory process of landslide initiation in any region. Slovenia occupies the territory of the still active boundary of the African and Eurasian plates and, respectively, three large geotectonic units—the Alps, the Dinarides, and the Pannonian Basin, resulting in a very complex and diverse geology. Within a small area rock of the most diverse origin, composition, and age, ranging from Palaeozoic to the Quaternary age, can be found (Fig. 4.1).

Areas that are exposed to the slope mass movement are related to cherts, slaty claystone, sandstone, flysch, metamorphic slate, mica schists, gneisses,

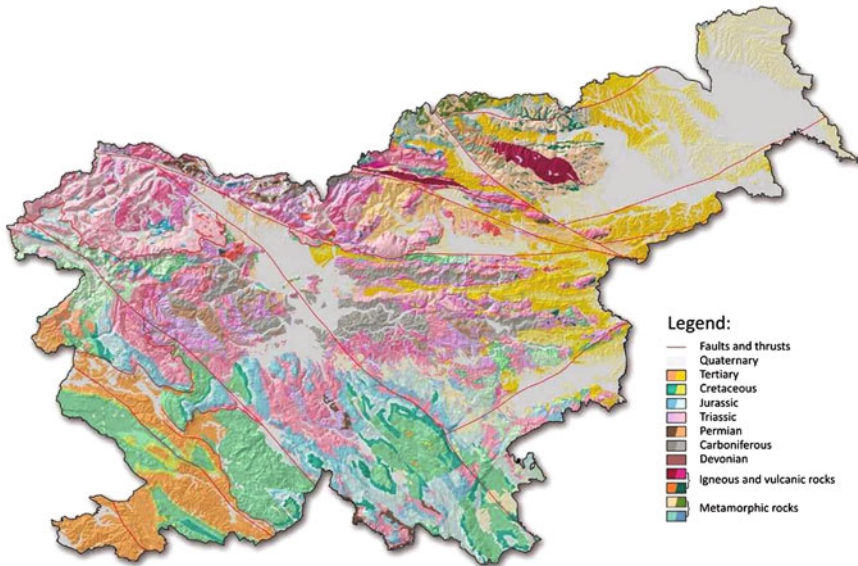


Fig. 4.1 Geological structure of Slovenia. Main faults and thrusts are marked with *red lines*

keratophyres, diabases, limestone with the inclusion of cherts and other rocks, non-consolidated sediments (gravels, alluvial fans, scree deposits), and anthropogenic sediments. From stratigraphic view, slope mass movements are related to Quaternary, Tertiary, Triassic and Permo-Carboniferous rock formation.

4.3 Background and Methodology

In order to quickly respond to natural calamities or even to be better prepared for them with the goal to avoid casualties, environmental data need to be transmitted and processed in a near real time. The Web-based services can be used to implement a system to predict landslide hazard and to enable easy access to end-users. Considering the latter, the information needs to be provided in an understandable format and at the same time remains scientifically correct. The developed model to predict landslide probability occurrence through time will combine knowledge from geological and also from societal aspect. The general conceptual scheme is shown in Fig. 4.2. The designed system will be based on real-time rainfall data, landslide triggering precipitation values or thresholds, and landslide susceptibility model. Each individual parameter that plays an important role in the model is described in the subsections that follow.

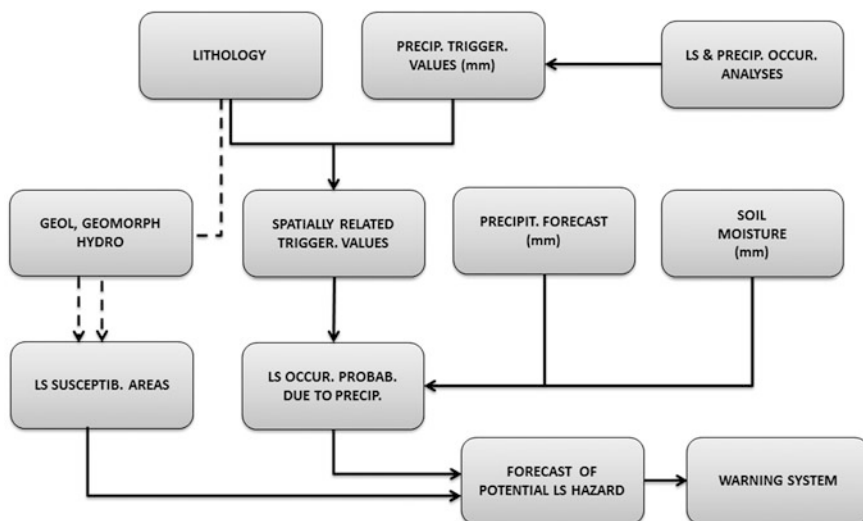


Fig. 4.2 Conceptual model for modelling the landslide hazard forecast system

4.3.1 Climate and Precipitation Regime

The interaction between the three major climate systems (Continental, Alpine, and sub-Mediterranean) in the territory of Slovenia strongly influences the country's precipitation regime. The spatial variability of precipitation is high—the annual precipitation sum varies from 800 mm in the NE part of the country to more than 3500 mm in the NW part of the country—the Alpine area, where one of the precipitation maximum is detected (Fig. 4.3). The maximum 24-h rainfall records with a 100-year return period from 100 to 510 mm (Fig. 4.4). The spatial distribution of precipitation is also highly influenced by the country's complex morphology. Due to an orographic effect, the Julian Alps and the Dinaric barrier receive the highest amount of precipitation; the second maximum is recorded in the Alps above the Savinja River Valley in the Kamniško-Savinjske Alps. The yearly amount of precipitation decreases with the distance from the sea and the Dinaric-Alpine barrier towards the NE part of the country, which is already influenced by the Continental climate. In the outmost NE part of the country (Prekmurje), the mean annual precipitation sum does not exceed 900 mm. The study of daily rainfall patterns (Jemec Auflič and Komac 2011) reveals that precipitation occurs in three peak periods. The first peak is from March to May, the second is characterised by intense summer rainfall storms, and the third is from September to November, of which October and November are usually the wettest months. It is not a surprise that the temporal landslide occurrence is in high correlation with the highest peak of rainfall. Individually, these landslides are small in size (200–1200 m³), and they usually cause damage to property or infrastructure. In

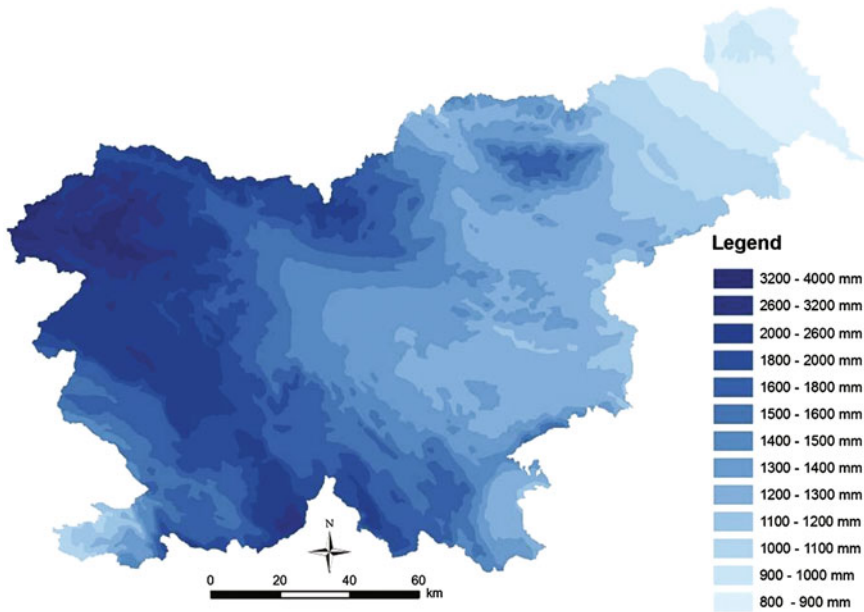


Fig. 4.3 Map of average annual rainfall in Slovenia for the period of 1971–2000 (in mm) (ARSO 2012)

most cases, shallow landslides occur at steep valley slopes (mean slope angle = 23°), and they affect the soil material (colluvium deposits) that overlays impermeable rocks, such as volcanic tuffs, marls, and clays (Zezeze et al. 2005). Over the period from 1990 to 2010, twelve individual rainfall events were detected, of which eight occurred during the months of September to November. An analysis of all occurrences on the slopes revealed that two main factors are required to initiate landslides: (1) intense, short rainstorms exceeding certain levels of intensity for a specified duration and (2) antecedent precipitation at the time of the storm exceeding a minimum threshold. This is in accordance with Wieczorek (1987).

4.3.1.1 Real-Time Rainfall Data

Different types of numerical weather forecast models exist: (1) a short-range forecast where weather forecast is made for a time period up to 48 h; (2) medium range forecasts are for a period extending from about three days to seven days in advance; and (3) long-range forecasts are for a period greater than seven days in advance, but there are no absolute limits to the period. Due to the chaotic nature of the atmosphere, short-range forecasts are generally more accurate than the other types of forecasts (Mercogliano 2010).

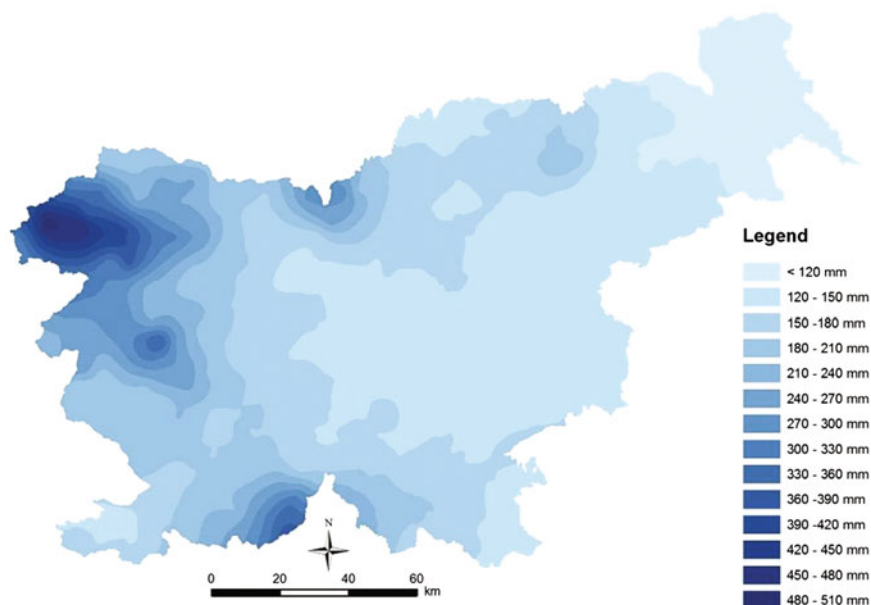


Fig. 4.4 Map of maximum 24-h rainfall with a 100-year return period (in mm/24 h) for the period of 1961–2000 (ARSO 2012)

Quality of warning system based on rainfall forecast models is largely dependent upon the spatial resolution of these models, which is usually far less detailed than the spatial scale of landslides. For instance, the New Zealand Limited Area Model (NZLAM) used at the United Kingdom Met Office has a horizontal resolution of 12 km (Schmidt et al. 2008). The WRF, a mesoscale numerical weather prediction model used at Ningbo City Weather Station, Zhejiang, China, has a horizontal resolution of 15 km, whereas the early warning system Cathalac at the level of detail of 1 km² (CATHALAC 2012). ALADIN (Aire Limitee Adaptation dynamique Development International) is a regional mesoscale model for numerical forecast of weather that simulates events in the atmosphere over much of continental Europe (Bubnová et al. 1995). ALADIN system is used in Slovenia operational weather forecast system since 1997. A regional ALADIN/SI model for Slovenia predicts status of the atmosphere over the area of Slovenia up to 72-h ahead. A model simulates the precipitation (kg/m²), snowfall, water in snowpack, and air temperature data. ALADIN/SI is a grid point model (439 × 2421 × 43), where the horizontal distance between the grid points is 4.4 km and it runs in a 6-h cycling mode for the future 54 h. The background fields, 6-h forecasts, are derived from the previous forecast cycle. This ensures that the model forecast is as close to real conditions as possible. ALADIN/SI model is run twice per day by the Environmental Agency of Republic of Slovenia (ARSO). The forecast is prepared at 12 PM, 6 AM, 12 AM, and 6 PM UTC and tends to provide the availability of

boundary conditions model (Pristov et al. 2012). Figure 4.5 shows the schematic design of assimilation and production cycles of the ALADIN-SI model, where RP stands for the boundary conditions and OBS for the observations.

4.3.2 Rainfall Thresholds for Landsliding

Analyses of landslide occurrence in the area of Slovenia have shown that in areas where intensive rainstorms occur (maximal daily rainfall for the 100-year period), and where the geological settings are favourable (landslide prone), abundance of the landslide can be expected. This clearly indicates the spatial and temporal dependence of landslide occurrence upon the intensive rainfall.

One hundred and seventy-six rainfall stations are located in the territory of Slovenia, and daily data are provided at 7 AM (ARSO 2012). Due to lack of data on landslide location and dates of failures, we cannot implement daily rainfall of each gauge for defining rainfall threshold at the national level. Despite the fact that the landslide occurrence in Slovenia is strongly related to lithological conditions and

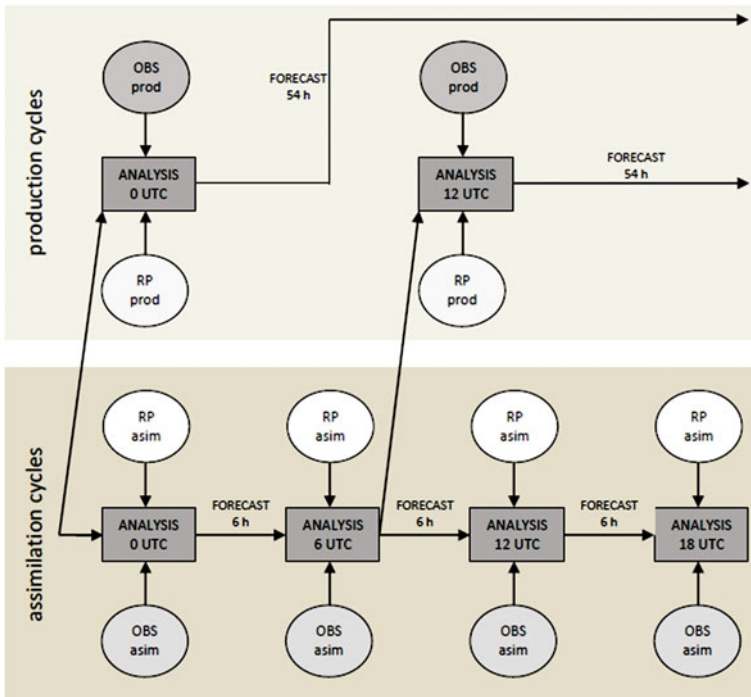


Fig. 4.5 Schematic design of assimilation and production cycles of the ALADIN-SI model. “RP” stands for the boundary conditions and “OBS” for the observations (Pristov et al. 2012)

that the rainfall patterns within the country vary significantly, we selected a more robust approach. For example, one proof of the high variability of the rainfall patterns is more frequent extreme precipitation events in NW part of Slovenia in comparison with the NE part, where these are extremely rare and where the extreme amounts of rain are the consequence of long-lasting precipitation or the consequence of several consecutive storms during the period of one measurement (Ceglar et al. 2008). Rainfall maps derived from the rainfall data from a longer observation period (several decades) and interpolated for the whole Slovenia are usually used as an input for spatial distribution studies of phenomena on the national level. Consequently, a maximum 24-h rainfall with 100-year return period (in mm/24 h) based on a 40-year observation period and obtained from interpolated data for the whole Slovenia with 100-m pixel resolution was used. Maximum daily rainfall above 100 mm proved to be critical for landslide occurrence, especially in more loose soils and in less resistant rocks (Quaternary, Tertiary, Triassic, and Permo-Carbonian rocks) (Komac and Ribičič 2006). Also, numerous other researchers demonstrated the influence of intensive short rainfall on landslide occurrences (Zeze et al. 2005; Caine 1980; Glade 1998; García-Ruiz et al. 2003).

For defining rainfall threshold, the frequency of spatial occurrence of landslide per spatial unit was correlated with lithological unit, and 24-h maximum rainfall data with the return period of 100 years. The result of frequency of landslide occurrence and rainfall data provides a good basis for determining the critical rainfall threshold over which landslides occur with high probability. Thus, the rainfall thresholds for each lithological unit were determined using a nonparametric statistical method chi-square (X^2). In this order, we separately cross-analysed the occurrence of landslides within each unique class derived from the spatial cross-analysis of lithological units and classes of 24-h maximum rainfall (Fig. 4.6) (Komac 2005). The critical 24-h rainfall intensities (thresholds) can be found in Table 4.1 (Komac 2005).

4.3.3 Landslides Susceptibility Model

Landslides in Slovenia occur almost in all parts of the country. In the Alpine carbonate areas of the northern part of Slovenia rockfalls, rock slides and even debris flows have occurred in the (recent) past. In the highland regions of central Slovenia composed of different clastic rocks, large soil landslides are quite usual, and in the young soil sediments of eastern part of Slovenia, there is a large density of small soil landslides. This high exposure of Slovenian territory to landslides and slope mass movements is expected, given the geological factors, especially lithology and structural geology.

Based on the extensive landslide database that was compiled and standardised at the national level, and based on analyses of landslide spatial occurrence, a landslide susceptibility map of Slovenia at scale 1:250,000 was produced (Komac and Ribičič 2006; Komac 2012) (Fig. 4.7). Altogether more than 6600 landslides were

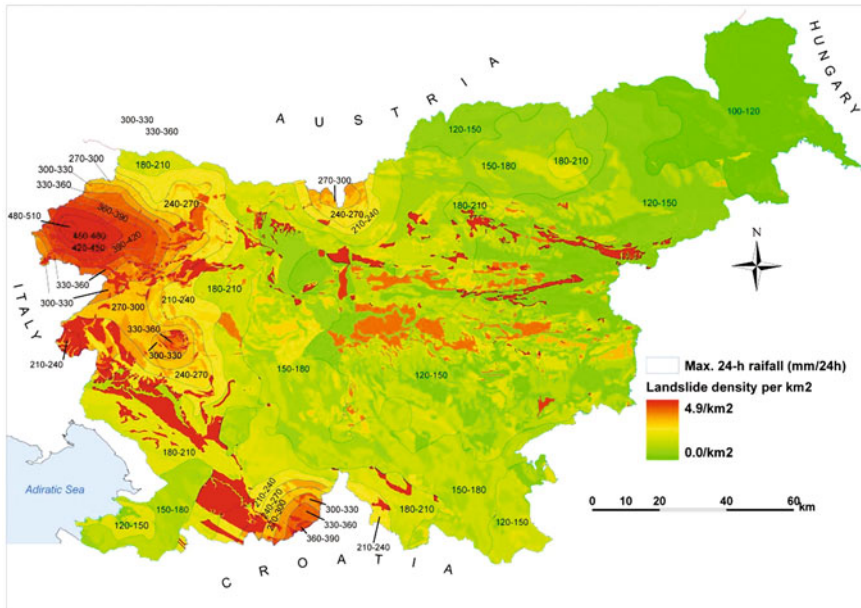


Fig. 4.6 Map of landslide density (number of landslides per square kilometre, represented with a green-red colour scale) per unique combination of lithological units and 24-h maximum rainfall classes with the return period of 100 years. Rainfall values are represented with 30 mm range rainfall classes that are divided by isolines (*blue lines*) (Komac 2005)

included in the national database, of which roughly half are on known locations. Of 3241 landslides with known location, random but representative 67% were selected (landslide learning set) and used for the univariate statistical analyses (X^2) to analyse the landslide occurrence in relation to the spatio-temporal precondition factors (lithology, slope inclination, slope curvature, slope aspect, distance to geological boundaries, distance to structural elements, distance to surface waters, flow length, and land-cover type). The analyses were conducted using GIS in raster format with the 25×25 m pixel size. The results of the analyses were later used for the development of a weighted linear susceptibility model where more than 156,000 automatically calculated models with random weight combinations were derived. The landslide testing subset (33% of landslides) and representative areas with no landslides were used for the validation of all models developed. The results showed that relevant precondition factors for landslide occurrence are as follows (with their weight in a linear model): lithology (0.33), slope inclination (0.23), land-cover type (0.27), slope curvature (0.08), distance to structural elements (0.05), and slope aspect (0.05).

Roughly 8% of Slovenia is extremely susceptible, and consequentially 8% of its population is exposed to potential hazards posed by landsliding. Approximately 11% of the population lives in the areas of high landslide susceptibility that spread

Table 4.1 Rainfall threshold for lithostratigraphic units

Lithostratigraphic unit	Critical 24-h rainfall intensities (mm)
Predominantly clay soils (soils)	–
Marsh and lake sediments (clay, silt, peat) (soils)	–
Alluvium, fluvial loose sediments in terraces (soils)	–
Clayey—diluvial, proluvial (soils)	<120
Gravelly with a clayey component (soils)	150–180
Gravelly (predominantly thick fraction), moraines (soils)	210–240
clayey (soils)	120–150
Alternation of fine and coarse grain soils (soils)	<120
pebbly (soils)	–
Mine tailings—gangues (soils)	120–150
Clayey, marly rocks (soft rocks)	120–150
Clayey, marly and limestone (soft rocks)	–
Alternation of different materials (marl, sand, sandstone, conglomerate pebble, clay) (soft rock)	120–150
Conglomerate (soft rock)	120–150
(Slaty) claystones with the inclusion of other rocks (rocks)	120–150
Marl and sandstone (flysch) with the inclusions of other rocks (rocks)	210–240
Sandstones and conglomerates with the inclusions of other rocks (rocks)	150–180
Stratified and cliff limestones (rocks)	–
Flat limestones (rocks)	–
Limestones and dolomites (rocks)	–
Dolomites (rocks)	210–240
Limestones with marls (rocks)	<120
Limestones with the inclusions of other rocks (rocks)	210–240
Limestone conglomerates and breccia (rocks)	150–180
Phyllites, schists, and slate (rocks)	180–210
Amphibolite and gneiss (rocks)	120–150
Diabase and other magmatic rocks with tuff (rocks)	120–150
Amphibolites, serpentinites, diaphthorites (rocks)	120–150
Tonalite, dacite, granodiorite (rocks)	–

Critical 24-h rainfall intensities are only present for lithostratigraphic unit where a number of observed landslides were statistically higher of number of expected landslides (Komac 2005)

over 16% of Slovenia. In the areas of moderate landslide susceptibility (10%) lives 5.7% of Slovenia's inhabitants. 6.7% of the population lives in the areas of low landslide susceptibility (20%), 3.7% of the population lives in the areas of insignificant (very low) landslide susceptibility (18%), and the rest of the population (65%) lives in the areas where landslide occurrence possibility could be neglected (28%).

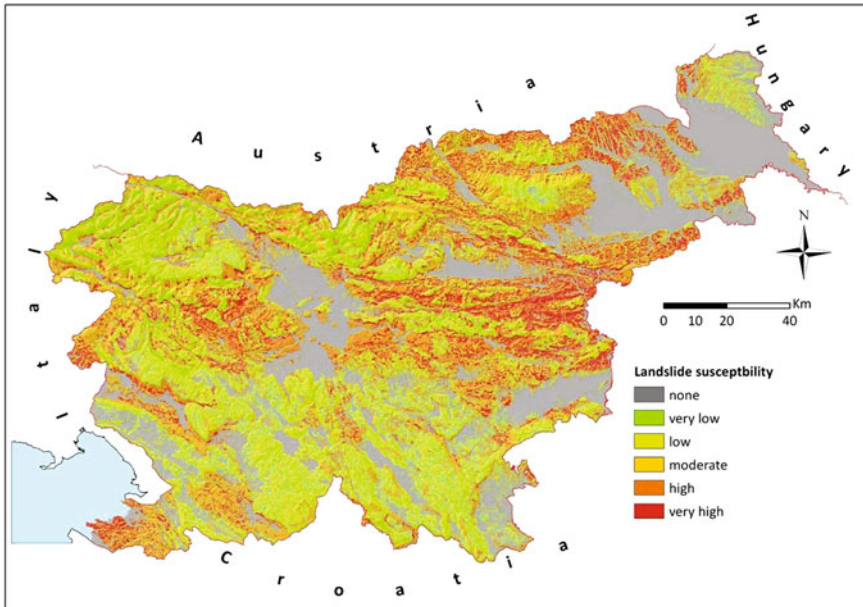


Fig. 4.7 Landslide susceptibility map of Slovenia (Komac 2012)

4.4 Landslide Hazard Forecast Model Development

The system of modelling a landslide hazard probability through time (landslide hazard forecast) will be designed as an integration of static and dynamic input data. In this regard, dynamic input data are represented by a real-time rainfall data that will be provided from the ALADIN model, acquired automatically from the server of Environmental Agency of Republic of Slovenia, transferred to local server, and transformed from ordinary text format into GIS raster format to be prepared for the spatial calculations and modelling part of the system. Static input data are represented by a landslide susceptibility map, and by the threshold information related to each location, both will be implemented through separate modules (Fig. 4.2). Spatial calculations and modelling will be performed on a GIS platform included within the GIS dynamic forecasting modelling module. A landslide hazard forecast model will predict hazards at the level of detail of 4.4 km^2 as this is the resolution of the rainfall forecast model ALADIN. Updating itself each day (ideally several times per day), the tool will indicate the potential for landslide hazards over the proceeding 24-h window in a form of five descriptive (instead of numerical representation that is confusing for non-experts) classes: “very low”, “low”, “moderate”, “high”, and “very high”. Conceptual model of the modelling of landslide

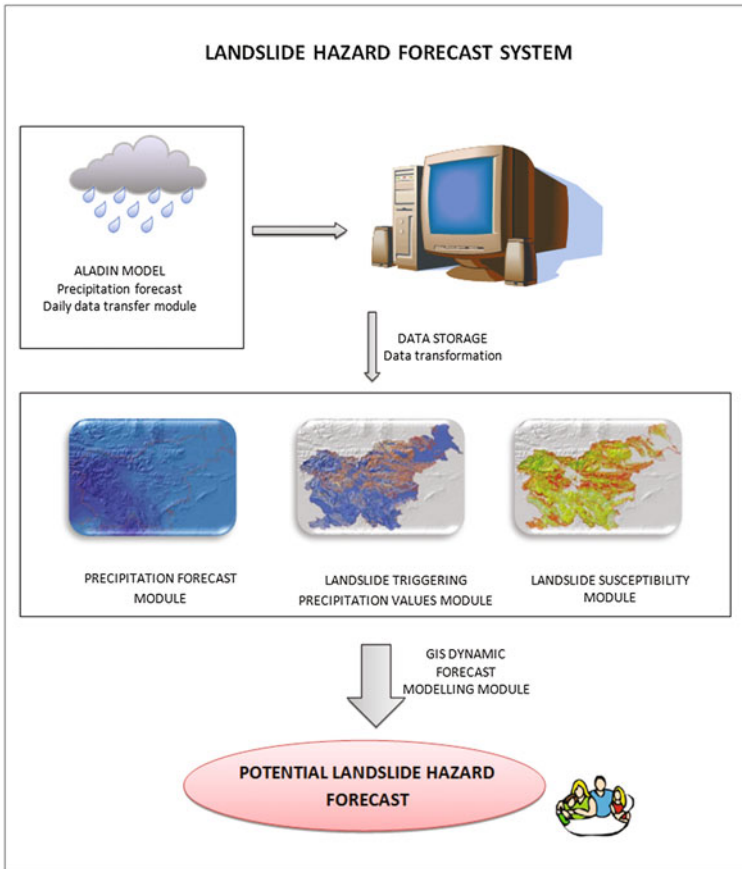


Fig. 4.8 Conceptual model of the operational phase of the modelling landslide probability through time (potential landslide hazard forecast)

probability through time is depicted in Fig. 4.8. Figure 4.9 shows the sample of potential landslide hazard forecast display panel as will be visualised through the Website.

4.5 Preliminary Testing

A key difficulty in using rainfall threshold is the definition of the critical rainfall values above which landslides occur. Threshold is affected by the combination of the intensity of short-term precipitation and accumulated antecedent rainfall. A detailed review of the literature reveals that numerous studies exist concerning various periods of antecedent rainfall: Kim et al. (1992) considered three days;

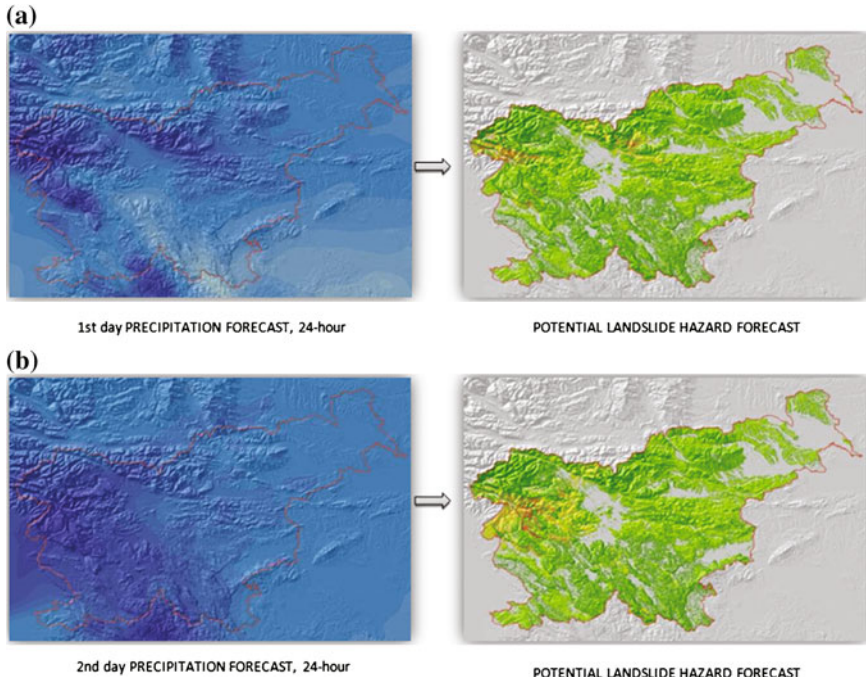


Fig. 4.9 Example of real-time potential landslide hazard forecast display panel as it will be visualised through the Website. Based on 24-h rainfall forecast, landslide triggering precipitation values, and landslide susceptibility map, the potential landslide hazard forecast will be visualised on the Website. Example **a** shows potential landslide hazard forecast based on the first day of 24-h rainfall forecast and **b** potential landslide hazard forecast for the next day. *Yellow and orange* colours indicate areas that are more exposed to landslides occurrence than areas marked with *green colour*

Heyerdahl et al. (2003) considered four days; Crozier (1999) and Glade et al. (2000) considered 10 days; Aleotti (2004) selected 7, 10, and 15 days; and Chleborad (2003) used 18 days (3-day event rainfall and 15-day antecedent rainfall). Then, Terlien (1998) tested 2-, 5-, 15- and 25-day periods before events. Pasuto and Silvano (1998) tested rainfall periods from 1 to 120 days. They found the best correlation with landslide occurrence to be that for 15-day antecedent rainfall. Zezere et al. (2005) performed cumulative absolute antecedent rainfall for 1, 5, 10, 15, 30, 45, 60, 75, and 90 days prior to slope failure, and they obtained significant results for a 5-day period.

In order to perform preliminary testing of real-time rainfall thresholds, the four different 24-h precipitation levels were used. The preliminary testing was applied to the Škofjeloško-Cerkljansko area where landslide threshold was already determined for the events in period from 1990 to 2010 (Jemec Auflič and Komac 2011). This study area was selected because of its highly diverse morphology and historical landslide records, including the dates of landslide occurrences and data on daily

rainfall from two rain gauges, approximately 10 km apart. The Davča site is underlain by an Upper Triassic layer comprising claystone and sandstone with interbedded limestone, and the ground slope inclination varies between 14° and 38° with an average of 26° . The Poljane area is covered with Lower Permian and Upper Carboniferous beds of shaly claystone and quartz conglomerate, and the slope angle varies between 7° and 31° with an average of 19° . The number of days with recorded rainfall did not vary, whereas the measurements detected a variation in the total annual rainfall during the landslide events between the two rain gauges. Figure 4.10 represents the daily rainfall accumulation associated with landslide occurrence at the two rain gauge stations. A little spatial variability of rainfall between the investigated stations was also detected (Fig. 4.11).

A rainfall event on 2 November 1990 was characterised by a heavy consecutive rainfall of 150–245 mm over seven days at an intensity of 78–90 mm/day. Approximately 200 shallow landslides and soil slips were detected. October and November 1992 were significantly wet, and the first rainstorm occurred on 18 October with an intensity of 67–96 mm/day, and with the 30-day antecedent rainfall, it resulted in a 200 mm accumulated precipitation. The second event followed on 1 November 1992, with a maximum intensity of 28–43 mm/day. Together, both rainstorm events triggered 30 recorded soil slips. October 1998 had two successive bursts. The first occurred on 6 October as a consequence of a 10-day consecutive rainfall of 130 mm precipitation with a maximum intensity of 44–90 mm/day. The second event, on 5 November, had seven days of continuous rainfall (47–80 mm) with a maximum intensity of 76–137 mm/day. November 2000 was one of the wet months in the last 20 years (ARSO 2012). The eight-day rainfall event with maximum intensities of 70–100 mm/day that accumulated in the precipitation of 170–260 mm on 7 November 2000 triggered five shallow landslides and numerous soil slips. On 19 September 2007, an exceptional meteoric

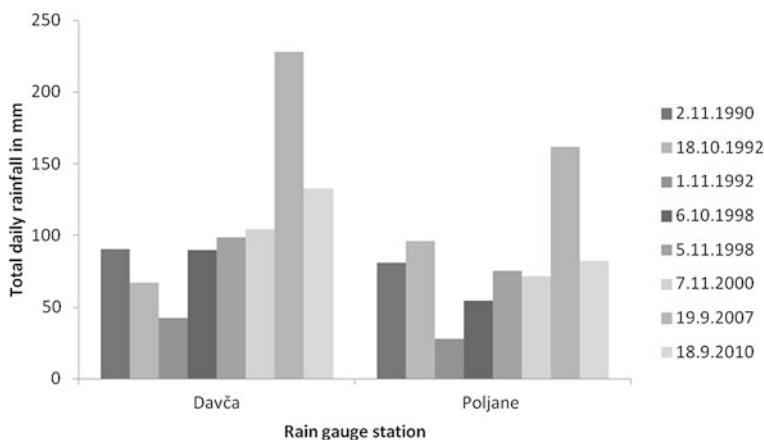


Fig. 4.10 Daily total accumulated rainfall for 8 examined events that triggered landslides at the two rain gauge stations

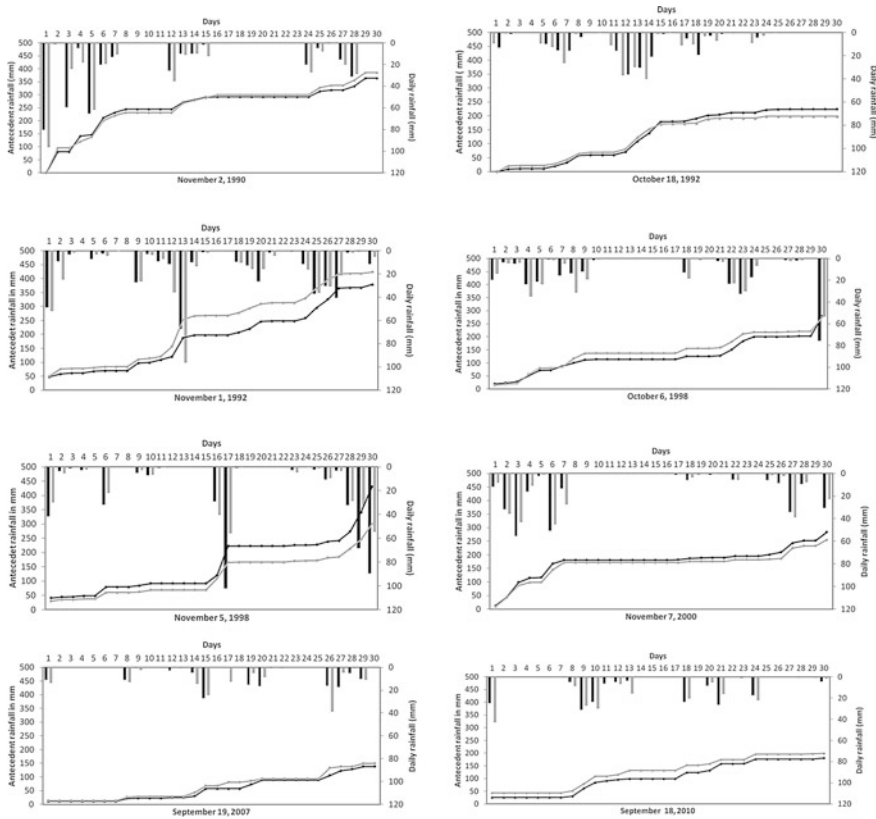


Fig. 4.11 Rainfall patterns defined on the basis of daily rainfall and antecedent rainfall. Each graph contains data from two rain gauges. Data shown with *bar* charts represent daily rainfall; data shown with *line* charts represent cumulative antecedent rainfall. Data for Davča are represented with *dark grey* and data for Poljane with *bright grey* colour

event triggered approximately 50 shallow landslides, when more than 200 mm of rain precipitated in only two days. After three years, on 18 September 2010, a very specific rainfall event with a maximum intensity of 82–138 mm/day triggered numerous soil slips and soil slides.

Due to the fact that Škofjeloško-Cerkljansko area is relatively small and occupies approximately 640 km² (approximately 5 × 6 cells of rainfall forecast model that has a resolution of 4.4 km²), we assumed that the forecast did not significantly vary across the test area. For the validation of the real-time forecast, we used the rainfall data from the two rain gauges for the eight rainfall events that triggered numerous landslides and tested these real data against the theoretical thresholds. For the theoretical thresholds, we used values of 60, 80, 100, and 120 mm/day. Figure 4.12 shows the plotted rainfall events that triggered landslides according to daily rainfall and antecedent rainfall. Red dashed lines represent the 24-h

precipitation level for four different forecast values—60, 80, 100, and 120 mm, starting from the lowest at the bottom, respectively. From the data of landslide occurrence, daily rainfall on the day of the events and on data of antecedent rainfall, the relation between the threshold values and cumulative rainfall (for each day from day 0) was assessed using a simple regression analysis for both sets of data. D_{th} and P_{th} shown in Fig. 4.12 and Table 4.2 represent threshold values at Davča and Poljane, respectively, and D_{cum} and P_{cum} represent the cumulative antecedent rainfall values at Davča and Poljane, respectively.

Figure 4.12 strongly indicates that landslides can occur after very short rainy periods, i.e. after a very brief rainy period of 2 days (rainfall events on 19 September 2007 and 18 September 2010 are an example of this group). With such events, high-intensity rainfall infiltrates into the soil more rapidly than the soil can drain. The soil then builds a perched groundwater table that can reach critical values

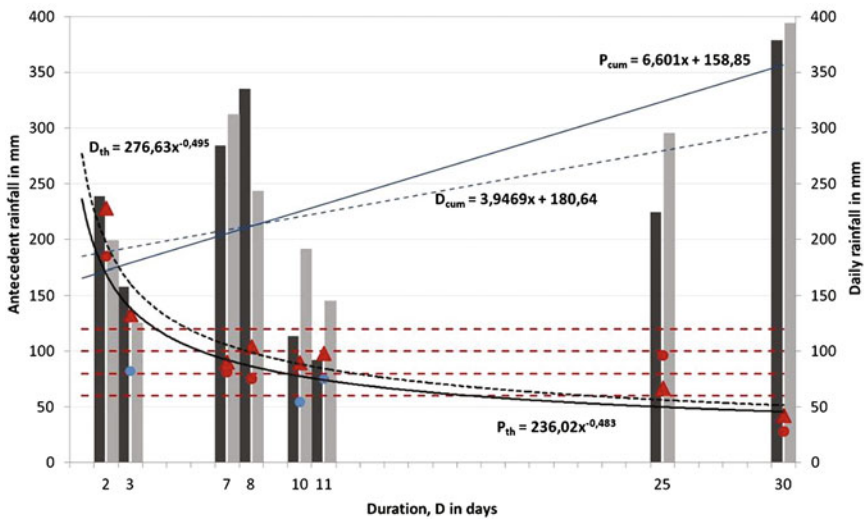


Fig. 4.12 Rainfall events that triggered landslides according to daily rainfall and antecedent rainfall. Rainfall data for the events that triggered landslides, marked by *red triangles*, were acquired by the Davča rain gauge, and rainfall data for the events marked by *red circles* were acquired by the Poljane weather station. Events that were not associated with landslides are shown in *blue*; these were the rainfall events on 6.10.1998, 5.11.1998, and 18.10.2010. Data shown with *bar charts* represent cumulative antecedent rainfall: *dark bars* represent Davča rain gauge and *bright bars* represent Poljane weather station. Regression functions of the threshold rainfall values are represented with *black lines*: *dashed trend line* corresponds to rainfall events at Davča area ($D_{th} = 276.63 \times x^{-0.495}$) and *solid trend line* corresponds to rainfall events at Poljane area ($P_{th} = 236.02 \times x^{-0.483}$). *Trend lines* were created only for rainfall events that triggered landslides. Regression functions of the cumulative antecedent rainfall values are represented with *blue lines*: *dashed trend line* corresponds to rainfall events at Davča area ($D_{cum} = 3.9469 \times x + 180.64$) and *solid trend line* corresponds to rainfall events at Poljane area ($P_{cum} = 6.3 \times x + 189$). *Red dashed lines* represent the 24-h precipitation levels—theoretical thresholds (60, 80, 100, and 120 mm precipitation)

Table 4.2 Results of the regression analysis for rainfall values on the day of the landslide event and for the antecedent rainfall values prior to the event

Day	D_{th}	P_{th}	D_{cum}	P_{cum}
	$D_{th} = 276.63 \times x^{-0.495}$	$P_{th} = 236.02 \times x^{-0.483}$	$D_{cum} = 3.947 \times x + 180.6$	$P_{cum} = 6.3 \times x + 189$
	$R^2 = 0.8935$	$R^2 = 0.613$	$R^2 = 0.1516$	$R^2 = 0.6419$
1	276.6	236.0	184.5	195.3
2	196.3	168.9	188.5	201.6
3	160.6	138.8	192.4	207.9
4	139.3	120.8	196.4	214.2
5	124.7	108.5	200.3	220.5
6	114.0	99.3	204.3	226.8
7	105.6	92.2	208.2	233.1
8	98.8	86.4	212.2	239.4
9	93.2	81.7	216.1	245.7
10	88.5	77.6	220.1	252.0
11	84.4	74.1	224.0	258.3
12	80.9	71.1	228.0	264.6
13	77.7	68.4	231.9	270.9
14	74.9	66.0	235.9	277.2
15	72.4	63.8	239.8	283.5
16	70.1	61.9	243.8	289.8
17	68.0	60.1	247.7	296.1
18	66.2	58.4	251.6	302.4
19	64.4	56.9	255.6	308.7
20	62.8	55.5	259.5	315.0
21	61.3	54.2	263.5	321.3
22	59.9	53.0	267.4	327.6

(continued)

Table 4.2 (continued)

Day	D_{th}	P_{th}	D_{cum}	P_{cum}
	$D_{th} = 276.63 \times x^{-0.495}$	$P_{th} = 236.02 \times x^{-0.483}$	$D_{cum} = 3.947 \times x + 180.6$	$P_{cum} = 6.3 \times x + 189$
	$R^2 = 0.8935$	$R^2 = 0.613$	$R^2 = 0.1516$	$R^2 = 0.6419$
23	58.6	51.9	271.4	333.9
24	57.4	50.9	275.3	340.2
25	56.2	49.9	279.3	346.5
26	55.1	48.9	283.2	352.8
27	54.1	48.0	287.2	359.1
28	53.2	47.2	291.1	365.4
29	52.2	46.4	295.1	371.7
30	51.4	45.7	299.0	378.0

Table presents the threshold and cumulative rainfall values for each day from the day 0 to day 30. D_{th} and P_{th} represent the threshold values at Davča and Poljane, respectively, and D_{cum} and P_{cum} represent the cumulative antecedent rainfall values at Davča and Poljane, respectively. R^2 represent the "goodness of fit" of the regression functions

of pore pressure and cause failure. On the other hand, some of the slope failures required a long-duration and less-intense rainfall periods where rainfall also infiltrated without appreciable build-up of pore pressure in a short period. Usually, in these cases, the cumulative rainfall was higher (rainfall events on 2 November 1990, 18 October 1992, and 1 November 1992 are an example of this group). Despite the fact that the latter is not always the rule, the amount of rainfall still plays a significant role for the landslide occurrence. Based on the available data of rainfall events and landslide occurrence from 1990 to 2010, it can be concluded that landslides occurred when the daily rainfall exceeded the antecedent rainfall or when rainfall lasted for at least 7 days. In the first case, more than 150 mm of antecedent rainfall (see dark bars in Fig. 4.12) or 130 mm of rainfall on the day of the event (see red triangles in Fig. 4.12) was required to initiate landslides for the Davča area, and approximately 200 mm of antecedent rainfall (see bright bars in Fig. 4.12) or 180 mm of rainfall on the day of the event (see red circles in Fig. 4.12) was required for the Poljane area. Interestingly, this threshold value is close to the one proposed by Komac (2005) for the whole Slovenian territory. Komac (2005) defined the rainfall values that range from 100 to 150 mm above which significant numbers of landslides occur in 24-h period and between 130 and 180 mm for a 48-h period. In the case of at least seven-day rainfall duration, a total (cumulative) rainfall of more than 200 or 45 mm of rainfall on the day of the event was required to initiate slope failure at Davča area and more than 250 or 30 mm of rainfall on the day of the event to trigger slope failure at Poljane area. Calculated values using regression functions show that cumulative values match rather well, whilst threshold values do not and that landslides can occur at much lower rainfall amounts than anticipated with statistical approach. Different thresholds (difference of 50 mm) between the two investigated stations could be the consequence of the mechanical properties of the rock mass, which are better in steep slopes and poorer in gentler terrain. Likewise, the formations with claystone retained more water than the clastic limestone, which fails rapidly under rainy conditions. Slightly higher number of landslides was documented in the Davča area where the slopes are steeper than in the Poljane area.

From the regression functions (Fig. 4.12 and Table 4.2), derived from the landslide distribution according to rainfall events in Davča and Poljane area, it can be calculated that when the 24-h rainfall forecast would be 60 mm, shallow landslides would occur only when (already) long-lasting rainfall would occur. For Poljane, this period would be around 17 days (with antecedent rainfall cumulative of 293 mm) and for Davča around 21 days (with antecedent rainfall cumulative of 263 mm). Close to this scenario is the event on 1 November 1992 that triggered 30 shallow landslides. A very similar result is in the case when the 24-h rainfall forecast is 80 mm (Table 4.2). In case of such forecast, landslides would almost certainly be triggered in Davča if the antecedent rainfall cumulative would be 228 mm (approximately in 12 days), or in Poljane 245 mm (approximately in 9 days). This group combines the rainfall events with at least 8 days of antecedent rainfall. The number of slope failures significantly increases when the 24-h rainfall amount exceeds 80 mm (6 rainfall events at Davča area and 2 rainfall events at

Poljane area, as in Fig. 4.12). If the forecast would anticipate 100 mm in proceeding 24-h, in Davča landslides would almost certainly occur if the antecedent rainfall cumulative would be 212 mm (approximately in 7–8 days), or in Poljane 227 mm (approximately in 6 days). In the case when the 24-h rainfall forecast increases above 120 mm in Davča landslides would almost certainly occur if the antecedent rainfall cumulative would be 200 mm (approximately in 5 days), or in Poljane 214 mm (approximately in 4 days). The proof that high-intensity rainfall events without significant antecedent rain could trigger landslides are the two rainfall events triggered landslides at Davča area (rainfall events on 19 September 2007 and 18 September 2010, as in Fig. 4.12) and one rainfall event at Poljane area (rainfall event on 19 September 2007, as in Fig. 4.12).

All rainfall events that triggered slope failures can be divided into three groups according to the different 24-h rainfall forecast values. In the first group of events landslides typically occurred after very short rainfall period when daily rainfall amount exceeded 200 mm at Davča area and 214 mm at Poljane area, or the highest chosen theoretical 24-h rainfall forecast. The last two rainfall events in the years 2007 and 2010 are examples of this group. The second group combines the rainfall events with rainfall forecast between 80 and 120 mm with a longer antecedent period of accumulation of 7–12 days (rainfall events on 2 November 1990, 6 October 1998, 5 November 1998, and 7 November 2000). Cumulative antecedent rainfall required to trigger landslides would be approximately between 212 and 228 mm for Davča area, and between 227 and 245 mm for Poljane area. In the last group of events, landslides resulted from the long-term rainfall that lasted approximately 25–30 days and occurred when the rainfall forecast would be between 45 and 55 mm (263 mm of antecedent cumulative rainfall for Davča and 293 mm for Poljane area). Therefore, based on preliminary testing of differently proposed 24-h rainfall forecast values, a daily rainfall forecasted amount, antecedent rainfall, and lithological units significantly influence whether landslides will occur or not.

General trend lines (Fig. 4.11) of rainfall events that triggered landslides at Davča area and Poljane area are not differed much. The small difference can be attributed to the rainfall extreme at Davča area where on 19 September 2007, more than 220 mm of rain precipitated in only two days. In case that the extreme rainfall event at Davča area is not including to trend line, the difference between trends are almost negligible.

4.6 Conclusions

During the past decade, the early warning system has been developed in many countries in the world. Most of these systems are still under development and need to be tested in the field. Nevertheless, there is a strong need to build more warning system prototypes in different parts of the world followed by their implementation to make landslide hazards (more) predictable.

In this paper, a system concept for the modelling a landslide probability through time in Slovenia is presented. A system for landslide hazard forecast will be based on the real-time rainfall data, rainfall threshold values, and landslide susceptibility map. The importance of their inclusion in the system was highlighted. Special attention was paid also to the preliminary testing of 24-h rainfall forecast as this information still bases on approximations and is the input data that we could manage in terms of enhancing its quality. A validation of different 24-h rainfall forecast values on the test area revealed that landslides occur in different rainfall periods with different intensities. Landsliding is seen to be generally related to the daily 24-h rainfall and the amount of the rainfall in a certain period over which accumulated rainfall initiates a slope failure. Based on the proposed 24-h rainfall levels, it was found that landslides significantly occurred when the daily rainfall exceeded antecedent rainfall and when the duration of rainfall exceeded certain levels of intensity for a specific duration. For a good landslide hazard forecast, antecedent rainfall for up to 30 days has to be calculated regularly on daily basis for every cell to get the real-time information on soil moisture/saturation conditions that could in combination with the daily precipitation trigger slope failures.

The development of a real-time early warning system due to the landslide hazard that is being developed and that is based on the concept described in this paper will certainly be beneficial to various stakeholders including the local authorities, relevant government agencies, and the public in the most exposed and highlighted areas. The developed early warning system, which will be consisted of the static and dynamic input data, data transfer module, landslide hazard forecast calculation module, and visualisation Web module, is hoped to achieve its purpose in providing early warning and alerting the authorities as well as the public, in general, in the potential high landslide hazard areas within the affected areas once there are incidences of heavy rainfall.

References

- Aleotti P (2004) A warning system for rainfall-induced shallow failures. *Eng Geol* 73:247–265
- ARSO Ministry for Environment and Spatial Planning (2012) Environmental Agency of the Republic of Slovenia. <http://meteo.arso.gov.si/met/en/app/webmet/>. Accessed 20 June 2012
- Bubnová RG, Hello P, Béenard P, Geleyn JF (1995) Integration of the fully elastic equations cast in the hydrostatic pressure terrain following coordinate in the framework of the ALADIN NWP system. *Mon Wea Rev* 123:515–535
- Buchanan P, Savigny KW (1990) Factors controlling debris avalanche initiation. *Can Geotech J* 27:659–667
- Caine N (1980) The rainfall intensity-duration control of shallow landslides and debris flows. *Geogr Ann A* 62:23–27. doi:10.2307/520449
- CATHALAC (2012) Water centre for the humid tropics of Latin America and the Caribbean. <http://portalgis.cathalac.org/cathalac/maps/>. Accessed 25 Aug 2012
- Ceglar A, Črepinšek Z, Zupanc V, Kajfež-Bogataj L (2008) A Comparative study of rainfall erosivity for eastern and western Slovenia. *Acta Agriv Slov* 91(2):331–341

- Cheleborad AF (2003) Preliminary evaluation of a precipitation threshold for anticipating the occurrence of landslides in the Seattle, Washington, Area, US Geological Survey Open-File Report 03-463
- Crosta G (1998) Rationalization of rainfall threshold: an aid to landslide hazard evaluation. *Environ Geol* 35:131–145
- Crozier MJ (1999) Prediction of rainfall-triggered landslides: a test of the antecedent water status model. *Earth Surf Proc Land* 24:825–833
- Crozier MJ, Eyles RJ (1980) Assessing the probability of rapid mass movement. In: Technical Groups (eds) Proceedings of 3rd Australia-New Zealand Conference on Geomechanics, vol 6. New Zealand Institution of Engineers, Wellington, pp 247–251
- Fukuzono T, Moriwaki H, Inokuchi T, Maki M, Iwanami K, Misumi R, Takami S, Shikoku T (2004) Landslide disaster prediction support system based on Web GIS. <http://gisws.media.osaka-cu.ac.jp/gisideas04/viewpaper.php?id=40>
- Garcia-Ruiz JM, Martí-Bono C, Lorente A, Beguería S (2003) Geomorphological consequences of frequent and infrequent rainfall and hydrological events in Pyrenees Mountains of Spain. *Mitig Adapt Strategies Glob Chang* 7:303–320
- Glade T (1998) Establishing the frequency and magnitude of landslide-triggering rainstorm events in New Zealand. *Env Geol* 35(2):160–174
- Glade T, Crozier MJ, Smith P (2000) Applying probability determination to refine landslide-triggering rainfall thresholds using an empirical “Antecedent Daily Rainfall Model”. *Pure Appl Geophys* 157(6/8):1059–1079. doi:10.1007/s000240050017
- Heyerdahl H, Harbitz CB, Domaas U, Sandersen F, Tronstad K, Nowacki F, Engen A, Kjekstad O, De'voli G, Buezo SG, Diaz MR, HernandezW (2003) Rainfall induced lahars in volcanic debris in Nicaragua and El Salvador: practical mitigation. In: Proceedings of international conference on fast slope movements—prediction and prevention for risk mitigation, IC-FSM2003. Patron Pub, Naples, pp 275–282
- IDD (2009) The international disaster database—<http://www.emdat.be/advanced-search>. Accessed 3 Sept 2012
- Jemec Auflič M, Komac M (2011) Rainfall patterns for shallow landsliding in perialpine Slovenia. *Nat Hazards*. doi: 10.1007/s11069-011-9882-9
- Keefer DK, Wilson RC, Mark RK, Brabb EE, Brown WM III, Ellen SD, Harp EL, Wieczorek GF, Alger CS, Zarkin RS (1987) Real-time landslide warning during heavy rainfall: *Science* 238:921–925
- Kim SK, Hong WP, Kim YM (1992) Prediction of rainfall-triggered landslides in Korea. In: Bell DH (ed) Landslides. Proc. of the sixth Int. Symp. on landslides, vol 2. Christchurch, Balkema, Rotterdam, pp 989–994
- Komac M (2005) Rainstorms as a landslide-triggering factor in Slovenia. *Geologija* 48(2):263–279
- Komac M (2012) Regional landslide susceptibility model using the Monte Carlo approach—the case of Slovenia. *Geol Q* 56(1):41–54
- Komac M, Ribičič M (2006) Landslide susceptibility map of Slovenia at scale 1:250.000. *Geologija* 49(2):295–309
- Mercogliano P, Schiano P, Picarelli L, Olivares L, Catani F, Tofani V, Segoni S, Rossi G (2010) Short term weather forecasting for shallow landslide prediction. In: Malet JP, Glade T, Casagli N (eds) Int. Conf. Mountain Risks: Bringing Science to Society, Firenze, pp 525–530
- Ortigao B (2000) Rio-watch: the Rio de Janeiro landslide watch. *MonoSys Guide to Monitoring Quarter 1 2000*. <http://www.terratek.com.br/downloads/Geotechnical%20Engineering%20papers%20English/2000%20Ortigao%20on%20Landslide%20Watch%20Guide%20to%20Monitoring.pdf>
- Pasuto A, Silvano S (1998) Rainfall as a triggering factor of shallow mass movements. A case study in the Dolomites, Italy. *Environ Geol* 35(2–3):184–189
- Pristov N, Cedilnik J, Jerman J, Strajnar B (2012) Priprava numerične meteorološke napovedi ALADIN-SI. *Vetrnica*, pp 17–23
- Schmidt J, Turek G, Clark MP, Uddstrom M, Dymond JR (2008) Probabilistic forecasting of shallow, rainfall-triggered landslides. *Nat Hazards Earth Syst Sci* 8:349–357

- Terlien MTJ (1998) The determination of statistical and deterministic hydrological landslide-triggering thresholds. *Environ Geol* 35(2–3):124–130
- White ID, Mottershead DN, Harrison J (1996) *Environmental Systems*, 2nd edn. Chapman & Hall, London, p 616
- Wieczorek GF (1987) Effect of rainfall intensity and duration on debris flows in central Santa Cruz Mountains, California. *Geol Soc Am, Rev Eng Geol* 7:93–104
- Wilson RC (2000) Climatic variations in rainfall thresholds for debris-flows activity. In: Claps P, Siccardi F (eds) *Proceedings 1st Plinius conference on mediterranean storms*. Maratea, pp 415–424
- Xiaoping L, Junling X, Hesheng L, Gongxian W (1996) Recent development of time prediction for landslide in China. In: Senneset (ed) *Landslides*. Balkema, Rotterdam
- Zezere JL, Trigo RM, Trig IF (2005) Shallow and deep landslides induced by rainfall in the Lisbon region (Portugal): assessment of relationships with the North Atlantic Oscillation. *Nat Hazards Earth Syst Sci* 5:331–344

Chapter 5

Development of a GIS-Based 3D Slope Stability Analysis System for Rainfall-Induced Landslide Hazard Assessment

Cheng Qiu and Yasuhiro Mitani

Abstract The assessment of landslide hazard should give answers to three key questions: the location, the magnitude, and the occurrence time of potential failures. This paper proposes a GIS-aided 3D methodology for quantitative assessment of regional landslide hazard and prediction of the three key questions. A revised 3D slope stability model is developed by coupling a dynamic rainfall infiltration model with a 3D limit equilibrium approach. To define the study object of the 3D model in regional assessment, an automatic methodology of slope-unit division is developed by using GIS hydraulic analysis functions. The location and shape of unknown slip surface(s) are identified by means of minimizing the 3D safety factor through an iterative procedure, based on a Monte Carlo simulation for the 3D shape of ellipsoid. Executing the searching calculation for each slope unit during rainfall can result in changing distribution of the critical slip surface(s) as well as their occurrence time related with rainfall. Incorporating all proposed methods, a standalone GIS system, called 3D slope stability analysis GIS system (3DSSAGS), is developed based on the Component Object Model technology. In this system, all the professional analyses are embedded within GIS for efficient use of GIS functions.

Keywords Landslide hazard · 3D slope stability model · Rainfall infiltration · GIS

C. Qiu (✉)

Hydro-soft Technology Institute Co., Ltd., Shiroyama Trust Tower 31F,
Toranomon 4-3-1, Minato-ku, Tokyo, Japan
e-mail: qiucheng321@gmail.com

Y. Mitani

Kyushu University, Motoooka 744, Nishi-ku, Fukuoka, Japan
e-mail: mitani@doc.kyushu-u.ac.jp

© Springer Japan KK 2017

H. Yamagishi and N.P. Bhandary (eds.), *GIS Landslide*,
DOI 10.1007/978-4-431-54391-6_5

5.1 Introduction

The assessment of landslide hazard has become a topic of major interests for both geoscientists and engineering professionals as well as for local communities and administrations in many parts of the world. Governments and research institutions worldwide have long attempted to assess landslide hazard and risks and to portray its spatial distribution in maps. Within this framework, earth sciences, and geomorphology in particular, may play a relevant role in assessing areas at high landslide hazard and in helping to mitigate the associated risk, providing a valuable aid to a sustainable progress.

Landslide hazard is defined as the probability of occurrence of a potentially damaging phenomenon within a given area and in a given period of time by Varnes (1984). The definition incorporates the concepts of magnitude, geographical location, and occurrence time. The first refers to the “dimension” or “intensity” of the natural phenomenon which conditions its behavior and destructive power; the second implies the ability to identify the place where the phenomenon may occur; the third refers to the temporal prediction of the event. Therefore, landslide hazard assessment study, which is commonly used for hazard mitigation, should give answers to three key questions: the magnitude, the location, and the occurrence time of a dangerous process.

However, so far, there are few reliable methodologies available for giving the answers. Historical information about landslides, with a more or less precise indication of slopes affected by instability and the dates of the active stages of the landslides, is important for an accurate temporal assessment relating data on triggering rainfall or on earthquakes to the resulting landslides. Although it is possible to observe relationships between current landslides and rainfall or earthquakes, the number of landslides for which temporal information is available may be so few that it is impossible to undertake a quantitative landslide hazard assessment.

On the other hand, once the slope geometry and subsoil conditions have been determined, the stability of a slope may be assessed using the deterministic methodologies. Most of the deterministic models are based on the limiting equilibrium approach for a two-dimensional (2D) model. The results of the 2D analysis are usually conservative, and although more expensive, three-dimensional (3D) analysis tends to increase the accuracy of result. It is well known that a 3D situation may become important in cases that the geometry of a slope varies significantly in the lateral direction, the material properties are highly anisotropic, or the slope is locally loaded (Chang 2002). Since the mid-1970s, increasing attention has been directed toward the development and application of 3D stability models (Hovland 1977; Chen and Chameau 1983; Hungr 1987; Lam and Fredlund 1993; Huang et al. 2002). Many studies concerning identification of critical slip surface adopted a 3D model (Baker 1980; Celestino and Duncan 1981; Nguyen 1985; Li and White 1987; Bardet and Kapuskar 1989; Bolton et al. 2003).

So far, however, an easy implementation method of 3D analysis for practical issues is still lacking. Also, 3D deterministic model should be applied to a wide

mountainous area for the purpose of landslide hazard assessment with accurate prediction of the magnitude, the location, and the occurrence time of the dangerous process. Concerning the occurrence time of slope failure, the trigger factors of the occurrence of landslide, such as rainfall and earthquakes, should be taken into account.

For realizing these desires, some new technologies are essential. GIS, as a tool for geotechnical engineers, has capabilities that range from convenient data storage to complex spatial analysis and graphical presentation. Combining the conventional geotechnical methodologies with GIS will significantly enhance the slope stability analysis. As the earlier study of this topic, the authors (Qiu et al. 2006; Xie et al. 2006) proposed a GIS-based 3D slope stability analysis model which is derived from Hovland's model in order to calculate the 3D safety factor within GIS, and further used this model for locating the critical slip surface in a large area by means of minimizing the 3D safety factor.

This study evolved the proposed 3D model into an improved one by combining with an infiltration model, to evaluate the variation of slope stability during rainfall event, and developed an advanced GIS-based system to efficiently assess regional landslide hazard as well as identifying the location, the magnitude, and the occurrence time of slope failure.

5.2 Model Description

5.2.1 *Mechanism of Rainfall-Induced Landslide*

During heavy rains, water seeps into the ground and travels through unsaturated soils. This water may perch on lower permeability materials or a drainage barrier such as bedrock and highly impermeable clays, creating a temporary, localized saturated zone, calls wetting band. The wetting band approach (Lumb 1975) assumes that the wetting band descends vertically under the influence of gravity, until either the main water table or a zone of lower permeability (e.g., a clay stratum) is reached. When the descending wetting band reaches the main water table, the surface of the main water table will rise with an increase in pore pressure. Under the latter condition, a perched water table will form above the zone of lower permeability, and pore pressure will become positive. The perched water table is considered to be the key factor in triggering rainfall-induced slope failures, which are often shallow in nature.

The groundwater table is usually located at a considerable depth below the ground surface, and there is no evidence that heavy rainfall causes a rise in the water table sufficient to trigger shallow failures (Kim et al. 2004). Instead, this kind of failures may be attributed to the deepening of a wetting front into the slope due to rainfall infiltration which results in an increase in moisture content, a decrease in soil matric suction, and a decrease in shear strength on the potential failure surface

(Lumb 1975; Kim et al. 2004; Rahardjo et al. 1995; Ng and Shi 1998; Fourie et al. 1999). Therefore, when shallow failure of a soil slope is caused by rainfall, the mechanism is that water infiltration causes a reduction in soil suction (or negative pore pressure) in the unsaturated soil. Soil suction will be lost upon full saturation. This results in a decrease in the effective stress on the potential failure surface, which is reflected in a decrease in the soil strength to a point where equilibrium cannot be sustained in the slope. Also, during and after periods of prolonged intense rainfall, significant seepage forces may develop and add to the gravity-induced shear stress. Failure occurs under constant total stress and increasing pore pressure.

5.2.2 Infiltration Model

There are numerous models formulated on the basis of soil characteristics that have been proposed to evaluate infiltration (Green and Ampt 1911; Neuman 1976; Smith et al. 1993; Ogden and Saghafian 1997; Iverson 2000). However, it is still difficult to quantify the amount of infiltration and the corresponding effect on the stability of slope for a regional area due to the complex mechanism and many parameters that are used in the models. Those availabilities often require detailed geotechnical information on the existing conditions and long-time computation. Because of the high cost involved, they are generally only achievable at the site investigation level in cases where high risk is anticipated.

The Green and Ampt method (Green and Ampt 1911) remains popular to this day because of its succinct concept of the “piston” wetting front and the inclusion of soil suction head and hydraulic conductivity parameters. Four assumptions are made in this model: (1) Soil surface is maintained constantly wet by water ponding; (2) a sharp wetted front exists; (3) the hydraulic conductivity is constant through the soil; and (4) the soil matrix suction at the front remains constant. These assumptions mean that the soil is fully saturated from the surface to the depth of the wetting front, while the soil below the wetting front is at the initial degree of saturation.

According to Darcy’s law, the infiltration rate is given by

$$f = K_s \frac{\psi_f + Z_f}{Z_f} \quad (5.1)$$

The depth of the wetting front can be related to the cumulative amount of infiltrated water by

$$F = Z_f(\theta_s - \theta_i) \quad (5.2)$$

Rearranging Eq. (5.2) to solve for Z_f and applying it to Eq. (5.1), the infiltration rate at any time t becomes

$$f(t) = K_s + K_s \frac{\psi_f(\theta_s - \theta_i)}{F} \quad (5.3)$$

The expression of $f(t)$ can be stated as follows:

$$t = t_p + \frac{1}{K_s} [F - F_p + \psi_f(\theta_s - \theta_i) \ln(n)] \quad (5.4)$$

$$n = \frac{\psi_f(\theta_s - \theta_i) + F_p}{\psi_f(\theta_s - \theta_i) + F} \quad (5.5)$$

t_p and F_p can be calculated from the following equations:

$$t_p = \frac{F_p}{P} \quad (5.6)$$

$$F_p = \frac{\psi_f K_s (\theta_s - \theta_i)}{P - K_s} \quad (5.7)$$

where $f(t)$ is the infiltration rate (m/h) at time t (h); K_s is the soil saturated hydraulic conductivity (m/h); ψ_f is the matrix suction at the wetting front (m); Z_f is the depth of the wetting front (m); F is the cumulative amount of infiltrated water (m); θ_s is the soil saturated volumetric water content; θ_i is the initial soil volumetric water content; t_p is the time when water begins to pond on the soil surface (h); F_p is the amount of water that infiltrates before water begins to pond at the surface (m); and P is the rainfall rate (m/h).

5.2.3 Applicability of GIS

A geographical information system, or simply GIS, has functional capabilities for data capture, input, manipulation, transformation, visualization, combination, query, analysis, modeling, and output (Bonham-Carter 1994). GIS is equipped with many functions that made GIS a powerful tool to model possible situations under various conditions given by specified data values or attribute values.

Recently, GIS has attracted great attention in landslide hazard assessment. The role of GIS in landslide analysis can be summed up as three aspects: data and/or analysis results expression, data handling, and data analyses (or modeling). However, from a survey of the recent applications of GIS to landslide hazard assessment, it is found that most researchers are concentrated in using a statistical method to quantify the relationship between slope failure and influential factors while GIS performs regional data preparation and processing; only a few researches, using infinite slope model which allows for calculation of a safety factor for each pixel individually to evaluate the stability of a specific-site slope, have been

conducted into the integration of GIS and the deterministic model (Anbalagan 1992; Dai et al. 2002; van Westen 1993). Although many engineers are familiar with GIS technology, they remain unaware of its analytical power and potential for wide and varied use. Since GIS enables more complex analysis of multiple data, it is expected that incorporating a sophisticated engineering model into GIS.

Most 3D limit equilibrium methods for slope stability analysis use column-based method in which the failure mass is divided into a number of small soil columns. Therefore, as shown in Fig. 5.1, it is possible to use grid-based columns, which are derived from overlaying GIS raster layers, to represent soil columns, that derived from discretization of the sliding mass (Qiu et al. 2006).

Based on the Mohr–Coulomb criterion, the safety factor of a slope failure mass is evaluated by comparison of the magnitude of the available shear strength with the shear strength required just to maintain stability along a potential failure surface. In a column-based 3D model, the available and required shear strength can be approximately calculated by summing corresponding items of all soil columns:

$$SF_{3D} = \frac{\sum_J \sum_I F_{\text{resistance}}(i, j)}{\sum_J \sum_I F_{\text{sliding}}(i, j)} \tag{5.8}$$

where F_{3D} is the 3D safety factor; $F_{\text{resistance}}(i, j)$, $F_{\text{sliding}}(i, j)$ are the available and required shear strength function of the soil column (i, j) within the sliding mass, respectively; and I, J are number of rows and columns of the raster data within the sliding mass, respectively.

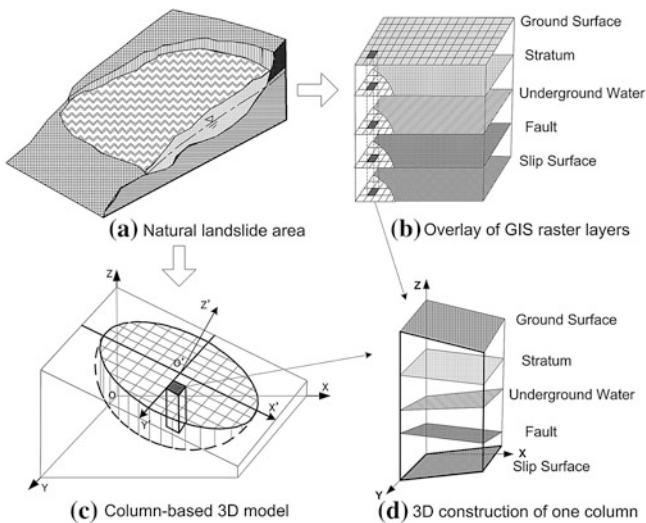


Fig. 5.1 Mechanism of GIS raster-based 3D model

The relevant items for calculation of safety factor should include elevation data of ground surface, slip surface, boundary of strata, and groundwater level (if it exists), and topographical parameters such as gradient and aspect of ground surface. In GIS, information of each item could be stored in a raster layer. Because a single raster layer can only represent certain information, it is not effective to treat so many raster layers at the same time. In contrast, vector data that comprise three geometry data types—point, line, and polygon—can describe many additional characteristics archived in an attribute table. Therefore, a point dataset is adopted here to manage the information of all raster layers. As shown in Fig. 5.2, the location of each point is set at the center of corresponding pixel of raster data, and the fields of the attribute table relate to each raster layer, respectively. The utilization of point dataset greatly expedites and simplifies the computation process for the safety factor.

5.2.4 Combination of Infiltration Model with 3D Slope Stability Model

Integrating Hovland’s 3D model and the GIS raster data format, a new GIS-based 3D model has been proposed (Xie et al. 2006).

$$SF_{3D} = \frac{\sum_J \sum_I [c'A + (W \cos \theta - U) \tan \phi'] \cos \theta_{Avr}}{\sum_J \sum_I W \sin \theta_{Avr} \cos \theta_{Avr}} \tag{5.9}$$

where F_{3D} is the 3D safety factor of the slope; c' is the cohesion (kN/m^2); A is the area of the slip surface (m^2); W is the weight of one soil column (kN); ϕ' is the friction angle ($^\circ$); θ is the inclination of the slip surface ($^\circ$); θ_{Avr} is the angle between

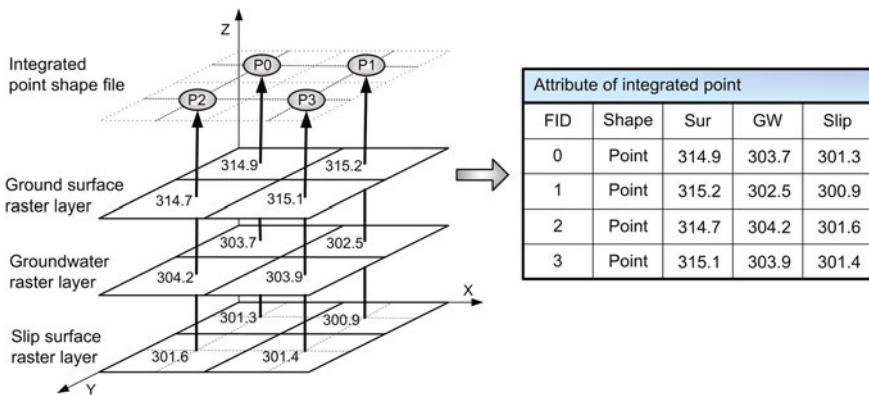


Fig. 5.2 Point dataset for integrating multiple raster layers

the direction of movement and the horizontal plane ($^{\circ}$); and I, J are the numbers of rows and columns of the cell within the range of failure mass.

It is widely known that rainfall causes a rise of groundwater level as well as an increase in pore water pressure that results in slope failure. As mentioned above, the wetting front causes a reduction in soil suction (or negative pore pressure) and an increase in the weight of soil per unit volume. These result in a process in which soil resistant strength decreases while total stress increases, until failure occurs on the potential failure surface where equilibrium cannot be sustained.

Under these conditions, there are four possible situations regarding the slip surface that can be anticipated, and four models, based on the Eq. (5.9), are thus proposed to calculate the corresponding safety factors (Qiu et al. 2007).

Model 1: The slip surface forms in the unsaturated zone between the wetting front that is advancing from the ground surface and the groundwater table. In this situation, the horizontal resistance force and the horizontal sliding force acting on the slip surface can be calculated using Eqs. (5.10) and (5.11), respectively.

$$F_1 = \{c'_i A' + [\gamma_i z + (\gamma_{\text{sat}} - \gamma_i) H_w] A \cos \theta \tan \phi'\} \cos \theta_{\text{Avr}} \quad (5.10)$$

$$F_2 = [\gamma_i z + (\gamma_{\text{sat}} - \gamma_i) H_w] A \sin \theta_{\text{Avr}} \cos \theta_{\text{Avr}} \quad (5.11)$$

Model 2: The slip surface forms in the saturated zone between the ground surface and the wetting front that is advancing from the ground surface. In this situation, the horizontal resistance force and the horizontal sliding force can be calculated using Eqs. (5.12) and (5.13), respectively.

$$F_1 = [c'_w A' + (\gamma_{\text{sat}} z \cos \theta - u_w) A \tan \phi'] \cos \theta_{\text{Avr}} \quad (5.12)$$

$$F_2 = \gamma_{\text{sat}} z A \sin \theta_{\text{Avr}} \cos \theta_{\text{Avr}} \quad (5.13)$$

Model 3: The slip surface forms in the saturated zone under the groundwater table and the wetting front that has reached the groundwater table. The horizontal resistance force and the horizontal sliding force can be calculated using Eqs. (5.12) and (5.13), respectively.

Model 4: The slip surface forms in the saturated zone under the groundwater table and the unsaturated zone that exists between the wetting front and the groundwater table. In this situation, the horizontal resistance force and the horizontal sliding force can be calculated using Eqs. (5.14) and (5.15), respectively.

$$F_1 = \{c'_w A' + [(\gamma_i (z_w - H_w) + \gamma_{\text{sat}} (H_w + z - z_w)) \cos \theta - u_w] A \tan \phi'\} \cos \theta_{\text{Avr}} \quad (5.14)$$

$$F_2 = [\gamma_i (z_w - H_w) + \gamma_{\text{sat}} (H_w + z - z_w)] A \sin \theta_{\text{Avr}} \cos \theta_{\text{Avr}} \quad (5.15)$$

Assuming that the vertical sides of each soil column are frictionless, the 3D safety factor can thus be calculated by summing F_1 and F_2 of all soil columns of failure mass.

$$SF_{3D} = \frac{\sum_J \sum_I F_1}{\sum_J \sum_I F_2} \tag{5.16}$$

where SF_{3D} is the 3D safety factor of the slope; F_1 is the horizontal resistance force (kN); F_2 is the horizontal sliding force (kN); γ_{sat} is the saturated unit weight of soil (kN/m³); γ_i is the initial unit weight of soil (kN/m³); c'_i is the initial effective cohesion of soil (kN/m²); c'_w is the saturated effective cohesion of soil (kN/m²); ϕ' is the effective friction of soil (°); Z_w is the depth of the wetting front (m); H_w is the depth of the groundwater table (m); Z is the depth of the slip surface (m); u_w is the pore stress (kN/m²); A is the area of the soil column (m²); A' is the area of the slip surface of the soil column; θ is the inclination of the slip surface (°); θ_{Avr} is the dip angle of the main sliding direction (°); and J, I are the numbers of rows and columns of the cell in the range of failure mass.

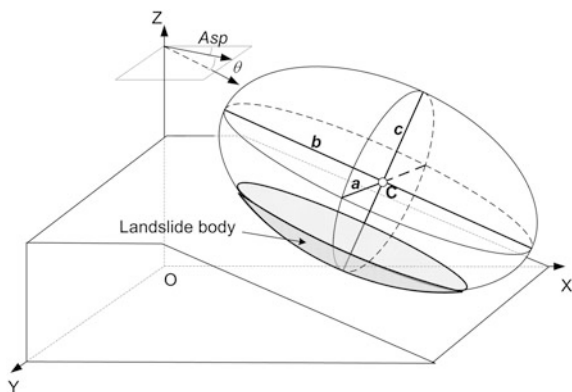
It should be noted that in Eq. (5.16), F_1 and F_2 of each soil column would be calculated using an appropriate equation that is selected from Eqs. (5.10) to (5.15) depending on the different conditions described above.

5.2.5 Search for Potential Slip Surface

Considering that many practical failure surfaces presented an ellipsoidal shape, in this study, the initial slip surface is assumed to be the lower portion of an ellipsoid.

Six parameters, namely three axial parameters “ $a, b,$ and c ”, the central point “ C ”, the inclination angle “ $\theta,$ ” and the inclination direction “ Asp ” of the ellipsoid, are selected to define the spatial posture of ellipsoid, as illustrated in Fig. 5.3.

Fig. 5.3 Definition of the spatial posture of ellipsoid



For implementing the critical slip surface searching, the random variables are firstly produced by Monte Carlo simulation to generate a random ellipsoid. The local posture of the ellipsoid is determined by the randomly selected central point and the coordinate conversion. The slip surface is identified by calculating the boundary surface of the lower part of the ellipsoid and the ground using the GIS raster data. Then, the 3D safety factor for each random trial slip surface can be calculated based on the GIS raster-based 3D model. After enough times of trial calculations, finally, the 3D critical slip surface and its associated safety factor can be obtained based on the minimum safety factor of trial calculations.

Each randomly produced slip surface is changed according to the different strata strengths and presence of weak discontinuities. If a randomly produced slip surface, based on the lower part of an ellipsoid, is lower than a weak discontinuous surface or the confines of the hard stratum, the weak discontinuity or the confined surface of the hard stratum will be prioritized for selection as one part of the assumed slip surface.

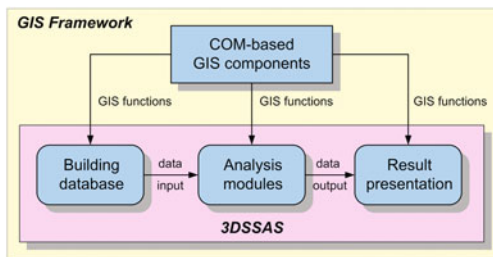
5.3 System Development

All of the analytic models have been modularized and incorporated into a standalone GIS system, called 3D slope stability analysis system (3DSSAS). Figure 5.4 is a simplified representation of the interaction between GIS and the 3DSSAS. All GIS functions that are used to perform the database construction, the analyses, and the result presentation are delivered from the Component Object Model-based GIS components assembly, ArcObjects. The main interface of 3DSSAS is shown in Fig. 5.5.

Figure 5.6 illustrates the basic architecture of 3DSSAS. The 3DSSAS system consists of six main modules:

- (1) The 3D slope stability analysis module: This module contains three GIS raster-based 3D models, namely the 3D extension of Bishop’s method, the 3D extension of Janbu’s method, and the revised Hovland’s method, and is used to calculate 3D safety factor of a specified sliding mass.

Fig. 5.4 Conceptual view of interactions between GIS and 3DSSAS



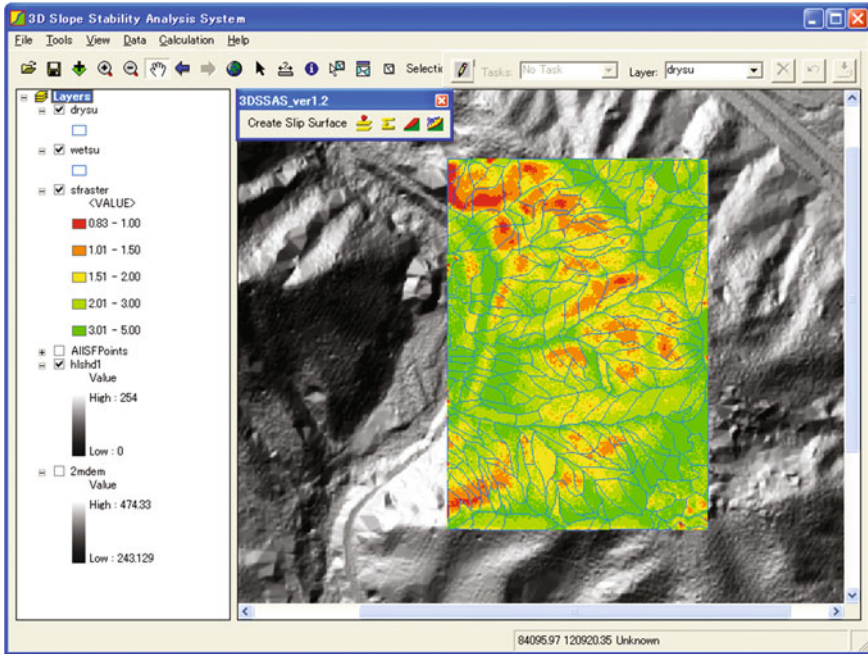


Fig. 5.5 Main interface of 3DSSAS

- (2) The slip surface identification module: This module provides functions for simulating possible shape and posture of sliding mass and for locating critical slip surface by using the Monte Carlo simulating method.
- (3) The slope-unit division module: By using this module, slope units are divided from DEM data, and subsequently, the topographical characteristics of slope units can be statistically calculated.
- (4) The slope stability probabilistic analysis module: This module achieves the slope-unit-based probabilistic analysis aiming to slope stability estimate of a regional area, while maintaining the 3D deterministic model.
- (5) The rainfall infiltration module: In this module, the temporal infiltration process of rainfall is quantitatively simulated by using an approximate formula of the Green and Ampt method.
- (6) The rainfall-infiltration-integrated slope stability analysis module: The core module of the 3DSSAS system provides an integrated model that combined the infiltration model and the 3D slope stability analysis model to achieve the spatio-temporal estimation of shallow landslide hazard triggered by rainfall.

Besides these main modules, 3DSSAS also offers some useful functions, such as surface analysis functions, shapefile editing tool, and 3D viewer, for efficient data processing and result presentation. These modules are then combined together

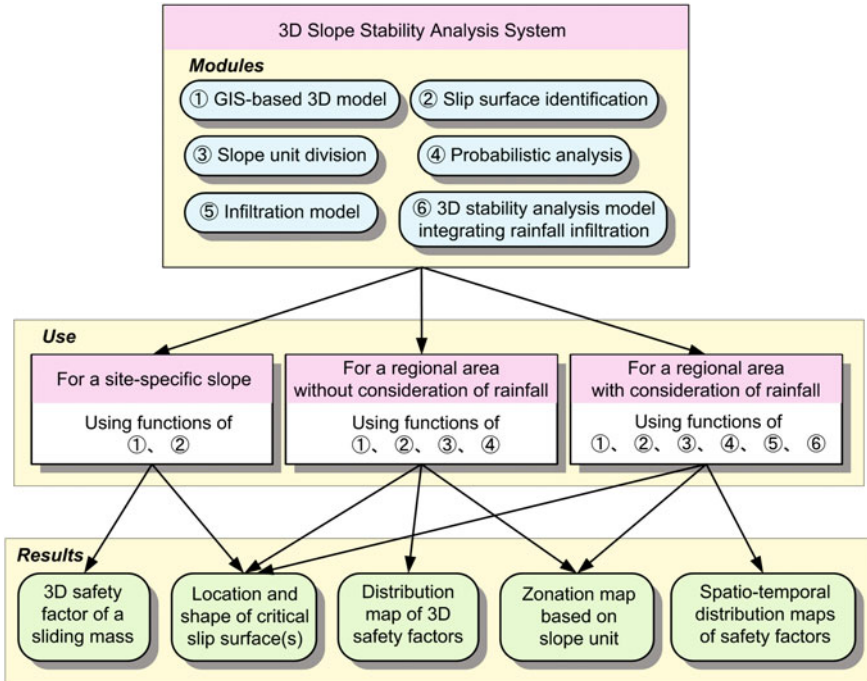


Fig. 5.6 Structure of 3DSSAS

effectively to enable the user to perform slope stability analyses in varying scales and under different conditions.

Analyzing the stability of a site-specific single slope with known slip surface is probably the simplest utilization of 3DSSAS. The prepared slip surface dataset is inputted into 3DSSAS with other necessary data. The 3D safety factor of this sliding mass is subsequently calculated by an appropriate 3D deterministic model that is provided by the slope stability analysis module. For the case of slip surface unknown, the slip surface identification module will be applied to perform randomly trial calculation to locate the critical slip surface by means of the minimum safety factor. The resultant data of slip surface is saved in raster format.

When targeting a regional area without rainfall effect considered, the slope-unit data is delivered firstly from the ground surface DEM data by using the slope-unit division module. For each slope unit, randomly trial calculations are performed by the slip surface identification module and the 3D slope stability analysis module to result in a series of slip surfaces with corresponding 3D safety factor. The critical slip surface is then extracted by means of the minimum safety factor and being saved into a polygon shapefile. The distribution of the 3D safety factors is saved as a raster data that are created by interpolation. Furthermore, the probabilistic analysis performed by the probabilistic analysis module for the distribution of the safety

factors delivers a reliability index, which is used to present the probabilistic stability of corresponding slope unit.

In the case of rainfall effect considered, in addition to the input data which are necessary for the analysis without rainfall considered, the rainfall data and the related hydraulic parameters are also needed for performance of the infiltration module. The spatio-temporal distribution of 3D safety factors is then derived by the rainfall-infiltration-integrated 3D slope stability analysis module.

The same as other engineering-aided software, the accuracy of the analytic result of 3DSSAS is data dependent. It raises a problem of the high cost involved in site investigation and indoor experiment for gathering detailed geotechnical information over a regional natural area. This is still a main difficulty in regional landslide hazard assessment.

In 3DSSAS, the evaluation of slope stability is based on the 3D safety factor. Basically, the calculation of the safety factor requires geometrical data (ground surface data, stratum data, and, if exists, and discontinuity data), data on the shear strength parameters (cohesion and angle of internal friction), and information on pore water pressure (groundwater data). Generally speaking, the best option for accomplishing an assessment is the application of 3DSSAS using all above-mentioned data with high precision, but is very cost demanding over large areas. Fortunately, using 3DSSAS, the ground surface data and the shear strength parameters which are the requisite minimum data are enough to complete a sketchy analysis. The ground surface data of a specific area can be conveniently obtained from aerial photographs or satellite images; the shear strength parameters could be obtained from test data or be estimated from geology. This paves a recommended way to a wise and efficient solution that using the requisitely minimal data, 3DSSAS allows a rapid assessment of stability in a given area to identify the parts where the possibility of occurrence of slope failure exists. The result of this kind of pre-analysis, even it is not exactly accurate, gives the information on possible location of landslide. The site investigation and indoor experiment can then be done purposefully for the possible locations, as well as subsequently detailed analysis.

5.4 Practical Application

National Route 49 runs from Iwaki city in Fukushima province to Niigata city in Niigata province, crossing Honshu Island, Japan. The Goto section, with a length of 1.3 km, is located about 10 km west of Iwaki city (Fig. 5.7), where slope disasters frequently occur and traffic regulations have to be issued during abnormal weather conditions. This seriously impacts on the use of the road. To evaluate the condition of slope stability and to support the decision-making process for suitable countermeasures, the 3DSSAS system was applied for landslide mapping.

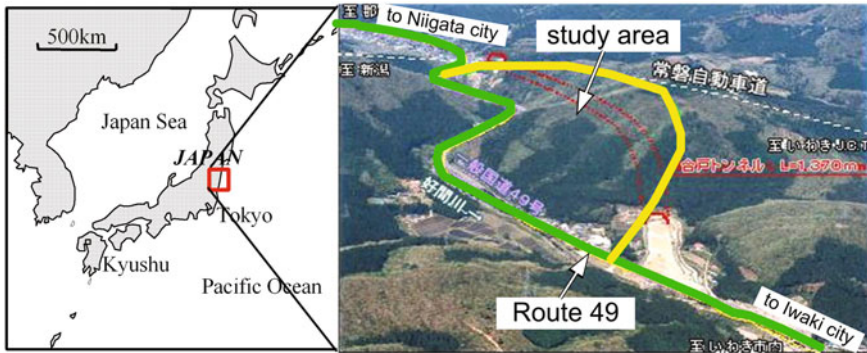


Fig. 5.7 Location of the Goto section of National Route 49

5.4.1 Description of the Study Area

The study area is located at the transition boundary between the eastern flat lands on the coast of the Pacific and the western Abukuma Plateau which is a late-Mesozoic metamorphic belt of the standard andalusite-sillimanite type. The area has a larger relative elevation of about 180 m compared to its surrounding area, and exhibits a morphology of U-shaped valley profile, with steep slopes in Mesozoic granites. The Route 49 runs beneath the slopes on the eastern side of the valley, along a north-south direction as shown in Fig. 5.7.

To obtain first-hand information about the engineering geological and geotechnical conditions regarding slope stability, a detailed field investigation was carried out for an area of 370×520 m on the upper slope of the Route 49, and this area is used as the study area of this research. The investigation results show that the granites are newly exposed in places over intermediate levels of the slope, which form very steep slopes with an angle greater than 50° , up to 70° . The upper slope is characterized by a relatively low-gradient terrain with a covering of quaternary deposits. Similar terrain is exhibited at lower levels of the slope, covered by colluvium and residual deposits formed by weathering of granites and accumulation of debris as result of landslide activities.

A field landslide mapping was performed for a part of the investigated area. Figure 5.8 shows this landslide map and summarizes the main geomorphological features of this area. A few old trails of soil creep, in a width of 10–15 m, are found at middle and near upper levels of the slope where the depth of the soil cover is greater than 2 m. Meanwhile, relatively fresh trails of landslides, in a smaller width of 5–10 m, are frequently seen at middle slope with underneath granites exposed, and at lower part of the slope where residual deposits underlaid.

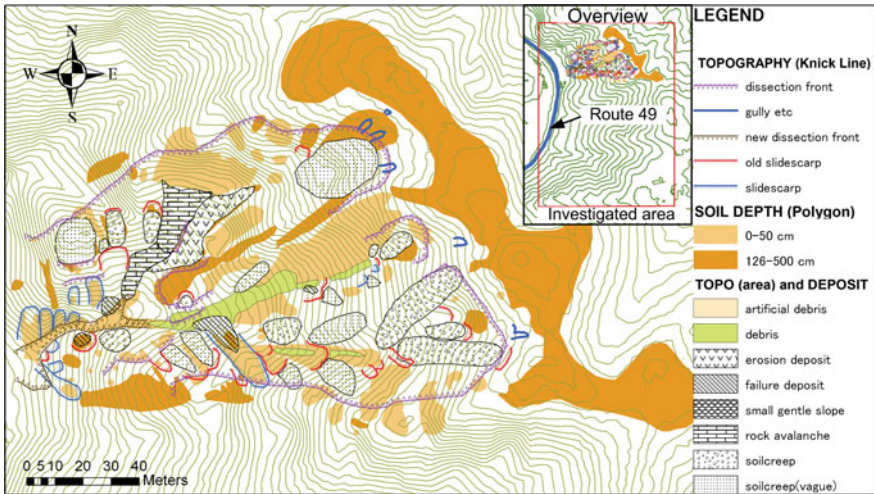


Fig. 5.8 Field investigation map showing the landslides occurring in the study area

5.4.2 Data Collection and Preparation

For a larger range of 1×1 km, a surface DEM dataset in grid form with 2 m mesh size was obtained by an airborne laser scanning. Figure 5.9 shows this DEM dataset with overlaying the range of the study area. The distribution of the slope angle is subsequently generated by corresponding GIS analytic function, in the same grid form as the DEM's. The result shows that in the range of the study area, the maximum slope angle is 69° with a mean of 31° and a standard deviation of 12.74, which is in agreement with the field observation. In addition, during the field investigation, a special surveying method was carried out to obtain the detailed data for soil depth in the study area. The bedrock surface was then constructed as a GIS raster dataset by subtraction of the soil depth from the surface elevation. Figure 5.10 shows a 3D view of the topography of the bedrock surface with the ground surface cover.

The physical properties and the mechanical behaviors of the soils in the study area have been studied by laboratory tests that include a permeability test and triaxial compression tests, for soil samples collected from three different spots. Due to the little variance in value of the test result of three soil samples, an average value of each geomechanical parameter of the surficial soil is used for the whole study area, as the c (cohesion), ϕ (friction angle), and γ (unit weight) are 2.0 kN/m^2 , 41° , and 15.3 kN/m^3 , respectively. Because there is no field groundwater level monitoring, the influence of the groundwater on slope stability was ignored in this study.

Fig. 5.9 DEM dataset with overlaying the range of the study area

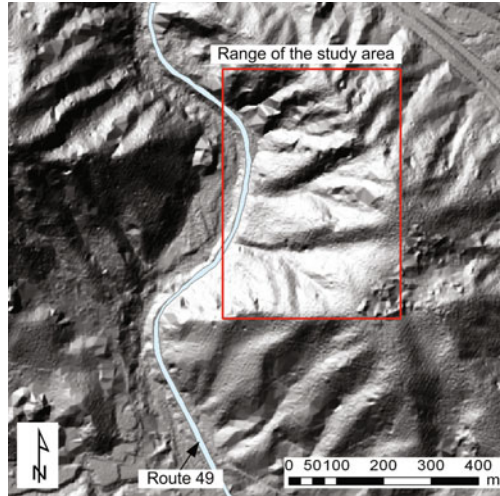
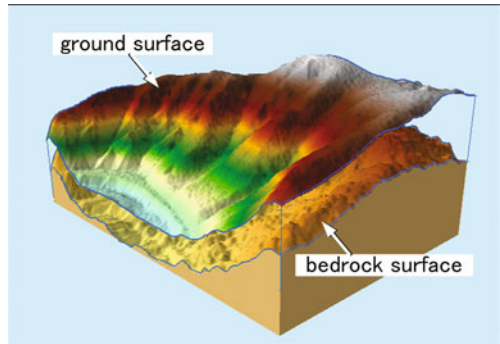


Fig. 5.10 3D view of the bedrock surface with ground surface covering



5.4.3 Analysis and Evaluation

The Monte Carlo calculation was then used to map the distribution of 3D safety factors and to detect the critical slip surfaces. Because the soil cover in the area is composed mainly of colluvium and residual deposits formed by weathering of granites underneath, according to the characteristics of the geological formation, the possible collapse mode is considered to be a shallow slope failure with a sliding surface along the boundary surface of the bedrock or within the soil layer. Hence, in the trial search process, if the lower part of a randomly produced ellipsoid is lower than the boundary surface of the bedrock, the surface of the bedrock will be prioritized for selection as part of the assumed slip surface. Considering the time consumed and effectiveness, the number of calculations in the Monte Carlo simulation for one center point was set to 100, which taking around 8 s.

After the trial calculation, 100 values of the 3D safety factor were obtained for each center point. The distribution of the resultant safety factors of each point tends to be lognormal. In this study, the minimum value of the resultant safety factors, which reflects the maximum degree of danger, was used as the final result of the 3D safety factor of the center point.

Assuming that the resultant 3D safety factors of all center points have a PDF that corresponds to a lognormal distribution, a reliability index was then calculated for each slope unit. The zonation map of slope stability was thus obtained. Figure 5.11 shows this slope-unit-based zonation map, which can stochastically represent the sensitivity to slope failure of the study area. The lognormal distribution of 3D safety factors of two slope units, which are labeled as slope unit 129 and 20 in Fig. 5.11, is shown in Fig. 5.12. It is seen that slope unit 129 has a mean safety factor of 1.382, and slope unit 20 has a higher safety factor of 1.528. In a deterministic sense, it would appear that slope unit 20 is safer than slope unit 129. However, the safety factor PDF for slope unit 129 has a much smaller standard deviation in comparison with slope unit 20, which leads to a reliability index value of slope unit 129 of 2.454, while that of slope unit 20 is 1.377. So slope unit 129 is considered safer than slope unit 20 as there is less uncertainty associated with slope unit 129. On the basis of Table 5.1, slope unit 129 would be descriptively classified as “poor” and slope unit 20 would be assigned a “hazardous” rating.

For the study area, a uniform rainfall event with duration of 10 h and an intensity of 8 cm/h was assumed, and the method proposed above was applied. The detection of critical slip surfaces was achieved through trial searching and calculation of the 3D safety factor. In the trial searching process, if the lower part of a randomly

Fig. 5.11 Slope-unit-based landslide hazard zonation map

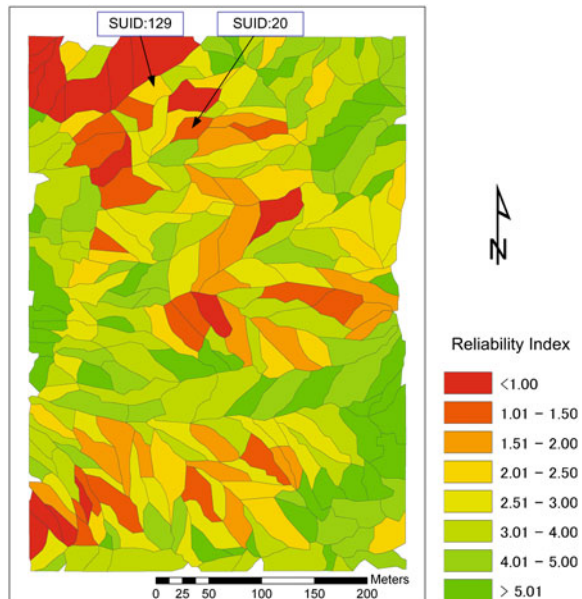
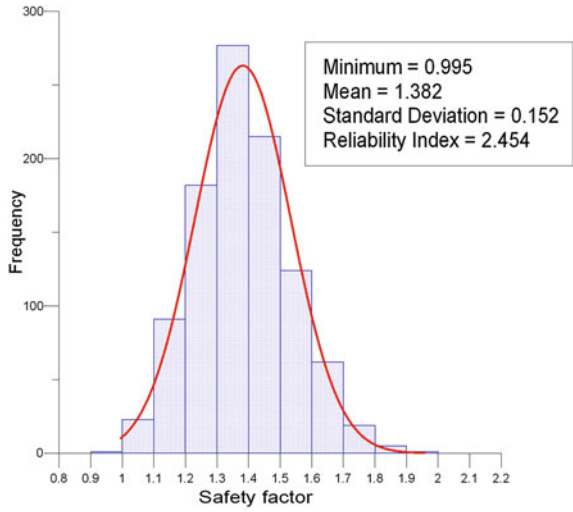
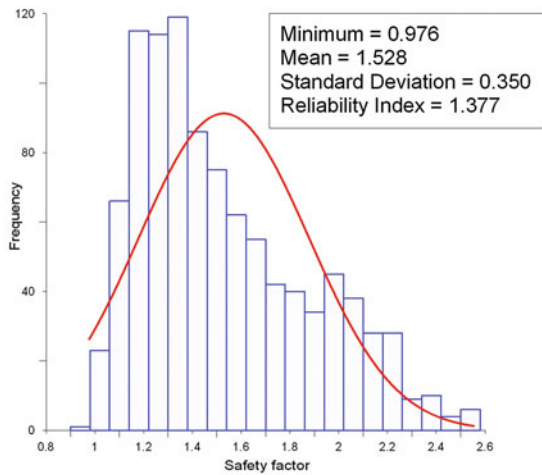


Fig. 5.12 Distribution of 3D safety factors of two slope units



(a) SUID:129



(b) SUID:20

Table 5.1 Example values of β and P_F

Performance level	Reliability index β	Probability $P_F = P(F < F_c)$
High	5.0	2.871×10^{-7}
Good	4.0	3.169×10^{-5}
Above average	3.0	0.00135
Below average	2.5	0.00621
Poor	2.0	0.02275
Unsatisfactory	1.5	0.06681
Hazardous	1.0	0.15866

produced ellipsoid is lower than the boundary surface of the bedrock, the confined surface of the bedrock will be prioritized for selection as one part of the assumed slip surface.

After 100 trial calculations for each raster cell taken as the central point of a trial ellipsoid in the study range, finally, the variation of safety factors over time was mapped. Figure 5.13 illustrates six distribution maps of the safety factors changing over time. From these maps, a high correlation between rainfall and the decrease of the safety factor can be recognized. The calculating result, however, presents slight overestimation for the possibility of failure occurrence as the lowest safety factor was nearly 0.4. The reason was considered as the presumption of the constantly high intensity of rainfall event which actually seldom, if not never, occurs in the reality. Also, the neglect of the lateral outflow of infiltrated water in the infiltration model is another reason that derived the overestimation of failure possibility.

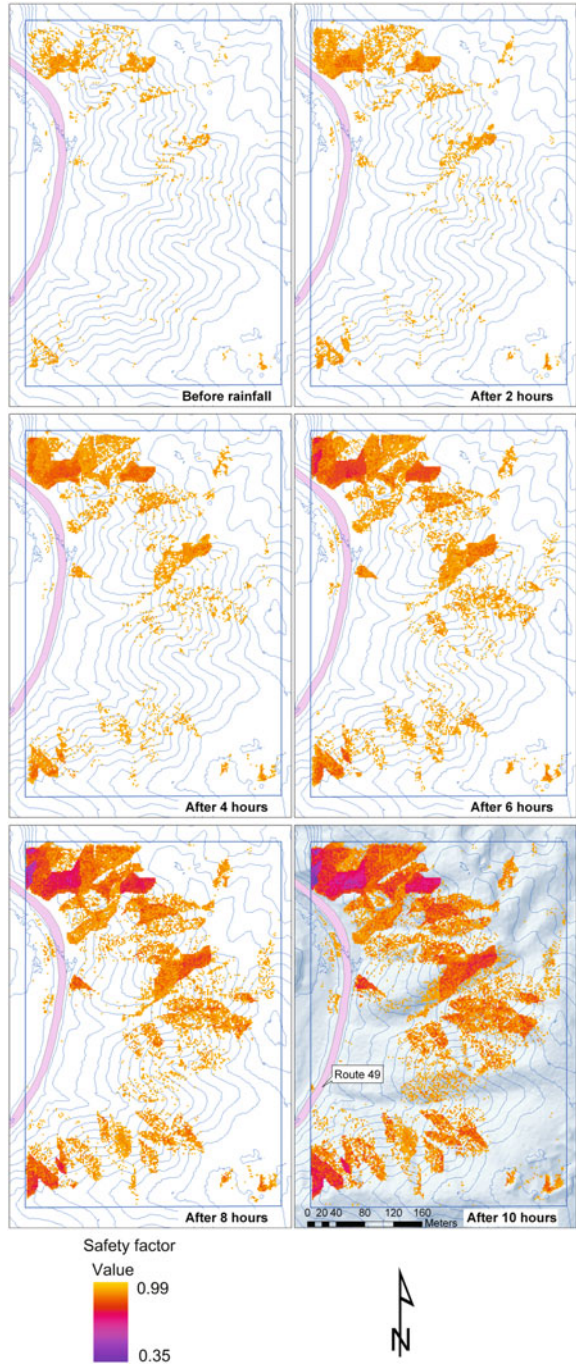
5.5 Concluding Remarks

In this study, responding to the question regarding the occurrence time of slope failures, a challenge has been done for dealing with deterministic slope stability analysis related to shallow rainfall-induced landslides. A new 3D slope stability model was developed by coupling a dynamic hydrological model that simulates the rainfall infiltration over time with the developed 3D slope stability model that quantifies the varying safety factor during rainfall. Using this model, the location and the magnitude of potential failures can be identified through a random search procedure for minimizing 3D safety factor; furthermore, the time of occurrence of failures can be forecasted by mapping the changing distribution of safety factors during rainfall.

For typical slopes, the material is originally unsaturated and the surface of the slope is continuously being wetted by rainfall. Short heavy rainfall after a prolonged dry period cannot create the conditions leading to saturation, while a heavy rainfall after a period of moderate rainfalls may saturate the remaining upper few inches of unsaturated soil. Hence, the consideration concerning the antecedent rainfall would be necessary, although is uncompleted at the present stage in this study, for simulating a gradual buildup of moisture in the ground over a prolonged period of time. In addition, owing to limited data about rainfall records related to occurrence times of landslide, calibration and validation of the model are difficult.

Incorporating all proposed technologies and models, a comprehensive GIS-based system, called 3D slope stability analysis system (3DSSAS), has been developed for efficiently assessing and mapping regional landslide hazard. Once necessary data, including slope-related data and hydraulic data, are acquired, this system is shown to have the abilities both to estimate the variation of slope stability over a wide natural area during rainfall which answers the question about occurrence time of failures and to identify the location and shape of potential failure surfaces which answers the questions of location and magnitude. The effectiveness

Fig. 5.13 Distribution maps of safety factors changing over time



of the system has been tested by two practical applications for landslide-prone area in Japan.

3DSSAS was designed to be an architecture that has capabilities to implement multiple purposes by interconnecting appropriate models and technologies to be a subsystem. For instance, the stability of a specific slope with a known slip surface can be quantified by means of the 3D safety factor using the 3D slope stability analysis model; techniques of slope-unit division and slip surface location would be used with the 3D mode together for a regional assessment; and, when rainfall is considered as a trigger factor, the hydraulic model should be added.

Landslide hazard is considered a continuous, spatially aggregated variable. Natural slopes that have been stable for many years may suddenly fail because of changes in topography, seismicity, groundwater flows, and weathering. Hence, the renewal of the data would result in a different assessment for same site. With the fast development in geoinformation science and earth observation, there are more and more tools available for quickly data acquisition. For example, high resolution remote sensing products can be used to derive DEMs in any desired time period. Based on these considerations, besides being robust for a reliable landslide hazard assessment, the developed system also provides powerful capabilities for data processing and easy application to quickly reestablish the hazard assessment at any time responding to data renewal.

The accuracy of landslide assessment systems is generally data dependent. A comprehensive and exhaustive evaluation of landslide hazard often requires detailed and accurate datasets about the spatial variation of parametric values which form the input of the slope stability and hydrological models. However, the spatial distribution of these datasets is extremely difficult to measure. Material properties are also difficult to measure for many points over large areas and show a high spatial variability. At the present stage, because of the high cost involved, they are generally only achievable at the site investigation level in cases where high risk is anticipated. Responding to this problem, a cost-benefit solution given by this study is that a sketchy evaluation for whole studying area, even maybe being a little inaccuracy, can be firstly completed by 3DSSAS using the most sensitive parameters consists of DEM (which can easily be obtained from accurate aerial photographs or satellite survey data nowadays) and geomechanical parameters (which can be empirically supposed from various sources such as a existing geology map), in order to select areas with relative high susceptibility related to failure occurrence for more detailed investigation. Based on the detailed investigation available for specific slopes, stricter analysis can then be performed with detailed data to quantify the possibility with higher precision. It is believed that the analysis would end in more accurate results when the number and precision of parameters increase.

On the other hand, considering that the limitations in the theory and the parameterization of the analytic models leave many uncertainties concerning the absolute value of the 3D safety factor, a slope-unit-based probabilistic method was proposed by combining the Monte Carlo calculations with probabilistic statistics related to the variability of the 3D safety factors distributed in each slope unit to result in a reliability index as the probability of failure. The final result of such an

approach is a zonation of the entire area into landslide hazard units. The same probability of experiencing landslides is given to the entire slope unit; however, abrupt changes may occur between adjacent units.

Due to the insufficiencies in data acquisition and handling, and uncertainties in model selection and calibration, the validation of the developed system is still lack. In general, predictive models of landslide hazard can not be readily tested by traditional scientific methods. Indeed, the only way a landslide predictive map can be validated is through time.

With the fast development in earth observation science and geotechnics, there are more and more techniques available for carrying out a more reliable and quickly landslide hazard assessment. For example, high resolution remote sensing products can be used to derive DEMs in any desired time period for reassessing the landslide hazard at any time. Using these technologies, a comprehensive and advanced system can be established. In such a system, real-time monitoring data on rainfall, earthquake, pore pressure, and displacement of landslides, which may be a trigger for landslide occurrence, or indications of the movement of specific landslides, should be communicated into the database in real time for the purpose of landslide warning. This information can be acquired at sites by local monitoring units and be transmitted to management center by network links. Once the spatial database has been developed, the manipulation and analysis of the data allow it to be combined in various ways to evaluate what will happen in certain situations. The overlay operation of the GIS allows experts to combine the analytic results with factor maps of site characteristics in a variety of ways to produce landslide hazard maps to distribute.

Although due to the limitations of time and techniques, some concepts of this study are still unaccomplished; it is hoped that this study may be helpful to provide a rational framework for future research work and will present some aid to other researchers in the field of landslide hazard assessment.

References

- Anbalagan R (1992) Terrain evaluation and landslide hazard zonation for environmental regeneration and land use planning in mountainous terrain. Proc. VI Int Symp On landslides, vol 2. Christchurch, New Zealand, pp 861–868
- Baker R (1980) Determination of the critical slip surface in slope stability computations. Int J Numer Anal Methods Geomech 4:333–359
- Bardet JP, Kapuskar MM (1989) A simplex analysis of slope stability. Comput Geotech 8:329–348
- Bonham-Carter GF (1994) Geographic information systems for geoscientists: modeling with GIS. Pergamon, Ottawa, 398 pp
- Bolton Hermanus PJ, Heymann G, Groenwold A (2003) Global search for critical failure surface in slope stability analysis. Eng Opt 35(1):51–65
- Celestino TB, Duncan JM (1981) Simplified search for non-circular slip surface. Proceedings of the 10th international conference on soil mechanics and foundation engineering, Stockholm, Sweden, pp 391–394

- Chen RH, Chameau JL (1983) Three-dimensional limit equilibrium analysis of slopes. *Geotechnique* 32(1):31–40
- Chang M (2002) A 3D slope stability analysis method assuming parallel lines of intersection and differential straining of block contacts. *Can Geotech J* 39:799–811
- Dai FC, Lee CF, Ngai YY (2002) Landslide risk assessment and management: an overview. *Eng Geol* 64:65–87
- Fourie AB, Rowe D, Blight GE (1999) The effect of infiltration on the stability of the slopes of a dry ash dump. *Geotechnique* 49(1):1–13
- Green WH, Ampt GA (1911) Studies of soil physics: I. The flow of air and water through soils. *J Agric Sci* 4:1–24
- Hovland HJ (1977) Three-dimensional slope stability analysis method. *J Geotech Eng Div, ASCE* 103(GT9):971–986
- Hungri O (1987) An extension of Bishop's simplified method of slope stability analysis to three dimensions. *Geotechnique* 37(1):113–117
- Huang C, Tsai C, Chen Y (2002) Generalized method for three-dimensional slope stability analysis. *J Geotech Geoenviron Eng* 128(10):836–848
- Iverson RM (2000) Landslide triggering by rain infiltration. *Water Resour Res* 36(7):1897–1910
- Kim J, Jeong S, Park S, Sharma J (2004) Influence of rainfall-induced wetting on the stability of slopes in weathered soils. *Eng Geol* 75:251–262
- Lumb P (1975) Slope failures in Hong Kong. *Q J Eng Geol* 8:31–65
- Li KS, White W (1987) Rapid evaluation of the critical slip surface in slope stability problems. *Int J Numer Anal Methods Geomech* 11:449–473
- Lam L, Fredlund DG (1993) A general limit equilibrium model for three-dimensional slope stability analysis. *Can Geotech J* 30:905–919
- Neuman SP (1976) Wetting front pressure head in the infiltration model of Green and Ampt. *Water Resour Res* 12(3):564–566
- Nguyen VU (1985) Determination of critical slope failure surface. *J Geotech Eng, ASCE* 111(2):238–250
- Ng CWW, Shi Q (1998) A numerical investigation of the stability of unsaturated soil slopes subjected to transient seepage. *Comput Geotech* 22(1):1–28
- Ogden F, Saghafian B (1997) Green and Ampt infiltration with redistribution. *J Irrig Drainage Eng* 123(5):386–393
- Qiu C, Esaki T, Xie M, Mitani Y, Wang C (2006) New implementation approach of three-dimensional slope stability analysis using geographical information system. In: Leung CF, Zhou YX (eds) *Rock mechanics in underground construction, the 4th Asian rock mechanics symposium*. World Scientific Publishing, Singapore, 488 pp
- Qiu C, Esaki T, Xie M, Mitani Y, Wang C (2007) Spatio-temporal estimation of shallow landslide hazard triggered by rainfall using a three-dimensional model. *Environ Geol* 52:1569–1579
- Rahardjo H, Lim TT, Chang MF, Fredlund DG (1995) Shear strength characteristics of a residual soil. *Can Geotech J* 32:60–77
- Smith RE, Corradini C, Melone F (1993) Modeling infiltration for multistorm runoff events. *Water Resour Res* 29:133–144
- Varnes DJ (1984) *Landslide hazard zonation: a review of principles and practice*. IAEG Commission on Landslide and other Mass-Movements. UNESCO press, Paris, 63 pp
- van Westen CJ (1993) *Application of geographical information system to landslide hazard zonation*. ITC Publication no. 15, ITC, Enschede, The Netherlands, 245 pp
- Xie M, Esaki T, Qiu C, Wang C (2006) Geographical information system-based computational implementation and application of spatial three-dimensional slope stability analysis. *Comput Geotech* 33:260–274

Part III

Mapping

Chapter 6

Large-Scale Landslide Inventory Mapping in Lesser Himalaya of Nepal Using Geographic Information System

Manita Timilsina, Netra Prakash Bhandary, Ranjan Kumar Dahal and Ryuichi Yatabe

Abstract Large-scale landslides are huge deep-seated failed masses that occurred in the geological past. Some of them are dormant while some are still active, creeping, and reactivating causing problems in the form of small-scale failures. Unlike small-scale failures in which the failed masses were already replaced, large-scale landslides built and modified the topography that makes it unique and differentiate from the other stable slope. In the Nepal Himalaya, large-scale landslides are widely distributed in the Lesser Himalayan and Higher Himalayan zones. But, systematic database regarding the large-scale landslide is not available. So, this paper describes a methodology to delineate large-scale landslides and preparation of the inventory map in the Himalayan terrain. Different approaches of landslide inventory mapping using GIS techniques are discussed, and validation methods are proposed.

Keywords Large-scale landslides · Lesser Himalayan Zone · GIS

Nepal lies in the continent-continent collision zone of the Indian and Eurasian tectonic plate encompassing 800 km of the central Himalaya. 83% of its total territory is covered with mountains of varying elevation range which suffer from landslides and related problems every year (Gerrard and Gardner 2000; Petley et al. 2006), and others pointed out that landslides occur extensively in the Himalaya and particularly in Nepal. A combination of dynamic geology, fragile topography, adverse climatic condition, and human intervention has played a key role in the

M. Timilsina (✉)

Himalaya Conservation Group Nepal, Kalika Marga,
Sanepa-2 Lalitpur, P.O. Box 9669, Kathmandu, Nepal
e-mail: manitatimilsina@gmail.com

N.P. Bhandary · R. Yatabe
Graduate School of Science and Engineering,
Ehime University, Matsuyama, Japan

R.K. Dahal
Central Department of Geology, Tribhuvan University, Kirtipur, Nepal

occurrence and reactivation of landslides in the Nepal. On the other hand, landslides in the Nepal also serve as an erosional mechanism to maintain the equilibrium with the tectonic uplift and help in the evolution of landscape. However, landslides also claim a few hundreds of lives every year and cause enormous damage to infrastructures and properties in Nepal.

Landslides in the Nepal Himalaya are scale dependent, from the massive extent of a whole mountain range to very minor slope failures (Shroder and Bishop 1998; Shang et al. 2003; Hasegawa et al. 2009). Therefore, term landslide in Nepal is used for all kinds of slope failure-related disaster such as cut-slope failures, debris flow, mud flow, flash flood, and deep-seated large-scale landslides. This indicates the landslide classification system is not well practiced in Nepal. Due to the different physiographical and climatic settings, the international landslide classification systems are difficult to adopt directly and demand our own classification system which is still to be carried out. However, for simplicity, landslides in the Himalaya can be divided into two broad categories (1) small-scale landslides (debris flows, debris slides, rock falls, and rock slides) and (2) large-scale landslides (deep-seated mountain slope creeping). Landslide-related studies in Nepal are mostly oriented toward the small-scale landslides due to their frequent occurrence and disastrous nature. However, large-scale landslides are also very common in many parts of Nepal and mainly distributed in the Lesser Himalayan Zone. We know that these large-scale landslides can be accelerated or reactivated as a result of natural disturbances, seismic events, stream undercutting, and human intervention. Comparing to small-scale landslides, large-scale landslides are less dangerous but if left unchecked can completely destroy the structure or settlement over time. Therefore, identification of large-scale landslide location is very essential, and landslide inventory mapping can be a good alternative. Large-scale landslides are not as frequent as small-scale landslides, and their future new occurrence depends only on future mega-earthquakes, but they are present in the topography through geological times, and risk of reactivation is always there. Therefore, in case of large-scale landslides, present spatial distribution is more important than landslide susceptibility or hazard map to reduce their future impact. On the other hand, the extraction of landslide data is still difficult in developing countries like Nepal due to lack of high resolution data and sometimes expensive to acquire the available data. The next important thing is how to use the available resources so that the acquired data are as accurate as possible and reliable for further study. Therefore, in this study, proper procedure to extract landslide inventory from the available resources especially in the developing countries context has been illustrated.

The main objective of this work is to prepare landslide inventory map for large-scale landslide in Lesser Himalayan Zone of Nepal. We attempt a critical review of conventional, and new experimental techniques used to prepare landslide inventory maps at different spatial scales and selection of suitable techniques for large-scale landslides. In order to achieve this, first of all an identification guideline to facilitate the description and classification of large-scale landslides in the Himalaya is prepared. Secondly, based on the identification criteria, large-scale landslides are identified by interpretation of aerial photographs using stereoscope.

6.1 Lesser Himalayan Zone

The Himalayan Orogeny began with the collision of Indian and Eurasian tectonic plates around 55 million years ago. The tectonic activity is still active and can be noticeable by present day northward movement of India at a rate of 2–5 cm per year and the occurrence of frequent seismic shakes all along the Himalaya and its surroundings (Pandey et al. 1995; Bilham et al. 1997). Longitudinally, it is divided into five geological and tectonic zones (Ganser 1964) extending from east to west. 1. Gangetic Plain (Terai Zone), 2. sub-Himalayan Zone, 3. Lesser Himalayan Zone, 4. Higher Himalayan Zone, and 5. Tibetan-Tethys Himalayan Zone. These east–west extending zones run almost parallel to each other and have different lithology, structure, and geological history as shown in Figs. 6.1, 6.2 and 6.3. All geological zones are separated from each other by the major thrust faults system. The southernmost thrust, known as Main Frontal Thrust (MFT) separates the sub-Himalayan (Siwaliks) Zone from Gangetic Plains or Terai Zone. The Main Boundary Thrust (MBT) separates the Lesser Himalayan Zone from Siwaliks, and the Main Central Thrust separates the Higher Himalayan Zone from the Lesser Himalayan Zone. Nepal occupies the central sector of Himalayan arc and shares the similar geological and tectonical settings (Fig. 6.2).

The Lesser Himalayan Zone is separated from the Siwaliks and the Higher Himalayan Zone by the Main Boundary Thrust (MBT) in the south and the Main Central Thrust (MCT) in the north, respectively. From the geological history, movement along the MBT (Meigs et al. 1995) effectively created the high mountain

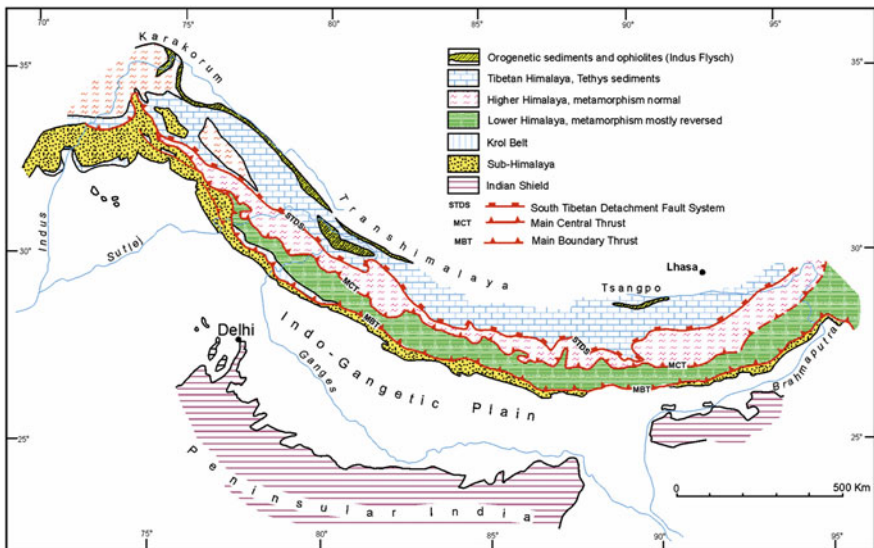


Fig. 6.1 Longitudinal subdivision of the Himalaya (modified after Ganser 1964; Upreti and Yoshida 2005)

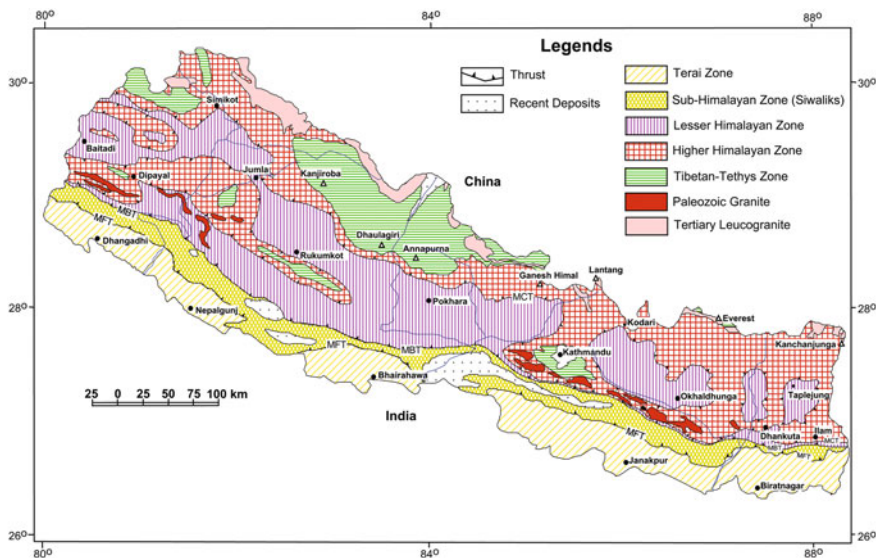


Fig. 6.2 Simplified geological map of Nepal (modified from Amatya and Jnawali 1994; Dahal 2006)

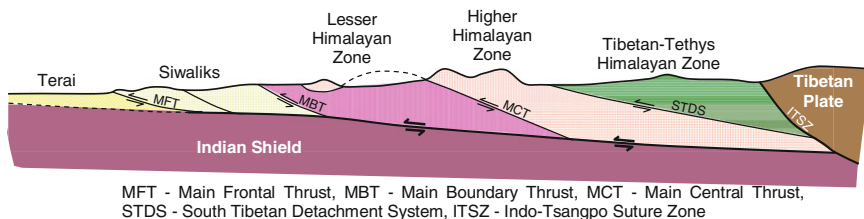


Fig. 6.3 Generalized cross section of Himalaya (modified after Dahal 2006)

ranges in the Lesser Himalaya known as the Mahabharat Ranges. Later, the river flowing from the Higher Himalaya to the south started to erode the elevated Mahabharat Range, resulting in V-shaped valleys and ridges with several levels of river terraces. The MBT is active even today, and the frontal part of the Lesser Himalaya is still rising. Similarly, lying between the MBT and MCT, the Lesser Himalayan Zone is found to be structurally very complex because several thrust sheets laid stacked one over the other and are folded and faulted on a large scale (Stöcklin 1980). Regarding the seismicity, most of the earthquakes in the Himalaya are also concentrated along a 50–100-km-wide zone between the MBT and MCT. Therefore, the tectonic history of the Lesser Himalaya supports the complex geological structure and highly faulted and fractured rock strata in central Nepal and is very favorable for the formation of large-scale landslides.

6.2 Large-Scale Landslides in Lesser Himalaya of Nepal

The information on large-scale landslides in the scientific literature is very limited. The term “large-scale landslide” originated in Japan symbolizing a huge landslide. However, similar types of landslides in the scientific literatures are termed with different names, for example, large landslides (Dortch et al. 2009), giant landslides (Korup et al. 2007), historical landslides (Van Den Eeckhaut et al. 2007), old deep-seated landslides (Van Den Eeckhaut et al. 2009), and deep-seated gravitational slope deformations (DSGSD) (Dramis and Sorriso-Valvo 1994; Hradecky and Pa’nek 2008; Agliardia et al. 2001; Aucelli et al. 2012). Thus, large-scale landslides have been defined by the authors in different ways, depending on the research approach and on the involved evolutionary mechanisms. Large-scale landslide studies are mostly focused on exploring geological and geomorphological attributes and spatial distribution patterns and causes and are usually limited to site-specific cases.

Concerning about large-scale landslides in the Himalaya, some studies in the Higher Himalaya explore the large-scale landslides; however, most of them are site-specific studies, and the landslides are termed as huge or massive rock-slope slides of a particular location (Waltham 1996; Korup et al. 2006). Yagi and Nakamura (1995), Yagi (2001), and Yatabe et al. (2005) identified the large-scale landslide problems in the Lesser Himalayan Zone of central Nepal. Similarly, Hasegawa et al. (2009) explored the causes of the large-scale landslides in the Lesser Himalayan Zone. Moreover, the progress report submitted by (JICA 2007) for the disaster risk management for the Narayanghat–Muglin Highway also indicates the presence of large-scale landslide masses as shallow landslide potential zones. Thus, the concept of large-scale landslides in the Lesser Himalayan Zone is in an emerging state, and researchers are still not ready to accept its one common concept. Therefore, the authors attempt to develop a proper definition along with identification guidelines for large scale in this study.

A large-scale landslide is defined as the huge slipped slope mass that is still intact and present in the topography (Timilsina et al. 2013). The authors propose that large-scale landslides were induced in the geological past and that their future occurrences may depend upon future mega-earthquake events. Here, the term “geological past” indicates a long time gap. Some studies (JICA 2007; Waltham 1996; Heuberger et al. 1984; Purtscheller et al. 1995; Pande et al. 2002) suggest that the large-scale landslides in the Himalaya occurred within the last few hundred years. The exact age of the landslides is difficult to determine, but their geomorphological attributes indicate that the landslides are indeed very old and occurred during geological history rather than human history. Yatabe et al. (2005) described various types of large-scale landslides, and Hasegawa et al. (2009) provided a schematic diagram of typical large-scale landslides in the Lesser Himalaya of Nepal. Basically, landslides can be classified on the basis of the materials involved,

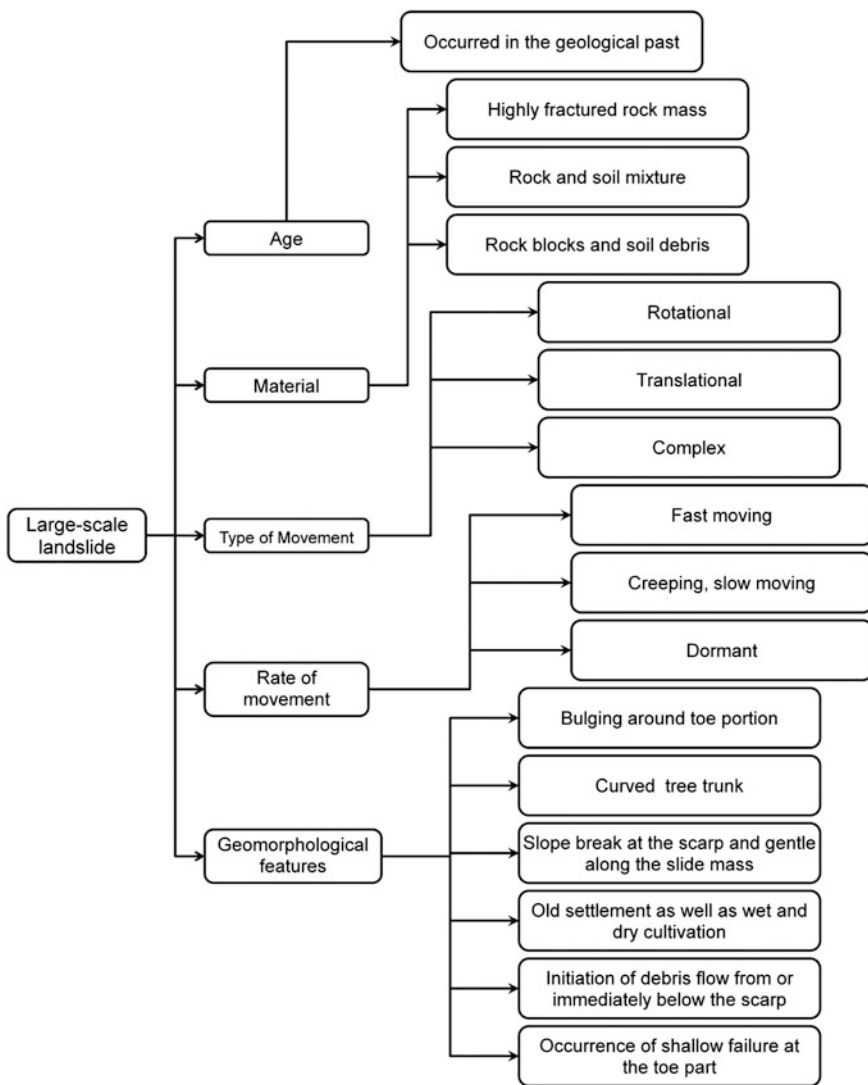


Fig. 6.4 General typical characteristic features of large-scale landslides

the type of movement, the rate of movement, and many other additional factors mentioned in Varnes (1978), Cruden and Varnes (1996), Hutchinson (1988), EPOCH (1993), Dikau et al. (1996), and Hungr et al. (2001). The large-scale landslides in this study include all the characteristics given in Fig. 6.4. A schematic diagram is also prepared to illustrate the large-scale landslide characteristics as shown in Fig. 6.5.



Fig. 6.5 Schematic diagram along with a photograph of a large-scale landslide and its characteristics features in the Lesser Himalayan Zone of Nepal. *Red and yellow dotted lines* (right photo) indicate two large-scale landslide masses moving in two different directions, also indicated by *red and yellow arrows* (right photo). Similarly, the *white line* (right photo) indicates the detachment zone or scarp

6.3 Landslide Inventory

A landslide inventory map records the location and, where known, the date of occurrence and the types of mass movements that have left discernable traces in an area (Wieczorek 1984; Guzzetti et al. 2000; etc.) and provides database for any landslide hazard assessment study. They are effective and easily understandable products for both experts, such as geomorphologists, and non-experts, including decision makers, planners, and civil defense managers. Based on the purpose, landslide inventory also varies. Similarly, the techniques to prepare landslide inventory also vary depending on the available resources, physiological and climatic settings of the area. Many methodological approaches have been developed to identify the occurrence of landslides in space and time. Landslide maps and inventories are frequently prepared based on the analysis of remote sensing data such as stereographic aerial photographs, space-borne images, and digital terrain models (DTM) coupled with field investigation. Detail reviews on landslide mapping and inventories can also be found in various literature sources (e.g., Soeters and Van Westen 1996; Malamud et al. 2004; Guzzetti et al. 2006; Van Westen 2007, 2008). This section will also give a simple overview on the methods most used in research practice and to highlight their advantages and disadvantages for landslide inventory in terms of large-scale landslides.

6.3.1 Conventional Methods for Preparing Landslide Inventory Maps

Conventional methods used to prepare landslide inventory maps can be broadly classified into: (i) geomorphological field mapping and (ii) visual interpretation of stereoscopic aerial photographs, as described below.

6.3.1.1 Geomorphological Field Mapping

A basic method to detect landslides in space or to prepare landslide inventories is geomorphological mapping in the field. Geomorphological mapping requires expert knowledge and experience of landslides and the study area which are subjective in nature. Therefore, the results can vary drastically depending on the specialists who prepared the map, the knowledge on the study area (Guzzetti et al. 2000; Ardizzone et al. 2002). Similarly, recognition of landslide types also affect the results. For example, small-scale landslides such as debris flow, slides, and rock fall can be easily identified in the field, but large-scale landslides in which the aerial extent of slide is beyond the limit of human eye. Namely it makes difficult for mapping in the field, therefore, geomorphological mapping is not suitable for the large-scale landslide inventory mapping, but it could be very useful in later stages such as verification and addition of typical field attributes.

6.3.1.2 Visual Interpretation of Stereoscopic Aerial Photographs

The use of aerial photography is well established in landslide research (Soeters and Van Westen 1996). Aerial photography allows one to obtain an overall view of the terrain as a 3D image. Interpretation of such images gives wide range of information on landform as the geomorphological features are visible on a larger scale than is generally possible from a ground survey. Landforms directly reflect the ongoing and past evolutionary processes related to geomorphological change. Interpretation of aerial images is primarily qualitative; however, photogrammetric methods can be used to extract quantitative information. While qualitative interpretation is common, quantitative studies are rare, probably due to limited availability of good-quality photographs, adequately fixed control points, and cost (Morgenstern and Martin 2008). However, several landslide-related quantitative photogrammetric studies have been described (Maria et al. 2004; Liu and Wang 2008; Smith et al. 2009). Similarly, when using aerial photographs, accuracy of an inventory depends also on the type, quality, and characteristics of the stereoscopes used to complete the inventory (Guzzetti et al. 2012), and hence, care should be taken in selecting the stereoscope.

Regarding the large-scale landslide inventory mapping, interpretation of aerial photographs is most suitable to use because they are useful to detect and identify

the surface expression of present and past movements of slope material. Therefore, mapping large-scale landslides and identifying landslide-susceptible slopes from stereoscopic interpretation of aerial photographs is faster, and sometimes more effective, than field survey. On the other hand, large-scale landslides are not so frequent like other landslides, and hence, old stereoscopic images can also be used for the mapping purpose. However, adequate experience in the complex techniques of geomorphologic interpretation is required in order to produce good results.

6.3.2 *New Methods for Preparing Landslide Inventory Maps*

The major limitation associated with the conventional methods is subjectivity, lack in coverage, hard and expensive in terms of time and money. Therefore, new methods have been developed to overcome these limitations. In new methods, earth observation data are increasingly used for the landslide mapping with automatic methods as well as visual interpretation of high resolution data for obtaining quicker results over large area.

6.3.2.1 Visual Interpretation

The newer methods also include the visual interpretation and analysis approach for example (i) surface morphology, chiefly exploiting very high resolution digital elevation models (DEMs), (ii) interpretation and analysis of satellite images, (iii) optical image, (iv) multispectral image, and (v) SAR data and so on. Visual interpretation approach still has the limitation of the subjectivity, but higher resolution and accuracy in data helps to produce more reliable and accurate landslide inventory comparing substituting the conventional aerial photograph imagery interpretation. Detail review about the visual interpretation using very high resolution satellite imageries can be found in van Westen et al. (2008).

6.3.2.2 Automatic or Semi-automatic Delineation of Landslide

Automatic or semi-automatic delineation of landslide is an intriguing task. Therefore, few attempts for the automatic or semi-automatic recognition of landslide are found in literatures. McKean and Roering (2003) were probably the first to attempt the automatic extraction of landslide features from a very high resolution, 1 m × 1 m LiDAR DEM. After that, various other researchers worked in the filed using automatic delineation methods; for examples such as Tarantino et al. (2004), Sato et al. (2007) Booth et al. (2009), Martha et al. (2010), Mondini et al. (2011). Automatic or semi-automatic delineation is a quick mapping approach but has various limitations which will be resolved with the advancement of algorithm. The basis of any automatic or semi-automatic delineation is comprehensive

characterization of landslides using combination of spectral, shape, and contextual information and putting them into one algorithm. A few literatures regarding the automatic delineation of large-scale landslide are available, but in case of Nepal, it is difficult to get that accurate data.

6.3.3 *Others*

Historic data such as newspaper articles, eyewitness records, road construction office reports, city archives, old photographs, and many more sources can be utilized for landslide mapping. In many cases, spatial and temporal information regarding landslide occurrence can be found which are exceptionally useful for understanding the magnitude-frequency characteristics of mass movements (Tarantino et al. 2004; Sato et al. 2007; Booth et al. 2009; Martha et al. 2010; Mondini et al. 2011). Some examples of landslide inventories based on historic data can be found in, for example, such as Calcaterra et al. (2008), Carrara et al. (2003). In case of Nepal, this method can be very useful to prepare landslide inventory database.

6.4 Use of GIS in Landslide Analysis

Geographic Information System (GIS) is one of computer system for understanding the earth surface based on the information of location. The word geographic meaning that location of the data is known or can be calculated in terms of geographic coordinates. The word information meaning that data in the GIS are used to obtain some useful knowledge in the form of colored maps, images, and tables. The word system meaning GIS is made up of linked to various components of different functions. The ultimate purpose of GIS is to provide support for making decisions based on data analysis. According to Carrara et al. (1999), the earliest GIS tools were created at about early 1970s, but the method achieved great popularity only in the mid-1980s. During the past 40 years, awareness of geographical data processing has become widespread across all nations, and across almost all disciplines that deal with or rely on geographically referenced data.

Advances in Geographical Information System (GIS) technology have led to the growing application in many areas of the earth sciences such as geological and geotechnical hazards and many others. Geological hazards represent one of the most complicated phenomena and involve so many different disciplines from mineralogy, structural geology, tectonics, geophysics, geochemistry, environmental sciences, etc. In case of landslides also, the occurrence of landslide is caused by the complex interaction between various factors. For the representation of landslide only, a combination of points (symbols), lines (to show escarpments, traces of debris low path, etc.), and polygons (to represent landslide crown areas, landslide

deposits, debris fans, etc.) is necessary. With analog techniques, expressing all these information in the same map was a very difficult task. It was difficult to portray landslides of a different type or age in a single map, maintaining the cartographic representation clear. For example, Cardinali et al. (1990) prepared, in a landslide inventory map of New Mexico, USA, four sheets showing deep-seated landslides, shallow landslides, rock falls and topples, and he displayed also the escarpment and scarps especially for small landslide. Similarly, update of landslide inventory was also another difficult job because one change will add loads of work as they have to repeat each and every work. For example, to update the map of sites historically affected by landslides and floods in Italy, first published by Guzzetti et al. (1996), Reichenbach et al. (1998) published a second edition of the map. The availability of geographical information system (GIS) technology solved several problems related to the production, update, and visualization of landslide maps (Guzzetti et al. 2012). A GIS provides the freedom to separate the landslide information in multiple layers, maintaining the geometrical consistency between the GIS layers. GIS is also able to handle the landslide information in combination with environmental information (e.g., on morphometry, geology, land use, and land cover), which is very useful for susceptibility, hazard, and risk modeling. Recently, in a GIS environment, 3D visualization is possible which could be very useful in obtaining three-dimensional information on the location and geometry of the landslides and of the associated features. Therefore, use of GIS has made the production easy; update and visualization for landslide inventory map. They were not easy and complicated tasks in the analog age. Various GIS softwares are available such as, ArcGIS, ILWIS, and GRASS.

6.5 Landslide Inventory in Context of Nepal

The landslide inventory techniques have been improved from manual detection using simple topographical map to automatic detection using very high resolution satellite imageries. Preparation of landslide inventory in context of developing countries like Nepal is always governed by available resources. The available resources here mean the data as well as the financial resources. On the other hand, types of landslides also govern the techniques for landslide inventory preparation. For example, for small-scale landslides, field mapping or time series data can be used, but for the large-scale landslides, aerial photographs are more useful comparing to field mapping and time series data. Therefore, in context of Nepal, aerial photograph interpretation, the conventional approach, is best for the large-scale landslide inventory mapping. Hence, using the available resources in the best possible way is more important in Nepal.

Most of the landslide-related studies in Nepal use aerial photograph interpretation for all small- and large-scale landslides inventory mapping. While preparing GIS database from landslide inventory marked in the aerial photographs, visual judgment is used often to transfer the spatial location of landslides. This transfer sometimes results in error to place the exact location as marked in aerial photographs.

The major reason behind this is the difference in the scale of aerial photographs and the topographical maps. In Nepal, readily available aerial photographs are of scale 1:50,000, and topographical maps are of scale 1:25,000. Therefore, transferring the landslide from aerial photographs of scale 1:50,000 to topographical maps of scale 1:25,000 always poses risk of erroneous location. For the regional scale analysis, the erroneous location does not affect much, but for the basin-scale analysis may affect the results. Therefore, in order to make accurate landslide inventory maps, using the available resources is very necessary. In the following section, large-scale landslide inventory using interpretation of scanned-digital aerial photographs has been illustrated. Use of this approach will help to eliminate erroneous location of the landslides caused by the transfer from large-scale aerial photographs to small-scale topographical map.

6.5.1 Digital Landslide Inventory Using Epipolar Stereo Pair Operation

Epipolar stereo pair operation of ILWIS creates a stereo pair from two scanned aerial photographs with overlap. In short, first two overlapping aerial photographs (left and right) are scanned and geo-referenced with the known topographical map. Next, mark four fiducial marks in each of the photographs. Then, mark principal point (PP) of left photograph and transferred principal point in right photograph. After that, mark principal point (PP) of right photograph and transferred principal point in left photograph. In case of differences in scale between the two aerial maps, mark the position of one or two scaling points (SP) in both photographs. This will resample both photographs and rotation differences, and possible scale differences between the photographs will be removed. Now open the geo-referenced and resample aerial photographs in stereo pair-stereoscope window or anaglyph map window and mount the stereoscope or 3D glass to view the 3D image of the terrain. After this, landslides were identified and marked over the computer screen to make line map of the landslide. The landslide map will be of the same geo-reference as the topographical map, and the digital landslide inventory is prepared with any error in its spatial location. The detail description of epipolar stereo pair operation can be found in ILWIS manual.

Figure 6.6 shows a large-scale landslide inventory prepared from the conventional aerial photographs interpretation. In order to illustrate the difference between the landslides identified from the conventional aerial photographs interpretation and from the epipolar stereo pair interpretation, landslides at some location are identified using the epipolar stereo pair interpretation. Figure 6.6 also shows three examples comparing the location of landslide identified from the two different approaches. From Fig. 6.6, landslide inventory prepared from the conventional aerial photographs interpretation is slightly dislocated from its original position and in some position correctly located. Hence, what we can say that such landslide

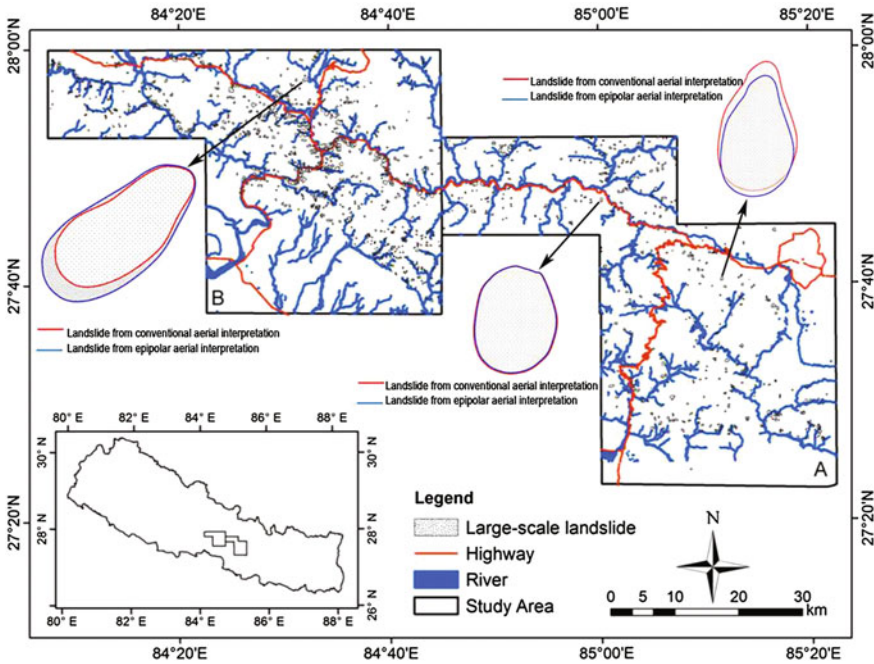


Fig. 6.6 Digital landslide inventory mapping using stereo pair operation

identified from epipolar stereo pair operation helps to eliminate the human errors created while transferring the spatial location of landslides and also helps to maintain a standard in inventory mapping. The effect of wrongly positioned landslide may have crucial role in the susceptibility and hazard mapping.

6.6 Conclusions

A comprehensive landslide inventory is a prerequisite for any landslide susceptibility and hazard assessment. Any error in landslide inventory will ultimately affect the reliability of landslide susceptibility and hazard assessment. However, lack of standard techniques to prepare landslide inventory always affects the consistency in the quality of landslide inventory. A simple review regarding the different techniques in landslide inventory preparation has been presented which enables us that aerial photograph interpretation is the most suitable method for large-scale landslide inventory mapping in Nepal. With the advancement in the remote sensing and satellite data, landslide inventory has been improved a lot, but in case of Nepal, availability of such digital data is not easy, although it is the best important situation for GIS landslide studies. Therefore, in this study, we tried to illustrate how simple modification in the general method can result in accurate data acquisition.

On screen digitization of landslide using epipolar stereo pair operation to identify large-scale landslides has been illustrated which helps to eliminate the error in spatial location of landslides. Even though the error cannot be eliminated from this approach, accurate location should be identified for the standardization of landslide inventory mapping.

References

- Agliardina F, Crosta G, Zanchi A (2001) Structural constraints on deep-seated slope deformation kinematics. *Eng Geol* 59(1–2):83–102
- Amatya KM, Jnawali BM (1994) Geological map of Nepal. Scale: 1:1,000,000. Department of Mines and Geology, Kathmandu, Nepal
- Arduzzone F, Cardinali M, Carrara A et al (2002) Impact of mapping errors on the reliability of landslide hazard maps. *Nat Hazards Earth Syst Sci* 2:3–14
- Aucelli PPC, Casciello E, Cesarano M et al (2012) A deep, stratigraphically and structurally controlled landslide: the case of Mount La Civita (Molise, Italy). *Landslides*. doi:[10.1007/s10346-012-0351-7](https://doi.org/10.1007/s10346-012-0351-7)
- Bilham RK, Larson JF, Project Idylhim Members (1997) GPS measurements of present-day convergence across the Nepal Himalaya. *Nature* 386:61–64
- Booth AM, Roering JJ, Perron JT (2009) Automated landslide mapping using spectral analysis and high-resolution topographic data: Puget Sound lowlands, Washington, and Portland Hills, Oregon. *Geomorphology* 109(3–4):132–147
- Calcaterra D, Ramondini M, Calò F, Longobardi V, Parise M, Galzerano CM (2008) DInSAR techniques for monitoring slow moving-landslides. In: Chen Z, Zhang J-M, Ho K, Wu F-Q, Li Z-K (eds) *Landslides and engineered slopes. From the past to the future proceedings of the tenth international symposium on landslides and engineered slopes*
- Cardinali M, Guzzetti F, Brabb EE (1990) Preliminary map showing landslide deposits and related features in New Mexico. U.S. Geological Survey Open File Report 90/293, 4 sheets, scale 1:500,000
- Carrara A, Guzzetti F, Cardinali M, Reichenbach P (1999) Use of GIS technology in the prediction and monitoring of landslide hazard. *Nat Hazards* 20(2):117–135
- Carrara A, Crosta G, Frattini P (2003) Geomorphological and historical data in assessing landslide hazard. *Earth Surf Proc Land* 28(10):1125–1142
- Cruden DM, Varnes DJ (1996) *Landslides Types and Processes*. In: Turner AK, Schuster RL (eds) *Landslides: investigation and mitigation*. Transportation research board special report 247. National Academy Press, WA
- Dahal RK (2006) *Geology for technical students*. Bhrikuti Academic Publication, Kathmandu
- Dikau R, Brunsden D, Schrott L et al (1996) *Landslide recognition. Identification, movement and causes*. Wiley & Sons, Chichester, Chichester
- Dortch JM, Owen LA, Haneberg WC et al (2009) Nature and timing of large landslides in the Himalaya and Transhimalaya of northern India. *Quatern Sci Rev* 28:1037–1054
- Dramis F, Sorriso-Valvo M (1994) Deep-seated gravitational slope deformations, related landslides and tectonics. *Eng Geol* 38(3–4):231–243
- EPOCH (1993) *The temporal occurrence and forecasting of landslides in the European community* (Ed: Flageollet, J. C.). Contract No. 90 0025, 3 Volumes
- Ganser A (1964) *Geology of the Himalaya*. Inter Science John Wiley, London
- Gerrard AJ, Gardner RAM (2000) The role of landsliding in shaping the landscape of the middle hills, Nepal. *Geomorphol Suppl Bd* 122:47–62
- Guzzetti F, Cardinali M, Reichenbach P (1996) Map of sites historically affected by landslides and floods in Italy. Publication CNR GNDCI n. 1356, Scale 1:1,200,000

- Guzzetti F, Cardinali M, Reichenbach P et al (2000) Comparing landslide maps: a case study in the upper Tiber River Basin, Central Italy. *Environ Manag* 25(3):247–363
- Guzzetti F, Reichenbach P, Ardizzone F, Cardinali M, Galli M (2006) Estimating the quality of landslide susceptibility models. *Geomorphology* 81(1–2):166–184
- Guzzetti F, Mondini AC, Cardinali M (2012) Landslide inventory maps: new tools for an old problem. *Earth Sci Rev* 112:42–66
- Hasegawa S, Dahal RK, Yamanaka M et al (2009) Causes of large-scale landslides in the Lesser Himalaya of central Nepal. *Environ Geol* 57:1423–1434
- Heuberger H, Masch L, Preuss E (1984) Quaternary landslides and rock fusion in Central Nepal and in the Tyrolean Alps. *Mt Res Dev* 4(4):345–362
- Hradecky J, Pa'nek T (2008) Deep-seated gravitational slope deformations and their influence on consequent mass movements (case studies from the highest part of the Czech Carpathians). *Nat Hazards* 45:235–253
- Hungr O, Evans SG, Bovis M (2001) Review of the classification of landslides of the flow type. *Environ Eng Geosci* VII:221–238
- Hutchinson JN (1988) General report: morphological and geotechnical parameters of landslides in relation to geology and hydrogeology. In: *Proceedings of fifth international symposium in landslides* Rotterdam, Balkema
- Japan International Cooperation Agency (JICA), Department of Water Induced Disaster Prevention, Department of Road, Government of Nepal (2007) Progress report on the study on disaster risk management for Narayanghat-Mugling highway. Nippon Koei Co., Ltd
- Korup O, Strom AL, Weidinger JT (2006) Fluvial response to large-scale rock-slope failures—examples from the Himalayas, Tien Shan, and the Southern Alps in New Zealand. *Geomorphology* 78:3–21
- Korup O, Clague JJ, Hermanns RL et al (2007) Giant landslides, topography, and erosion. *Earth Planet Sci Lett* 261:578–589
- Liu S, Wang Z (2008) Choice of surveying methods for landslides monitoring. In: Chen Z, Zhang J-M, Ho K, Wu F-Q, Li Z-K (eds) *Landslides and engineered slopes: from the past to the future*. In: *Proceedings of the tenth international symposium on landslides and engineered slopes*. Taylor & Francis, Xi'an
- Malamud BD, Turcotte DL, Guzzetti F et al (2004) Landslide inventories and their statistical properties. *Earth Surf Proc Land* 29(6):687–711
- Maria FA, Gianfranco F, Hélène VI (2004) Rock slope stability analysis based on photogrammetric surveys. In: Lacerda W, Ehrlich M, Fontoura SAB, et al (eds) *Landslides: evaluation and stabilization*. Ninth international symposium on landslides. A.A. Balkema Publishers, Leiden, pp 789–794
- Martha TR, Kerle N, Jetten V et al (2010) Characterising spectral, spatial and morphometric properties of landslides for semi-automatic detection using object-oriented methods. *Geomorphology* 116:24–36
- McKean J, Roering J (2003) Objective landslide detection and surface morphology mapping using high-resolution airborne laser altimetry. *Geomorphology* 57(3–4):331–351
- Meigs AJ, Burbank DW, Beck RA (1995) Middle-Late Miocene (>10 Ma) formation of the main boundary thrust in the western Himalaya. *Geology* 23(5):423–426
- Mondini AC, Guzzetti F, Reichenbach P et al (2011) Semi-automatic recognition and mapping of rainfall induced shallow landslides using satellite optical images. *Remote Sens Environ* 115:1743–1757
- Morgenstern NR, Martin CD (2008) Landslides: seeing the ground. In: Chen Z, Zhang J-M, Ho K, Wu F-Q, Li Z-K (eds) *Landslides and engineered slopes: from the past to the future*. *Proceedings of the tenth international symposium on landslides and engineered slopes*. Taylor & Francis, Xi'an
- Pande A, Joshi RC, Jalal DS (2002) Selected landslide types in the Central Himalaya: their relation to geological structure and anthropogenic activities. *Environmentalist* 22:269–287
- Pandey MR, Tandukar RP, Avouac JP et al (1995) Inter-seismic strain accumulation on the Himalayan crustal ramp (Nepal). *Geophys Res Lett* 22:751–754

- Petley DN, Owen K, Mitchell W et al (2006) The role of global and regional precipitation pattern in landslide generation. In: Ashaari M (ed) Proceedings of the international conference on slopes Malaysia 2006. Public Works Department, Kualalumpur
- Purtscheller F, Pirchl T, Sieder G (1995) Radon emanation from giant landslides of Koefels (Tyrol, Austria) and Lang Tang Himal (Nepal). *Environ Geol* 26:32–38
- Reichenbach P, Guzzetti F, Cardinali M (1998) Map of sites historically affected by landslides and floods in Italy, 2nd ed. CNR, Gruppo Nazionale per la Difesa dalle Catastrofi Idrogeologiche, Publication n. 1786, scale 1:1,200,000
- Sato HP, Yagi H, Moarai M et al (2007) Airborne lidar data measurement and landform classification mapping in Tomari-no-tai landslide area, Shirakami Mountains, Japan. In: Sassa K, Fukuoka H, Wang F, Wang G (eds) Progress in landslide science. Springer, Berlin
- Shang Y, Yang Z, Li L et al (2003) A super large landslide in Tibet in 2000: background, occurrence, disaster, and origin. *Eng Geol* 54:225–243
- Shroder JF, Bishop MP (1998) Mass movement in the Himalaya: new insights and research directions. *Geomorphology* 26:13–35
- Smith MJ, Chandler J, Rose J (2009) High spatial resolution data acquisition for the geosciences: kite aerial photography. *Earth Surf Proc Land* 34(1):155–161
- Soeters R, Van Westen CJ (1996) Slope instability recognition, analysis, and zonation. In: Turner AK, Schuster RL (eds) Landslides: investigation and mitigation (special report). National Research Council, Transportation and Research Board Special Report 247, Washington, DC, USA
- Stöcklin J (1980) Geology of Nepal and its regional frame. *J Geol Soc Lond* 137:1–34
- Tarantino C, Blonda P, Pasquariello G (2004) Application of change detection techniques for monitoring man-induced landslide causal factors. In: Geoscience and remote sensing. Proceedings of the IGARSS symposium
- Timilsina M, Bhandary NP, Dahal RK, Yatabe R (2013) Distribution probability of large-scale landslides in central Nepal. *Geomorphology* 226:236–248
- Upreti BN, Yoshida M (2005) Guidebook for Himalayan trekkers, series no. 1, geology and natural hazards along the Kaligandai Valley, Nepal. Department of Geology, Tri-Chandra Campus, Tribhuvan University, Kathmandu, Nepal
- Van Den Eeckhaut M, Poesen J, Govers G et al (2007) Characteristics of the size distribution of recent and historical landslides in a populated hilly region. *Earth Planet Sci Lett* 256:588–603
- Van Den Eeckhaut M, Moeyersons J, Nyssen J et al (2009) Spatial patterns of old, deep-seated landslides: a case-study in the northern Ethiopian Highlands. *Geomorphology* 105:239–252
- Van Westen CJ (2007) Mapping landslides: recent developments in the use of digital information. In: Turner A, Schuster RL (eds) Landslides and society? Proceedings of the first North American conference on landslides, Vail, Colorado, USA, June 3–8, 2007. Association of Environmental and Engineering Geologists, Vail Colorado
- van Westen CJ, Castellanos Abella EA, Sekhar LK (2008) Spatial data for landslide susceptibility, hazards and vulnerability assessment: an overview. *Eng Geol* 102:112–131
- Varnes DJ (1978) Slope movement types and processes. In: Schuster RL, Krizek RJ (eds) Special report 176: landslides: analysis and control. Transportation and Road Research Board, National Academy of Science, Washington D.C.
- Waltham T (1996) Very large landslides in the Himalayas. *Geol Today* (Sept–Oct), pp 181–185
- Wieczorek GF (1984) Preparing a detailed landslide-inventory map for hazard evaluation and reduction. *Bull Assoc Eng Geol* 21(3):337–342
- Yagi H (2001) Landslide study using aerial photographs. In: Tianchi L, Chalise SR, Upreti BN (eds) Landslide hazard mitigation in the Hindu Kush-Himalayas. ICIMOD, Nepal
- Yagi H, Nakamura S (1995) Hazard mapping on large scale landslides in the lower Nepal Himalayas. Proceedings of International Seminar on Water Induced Disasters. DPTC-JICA, Kathmandu
- Yatabe R, Bhandary NP, Bhattarai D (2005) Landslide hazard mapping along major highways of Nepal. Ehime University and Nepal Engineering College

Chapter 7

A Joint Regional Slope Mass Movement Susceptibility Map

Marko Komac

Abstract The paper introduces an approach to create a jointed slope mass movement susceptibility map at a regional scale using a combination of three different susceptibility maps. For this purpose, two approaches were chosen, maximum value and unique value. Slightly different approaches were used to produce the three models that represent landslide, debris-flows, and rockfall susceptibility maps of Slovenia at scale 1:250,000. Nevertheless, the joint susceptibility indicates that 32.5% of Slovenian territory is highly susceptible to slope mass movements, while in the same area approximately 23% of population lives.

Keywords Landslides · Debris-flows · Rockfalls · Susceptibility map · Slovenia

7.1 Introduction

Slovenia is a small Central European country. It is located between the Alps and the Mediterranean Sea, positioned on the complex Adria–Dinaridic–Pannonian structural junction. Slovene territory is very heterogeneous from the geological setting perspective, its geomorphologic terrain specifics are diverse—elevation ranges from the sea level to 2864 m a.s.l., while terrain ranges from flat to near vertical cliffs, and its precipitation conditions vary significantly—maximum 48 h rainfall intensity with a 50 year return period ranges from 120 in the eastern parts to 570 mm in the western parts. Consequently, Slovenia is severely affected by different slope mass movements—landslides, rockfalls, and debris-flows. Almost one-quarter of Slovenian territory is subjected to processes of slope mass movements, and based on rough estimations, around 19% of population is subjected to potential landslides (Jemec and Komac 2012). Depending on yearly weather conditions, from several tens to several hundreds, new instability phenomena occur every year. The consequences of

M. Komac (✉)

Faculty of Civil and Geodetic Engineering, University of Ljubljana,
Jamova c. 2, p.p. 3422, SI- Ljubljana, Slovenia
e-mail: mkomac@fgg.uni-lj.si; m.komac@telemach.net

different slope mass movements in the period from 1994 to 2008 can be documented with the total direct damage value of nearly 100 million euros (SORS 2012). Areas, potentially affected by landslides, spread from agricultural areas (30% of all farmland), built environment (25% of residential buildings) to forests (21% of forests) (Jemec and Komac 2012). In addition, landslides potentially endanger 10% of railway network (Jemec and Komac 2012) and 30% of all roads in Slovenia.

Despite its tininess, geologically speaking Slovenian territory is due to the above-mentioned structural junction highly diverse and complex (Komac 2005). According to Komac (2005), almost half of Slovenia is constituted of clastic rocks, almost 40% of carbonate rocks, 4.5% of the combination of the two, 4% of metamorphic, 1.8% of pyroclastic, and 1.5% of igneous rocks (Fig. 7.1). The north-western part belongs to carbonate Alps, while majority of south-western part belongs to carbonate karstic areas with some parts of clastic rocks. The central Slovenia is mainly constituted of mixed sediments—clastic rocks with occasional carbonates. In south- and north-eastern parts of Slovenia, young sediments prevail, among them also some with very poor litification.

Considering the general occurrence of slope mass movements (Fig. 7.2), landslides mainly occur in the lower mountainous areas with altitudes up to 1500 m.a.s.l. and slopes up to 30°, in the Alpine foothills and hilly central part of Slovenia with very complex lithological structure, in the flysch areas in western Slovenia, and in the low hills, primarily build up of soft, low lithified rocks of eastern and north-eastern Slovenia. Rockfalls and rock slides are most common in the northern

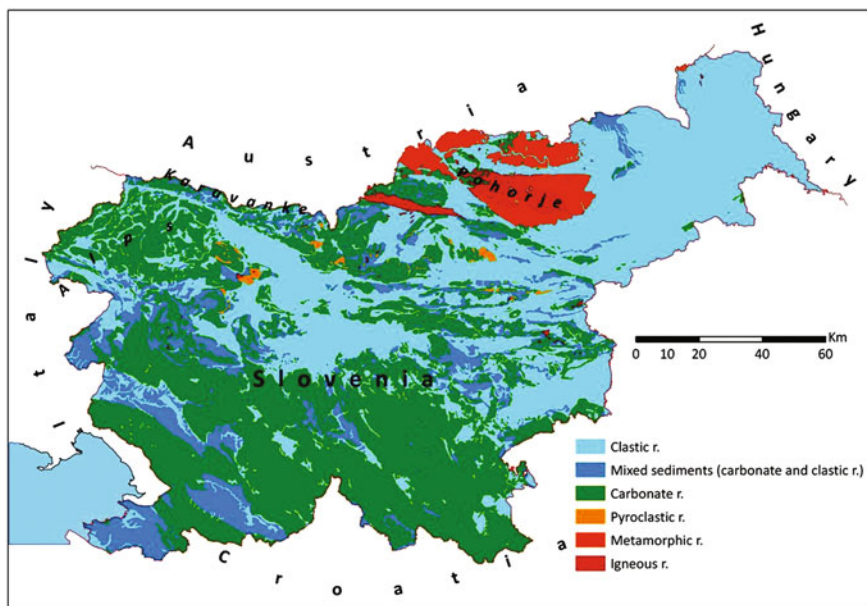


Fig. 7.1 Simplified lithological map of Slovenia (Komac 2005)

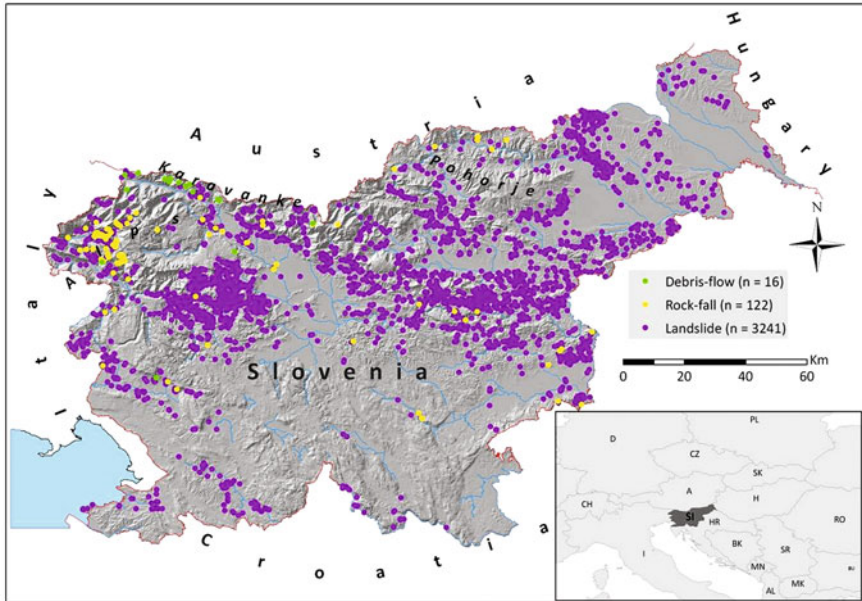


Fig. 7.2 A known/detected slope mass movements in Slovenia. Locations of known landslides (3241 events represented with 3241 cells) are marked with purple, rockfalls (122 events represented with 122 cells) with yellow, and debris-flows (16 events represented with 6385 cells) with green dots

and north-western Slovenia, in steep gorges or canyons, where carbonate rocks of different ages prevail, and also on thrusts areas where carbonate rocks overthrust the softer rocks. Debris-flows are rare events and (could) occur in the Alps, in Karavanke Mountain chain, and on Pohorje and the Alpine foothills.

7.2 Methodology

Slope mass movements in Slovenia can generally be grouped into three main processes—landslides, rockfalls, and debris-flows. Susceptibility maps for all three types of slope mass movements were developed with slightly different approaches. While the landslide susceptibility map was derived using *chi-square* analyses of the phenomena occurrence in relation to relevant spatio-temporal factors, the rockfall and debris-flow susceptibility maps were calculated based on the expert decision approach. Usage of spatio-temporal factors varied depending upon the slope mass movement type (Table 7.1). All models were calculated at scale 1:250,000 and by using a linear weighted sum model approach where input values (representing ranked classes of relevant spatio-temporal factors) at each cell were weighted according to the presumed relevance of each spatio-temporal factor and summed to

Table 7.1 Overview of the spatio-temporal factors used for the calculation of the three slope mass movement-type susceptibility models for the area of Slovenia at scale 1:250,000

Spatio-temporal factors (minimum weight–maximum weight)	Landslide susceptibility ($W_{\text{Min}} - W_{\text{Max}}$)	Debris-flow susceptibility ($W_{\text{Min}} - W_{\text{Max}}$)	Rockfall susceptibility ($W_{\text{Min}} - W_{\text{Max}}$)
Weight step	0.02	0.03	0.02
Lithology (engineering geology classification) (original data in scale 1:250,000)	X(0.2 – 0.6)	X(0.14 – 0.23)	X(0.3 – 0.7)
Slope inclination (original data DEM pixel size 25 × 25 m)	X(0.2 – 0.6)	X(0.14 – 0.23)	X(0.3 – 0.7)
Slope curvature (original data DEM pixel size 25 × 25 m)	X(0 – 0.3)	X(0.09 – 0.18)	
Slope aspect (original data DEM pixel size 25 × 25 m)	X(0 – 0.2)	–	
Distance to structural elements (original data in scale 1:100,000)	X(0 – 0.2)	–	X(0 – 0.3)
Land-cover type (Corine nomenclature) (original data in scale 1:100,000)	X(0 – 0.4)	–	–
Distance to surface waters (original data in scale 1:50,000)	–	X(0.10 – 0.19)	–
Energy potential related to elevation (original data DEM pixel size 25 × 25 m)	–	X(0.06 – 0.15)	–
48 h rainfall intensity (original data pixel size 1000 × 1000 m)	–	X(0.14 – 0.23)	–
Stream energy potential (original data in scale 1:50,000 and DEM pixel size 25 × 25 m)	–	X(0.14 – 0.23)	–

W_{Min} represents the minimum weight value, and W_{Max} represents the maximum weight value

give the final score of susceptibility. For all three susceptibility maps, several models, where factors were assigned with different weights (sum of weights was always 1), were calculated to find the best possible (yet not over trained) weight combination. The calculations were performed using pseudo-random approach as the range [minimum weight (W_{min}) and maximum weight (W_{Max})] of factors' weight values, and the steps were defined. Conceptual model of the algorithm of is presented in Fig. 7.3. The approach as described was chosen to simplify the procedure, to make it economically appealing, and to make it transferable to other regions. A nonparametric univariate statistical analyses (*chi-square*; X^2) were conducted using ESRI GIS platform (ArcMap© and ArcView©) in raster format with the 25 × 25 m pixel size. The success rate for each of the calculated susceptibility models was calculated using the test subset (landslides) or the whole set (debris-flows and rockfalls), where the occurrence of events within the half of the analyses area with the highest susceptibility values was assessed. Logically, models

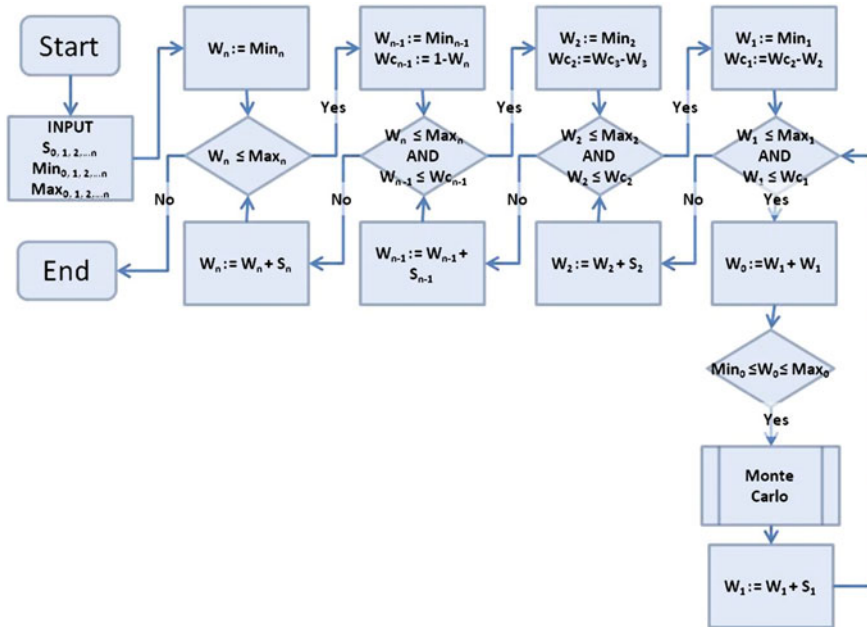


Fig. 7.3 Conceptual model of algorithm for the susceptibility model calculation. S represents step, Min represents minimum weight value, Max represents maximum weight value, W represents current weight value, and W_c represents the difference between 1 and sum of weights

where more test events occur in the classes with highest susceptibility values were ranked among best. Overtraining (also overfitting) of the selected final models was avoided by averaging the factor weight values of the best models.

The methodology presented includes spatial modelling of initial (also triggering) areas, while accumulation areas of debris-flows and rock falls were not included. The latter remains the challenge for future susceptibility modelling on regional scale. Values of the selected final susceptibility models were classified into six descriptive classes of susceptibility with a purpose to be more understandable to non-professionals—negligible, insignificant, low, moderate, high, and very high. The chi-square test was also used to assess the correctness of the descriptive susceptibility classification for all final susceptibility models. In addition, the relation between the observed (O) and the expected (E) event occurrences within the descriptive susceptibility classes was analysed to assess the type of the occurrence—whether a positive or a negative ($O - E$), where the first represented proneness to events and later represented the opposite. The combination of X^2 and $O - E$ indexes for each class is presented in the last row of Tables 7.3, 7.4, and 7.5 as $(\mp)X^2$.

For the purpose of deriving the joint slope mass movement susceptibility map, two approaches were chosen: (i) a maximum susceptibility value approach and (ii) a unique value approach. With the first approach, the maximum susceptibility value

Table 7.2 Susceptibility values of the three models that were used for the derivation of the joint susceptibility map using the unique value approach

Susceptibility model	Negligible	Insignificant	Low	Moderate	High	Very high
Landslides	0	1	2	3	4	5
Debris-flows	0	6	12	18	24	30
Rockfalls	0	36	72	108	144	180

from all three susceptibility maps at each cell is assigned to the output map that has only six classes of susceptibility. With the second approach, for each combination of the three input susceptibility maps, a unique value was assigned to the cell enabling that the multilevel susceptibility information was preserved in the output. To achieve this, the three susceptibility models were added (summed) together based on the principle of the binary card game using models' values that are presented in Table 7.2. For example, the value 55, a unique combination—sum—of values 36, 18, and 1, would mean that at that specific location the susceptibility levels would be: 36—insignificant for rockfalls, 18—low for debris-flows, and 1—insignificant for landslides).

7.3 Results and Discussion

7.3.1 *Landslide Susceptibility Map*

An extensive national landslide database was produced in the early 2000s (Jemec and Komac 2012). Based on it, the landslide susceptibility map of Slovenia at scale 1:250,000 was first completed in 2008 (Komac and Ribičič 2008) and latter upgraded in 2012 using Monte Carlo approach (Komac 2012) (Fig. 7.4). At the first step, univariate statistical analyses (X^2 —*chi-square*) of landslide spatial occurrence in relation to preparatory factors were performed on 65% of the landslide population (2165 landslides) in GIS with the pixel size 25×25 m using the following spatio-temporal factors: lithology (grouped into 29 engineering geological units), slope inclination, slope curvature, slope aspect, distance to structural elements, Corine land-cover type, distance to geological boundaries, distance to surface waters, elevation, and flowlength. The list of the relevant spatio-temporal factors was compiled based on previous research results (Carrara 1983; Carrara et al. 1991; Kojima et al. 2000; Fabbri et al. 2003; Crozier and Glade 2005; Dahal et al. 2008; Van den Eeckhaut et al. 2009). The analyses results showed that only the first six factors were statistically significant and were latter included in the susceptibility model development using weighted linear sum modelling (Fig. 7.5) where 156 and 169 models with various factor weight variations were developed and their success tested on the remaining 35% of the landslide population (1076 landslides) and on representative areas with no landslides (729 locations represented with cells) (Komac 2012). For the test method, the Cohen kappa (κ) index was used.

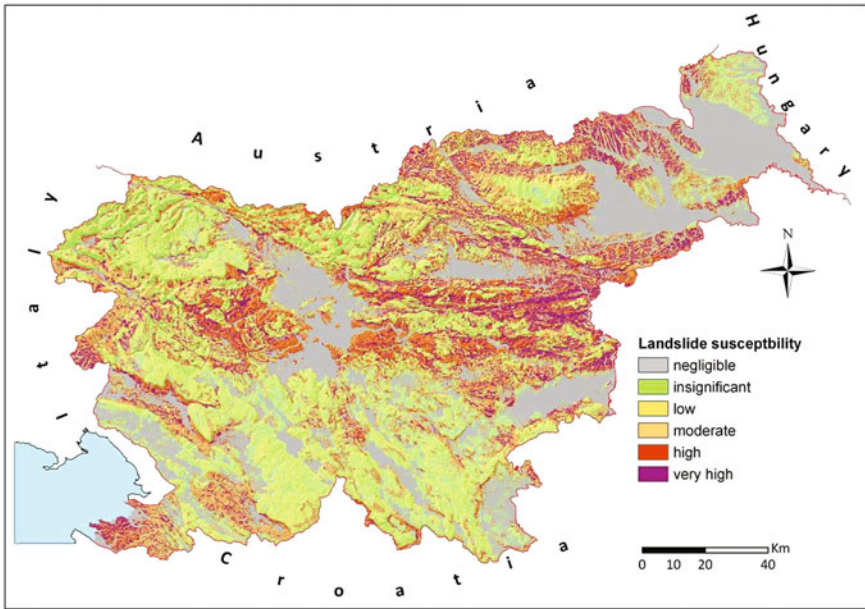


Fig. 7.4 A landslide susceptibility map of Slovenia (Komac 2012)

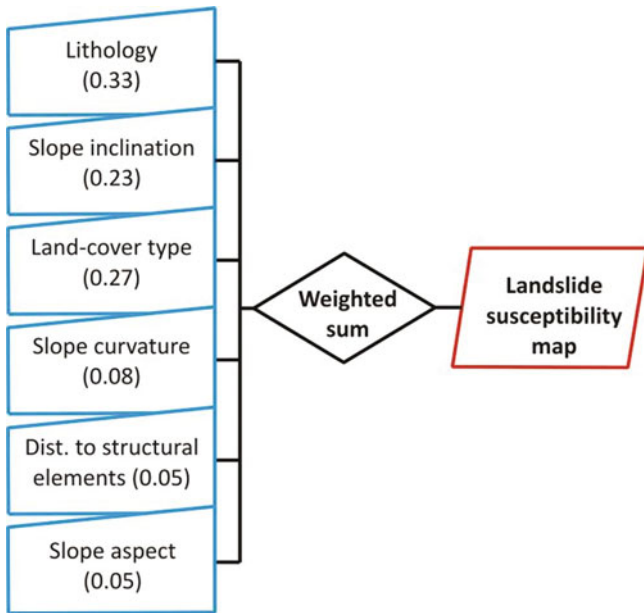


Fig. 7.5 Conceptual landslide susceptibility model with spatio-temporal factors' weight values

Table 7.3 Landslide susceptibility model classification and distribution of landslides according to susceptibility classes

A (%)	Model values	Landslide susceptibility	Landslide proportion (%)	LP to A ratio	(\mp) X^2
27.88	0–0.97	Negligible	4.46	0.16	(–)211.9
18.45	0.97–2.67	Insignificant	6.78	0.37	(–)79.4
19.82	2.67–4.15	Low	8.45	0.43	(–)70.2
10.43	4.15–5.50	Moderate	11.61	1.11	1.4
15.58	5.50–7.09	High	26.18	1.68	77.6
7.84	7.09–9.88	Very high	42.53	5.43	1651.6

“A (%)” represents the proportion of the area the class covers, “LP to A” represents the ratio between the landslide proportion within a given susceptibility class and the area this susceptibility class covers, and “(\mp) X^2 ” represents a joint chi-square and the observed-expected events difference index

Landslide learning set was selected randomly but geologically representative so all 29 engineering geological units were represented in the analyses. To avoid the risk of overtraining, the average of the upper 5% of most successful models was selected. The results indicated that the following precondition spatio-temporal factors have a significant impact on landslide occurrence (weights are represented in brackets): lithology (0.33), slope inclination (0.23), land-cover type (0.27), slope curvature (0.08), distance to structural elements (0.05), and slope aspect (0.05). The final landslide susceptibility model values were classified into six classes of susceptibility as listed in the Table 7.3. The distribution of the test landslide population was tested, and the ratio of landslide proportion versus area proportion in each class was assessed. The results presented in the last two columns in Table 7.3 show that the model and the selection of its descriptive classes give an excellent prediction of the landslide susceptibility and this is supported by the chi-square analysis ($X^2 = 2092.1$) and by the constant positive trend of the values (\mp) X^2 .

7.3.2 Debris-Flow Susceptibility Map

Similarly as calculating the landslide susceptibility model, the debris-flow susceptibility model (represented with a debris-flow susceptibility map) was derived (Fig. 7.6) (Komac et al. 2009). The difference here was that due to very limited occurrence of debris-flows an expert decision approach was selected. The expert defined upper and lower values of weights for the spatio-temporal factors that were used to calculate 672 different susceptibility models in GIS with the pixel size 25×25 m. The spatio-temporal factors used for the modelling were selected based on the results of previous research (Komac et al. 2009; Fleming et al. 1989; Rickenmann and Zimmerman 1993; Mainali and Rajaratnam 1994; Anderson 1995; Cruden and Varnes 1996; Alzate et al. 1999; Dai et al. 1999; Lin et al. 2002; Mikoš 2001; Archetti and Lamberti 2003; Delmonaco et al. 2003;

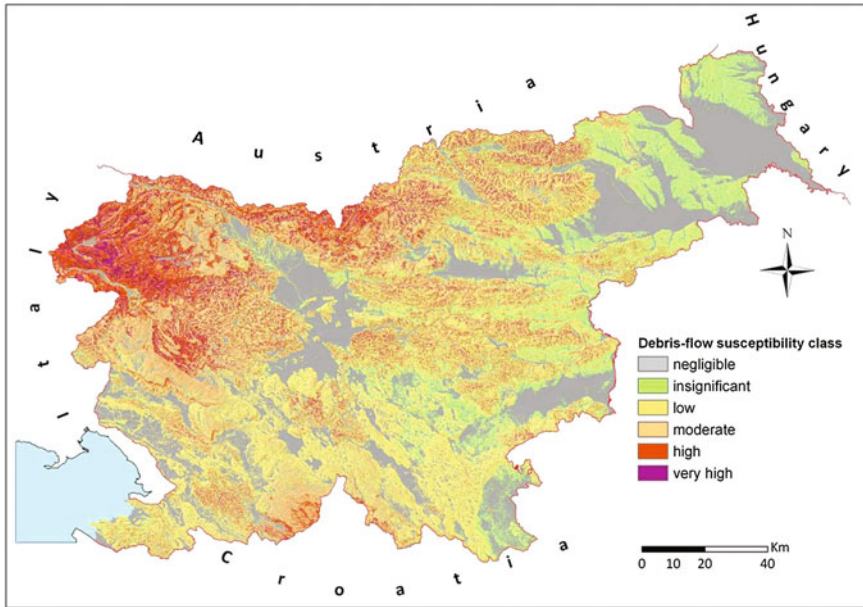


Fig. 7.6 Debris-flow susceptibility map (Komac et al. 2009)

Fiorillo and Wilson 2004; Lan et al. 2004; Melelli and Taramelli 2004; Wen and Aydin 2005; Guinau et al. 2007; Di et al. 2008; Jež et al. 2008; Mergili 2008; Toyos et al. 2008) and Slovenian own experiences. The following factors were used for the modelling of debris-flow susceptibility prediction (flowchart in Fig. 7.7): lithology, distance from the structural elements, slope inclination, energy potential related to elevation, 48 h rainfall intensity, slope curvature, stream energy potential, and distance from streams. Due to the lack of the representative sample, we have founded our susceptibility model on the expert decision approach and validated it with 16 debris-flow occurrences in Slovenia, represented with 6385 cells. Subjectivity of the approach was minimised by (1) good knowledge of the actual on-site conditions, (2) years of experiences in the field of slope mass movement research and engineering works, and (3) numerous weight combinations. Analyses and modelling were performed on a raster 25×25 m cell grid in GIS. Similarly, as for the landslide susceptibility model, a weighted linear sum modelling was used for deriving the debris-flow susceptibility models (Fig. 7.7). A logical sum was introduced to derive more susceptible areas regarding the presence of linear structures where lithological susceptibility was elevated by one level in the 50 metres zone around structural elements (faults and thrusts). Analyses of 672 susceptibility models have shown that among chosen spatio-temporal factors the most important factors for the occurrence of debris-flow are (weights in the chosen model are represented in brackets) as follows: 48 h rainfall intensity (0.2), lithology (0.19), stream energy potential (0.17), and slope inclination (0.15). Despite the fact that

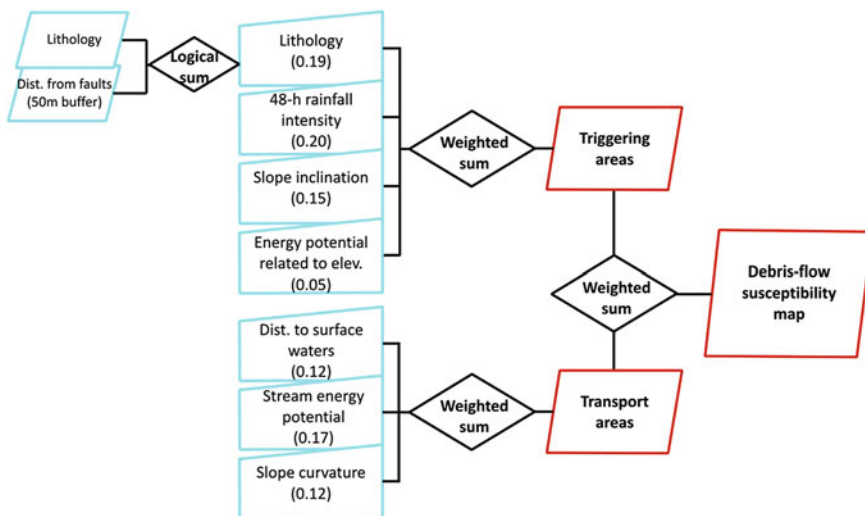


Fig. 7.7 Conceptual debris-flow susceptibility model with spatio-temporal factors’ weight values

Table 7.4 Debris-flow susceptibility model classification and distribution of debris-flow according to susceptibility classes

A (%)	Model values	Debris-flow susceptibility	Debris-flow proportion (%)	DF to A ratio	(\mp) X^2
27.88	–	Negligible	0.38	0.01	(–)270.9
10.18	0–1.34	Insignificant	0.00	0.00	(–)101.8
27.86	1.34–2.43	Low	0.96	0.03	(–)259.8
19.48	2.43–3.53	Moderate	17.92	0.92	0.1
10.66	3.53–4.94	High	43.40	4.07	100.5
3.99	4.94–10	Very high	37.35	9.36	279.2

“A (%)” represents the proportion of the area the class covers, “DF to A” represents the ratio between the debris-flow proportion within a given susceptibility class and the area this susceptibility class covers, and “(\mp) X^2 ” represents a joint chi-square and the observed-expected events difference index

other factors—distance to surface waters (0.12), slope curvature (0.12), and energy potential related to elevation (0.05)—are of lesser importance, their contribution is still essential. To avoid overfitting of the debris-flow susceptibility model, as the final result the model was selected where its weights represent the average values of weights from the first hundred models (best 15% of models). The final debris-flow susceptibility model values were classified into six classes of susceptibility as listed in Table 7.4. The distribution of the debris-flow population was tested, and the ratio of debris-flow proportion versus area proportion in each class was assessed. The results presented in the last two columns in Table 7.4 show that the model and the selection of its descriptive classes give very good prediction of the debris-flow

susceptibility and this is also supported by the chi-square analysis ($X^2 = 443.07$) and by the positive trend of the values ($\mp X^2$) that turn significantly negative once.

7.3.3 Rock Fall Susceptibility Map

A rockfall susceptibility map for the area of Slovenia in scale 1:250,000 was produced in 2011 (Čarman et al. 2011) and recalculated using wider range of weight values for this analysis (and consequentially more models), using GIS with the latest spatial data, such as the latest lithological map of Slovenia in scale 1:250,000 (Fig. 7.8). Based on the (Mazengarb 2010; Dorren and Seijmonsbergen 2003; Yawen 2011; Shirzadi et al. 2012; Antonioua and Lekkas 2010; Volkwein et al. 2011; Ruff and Rohn 2008; Guzzetti and Reichenbach 2010) expert decision for the most important factors for deriving the rockfall susceptibility map, the lithology, slope angle, and distance to structural elements were selected (flowchart in Fig. 7.9).

Unfortunately, there are not enough representative data about rockfalls in Slovenia (consistent rockfall cadastre does not exist and not many historical studies have been done so far) for the quantitative statistical analysis to be performed. That was the reason that expert estimation of important factors was used instead of chi-square analysis, with the emphasis on location rather than on time of a rockfall

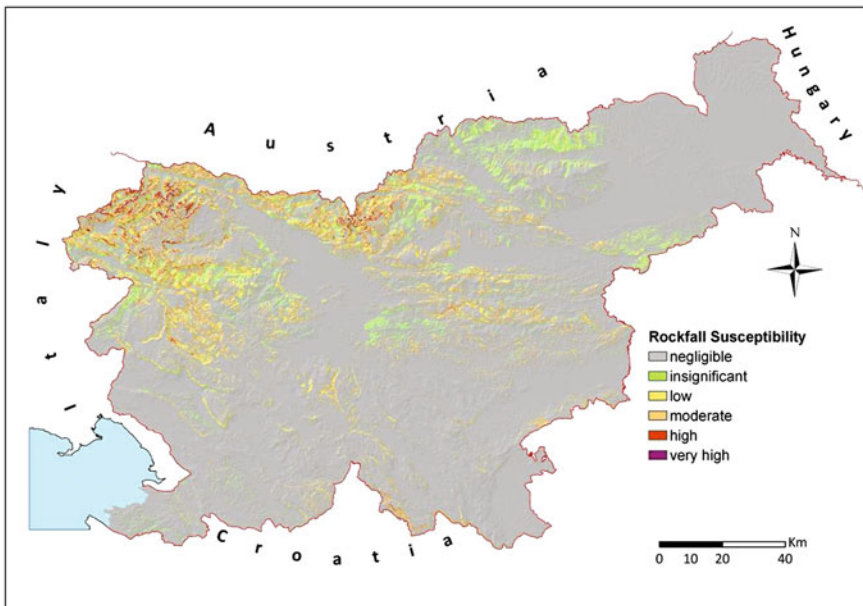


Fig. 7.8 Rockfall susceptibility map of Slovenia

Fig. 7.9 Conceptual rockfall susceptibility model with spatio-temporal factors’ weight values

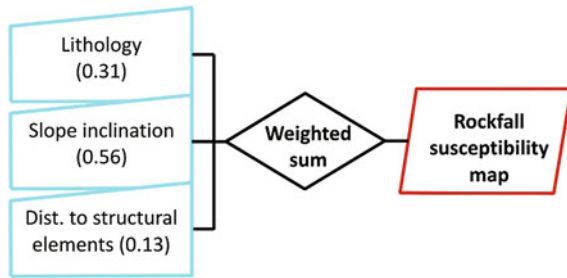


Table 7.5 Rockfall susceptibility model classification and distribution of rockfall according to susceptibility classes

A (%)	Model values	Rockfall susceptibility	Rockfall proportion (%)	RF to A ratio	(\mp) X^2
85.34	–	Negligible	20.3	0.24	(–)58.4
3.62	0–2.88	Insignificant	7.6	2.11	5.2
5.18	2.88–3.53	Low	13.6	2.62	16.0
5.07	3.53–4.64	Moderate	32.2	6.35	171.2
0.6	4.64–7.53	High	18.6	31.22	643.5
0.18	7.53–10	Very high	7.6	41.27	353.6

“A (%)” represents the proportion of the area the class covers, “RF to A” represents the ratio between the rockfall proportion within a given susceptibility class and the area this susceptibility class covers, and “(\mp) X^2 ” represents a joint chi-square and the observed-expected events difference index

occurrence—a geomorphological approach (Guzzetti and Reichenbach 2010). Expert estimation approach was based on the experience and historical events gathered from chronicles and eyewitnesses. Using the three important spatio-temporal factors selected by the expert, 216 linear rockfall susceptibility models with different weight combinations were calculated and cross-validated with 122 known historical rockfall events. This approach is limited mainly by subjectivity and has difficulties with sound argumentation, but at the given state, it was a reasonable approach to define areas with high(er) probability of rockfall occurrence. To minimise the error of the final rockfall susceptibility model, the most appropriate factors’ weight combination was selected by averaging the weights of the best eleven models (the best 5% of all models). Validations of models have shown that the chosen spatio-temporal factors for the occurrence of rockfall have the following role (weights in the chosen model are represented in brackets): slope inclination (0.56), lithology (0.31), and distance to structural elements (0.13). The final rockfall susceptibility model values were classified into six classes of susceptibility as listed in the Table 7.5. The distribution of the rockfall population was tested, and the ratio of rockfall proportion versus area proportion in each class was assessed. The results presented in the last two columns in Table 7.5 show that the model gives medium good prediction of the rockfall susceptibility. When considering all 122 rockfalls, the best model has a 62.3% success rate. The reason of bad prediction success of the

models is the fact that 22.1% of rockfalls occur in areas with less than 5° inclination, 10% of rockfalls occur in lithological units that are not susceptible to rockfalls and additional 21% in lithological units that are moderately susceptible to rockfalls, and almost 40% of rockfalls occur more than 250 metres away from the structural elements. When neglecting the 27 rockfalls that occur on terrains with low inclination slopes (angles less than 5°), the unfavourable lithology (soft rocks and soils), and large distance from structural elements exists (more than 250 m) in unfavourable for rockfall occurrence, the success is much better—just over 80%. These errors are acknowledged, and they obviously show that for a quality rockfall susceptibility model better digital elevation model (higher resolution) is needed and strata direction and dipping angle information should also be included in the calculations. Nevertheless, the results presented in the last two columns in Table 7.5 show that the model and the selection of its descriptive classes give good prediction (with a reservation related to the 27 rockfalls) of the rockfall susceptibility and this is also supported by the chi-square analysis ($X^2 = 1248$) and by the positive trend of the values (\mp) X^2 that turn significantly negative once, at the last susceptibility class.

7.4 A Joint Slope Mass Movement Susceptibility Model

From the input susceptibility models from all three types of slope mass movements, a joint susceptibility map was derived using the two approaches described in the chapter Methods. The maximum value approach resulted in a new maximum slope mass movement susceptibility map (Fig. 7.10), again with six classes of susceptibility. This approach is highly transparent, simple to present, easily understandable and is hence useful for non-experts. Its drawback is that it lacks the basic information of the type of slope mass movement that the specific location is exposed to. In Table 7.6, the distribution of susceptibility classes of maximum slope mass movement susceptibility map is presented with the overview of basic statistics related to geomorphology, land use, and population distribution for each class. According to the maximum slope mass movement susceptibility map, almost one-third (32.6%) of Slovenia could be highly subjected to at least one type of slope mass movements. When considering the population distribution, 22.8% (\mp 1.6%) of population lives in the areas with high or very high slope mass susceptibility areas. While the proportion of railway network, subjected to potential slope mass movements, is the same as was it defined by (Jemec and Komac 2012) for landslide hazard (10%), the proportion of road network subjected to potential slope mass movements is slightly higher (34%) as it is when analysing only landslide susceptibility. Slight increase of population in the highest class of the joint susceptibility in relation to the findings' analyses of solely landslide susceptibility (Jemec and Komac 2012) is most probably related to fact that settlements gravitate towards valley bottom and towards the river net where, if conditions are suitable, the susceptibility to debris-flows is also higher than in the surrounding locations.

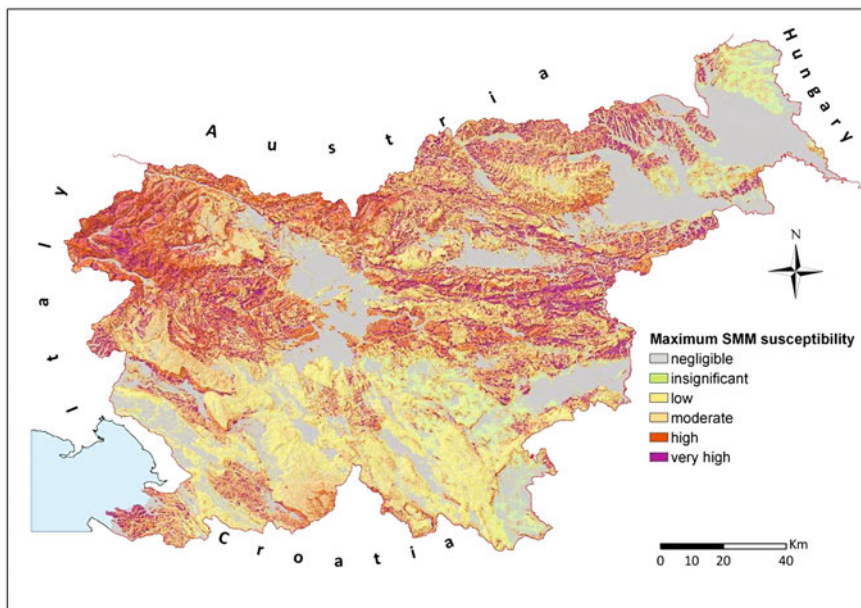


Fig. 7.10 Joint slope mass movements' susceptibility map derived with maximum value approach

Table 7.6 General statistics of the maximum slope mass movement susceptibility map

Susceptibility class	A (%)	Average slope (°)	Average elevation (m)	Inhabitants (%)	Railway (%)	Roads (%)
Negligible	27.8	2.7	341.1	61.9 (± 2.5)	33.1	63.9
Insignificant	2.9	9.4	311.1	1.9 (± 0.1)	2.2	2.9
Low	17.6	13.2	593.1	7.2 (± 0.2)	15.4	14.9
Moderate	19.0	22.2	714.1	6.1 (± 0.6)	15.4	7.2
High	20.8	21.9	686.8	11.7 (± 0.5)	19.4	7.8
Very high	11.8	21.0	589.0	11.1 (± 1.1)	14.4	3.3

“A (%)” represents the proportion of the area the specific class covers, the inhabitant proportions are presented with the error estimations (i.e. ± 2.5) as the values were calculated on the same data with two different approaches—ArcMap© Zonal Statistics and ArcMap© Cross Tabular analysis—and minor deviations occurred

Similar reasons could be assigned also to the road share increase in the highest susceptibility class as road network follows settlements mentioned in the previous sentence.

The approach of the unique value calculation (Fig. 7.11) results in a more complex model (but only to human perception) as the new susceptibility values are the combination of all six values (0-5 or descriptive values negligible to very high) within the three input models and the number of different combinations

(and susceptibility values, respectively) is 216 (6^3). With the high number of new susceptibility values, the good visualisation of the map is a challenging task nevertheless here and attempt was made to present the map with the combination of different colour scales as presented in Fig. 7.11. Table 7.7 represents the distribution of susceptibility values for the unique value slope mass movement susceptibility model. When cross-analysing the overlapping areas with the same susceptibility values between the pairs of the three input models, the proportion of overlapping for the landslide/debris-flow pair is 16.5%, for the landslide/rockfall pair it is 2.3%, and for the debris-flow/rockfall pair it is 2.8%. Even if the analysis is broadened to the cross-analysis of the neighbouring two susceptibility classes (to include potential errors due to class' transitions), these proportions are 43.1, 8.4, and 8.2%, respectively. Analysis of the overlapping areas where at least one input model has the susceptibility value 0 (negligible) shows that with the landslide/debris-flow pair this proportion is 27.9%, for the landslide/rockfall pair it is 85.3%, and for the debris-flow/rockfall pair it is 85.4%.

These results imply that the landslide and the debris-flow susceptibility models overlap much more than the rockfall model does with the each of them. This is to some extent expectable as the rockfall occurrence and its movement process differ

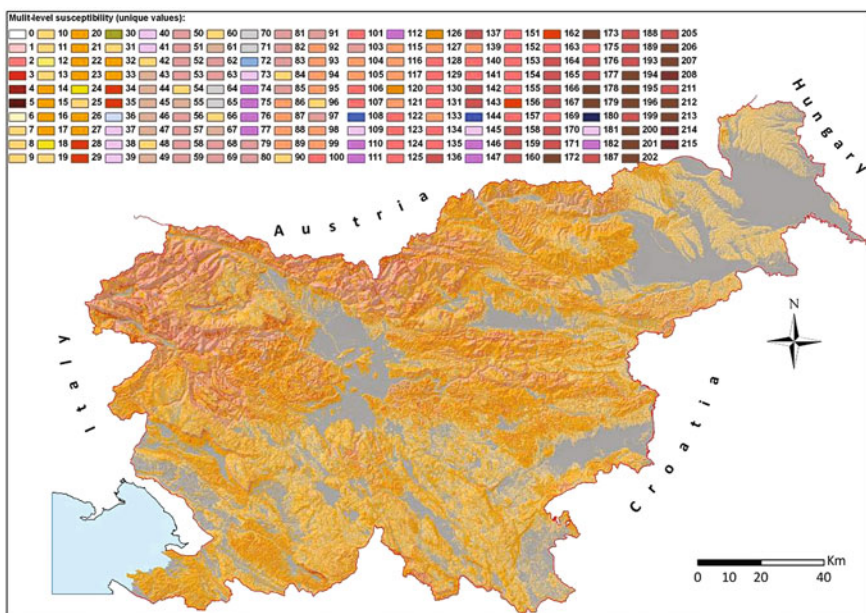


Fig. 7.11 Joint slope mass movements' susceptibility map derived with the unique value approach. Colour scheme in the legend is as follows: *red shades*, landslide susceptibility; *yellow shades*, debris-flow susceptibility; *blue shades*, rockfall susceptibility; *orange shades*, a combination of landslide and debris-flow susceptibility; *violet shades*, a combination of landslide and rockfall susceptibility; *green shades*, a combination of rockfall and debris-flow susceptibility; and *brown shades*, a combination of landslide, rockfall, and debris-flow susceptibility

Table 7.7 General statistics of the unique value slope mass movement susceptibility map

#	Σ	A (%)	#	Σ	A (%)	#	Σ	A (%)
0	LS_0+DF_0+RF_0	27.79	63	LS_3+DF_24+RF_36	0.2235	133	LS_1+DF_24+RF_108	0.46218
1	LS_1+DF_0+RF_0	0.008	64	LS_4+DF_24+RF_36	0.0484	134	LS_2+DF_24+RF_108	0.15841
2	LS_2+DF_0+RF_0	0.010	65	LS_5+DF_24+RF_36	0.000003	135	LS_3+DF_24+RF_108	0.09270
3	LS_3+DF_0+RF_0	0.004	66	LS_0+DF_30+RF_36	0.0315	136	LS_4+DF_24+RF_108	0.03440
4	LS_4+DF_0+RF_0	0.005	67	LS_1+DF_30+RF_36	0.1672	137	LS_5+DF_24+RF_108	0.000003
5	LS_5+DF_0+RF_0	0.002	68	LS_2+DF_30+RF_36	0.1621	139	LS_1+DF_30+RF_108	1.00160
6	LS_0+DF_6+RF_0	0.029	69	LS_3+DF_30+RF_36	0.1559	140	LS_2+DF_30+RF_108	0.57746
7	LS_1+DF_6+RF_0	2.858	70	LS_4+DF_30+RF_36	0.0197	141	LS_3+DF_30+RF_108	0.16403
8	LS_2+DF_6+RF_0	2.236	71	LS_5+DF_30+RF_36	0.0030	142	LS_4+DF_30+RF_108	0.07538
9	LS_3+DF_6+RF_0	1.440	72	LS_0+DF_0+RF_72	0.0009	143	LS_5+DF_30+RF_108	0.0203
10	LS_4+DF_6+RF_0	1.802	73	LS_1+DF_0+RF_72	0.0013	144	LS_0+DF_0+RF_144	0.2852
11	LS_5+DF_6+RF_0	1.689	74	LS_2+DF_0+RF_72	0.0002	145	LS_1+DF_0+RF_144	0.2643
12	LS_0+DF_12+RF_0	0.029	75	LS_3+DF_0+RF_72	0.0001	146	LS_2+DF_0+RF_144	0.0989
13	LS_1+DF_12+RF_0	7.116	76	LS_4+DF_0+RF_72	0.00002	147	LS_3+DF_0+RF_144	0.0587
14	LS_2+DF_12+RF_0	7.739	77	LS_5+DF_0+RF_72	0.00001	151	LS_1+DF_6+RF_144	0.0095
15	LS_3+DF_12+RF_0	3.363	79	LS_1+DF_6+RF_72	0.0014	152	LS_2+DF_6+RF_144	0.0003
16	LS_4+DF_12+RF_0	5.023	80	LS_2+DF_6+RF_72	0.0006	153	LS_3+DF_6+RF_144	0.0002
17	LS_5+DF_12+RF_0	3.054	81	LS_3+DF_6+RF_72	0.0032	154	LS_4+DF_6+RF_144	0.0001
18	LS_0+DF_18+RF_0	0.007	82	LS_4+DF_6+RF_72	0.0037	155	LS_5+DF_6+RF_144	0.00002
19	LS_1+DF_18+RF_0	1.918	83	LS_5+DF_6+RF_72	0.0054	156	LS_0+DF_12+RF_144	0.00001
20	LS_2+DF_18+RF_0	4.140	84	LS_0+DF_12+RF_72	0.0001	157	LS_1+DF_12+RF_144	0.0027
21	LS_3+DF_18+RF_0	2.419	85	LS_1+DF_12+RF_72	0.1902	158	LS_2+DF_12+RF_144	0.00001
22	LS_4+DF_18+RF_0	3.264	86	LS_2+DF_12+RF_72	0.1301	159	LS_3+DF_12+RF_144	0.00004
23	LS_5+DF_18+RF_0	1.809	87	LS_3+DF_12+RF_72	0.0586	160	LS_4+DF_12+RF_144	0.00001

(continued)

Table 7.7 (continued)

#	Σ	A (%)	#	Σ	A (%)	#	Σ	A (%)
24	LS_0+DF_24+RF_0	0.002	88	LS_4+DF_12+RF_72	0.0352	162	LS_0+DF_18+RF_144	0.00001
25	LS_1+DF_24+RF_0	0.438	89	LS_5+DF_12+RF_72	0.0202	163	LS_1+DF_18+RF_144	0.0785
26	LS_2+DF_24+RF_0	1.651	90	LS_0+DF_18+RF_72	0.0002	164	LS_2+DF_18+RF_144	0.0025
27	LS_3+DF_24+RF_0	1.129	91	LS_1+DF_18+RF_72	1.4034	165	LS_3+DF_18+RF_144	0.0006
28	LS_4+DF_24+RF_0	1.706	92	LS_2+DF_18+RF_72	0.4823	166	LS_4+DF_18+RF_144	0.0001
29	LS_5+DF_24+RF_0	0.702	93	LS_3+DF_18+RF_72	0.1962	167	LS_5+DF_18+RF_144	0.000003
30	LS_0+DF_30+RF_0	0.0001	94	LS_4+DF_18+RF_72	0.1031	169	LS_1+DF_24+RF_144	0.00002
31	LS_1+DF_30+RF_0	0.0589	95	LS_5+DF_18+RF_72	0.0406	170	LS_2+DF_24+RF_144	0.1669
32	LS_2+DF_30+RF_0	0.4944	96	LS_0+DF_24+RF_72	0.00002	171	LS_3+DF_24+RF_144	0.0189
33	LS_3+DF_30+RF_0	0.4150	97	LS_1+DF_24+RF_72	0.9027	172	LS_4+DF_24+RF_144	0.0047
34	LS_4+DF_30+RF_0	0.7833	98	LS_2+DF_24+RF_72	0.5789	173	LS_5+DF_24+RF_144	0.0004
35	LS_5+DF_30+RF_0	0.2105	99	LS_3+DF_24+RF_72	0.2196	175	LS_1+DF_30+RF_144	0.0001
36	LS_0+DF_0+RF_36	0.0017	100	LS_4+DF_24+RF_72	0.1072	176	LS_2+DF_30+RF_144	0.182
37	LS_1+DF_0+RF_36	0.00005	101	LS_5+DF_24+RF_72	0.0272	177	LS_3+DF_30+RF_144	0.032
38	LS_2+DF_0+RF_36	0.0003	103	LS_1+DF_30+RF_72	0.00001	178	LS_4+DF_30+RF_144	0.009
39	LS_3+DF_0+RF_36	0.0005	104	LS_2+DF_30+RF_72	0.2039	179	LS_5+DF_30+RF_144	0.001
40	LS_4+DF_0+RF_36	0.0006	105	LS_3+DF_30+RF_72	0.2365	180	LS_0+DF_0+RF_180	0.0001
41	LS_5+DF_0+RF_36	0.0002	106	LS_4+DF_30+RF_72	0.1258	181	LS_1+DF_0+RF_180	0.066
42	LS_0+DF_6+RF_36	0.0302	107	LS_5+DF_30+RF_72	0.0883	182	LS_2+DF_0+RF_180	0.022
43	LS_1+DF_6+RF_36	0.0060	108	LS_0+DF_0+RF_108	0.0129	187	LS_1+DF_6+RF_180	0.007
44	LS_2+DF_6+RF_36	0.0211	109	LS_1+DF_0+RF_108	0.0026	188	LS_2+DF_6+RF_180	0.001
45	LS_3+DF_6+RF_36	0.0199	110	LS_2+DF_0+RF_108	0.00067	189	LS_3+DF_6+RF_180	0.0002
46	LS_4+DF_6+RF_36	0.0253	111	LS_3+DF_0+RF_108	0.00083	193	LS_1+DF_12+RF_180	0.00003
47	LS_5+DF_6+RF_36	0.00001	112	LS_4+DF_0+RF_108	0.00005	194	LS_2+DF_12+RF_180	0.00004

(continued)

Table 7.7 (continued)

#	Σ	A (%)	#	Σ	A (%)	#	Σ	A (%)
48	LS_0+DF_12+RF_36	0.0849	115	LS_1+DF_6+RF_108	0.00011	195	LS_3+DF_12+RF_180	0.00001
49	LS_1+DF_12+RF_36	0.0964	116	LS_2+DF_6+RF_108	0.000003	196	LS_4+DF_12+RF_180	0.00003
50	LS_2+DF_12+RF_36	0.1647	117	LS_3+DF_6+RF_108	0.00199	199	LS_1+DF_18+RF_180	0.000003
51	LS_3+DF_12+RF_36	0.0976	120	LS_0+DF_12+RF_108	0.00041	200	LS_2+DF_18+RF_180	0.000003
52	LS_4+DF_12+RF_36	0.0782	121	LS_1+DF_12+RF_108	0.00019	201	LS_3+DF_18+RF_180	0.000003
53	LS_5+DF_12+RF_36	0.00002	122	LS_2+DF_12+RF_108	0.00018	202	LS_4+DF_18+RF_180	0.044
54	LS_0+DF_18+RF_36	0.2001	123	LS_3+DF_12+RF_108	0.00009	205	LS_1+DF_24+RF_180	0.001
55	LS_1+DF_18+RF_36	0.4697	124	LS_4+DF_12+RF_108	0.00003	206	LS_2+DF_24+RF_180	0.0001
56	LS_2+DF_18+RF_36	0.3986	125	LS_5+DF_12+RF_108	0.26999	207	LS_3+DF_24+RF_180	0.00001
57	LS_3+DF_18+RF_36	0.2032	126	LS_0+DF_18+RF_108	0.12132	208	LS_4+DF_24+RF_180	0.072
58	LS_4+DF_18+RF_36	0.0961	127	LS_1+DF_18+RF_108	0.02624	211	LS_1+DF_30+RF_180	0.005
59	LS_5+DF_18+RF_36	0.0000	128	LS_2+DF_18+RF_108	0.02746	212	LS_2+DF_30+RF_180	0.004
60	LS_0+DF_24+RF_36	0.0894	129	LS_3+DF_18+RF_108	0.00724	213	LS_3+DF_30+RF_180	0.0001
61	LS_1+DF_24+RF_36	0.3933	130	LS_4+DF_18+RF_108	0.00008	214	LS_4+DF_30+RF_180	0.00002
62	LS_2+DF_24+RF_36	0.3332	131	LS_5+DF_18+RF_108	1.31266	215	LS_5+DF_30+RF_180	0.041

“#” represents the unique value, “ Σ ” represents the combination of the input values from landslide (LS), debris-flow (DF), and rockfall (RF) susceptibility models where the input values are expressed after each slope mass movement-type abbreviation, and “A (%)” represents the proportion of the area the specific class covers

much more from the other two slope mass movement types—landslides and debris-flows than these two types differ among each other. In fact, it has been observed that debris-flows often start with the sliding process that evolves into the debris-flow in later stage.

7.5 Conclusions

A first attempt was made to produce the joint slope mass movement mode for the area of Slovenia by combining the three susceptibility models—landslide, debris-flow, and rockfall. The first two were taken from previous research, while the latter was derived for the purpose of this paper. Models were evaluated for their accuracy and compared among themselves. The results of analyses have shown that among the three groups of slope mass movements rockfall occurrence is the most susceptible to very local morphological and lithological conditions and it has to be approached using more detailed spatial data. Results of cross-analysis of the three models show that one model cannot be used to predict the other two models, and hence, all three have to be included in the susceptibility assessment, either individually or as a joint model.

The joint slope mass stability susceptibility map of Slovenia is the first attempt to combine the models of the three types of slope mass movements. As legislation and consequentially planning and prevention measures in the field of slope mass movements are not at the satisfying level in Slovenia as the main focus is still towards tackling the consequences, susceptibility assessment is a basic stone for promoting the effective prevention approach at the decision-makers' level. In recent year, some progress has been made as the inclusion of methodologies for the production of susceptibility maps for landslides, rockfalls, and debris-flows in Slovenia is being prepared to be eventually included in the legislation. The individual and joint models represented in this paper play a crucial role for the synoptic susceptibility assessment that guides the focus of more detailed susceptibility, hazard, and ultimately risk assessment. The knowledge of risk assessment in certain region or municipality is essential for the sustainable and safe spatial planning, construction interventions, and environmental protection.

References

- Alzate ABE, Guevara C, Valero JAM (1999) Zonation on a large scale of mass movement hazards, using the GIS. In: Proceedings of the nineteenth annual ESRI user conference, p 23
- Anderson SA (1995) Analysis of rainfall-induced debris flows. *J Hydraul Eng* 121:544–552
- Antoniou AA, Lekkas E (2010) Rockfall susceptibility map for Athinios port, Santorini Island, Greece. *Geomorphology* 118:152–166. doi:[10.1016/j.geomorph.2009.12.015](https://doi.org/10.1016/j.geomorph.2009.12.015)
- Archetti R, Lamberti A (2003) Assessment of risk due to debris flow events. *Nat Hazard Rev* 4(3): 115–125

- Carrara A (1983) Multivariate models for landslide hazard evaluation. *Mathemat Geol* 15:403–426
- Carrara A, Cardinali M, Detti R, Guzzetti F, Pasqui V, Reichenbach P (1991) GIS techniques and statistical models in evaluating land slide hazard. *Earth Surf Process Landform* 16:427–445
- Crozier MJ, Glade T (2005) Land slide hazard and risk: issues, concepts and approach. In: Glade T, Anderson MG, Crozier MJ (eds) *Land slide hazard and risk*. John Wiley and Sons, Chichester, pp 1–40
- Cruden DM, Varnes DJ (1996) Landslide types and processes. In: Turner AK, Shuster RL (eds) *Landslides: investigation and mitigation*, Transp Res Board, Spec Rep 247, pp 36–75
- Čarman M, Kumelj Š, Komac M, Ribičič M (2011) Pregledna karta verjetnosti pojavljanja podorov v merilu 1: 250,000. In: Rožič B (ed) *20th Meeting of Slovenian geologists*, Ljubljana, November 2011. Razprave, poročila, (Geološki zbornik, 21). Ljubljana: Univerza v Ljubljani, Naravoslovnotehniška fakulteta, Oddelek za geologijo, pp 22–25
- Dahal RK, Hasegawa S, Nonomura A, Yamanaka M, Masuda T, Nishino K (2008) GIS-based weights-of-evidence modelling of rainfall-induced landslides in small catchments for landslide susceptibility mapping. *Environ Geol* 54:311–324
- Dai F, Lee CF, Wang S (1999) Analysis of rainstorm-induced slide-debris flows on natural terrain of Lantau Island, Hong Kong. *Eng Geol* 51:279–290
- Delmonaco G, Leoni G, Margottini C, Puglisi C, Spizzichino D (2003) Large scale debris-flow hazard assessment: a geotechnical approach and GIS modelling. *Nat Haz Earth Syst Sci* 3:443–455
- Di BF, Chen NS, Cui P, Li ZL, He YP, Gao YC (2008) GIS-based risk analyses of debris flow: an application in Sichuan, southwest China. *Int J Sedim Res* 23(2):138–148
- Dorren LKA, Seijmonsbergen AC (2003) Comparison of three GIS-based models for predicting rockfall runoff zones at a regional scale. *Geomorphology* 56:49–64
- Fabbri AG, Chung CF, Cendreo A, Remondo J (2003) Is prediction of future landslides possible with a GIS? *Nat Haz* 30(3):487–499
- Fiorillo F, Wilson RC (2004) Rainfall induced debris flows in pyroclastic deposits, Campania (southern Italy). *Eng Geol* 75:263–289
- Fleming RW, Ellen SD, Aligus MA (1989) Transformation of dilative and contractive landslide debris into debris flow—an example from Marin County, California. *Eng Geol* 27:201–223
- Guinau M, Vilajosana I, Vilaplana JM (2007) Gis-based debris flow source and runoff susceptibility assessment from DEM data—a case study in NW Nicaragua. *Nat Haz Earth Syst Sci* 7:703–716
- Guzzetti F, Reichenbach P (2010) Rockfalls and their Hazard. In: Stoffel M et al (eds), *Tree rings and natural hazards: a state-of-the-art, advances in global change research*, vol 41, pp 129–137. doi:[10.1007/978-90-481-8736-2_12](https://doi.org/10.1007/978-90-481-8736-2_12)
- Jemec M, Komac M (2012) From national landslide database to national hazard assessment. In: Mambretti S (ed) *Landslides (Safety & Security Engineering Series)*. Wit Press, Southampton, Boston, p 11–26
- Jež J, Mikoš M, Trajanova M, Kumelj Š, Bavec M (2008) Vršaj Koroška Bela—Rezultat katastrofičnih pobočnih dogodkov. *Geologija* 51(2):219–227 (in Slovene)
- Kojima H, Chung CF, van Westen CJ (2000) Strategy on the landslide type analysis based on the expert knowledge and the quantitative prediction model. *Int Archiv Photogram Remot Sens* 33 (Part-B7):701–708
- Komac M (2005) Statistics of the geological map of Slovenia at scale 1: 250,000. *Geologija* 48/1:117–126. doi:[10.5475/geologija.2005.011](https://doi.org/10.5475/geologija.2005.011)
- Komac M (2012) Regional landslide susceptibility model using the Monte Carlo approach—the case of Slovenia. *Geol Q* 56(1):41–54
- Komac M, Ribičič M (2008) Landslide susceptibility map of Slovenia 1:250,000. Geological Survey of Slovenia, Ljubljana
- Komac M, Kumelj Š, Ribičič M (2009) Debris-flow susceptibility model of Slovenia at scale 1: 250,000. *Geologija* 52(1):87–104. doi:[10.5474/geologija.2009.010](https://doi.org/10.5474/geologija.2009.010)
- Lan HX, Zhou CH, Wang LJ, Zhang HY, Li RH (2004) Landslide hazard spatial analysis and prediction using GIS in the Xiaojiang watershed, Yunnan, China. *Eng Geol* 76:109–128

- Lin PS, Lin JY, Hung JC, Yang MD (2002) Assessing debris-flow hazard in a watershed in Taiwan. *Eng Geol* 66:295–313
- Mainali A, Rajaratnam N (1994) Hydraulics of debris flows. *J Hydraul Eng* 120:104–123
- Mazengarb C (2010) Map 4, Ulverstone—rockfall susceptibility. Tasmanian landslide map series. Mineral Resources Tasmania, Department of Infrastructure Energy and Resources, Hobart
- Melelli L, Taramelli A (2004) An example of debris-flows hazard modeling using GIS. *Nat Haz Earth Syst Sci* 4:1–12
- Mergili M (2008) r.debrisflow, version 1.3. User's manual and model outline. A model framework for simulating mobilization and movement of debris flow, Institute of Geography, University of Innsbruck, Austria
- Mikoš M (2001) Značilnosti drobirskih tokov. Ujma, pp 14–15 (in Slovene)
- Rickenmann D, Zimmerman M (1993) The 1987 debris flows in Switzerland: documentation and analysis. *Geomorphology* 8:175–189
- Ruff M, Rohn J (2008) Susceptibility analysis for slides and rockfall: an example from the Northern Calcareous Alps (Vorarlberg, Austria). *Environ Geol* (55):441–452. doi:10.1007/s00254-007-0990-5
- Shirzadi A, Saro L, Hyun Joo O, Chapi K (2012) A GIS-based logistic regression model in rock-fall susceptibility mapping along a mountainous road: Salavat Abadca sestudy, Kurdistan, Iran. *Natural Hazards*, online first, doi:10.1007/s11069-012-0321-3
- SORS (2012) Statistical office of the Republic of Slovenia—SI-stat data portal, Environment and natural resources. <http://www.stat.si/>. Accessed 21 Aug 2012
- Toyos G, Oramas Dorta D, Oppenheimer C, Pareschi MT, Sulpizio R, Zanchetta G (2008) GIS-assisted modelling for debris flow hazard assessment based on the events of May 1998 in the area of Sarno, Southern Italy. Part I: maximum run-out. *Earth Surf Proc Land* 33(11): 1693–1708
- Van den Eeckhaut M, Reichenbach P, Guzzetti F, Rossi M, Poesen J (2009) Combined landslide inventory and susceptibility assessment based on different mapping units: an example from the Flemish Ardennes, Belgium. *Nat Haz Earth Syst Sc* 9:507–521
- Volkwein A, Schellenberg K, Labiouse V, Agliardi F, Berger F, Bourrier F, Dorren LKA, Gerber W, Jaboyedoff M (2011) Rockfall characterisation and structural protection—a review. *Nat Haz Earth Syst Sci* 11:2617–2651. doi:10.5194/nhess-11-2617-2011
- Wen BP, Aydin A (2005) Mechanism of a rainfall-induced slide-debris flow: constraints from microstructure of its slip zone. *Eng Geol* 78:69–88
- Yawen M (2011) Regional scale multi-hazard susceptibility assessment: a case study in Mtskheta—Mtianeti. Enschede, University of Twente Faculty of Geo-Information and Earth Observation (ITC), Georgia

Chapter 8

Landslide Inventory: Challenge for Landslide Hazard Assessment in Indonesia

Ngadisih, Guruh Samodra, Netra Prakash Bhandary and Ryuichi Yatabe

Abstract Landslide occurs almost every year in Indonesia which causes tremendous damages to life and properties. Landslide hazard map would allow the identification of hazard regions for the implementation of mitigation which can minimize the loss of human life and property from future landslide occurrences. Currently, the Indonesian Government and research entities as well as academic institutions are trying to develop landslide hazard assessment model for the prone area to support prevention program, mitigation action, and evacuation plan. However, there is a lack of attention in the landslide inventory mapping as a basic input of landslide hazard mapping. Ideally, landslide inventory mapping provides detailed information about the spatiotemporal distribution of landslide occurrence. It contains the date of occurrence, types, failure mechanisms, area/volume, depth, and so on. Landslide inventory map can be prepared by several methods such as image interpretation, remote sensing techniques, detailed geomorphological field-work, historical archive studies, interview, and combination among several methods. The aim of this paper is to review the possibility of using various methods of inventory in Indonesia. Furthermore, this paper is also purposed to explore the use of existing landslide database for producing a landslide inventory that can be used to assess landslide hazard.

Keywords Landslide inventory · Challenge · Hazard · Indonesia

Ngadisih (✉) · N.P. Bhandary · R. Yatabe
Graduate School of Science and Engineering, Ehime University, Matsuyama, Japan
e-mail: ngadisih@ugm.ac.id

Ngadisih
Department of Agricultural and Biosystem Engineering, Faculty of Agricultural Technology,
Gadjah Mada University, Yogyakarta, Indonesia

G. Samodra
Graduate School of Engineering, Kyushu University, Fukuoka, Japan

G. Samodra
Department of Environmental Geography, Faculty of Geography, Gadjah Mada University,
Yogyakarta, Indonesia

8.1 Introduction

Landslide is a complex natural phenomenon that causes a lot of casualties, property damage, and economic losses in mountainous areas of the world. In Indonesia, for example, there were 890 landslide events during the period 1998–2009 which killed 1280 people (Kirschbaum et al. 2009). These landslides damage agricultural lands and roads with subsequent economic disruption. Nowadays, the damages and casualties are increasing due to an increase of population growth and urbanization at prone areas; thus, landslide hazard and risk are essential for mitigation effort in Indonesia. However, landslide hazard and risk analysis can be successful only with a completion of landslide inventory (van Westen et al. 2008; Booth et al. 2009; Blahut et al. 2010).

Landslide inventory is a map representing the spatial distribution of landslide that includes information of location, type of landslide, landslide volume, state activity, date of occurrence, and other characteristics of landslides in the area as well as information on triggering factors (Fell et al. 2008). The landslides can be drawn as single point or areas, depending on the scale of the map (Parise 2001). This map is essential to understand the evolution of landscape (Galli et al. 2008) and to produce other maps such as susceptibility, hazard, and risk maps (Parise 2001; Galli et al. 2008). In addition, the inventory is also required before any analysis of the occurrence of landslide and their spatial relationship to environmental condition undertaken (Dumana et al. 2005) as a key for predicting landslide events (Marcelino et al. 2009). Landslide inventory has traditionally been prepared by combining the visual interpretation of aerial photographs and fieldworks which are often subjective, incomplete (Booth et al. 2009), time-consuming, and labor-intensive (Galli et al. 2008). Since the quality and completeness of the landslide inventory may affect the quality of the secondary analysis, new methods for producing landslide inventory have been proposed by several researchers such as semiautomated landslide detection (Mckean and Roering 2004; Glenn et al. 2006; Booth et al. 2009; Kasai et al. 2009; Martha et al. 2010). We noticed that the advance of inventory methods has been stimulated by remote sensing technologies and geographic information system (GIS). A good review of landslide inventory methods and their merits and demerits has been discussed by Guzetti et al. (2012). This paper attempts to review the possibility of using various methods of inventory in Indonesia and to explore the use of existing landslide database for generating a landslide inventory that can be used to produce landslide hazard map.

This paper is organized as follows. In Sect. 8.2, we describe the landslide disaster in Indonesia and the importance of hazard study. Section 8.3 clarifies the landslide inventory including definition, types, and completeness of landslide inventory. The methods of inventory and its challenge to apply them in Indonesia are discussed in Sect. 8.4. This section also illustrates the analysis of inventory for assessing landslide hazard. The last section discusses a proposed method of landslide inventory.

8.2 Landslide Disaster in Indonesia and the Importance of Hazard Study

Indonesia is located in Southeast Asia; it is a huge archipelago extending 5120 km from east to west and 1760 km from north to south along the equator. It is comprised of 13,667 islands, with only 6000 of which are inhabited. There are five main islands (Sumatra, Java, Kalimantan, Sulawesi, and Irian Jaya), two major archipelagos (Nusa Tenggara and the Maluku Islands), and sixty smaller archipelagos. Three of the islands are shared with other nations: Kalimantan (known in the colonial period as Borneo, the world's third largest island) is shared with Malaysia and Brunei, Irian Jaya is shared with Papua New Guinea, and Timor is shared with Timor-Leste (Fig. 8.1). Total land area is 1,919,317 km², while the water area is 3,257,483 km². The total population is 237,641,326 in 2010 (Central Bureau of Statistic Indonesia 2009), and it was listed as the fourth most populous country in the world.

The climate and weather of Indonesia are characterized by two tropical seasons, which vary with the equatorial air circulation (the Walker circulation) and the meridian air circulation (the Hadley circulation). The displacement of the latter follows the north–south movement of the sun and its relative position from the earth, in particular from the continents of Asia and Australia, at certain periods of the year. These factors contribute to the displacement and intensity of the Inter-Tropical Convergence Zone (ITCZ) which is an equatorial trough of low pressure that produces rain. Thus, the west and east monsoons, or the rainy and dry seasons, are a prevalent feature of the tropical climate in Indonesia.

The climate changes every six months. The dry season (June to September) is influenced by the Australian continental air masses, while the rainy season (December to March) is the result of the Asian and Pacific Ocean air masses. The transitional periods between the two seasons are April to May and October to November. Tropical areas have rains almost the whole year. Indonesia receives on average 1755 mm of precipitation annually or 146 mm each month. Annual rainfall



Fig. 8.1 Indonesian territory. Source <http://www.aseanbriefing.com/regions/indonesia>

map of Indonesia is shown in Fig. 8.2. Due to the large number of islands and mountains in the country, average temperatures may be classified as follows: (i) coastal plains 28 °C, (ii) inland and mountain areas 26 °C, and (iii) higher mountain areas 23 °C, varying with the altitude. Being in a tropical zone, Indonesia has an average relative humidity between 70 and 90%, with a minimum of 73% and a maximum of 87%.

Geologically, Indonesia is laid on the triple junction of Pacific, Eurasian, and Australian tectonic plates so it is one of the most active tectonic regions in the world (Fig. 8.3). The southern islands such as Sumatera, Java, and Bali are formed due to subduction of the Eurasian and Asian plate. The rate of subduction is some centimeters per year, for example, 6.0 cm per year in the West Java Trench at 0°S 97°E (azimuth 23°) and 4.9 cm per year in the East Java Trench at 12°S 120°E (azimuth 19°). Eastern Indonesia (e.g., Sulawesi, Maluku, Irian Jaya) is affected by another subduction area of the Pacific Plate that moves southwesterly under the Eurasian Plate. Most of the earthquakes are concentrated in the subduction zone. In December 2004, a 9.1 magnitude underwater earthquake caused a devastating tsunami, resulting in over 120,000 deaths in Aceh Province. In May 2006, a 6.2 earthquake struck Yogyakarta Province resulting in over 5700 fatalities and over 37,000 injuries. The subduction has also created volcanic ranges that run along



Fig. 8.2 Annual precipitation in Indonesia. Source http://www.bestcountryreports.com/Precipitation_Map_Indonesia.php

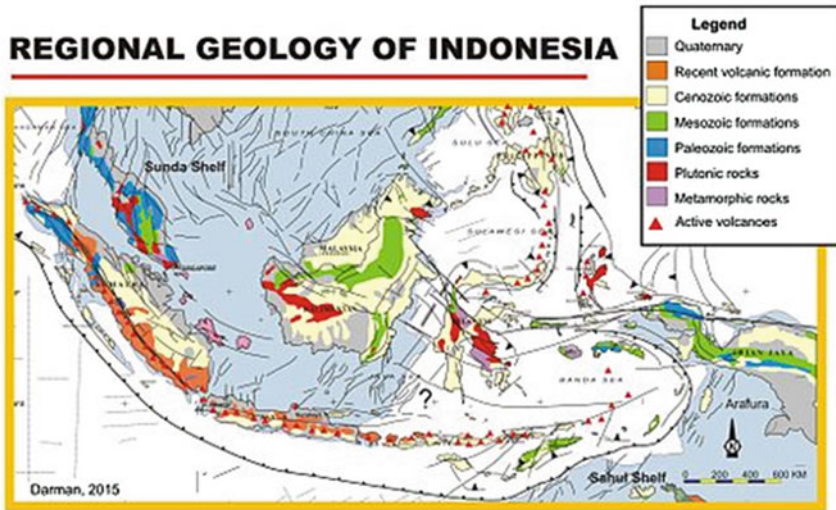


Fig. 8.3 Regional geological map of Indonesia. *Source* Geology of Indonesia-Wikipedia (https://en.wikipedia.org/wiki/Geology_of_Indonesia)

Sumatra, Java, Bali, North Sulawesi, Sangehe, and Halmahera islands (Fig. 8.3), and it is a part of Pacific Ring of Fire.

Morphologically, Indonesia consists of lowland (0–500 m), hilly land (500–1000 m), upland (1000–2000 m), and mountain (more than 2000 m). The volcanic mountains dominate the landscape of Indonesian islands (Fig. 8.3), and they spread along the tectonic zone (Fig. 8.4). Barisan Mountains are situated along west coastline of Sumatra. The highest peaks reach more than 3600 m with Kerintji (3805 m) being the highest. On Java, the mountains also lie close to the shoreline of the Indian Ocean. The highest peaks are in the Tengger Mountains (East Java). Sulawesi has mountainous terrains with peak of 2438 m. Many of the islands in Nusa Tenggara and the Maluku archipelagoes are mountainous. Irian Jaya has towering non-volcanic mountains, the highest in Indonesia where some peaks are covered with snow throughout the year, including Puncak Jaya (5030 m).

Due to its extreme geological and climatic conditions, mountainous areas in Indonesia are very frequently damaged by landslide and slope failure events. Cepede (2010) reported that landslide is the secondary greatest catastrophe in Indonesia which causes much loss of life and property. The major of victims due to landslides are in the Java (52%), Sulawesi (24%), and Sumatra (18%) within the period 2003–2007. The death toll by landslide in Java was the highest because of the high frequency of events and the high-density population (Hadmoko et al. 2010). As national economic and government center, Java becomes the most populated island (Fig. 8.5) and economically and socially marginalized communities are often forced to occupy landslide-prone areas (Cristianto et al. 2009). In addition, extensive infrastructure development, such as construction of national

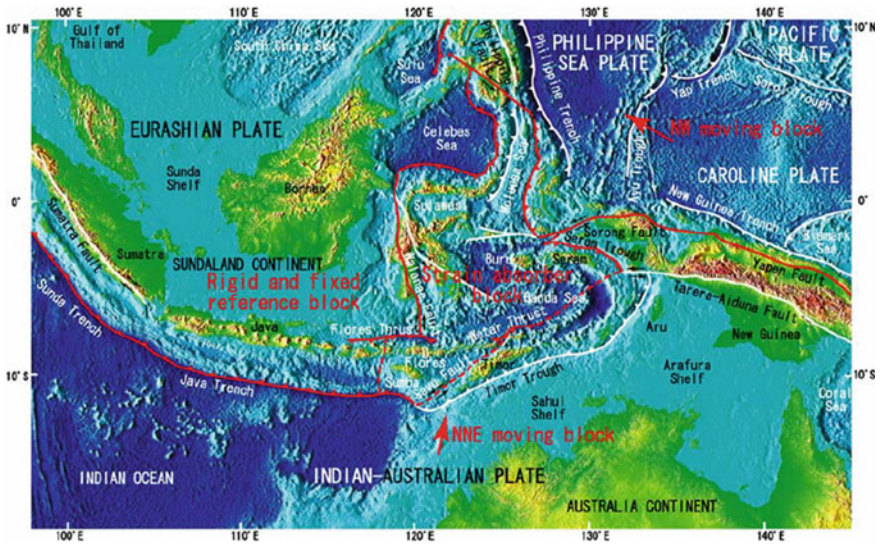


Fig. 8.4 Tectonic map of Indonesian islands. Source Muraoka et al (2004)

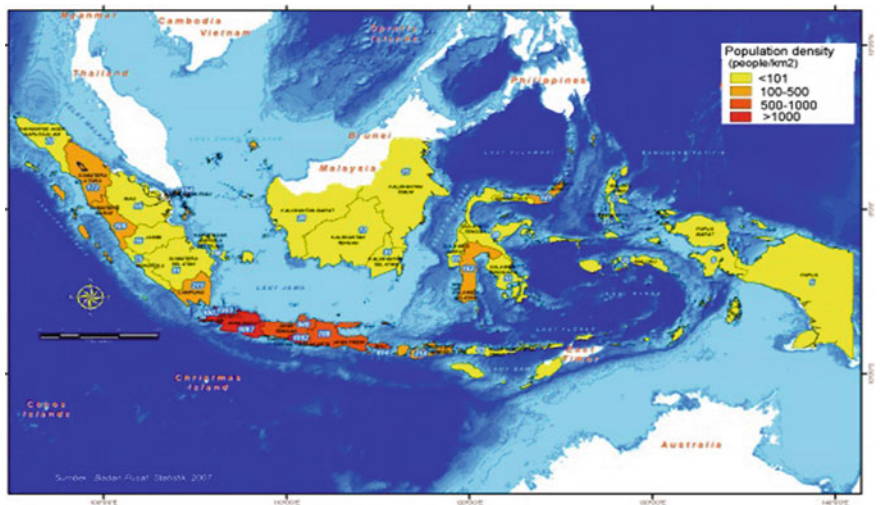


Fig. 8.5 Population density map according the province boundary. Source <http://keywordsuggest.org/gallery/149282.html>

highways, railways, and roads, has taken place in this island recently. All these activities have increased the risk of extensive landsliding in Java.

The loss of human life and property caused by any natural disasters can be minimized by mitigation efforts either by structural method (slopes, rock butters,

drainage tunnels, stone columns, retaining wall, and so on) or by non-structural techniques such as avoiding the disaster area for buildings. Because of limited financial resources, developing countries, like Indonesia, have difficulties to build the facilities or constructions to protect an area from natural disaster. Furthermore, the effort in relocating of residents to a safe area is also very expensive and impracticable. Therefore, the hazard study is very important and useful to inform the public about disaster-prone locations with the probability of the occurrence.

Hazard is defined as the probability of occurrence within a specified period of time and within a given area of a potentially damaging phenomenon (Varnes 1984). In case of landslide, this definition includes spatial and temporal probability of landslide events. Probability of spatial is well known as likelihood of occurrence of landslide in a given location of terrain unit and shown in map (Corominas and Moya 2008). It may be assessed either by computing probability of failure of the slopes or through the frequency analysis of past landslide events. Ideally, hazard can be characterized by statements of ‘what,’ ‘where,’ ‘when,’ ‘how strong,’ and ‘how often,’ demanding knowledge of variation in both spatial conditions and temporal behavior (Glade et al. 2005). Nevertheless, the temporal aspects (when and how often) are difficult to be included in most of landslide hazard maps because of several factors, i.e., (i) absence of multi-temporal data of landslide events, (ii) heterogeneity of the subsurface conditions, (iii) scarcity of input data, and (iv) absence or insufficient length of historical records of triggering events (van Westen et al. van Westen et al. 2005). The first and the fourth factors are related to landslide inventory map where generally detailed inventory map is available in only a few countries and mostly for limited areas.

Currently, most of regions in Indonesia has a low-scale susceptibility map that too on small scale is less than 1:100,000 (Karnawati et al. 2006). It does not estimate the temporal probability of landslide so it has limited function in management and mitigation strategy (Marfai et al. 2008). The absence of a complete landslide inventory causes the hazard assessment could not be conducted in Indonesia. Next heading will discuss about landslide inventory including techniques for producing an inventory and the possibility of using them in Indonesia.

8.3 Definition, Types, and Completeness of Landslide Inventory

The term ‘landslide’ describes a wide variety of processes that result in the downward and outward movement of slope-forming materials including rock, soil, artificial fill, or a combination of these materials. The materials may move by falling, toppling, sliding, spreading, or flowing. There are various classifications within the landslide literature, each dependent on a different landslide factor or author’s objective (Dikau et al. 1996). Hutchinson (1968) classified landslide types based on the existence of slip surface, following: (1) translational slide, the position

of slip surface is perpendicular with surface material; (2) rotational slide, the slip surface position is formed by the circular form; and (3) rock fall, no slip surface. Carson and Kirby (1972) grouped landslide based on water content of earth material (drier to wetter) and velocity of mass movement (slower to faster). Varnes (1978) classified mass movement into eight types that are as follows: creep, landslide, slump, toppling, lateral spreading, mudflow/earthflow, rockfall, and the combination of various landslides. Classification of landslide proposed by Cruden and Varnes (1996) and Hutchinson (1968) is used widely for the analysis of susceptibility, hazard, and risk today.

A landslide inventory is the simplest form of landslide mapping so that some of the researchers named it as landslide map. Chacon (2006) describes that landslide inventory map is a data set that represents single or multiple events as well as shows the locations and outlines of landslides. The landslide inventory map should involve information of the location, type of landslide, the volume, activity, date of occurrence, and other characteristic of landslides in the area (Fell et al. 2008) as well as information on triggering factors (Godt et al. 2008). In some cases, the landslide map just describes the distribution of landslide events. The map does not inform the different types of slope movement and time of occurrences. The scale of inventory influences the information should be included in this map. Inventories' scale 1:50,000 to 1:100,000 is purposed for regional analysis of hazard or risk. The minimum area covered by these inventories is 4 ha. The simplest information of the landslides may be presented as a dot, so it does not inform scarp features and deposit masses. Local analysis is used to be applied for mapping landslide at scale 1:10,000 to 1:25,000. It covers an area is less than 1600 m², and for a smaller landslides still be allowed to be plotted as point. The information in this inventory is more detail, e.g., illustration of physical dimension (minor and lateral scarps, upslope deformations, original mass, deposit masses, volume, velocity), types of the landslides, and the damages data. Landslide inventory at a scale greater than 1:5000 is purposed for specific analysis that should meet with criteria for inventory map, with a minimum area covered is 100 m².

Landslide inventory can be prepared using a variety of techniques (Guzetti 2006; van Westen et al. 2008). Selection of this technique is relied on the purpose, the extent of the study area, the scale of base maps and analysis, resolution and characteristics of the available imagery, and the skill and experience of the interpreter (Guzetti et al. 2000; van Westen et al. 2005). Traditionally, the inventories can be produced by the interpretation of aerial photographs coupled with field surveys, and it is known as geomorphological inventories. Landslide maps also can be prepared by collecting historical information on individual landslide events, and it is known as archive inventory (Guzetti et al. 2000; Malamud et al. 2004). The geomorphological inventories can be classified further as historical, event, seasonal, or multi-temporal inventories. The geomorphological historical inventory is a summation of many landslide events over period of tens, hundreds, or even many thousands year. This inventory map does not distinguish the age of landslide in

detail, but it is only given in relative terms, i.e., recent, old, or very old. An event inventory informs landslide occurrences that are caused by a single trigger, such as earthquake, rainfall, or snowmelt event. This inventory shows the date of the landslides which corresponds to the date (or period) of the trigger event. Seasonal and multi-temporal inventories are obtained by the interpretation of multiple sets of aerial or satellite images of different dates. The main difference in both of those inventories is the period (short/season or long period) of triggering event. A seasonal inventory shows landslide triggered by single or multiple events during a single season or a few seasons, while multi-temporal inventory indicates landslide occurrences triggered by multiple events over longer periods. Similar to the event inventory, the seasonal and multi-temporal inventories inform the date of the landslides which correspond to the period of the trigger event.

Based on the sources data and technique are used, the landslide inventories are classified into three groups: small-scale, medium-scale, and large-scale inventories. The small-scale inventories (<1:200,000 scale) compile landslide archives from public organizations, private consultants, journals, technical and scientific reports, newspapers, or by interviewing landslide experts (Glade 1998; Reichenbach et al. 1998; Salvati et al. 2003, 2009). An exception, Cardinali et al. (1990) produced a small-scale landslide map through aerial photograph analysis. Medium-scale landslide inventories (1:25,000 to 1:200,000) are prepared through the systematic interpretation of aerial photographs at print scales 1:60,000 to 1:20,000 and field checks for updating historical information of landslides (Cardinali et al. 2001; Dumana et al. 2005). Large-scale inventories (>1:25,000) are assembled through interpretation of aerial photographs at print scale >1:20,000, very high-resolution satellite images or digital terrain models, and intensive field investigations (Guzetti et al. 2000; Reichenbach et al. 2005; Ardizzone et al. 2007). But some of studies succeeded in making large-scale inventory for a wide area through interpretation of medium- to large-scale aerial photographs and field checks (e.g., Antonini et al. 2002), limited field checks, and medium scale of aerial photographs (e.g., Antonini et al. 2002).

An inventory map records the location of mass movements that have left discernible features on the ground. Since the natural process (e.g., erosion, vegetation) and the anthropogenic activities (e.g., urbanization, road construction, plowing), these features may not be recognized in the field or through the interpretation of aerial photographs. This condition created an issue regarding completeness of the inventory map, and specific criteria to assess the level of completeness of inventory is unavailable up to now. Guzzetti et al. (2012) contend that completeness of inventory refers to the proportion of landslides shown in the inventory compared to the real number of landslide in the study area. In fact, it is closely related to the comprehensiveness of depicting boundaries between the failure areas (depletion, transport, and deposition areas) and unaffected terrain, information of triggering, date of occurrences, as well as status activity of landslides. These criteria may possible for a small and shallow landslides, but for a large and complex landslide that happened ten or hundred year ago on vegetated areas is never meet. Thus, the completeness of inventory maps would be influenced by (i) the type and age of

landslides; (ii) land-use type and alteration; (iii) the scale, date, and quality of aerial photographs or the characteristic of the satellite imagery; (iv) the type, scale, and quality of the base map; (v) the tools used to interpret and analyze the imagery; (vi) the degree of experience of the interpreters (Malamud et al. 2004; Guzetti et al. 2012).

8.4 Methods for Generating Landslide Inventory and Its Challenge

8.4.1 Landslide Inventory Techniques

Producing an inventory can use conventional methods or innovative techniques. Geomorphological field mapping and visual interpretation of aerial photographs are considered as conventional method. Brusden (1985) argued that mapping landslide in the field is part of standard geomorphological mapping. Some of the literature argued that mapping landslides in the field is more accurate than mapping landslides by remotely; however, it is a misconception (Guzetti et al. 2012). This method contains many limitations which are found during fieldwork due to: (i) the terrain condition, (ii) the size of the landslide, and (iii) the age of landslides. In case of Indonesia, field survey is very hard for checking landslides in the forest areas and/or steeply terrains which have limited road paths. Landslides are often too large so investigator could not see completely all parts of a landslide such as the scarp, lateral edges, deposit, and toe. Furthermore, landslide boundaries become increasingly indistinct with the age of the landslide (Malamud et al. 2004). The old landslides are often partially or totally covered by vegetation or have been dismantled by other landslides, erosion process, and human actions, including agricultural and construction practices. The humid tropical climate leads a rapid vegetation growth so landslide signatures will be quickly disappeared. Thus, aerial photograph techniques become more popular.

Aerial photograph interpretation was the first method of remote sensing and even used today in the era of satellite and electronic scanner. It has been used extensively to recognize landslides in terms of landslide inventory maps. Unlike a map, features on an aerial photograph are not generalized or symbolized. Air photographs record all visible features on the Earth's surface from an overhead perspective. The landslide features are visible, but they are not always easily identifiable. The process of studying and gathering the information to identify the various cultural and natural features is called visual interpretation, where commonly it is conducted by the help of stereoscopes. The following factors are used to identify a landslide feature on aerial photograph: shape, pattern of object, color/tone, shadow, texture, and association/site. However, there are several problems in generating landslide inventory in Indonesia by aerial photograph interpretation such as (i) unavailability of multi-temporal aerial photographs especially in hilly and mountainous area,

(ii) limited number of well-trained geomorphologist and interpreter, and (iii) the difficulties on the detecting landslide in densely vegetated area.

The availability of an aerial photograph in Indonesia is usually based on the tentative project such as land evaluation and land resources inventory project. The aerial photograph only available in a single year, thus to generate the event-based or multi-temporal landslide inventories seems to be not possible. The visual interpretation is prone to subjectivity of interpreters because of unavailability of standard criteria for photograph interpretation. They identify and classify landslide from aerial photographs based on experience, so intense trainings for interpreters are needed to minimize misinterpretation. Another difficulty is the rapid vegetation growth that will remove the landslide signature. Regardless, the aerial photograph is taken several months or years after the event. The visual interpretation of aerial photograph is also affected by terrain condition and age of landslide. The morphological appearance of landslides is not concealed by vegetation in arid and semiarid regions because of sparse vegetation covering these regions. But the signature of landslide in tropical areas is disappeared in a matter of months or seasons by rapid vegetation growth.

Actually, the visual interpretation will be an excellent method if it is done by a trained interpreter: (i) because of the feeling of naturalness when a scene is being viewed through an aerial photograph so the images can be intuitively understood by observer, (ii) because the technology and tools are needed to interpret aerial photographs are simple (e.g., stereoscope) and inexpensive, (iii) because the size and scale of the aerial photographs allow for the coverage of large territories with a reasonable number of the photographs, (iv) because the availability of multiple sets of aerial photographs for the same area allows investigating the temporal and the geographical evolution of slope failures (Guzetti et al. 2005; Fiorucci et al. 2011).

Landslide inventory maps produced with traditional methods are often subjective, prone to error (Malamud et al. 2004), time-consuming, and difficult to carry out in forested terrain (Brardinoni et al. 2003; Van de Eeckhaut et al. 2005). For these reasons, new methods and technologies are proposed to overcome the drawbacks of traditional methods. It is driven by the availability of high-resolution satellite images, digital elevation models (DEMs), and GIS technologies. Guzetti et al. (2012) discussed the detail of innovative techniques of inventory including their advantages and disadvantages. Briefly, innovative remote sensing techniques and satellite image can facilitate the production of geomorphological inventories, particularly promising are: (1) very high-resolution (VHR) digital representations of surface topography obtained by LiDAR sensors and (2) VHR optical, monoscopic, and stereoscopic satellite images. LiDAR data proved effective method for the recognition of landslide in forested terrains where old and very old, deep seated landslides are difficult to identify using standard aerial photography or satellite imagery (Van de Eeckhaut et al. 2007; Razak et al. 2011). A good chance to apply VHR LiDAR terrain data for preparing geomorphological inventories for large areas such as Indonesia. But they are costly, and Indonesia has limited funding resource to purchase them.

8.4.2 Analysis of Landslide Inventory for Hazard Assessment

The definition of landslide hazard incorporates the concept of location, time, and size (Guzetti et al. 2005). It means hazard assessment has to predict quantitatively ‘where’ landslide will occur, ‘when’ or how frequently it will occur, and ‘how large’ the landslide will be. In mathematical terms, it can be written as:

$$P_N = P[N(t) \geq 1] \quad (8.1)$$

where A_L is the area of landslide greater or equal than a minimum size, a_L , measured (e.g., in square meters). For any given area, Eq. (8.1) expresses landslide hazard as the conditional probability of landslide size, P_{AL} , of landslide occurrence in an established period t , P_N , and of landslide spatial occurrence, S , given the local environmental setting. By assuming independence among the three probabilities, the landslide hazard is a combination probability that can be written as follow:

$$H_L = P_{A_L} \cdot P_N \cdot S \quad (8.2)$$

To calculate three probabilities of hazard (Eq. 8.2), it required a multi-temporal inventory that meets with criteria of completeness. Unfortunately, this inventory is not available in Indonesia. Heuristic and deterministic methods were more preferred for assessing landslide hazard in Indonesia because the analysis is not based on the inventory. Heuristic model is done by evaluating the factors causing landslide, subjectively depending on the experience of researchers. Deterministic models are often used for a relatively small area because measurements and studies of geotechnical are needed to assess the level of slope stability and it can be used for the spatial and temporal prediction of landslide. Due to simplicity of analysis for large area, the heuristic method was more frequently used in Indonesia for generating landslide hazard maps. These maps still do not provide an estimation of time “when” the landslide may occur; thus, it should be called as susceptibility maps. By using Eqs. (8.1) and (8.2), geographic information system (GIS) can model that investigated area will be affected by future landslide in a given time (when), location (where), and size (how large). This analysis requires data: (i) location and dimension of landslide phenomenon including types, failure mechanism and causal factors, (ii) date of occurrences or frequency of occurrences, and (iii) environmental factor data.

In this paper, the landslide inventory is analyzed based on the only available secondary data such as aerial photographs and disaster data archive from local government. The aerial photograph is aimed to analyze landslide size and spatial probability, whereas data archive is addressed for temporal probability analysis. It should be underlined that both data are not in the same location (e.g., aerial photograph of West Java, landslide archive of Yogyakarta). It is only intended to give an overview on how landslide inventory should be analyzed properly. The

incomplete data are a challenge for earth scientists, city planners, and decision makers in assessing landslide hazard as the key of mitigation and disaster risk reduction. In the future, several techniques (e.g., semiautomated method) should be adapted to provide a complete landslide inventory. However, the analysis of inventory in the following subheadings would provide an overview how Indonesia should produce a landslide hazard map. It may describe the best technique for generating a landslide inventory which is appropriate for hazard assessment in Indonesia.

8.4.3 Probability of Landslide Size

Investigators used to identify landslide features based on aerial photograph interpretation and field inspection. The only black and white aerial photographs on scale of 1:50,000 back in 1994 that produced by Bureau of Coordinating Survey and National Mapping of Indonesia are available in the country. Figure 8.6 shows an inventory that is prepared from interpretation of these photographs and field survey. The inventory also covered landslides that occurred from 1994 to date. Due to unavailability or recent aerial photographs, landslides that occurred from 1994 were referenced from newspapers and Google Earth image. Landslides were not distinguished as past and recent events because of unavailability of good archives for whole region. Furthermore, the typology of landslide was not stated in the inventory map because of limited field check for whole study area. The total landslide area considered the crown area and deposit. By using this inventory, the probability of landslide size and spatial can be calculated. First, we would illustrate the analysis of size probability in the following paragraph.

The probability of landslide will have an area greater or equal than a_L :

$$P_{A_L} = P[A_L \geq a_L] \quad (8.3)$$

This probability can be estimated from analysis of inventory maps, particularly the frequency–area distribution of known landslides. This analysis reveals that the abundance of landslide increases with landslide area up to a maximum value, where landslides are most frequent, and then, it decays rapidly along a power law (Guzetti 2002; Guthrie and Evans 2004; Malamud et al. 2004). Malamud et al. (2004) and Stark and Hovius (2001) proposed probability density function (PDF) of landslide area (A_L) than can be used to estimated landslide size. The probability density function of landslide areas and probability of landslide area are shown in Fig. 8.7.

The probability of landslide area is the probability a landslide will have an area smaller than a given size (left axis), or probability a landslide will have an area exceeds a given size (right size). Based on Fig. 8.8, probability landslide events in the area exceed an area of 10,000 and 100,000 m² (10 ha) that are found to be 0.80 and 0.30. Later, these values can be applied to assess landslide hazard representing the probability of size (P_{A_L}).

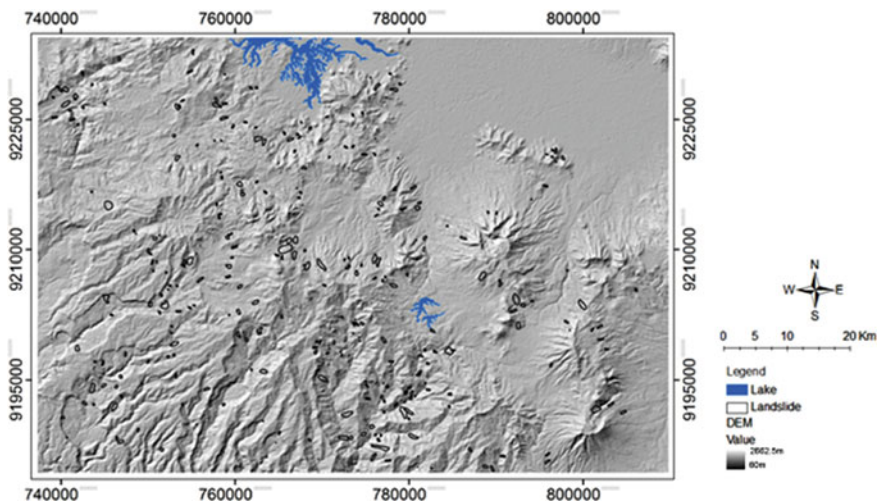


Fig. 8.6 Landslide inventory map of volcanic mountains of West Java Province overlain on digital elevation model (DEM). It was prepared from interpretation of *black* and *white* aerial photographs on scale 1:50,000 and field survey

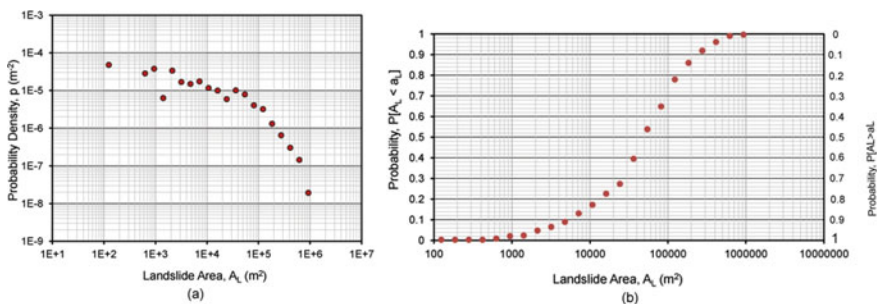


Fig. 8.7 **a** Probability density and **b** probability of landslide area that were analyzed from inventory map of volcanic mountains of West Java Province

8.4.4 Spatial Probability of Landslides

The spatial probability of landslide event is known as susceptibility which is commonly presented as a map. It demonstrates spatial distribution of landslides that already exist in an area or may potentially occur in the future so that it is also called as spatial probability map. In the literature, four main types of landslide susceptibility assessment techniques are available, i.e., landslide inventories, heuristic

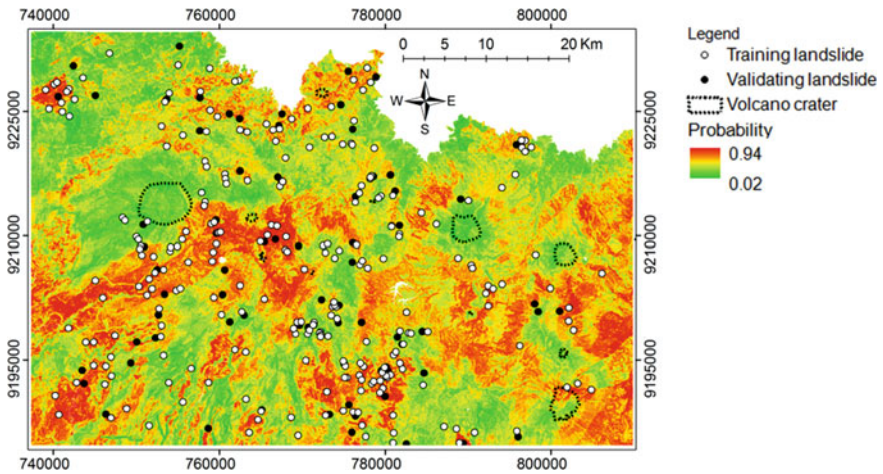


Fig. 8.8 Spatial probability map of volcanic mountain of West Java Province

methods, statistical approaches, and deterministic approaches (Carrara et al. 1995; Soeters and van Westen 1996; Guzetti et al. 1999; Ermini et al. 2005). A good overview of these techniques and their merits and demerits has been discussed by Soeters and van Westen (1996), Guzetti et al. (1999), Dai and Lee (2002), and so on. Among these techniques, statistical approach is considered the most appropriate method for landslide probability assessment in regional scale, primarily because it allows sufficient data collection.

In recent years, statistical approaches using bivariate or multivariate techniques are widespread in landslide probability assessment (Nandi and Shakoor 2009). The most frequently used statistical approach is multivariate technique, particularly the binary logistic regression. It analyzes the relationship of existence and nonexistence of a landslide with several predictors such as slope, aspect, curvature, road, river, soil type, lithology, and land use (Dai and Lee 2002; Ayalew and Yamagishi 2005; Garcia-Rodriguest 2008; Yalcin et al. 2011). Several researchers have successfully applied binary logistic regression for producing landslide probability maps such as Chang et al. (2007), Lee and Pradhan (2007), Garcia-Rodriguest (2008), Nandi and Shakoor (2009), Pradhan (2010), Choi et al. (2012), Bai et al. (2010), Yalcin et al. (2011), and Dahal et al. (2012). We used landslide database of West Java to illustrate spatial probability of landslide by using logistic regression. The regression model considered topographical parameters (e.g., slope, aspect, relief, distance to river), geological parameters (lithology, distance to thrust and fault, distance to volcanic crater), and anthropogenic parameters (distance to road and land use). The spatial probability map is presented in Fig. 8.8.

8.4.5 Temporal Probability of Landslides

Landslide hazard assessment requires an estimation of the temporal probability of landslide. We cannot analyze temporal aspect of hazard through the interpretation of single set of aerial photographs. It only can be achieved by using multi-temporal inventory map which allows us to estimate the frequency of landslide occurrence. We proposed archive inventory as an example for calculating frequency of landslide event. The landslide data were collected and documented from Wonosari Village office which include the 33-year period from 1978 to 2011 (51 landslide events).

The main assumption of temporal probability of landslide is that landslide can be considered as independent random point events in time (Crovelli 2000). Mathematically, the probability of landslide occurrence during time t is:

$$P_N = P[N(t) \geq 1] \quad (8.4)$$

where $N(t)$ is the number of landslides that occur during time t in the investigated area.

Two probability models are commonly used to investigate the occurrence of independent random point events in time, i.e., Poisson model and binomial model (Crovelli 2000; Onoz and Bayazit 2001). The Poisson model is the most frequently used to assess the temporal probability of landslide (e.g., Crovelli 2000; Coe et al. 2000; Guzetti 2000; Corominas and Moya 2008) because it considers naturally continuous landslide data (Guzetti et al. 2005). Crovelli (2000) adopted the Poisson model to develop mathematical model for the temporal occurrence of landslides as shown in Eq (8.5).

$$P[N(t) = n] = \exp(-\lambda t) \frac{(\lambda t)^n}{n!} \quad n = 0, 1, 2, \dots \quad (8.5)$$

where $P[N(t) = n]$ is the probability of experiencing n landslides during time t , and λ is the estimated average rate of occurrence of landslides which corresponds to $1/\mu$, with μ the estimated mean recurrence interval between successive failure events. The variables λ and μ can be obtained from a historical catalogue of landslide events or from a multi-temporal landslide inventory map. The probability of experiencing one or more landslides during time t (exceedance probability) is as follows:

$$P(N(t) \geq 1) = 1 - P[N(t) = 0] = 1 - \exp(-\lambda t) \quad (8.6)$$

$$P = (N(t) \geq 1) = 1 - \exp(-t/\mu) \quad (8.7)$$

By adopting a Poisson model (Eqs. 8.6 and 8.7), we computed the exceedance probability of having one or more landslides in the Wonosari Village. Figure (8.9) shows that the probability of having one or more slope landslide events increases

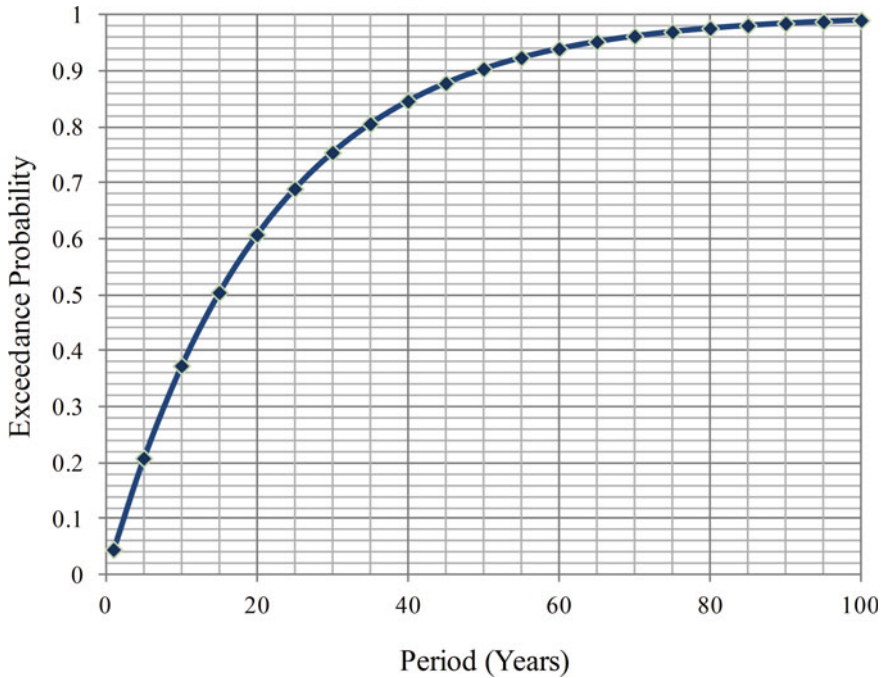


Fig. 8.9 Exceedance probability of landslide events which is obtained by adopting Poisson model using history inventory of Wonosari Village of Yogyakarta Province

with time. Temporal probability map can be produced for different periods, e.g., 5–50 years, and they will be applied to assess landslide hazard (as P_N in Eq. 8.2).

8.5 A Proposed Method of Landslide Inventory

A regional and detail landslide hazard assessment in Indonesia related with the availability of data. We discussed the main difficulties in acquiring and collecting landslide data in Indonesia in the previous heading. For example, aerial photographs of an area are available, but it is not the multi-year images, or there is no landslide archive. On the contrary, there is an archive of landslide covering several years, but the spatial data (aerial photograph or satellite image) are not available. The landslide archive generally contains information of landslide such as village-based location, date and time occurrence, name of victims, and material losses. It is provided in the village offices (e.g., inventory of Wonosari Village), where it was made by local government for a long period. The main purpose of this archiving is to inform to government so the aid, foods, and cloths can be distributed easily to victims.

In 2006, Disaster Management National Agency initiated to create a disaster database for whole Indonesia through DIBI data (<http://dibi.bnppb.go.id>), and it was recorded as good achievement for landslide studies in Indonesia. The DIBI database includes general information such as location (district-based), date of event, fatalities, injuries, and material losses for extreme landslide occurrences. The slope failures are not registered in this database. Producing hazard map that predicts the probability of landslide size, time, and location is not possible by relying on the DIBI database. Furthermore, it is only appropriate for small scale (<1:200.000) of inventory. A multi-scale of landslide inventories (obtained from archive of the national, regional, and village level) should be established for different purpose of land-use management. Urban spatial planning which considers the landslide prone areas only appropriate when the hazard map is produced by using the detailed spatial and temporal landslide data. Here, the DIBI database is only appropriate for landslide hazard mapping in regional or national scale. While, the national and regional land-use planning may can be conducted by using the DIBI database. It facilitates decision makers in developing policies for disaster risk reduction. Either traditional method of inventory or innovative techniques can be adopted to improve the landslide map in Indonesia.

We would propose the landslide archives in village level as basic geomorphological field mapping for producing a complete landslide inventory in Indonesia. Landslides or slope movements are natural phenomena, and they become disaster because of the presence of human activity so we consider only around populated areas in the proposed method. The proposed method may overcome the drawbacks of the use of existing methods. By referring the local archives, surveyors will visit the landslide location. People who live around the landslide location are asked to describe the landslide events by following the guidelines as seen in the Appendix 8.1. Based on information, landslide dimensions are reconstructed including geometry of landslide, typology, and material losses. Local communities are always involved during the landslide mapping so it is called 'participatory method.' This method is useful to avoid incomplete landslide inventory (i.e., smaller landslide are not included) due to various degrees of modification by erosion processes, anthropogenic activities, and vegetation growth. The recent condition should be photographed for laboratory investigation.

Later, landslides are recognized in the field must be transferred into paper. This activity is error-prone because the absolute coordinates of the landslide boundaries are seldom unavailable. To minimize the error, topographic and morphological features (e.g., river, road, and building) can be used as base maps to place the landslide boundaries (Malamud et al. 2004). The scarps, failed and moved masses, direction of mass movement, length, and breadth are also marked during mapping. After placing the landslides on the topographic map, digitalization of landslide maps is conducted in GIS environment. Any vector-based system in GIS can be used for the analysis of landslide dimension such as landslide areas, perimeter of landslide polygons, and length and breadth of landslide. Figure (8.10) illustrates the main idea of participatory-based inventory mapping.

As mentioned, hazard analysis presents spatial and temporal probability of landslide events. The temporal aspect of future events is not easy to be assessed

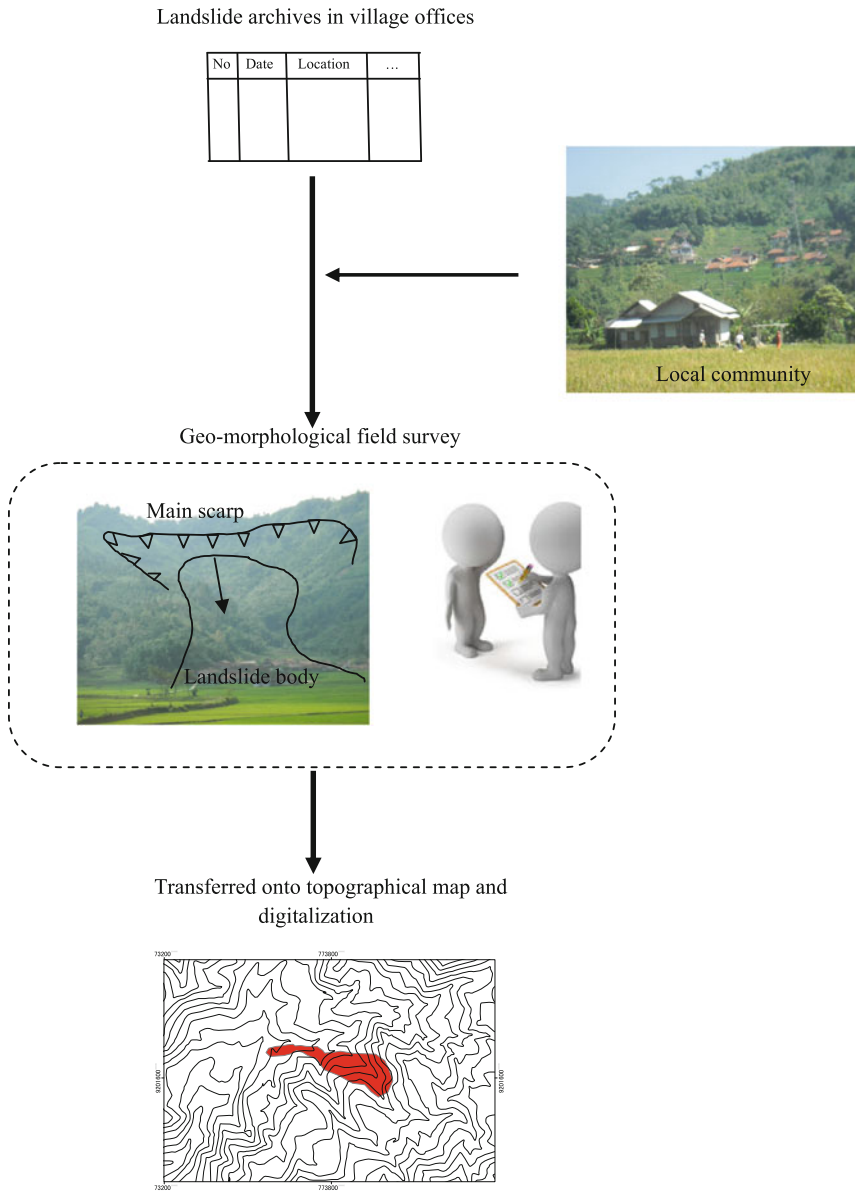


Fig. 8.10 A proposed method of landslide inventory for Indonesia

with single-set landslide data. The proposed inventory method includes temporal aspect of landslide because it is obtained from several periods of landslide event (multi-year). It also can avoid missing information of landslide due to the natural

condition (e.g., dense forest, vegetation growth) and human intervention (e.g., road construction, agricultural practices) on the landslide areas. Hence, the proposed method can be used to assess landslide hazard with the analytical procedure as seen in example (Sects. 8.4.3–8.4.4).

8.6 Conclusion

Landslide is one of the major natural disasters in Indonesia due to the extreme geomorphological condition and humid tropical climate associated with heavy rainfall that has often claimed life and property. Mitigation efforts can minimize the loss of human life and property caused by landslide disaster. Relocation of resident and structural methods of mitigation are not easy to be conducted in Indonesia. Hazard analysis that produces a map of potential disaster is the most required to mitigate the effect of disaster in the country. It is a basic tool for designing early warning system, preparedness activities, and other element of mitigation, as well as land-use management. The definition of hazard by Varnes (1984) includes temporal and spatial probability assessment. Due to lack of complete inventory, landslide hazard could not be assessed in Indonesia. Either conventional method or innovative techniques of inventory are not applicable for landslide mapping in the country because of the natural condition (dense forest area) and the limited human and economic resources. Archive inventory derived from the database of local government was proposed as basic information for geomorphological field mapping. It would produce multi-temporal inventory that can be used for assessing temporal probability of landslide. The completeness of landslide inventory would be acquired by involving the participation of local community during the field survey, and thus, the spatial probability and landslide size can be analyzed.

Appendix 1

Table for geomorphological field checking in the proposed method of landslide inventory

NAME OF RESPONDENT		:					
I	LOCATION	:					
	Village	:					
	District	:					
	Regency	:					
	Coordinate (x, y)	:					
	Information of coordinate (e.g. crown, toe, foot, etc.)	:					
	Elevation (m)	:					
	Number of photo	:					
	Photography of direction	:					
	Information of photo	:					
II	DATE OF OCCURENCE	:					
	Date/month/year	:					
	Local calendar	:					
	Time	:					
III	TIPOLOGY OF LANDSLIDE						
	Material of sliding	: 1) Rock		2) Earth		3) Debris	
	Process	: 1) Fall		2) Topple		3) Rotational slide	
				4) Slide		5) Lateral spread	
		7) Other		(.....)			
	Speed of sliding	: 1) High		2) Low			
	Slope of terrain (deg)	:					
	Landuse	: 1) Forest		2) Shrub		3) Settlement	
				4) Rainfed rice		5) Paddy field	
				6) Other			
	Type of vegetation	:					
	Cause of landslide	: 1) Rainfall		2) Earthquake		3) other	
IV	GEOMETRY OF LANDSLIDE						
	Length (m)	: L _r		L _d			
	Breadth (m)	: W _r		W _d			
	Depth (m)	: D _r		D _d			
	Volume (m ³)	: $\frac{1}{6} \pi L_d W_d D_d$					

References

- Antonini G, Ardizzone F, Cardinali M, Galli M, Guzzetti F, Reichenbach P (2002) Surface deposits and landslide inventory map of the area affected by the 1997 Umbria–Marche earthquakes. In: Guzzetti F, Mondini AC, Cardinali M, Fiorucci F, Santangelo M, Chang K-T (2012) Landslide inventory maps: new tools for an old problem. *Earth Sci Rev* 112:42–66. doi:[10.1016/j.earscirev.2012.02.001](https://doi.org/10.1016/j.earscirev.2012.02.001)
- Antonini G, Ardizzone F, Cacciano M, Cardinali M, Castellani M, Galli M, Guzzetti F, Reichenbach P, Salvati P (2002) In: Guzzetti F, Mondini AC, Cardinali M, Fiorucci F, Santangelo M, Chang K-T (2012) Landslide inventory maps: new tools for an old problem. *Earth Sci Rev* 112:42–66. doi:[10.1016/j.earscirev.2012.02.001](https://doi.org/10.1016/j.earscirev.2012.02.001)
- Ardizzone F, Cardinali M, Galli M, Guzzetti F, Reichenbach P (2007) Identification and mapping of recent rainfall-induced landslides using elevation data collected by airborne Lidar. *Nat Hazards Earth Syst Sci* 7:637–650
- Ayalew L, Yamagishi H (2005) The application of GIS based logistic regression for landslide susceptibility mapping in Kakudo-Yohiko Mountains Central Japan. *Geomorphology* 65:15–31. doi:[10.1016/j.enggeo.2005.08.004](https://doi.org/10.1016/j.enggeo.2005.08.004)
- Bai S-B, Wong J, Lu G-N, Zhou P, Hou S-S, Xu S-N (2010) GIS-based logistic regression for landslide susceptibility mapping of the Zhongxian segment in the three Gorges area, China. *Geomorphology* 115:23–31. doi:[10.1016/j.geomorph.2009.09.025](https://doi.org/10.1016/j.geomorph.2009.09.025)
- Blahut J, van Westen CJ, Sterlacchini S (2010) Analysis of landslide inventories for accurate prediction of debris-flow source areas. *Geomorphology* 109:36–51. doi:[10.1016/j.geomorph.2010.02.017](https://doi.org/10.1016/j.geomorph.2010.02.017)
- Booth AM, Roering JJ, Perron JT (2009) Automated landslide mapping using spectral analysis and high-resolution topographic data: Puget Sound lowlands, Washington, and Portland Hills, Oregon. *Geomorphology* 109:132–147. doi:[10.1016/j.geomorph.2009.02.027](https://doi.org/10.1016/j.geomorph.2009.02.027)
- Brardinoni F, Slaymaker O, Hassan MA (2003) Landslide inventory in a rugged forested watershed: a comparison between air-photo and field survey data. *Geomorphology* 54:179–196
- Brunsdon D (1985) Landslide types, mechanisms, recognition, identification. In: Guzzetti F, Mondini AC, Cardinali M, Fiorucci F, Santangelo M, Chang K-T (2012) Landslide inventory maps: new tools for an old problem. *Earth Sci Rev* 112:42–66. doi:[10.1016/j.earscirev.2012.02.001](https://doi.org/10.1016/j.earscirev.2012.02.001)
- Cardinali M, Guzzetti F, Brabb EE (1990) Preliminary map showing landslide deposits and related features in New Mexico U.S. geological survey open file. Report 90(293):4
- Cardinali M, Reichenbach P, Guzzetti F, Ardizzone F, Antonini G, Galli M, Cacciano M, Castellani M, Salvati P (2001) A geomorphological approach to the estimation of landslide hazards and risks in Umbria, Central Italy. *Nat Hazards Earth Syst Sci* 2:57–72
- Carrara A, Cardinali M, Guzzetti F, Reichenbach P (1995) GIS technology in mapping landslide hazard. In: Piancentini D, Troiani F, Soldati M, Notarnicola C, Savelli D, Schneiderbauer S, Strada C (2012) Statistical analysis for assessing shallow-landslide susceptibility in South Tyrol (South-eastern Alps, Italy). *Geomorphology* 151–152:196–206. doi:[10.1016/j.geomorph.2012.02.003](https://doi.org/10.1016/j.geomorph.2012.02.003)
- Carson MA, Kirkby MJ (1972) Hillslope form and process. Cambridge University Press. 475 pp
- Cepeda J, Smebye H, Vangelsten B, Nadim F, Muslim D (2010) Landslide risk in Indonesia. Global assessment report on disaster risk reduction, ISDR
- Chacón J, Irigaray C, Fernández T, El HR (2006) Engineering geology maps: landslides and geographical information systems. *Bull Eng Geol Environ* 65:341–411. doi:[10.1007/s10064-006-0064-z](https://doi.org/10.1007/s10064-006-0064-z)
- Chang K-T, Chiang S-H, Hsu M-L (2007) Modeling typhoon and earthquake-induced landslides in a mountainous watershed using logistic regression. *Geomorphology* 89:335–347. doi:[10.1016/j.geomorph.2006.12.011](https://doi.org/10.1016/j.geomorph.2006.12.011)

- Choi J, Oh H-J, Lee C, Lee S (2012) Combining landslide susceptibility maps obtained from frequency ratio, logistic regression, and artificial networks models using ASTER images and GIS. *Eng Geol* 124:12–23. doi:[10.1016/j.enggeo.2011.09.011](https://doi.org/10.1016/j.enggeo.2011.09.011)
- Christanto N, Hadmoko DS, van Westen CJ, Lavigne F, Sartohadi J, Setiawan MA (2009) Characteristic and behavior of rainfall induced landslides in Java island, Indonesia: an overview. *Geophys Res Abstr* 11:EGU2009-4069-7
- Coe JA, Michael JA, Crovelli RA, Savage WZ (2000) Preliminary map showing landslide densities, mean recurrence intervals, and exceedance probabilities as determined from historic records, Seattle, Washington. United States geological survey open file report 00-303
- Corominas J, Moya J (2008) A review of assessing landslide frequency for hazard zoning purposes. *Eng Geol* 102:193–213. doi:[10.1016/j.enggeo.2008.03.018](https://doi.org/10.1016/j.enggeo.2008.03.018)
- Crovelli RA (2000) Probability models for estimation of number and costs of landslides. USGS Denver, Colorado
- Cruden DM, Varnes DJ (1996) Landslide types and processes. In: Guzzetti F, Mondini AC, Cardinali M, Fiorucci F, Santangelo M, Chang K-T (2012) Landslide inventory maps: new tools for an old problem. *Earth Sci Rev* 112:42–66. doi:[10.1016/j.earscirev.2012.02.001](https://doi.org/10.1016/j.earscirev.2012.02.001)
- Dahal RK, Hasegawa S, Bhandary NP, Poudel PP, Nonomura A, Yatabe R (2012) A replication of landslide hazard mapping at catchment scale. *Geomat Nat Hazards Risk* 3(2):161–192. doi:[10.1080/19475705.2011.629007](https://doi.org/10.1080/19475705.2011.629007)
- Dai FC, Lee CF (2002) Landslide characteristics and slope instability modeling using GIS, Lantau Island Hongkong. *Geomorphology* 42:213–228. PII: S0169-555X(01)00087-3
- Dikau R, Cavallin A, Jäger S (1996) Databases and GIS for landslide research in Europe. *Geomorphology* 15:227–239. doi:[0169-555X\(95\)00072.0](https://doi.org/10.1016/0169-555X(95)00072.0)
- Dumanya TY, Tolga Can T, Emrea Ö, Kecera M, Dogana A, Ates X, Durmaza S (2005) Landslide inventory of northwestern Anatolia, Turkey. *Eng Geol* 77:99–114. doi:[10.1016/j.enggeo.2004.08.005](https://doi.org/10.1016/j.enggeo.2004.08.005)
- Ermioni L, Catani F, Casagli N (2005) Artificial neural networks applied to landslide susceptibility. *Geomorphology* 66:327–343. doi:[10.1016/j.geomorph.2004.09.025](https://doi.org/10.1016/j.geomorph.2004.09.025)
- Fell R, Corominas J, Bonnard C, Cascini L, Leroi E, Savage WZ (2008) Guidelines for landslide susceptibility, hazard, risk zoning for land-use planning. *Eng Geol* 102:99–111. doi:[10.1016/j.enggeo.2008.03.014](https://doi.org/10.1016/j.enggeo.2008.03.014)
- Fiorucci F, Cardinali M, Carlà R, Rossi M, Mondini AC, Santurri L, Ardizzone F, Guzzetti F (2011) Seasonal landslide mapping and estimation of landslide mobilization rates using aerial and satellite images. *Geomorphology* 129:59–70. doi:[10.1016/j.geomorph.2011.01.013](https://doi.org/10.1016/j.geomorph.2011.01.013)
- Galli M, Ardizzone F, Cardinali M, Guzzetti F, Reichenbach P (2008) Experimental acute renal failure. Dissertation, University of California. Comparing landslide inventory maps. *Geomorphology* 94:268–289. doi:[10.1016/j.geomorph.2006.09.023](https://doi.org/10.1016/j.geomorph.2006.09.023)
- Garcia-Rodriguez MJ, Malpica JA, Benito B, Diaz M (2008) Susceptibility assessment of earthquake-triggered landslides in El Salvador using logistic regression. *Geomorphology* 95:172–191. doi:[10.1016/j.geomorph.2007.06.001](https://doi.org/10.1016/j.geomorph.2007.06.001)
- Glade T (1998) Establishing the frequency and magnitude of landslide-triggering rainstorm events in New Zealand. *Environ Geol* 35:160–174
- Glade T, Anderson M, Crozier MJ (2005) *Landslide hazard and risks*. Wiley, NJ. doi: [10.1002/9780470012659](https://doi.org/10.1002/9780470012659)
- Glenn NF, David R, Streutker DR, Chadwick DJ, Thackray GD, Dorsch SJ (2006) Analysis of LiDAR-derived topographic information for characterizing and differentiating landslide morphology and activity. *Geomorphology* 73:131–148. doi:[10.1016/j.geomorph.2005.07.006](https://doi.org/10.1016/j.geomorph.2005.07.006)
- Godt JW, Baum RL, Savage WZ, Salciarini D, Schulz WH, Harp EL (2008) Transient deterministic shallow landslide modeling: requirements for susceptibility and hazard assessments in a GIS framework. *Eng Geol* 102:214–226. doi:[10.1016/j.enggeo.2008.03.019](https://doi.org/10.1016/j.enggeo.2008.03.019)
- Guhtrie RH, Evans SG (2004) Analysis of landslide frequencies and characteristics in a natural system, coastal British Columbia. *Earth Surf Process Landforms* 29:1321–1339. doi:[10.1002/esp.1095](https://doi.org/10.1002/esp.1095)

- Guzzetti F, Carrara A, Cardinali M, Peinchenbach P (1999) Landslide hazard evaluation, a review of current techniques and their application in a multi-scale study, Central Italy. *Geomorphology* 31:181–216. PII: S0169-555x(99)00078-1
- Guzzetti F, Cardinali M, Reichenbach P, Carrara A (2000) Comparing landslide maps: a case study in the upper Tiber River Basin, Central Italy. *Environ Manag* 25(3):247–363
- Guzzetti F, Malamud BD, Turcotte DL, Reichenbach P (2002) Power-law correlations of landslide areas in central Italy. *Earth Planet Sci Lett* 195:169–183
- Guzzetti F, Reichenbach P, Cardinali M, Galli M, Ardizzone F (2005) Probabilistic landslide hazard assessment at the basin scale. *Geomorphology* 72:272–299
- Guzzetti F, Galli M, Reichenbach P, Ardizzone F, Cardinali M (2006) Landslide hazard assessment in the Collazzone area, Umbria, central Italy. *Nat Hazards Earth Syst Sci* 6:115–131
- Guzzetti F, Mondini AC, Cardinali M, Fiorucci F, Santangelo M, Chang K-T (2012) Landslide inventory maps: new tools for an old problem. *Earth Sci Rev* 112:42–66. doi:[10.1016/j.earscirev.2012.02.001](https://doi.org/10.1016/j.earscirev.2012.02.001)
- Hadmoko DS, Lavigne F, Sartohadi J, Hadi P, Winaryo (2010) Landslide hazard and risk assessment and their application in risk management and landuse planning in eastern flank of Menoreh Mountains, Yogyakarta province, Indonesia. *Nat Hazards* 54:623–642. doi:[10.1007/s11069-009-9490-0](https://doi.org/10.1007/s11069-009-9490-0)
- Hutchinson JN (1968) Mass Movement. The encyclopedia of geomorphology. R.W. Fairbridge, Reinold, pp 688–695
- Karnawati D, Fathani TF, Wilopo W, Setianto A, Andayani B (2006) Promoting the hybrid socio-technical approach for effective disaster risk reduction in developing countries. doi:[495/DMAN110161](https://doi.org/495/DMAN110161)
- Kasai M, Ikeda M, Asahina T, Fujisawa K (2009) LiDAR-derived DEM evaluation of deep-seated landslides in a steep and rocky region of Japan. *Geomorphology* 113:57–69. doi:[10.1016/j.geomorph.2009.06.004](https://doi.org/10.1016/j.geomorph.2009.06.004)
- Kirschbaum DD, Adler R, Hong Y, Hill S, Lerner-Lam L (2009) A global landslide catalog for hazard applications-methods, results and limitations. *Nat Hazards*. doi:[10.1007/s11069-009-9401-4](https://doi.org/10.1007/s11069-009-9401-4)
- Lee S, Pradhan B (2007) Landslide hazard mapping at Selangor, Malaysia using frequency ratio and logistic regression models. *Int Consort Landslide* 4(1):33–41. doi:[10.1007/s10346-006-0047-y](https://doi.org/10.1007/s10346-006-0047-y)
- Malamud BD, Turcotte DL, Guzzetti F, Reichenbach P (2004) Landslide inventories and their statistical properties. *Earth Surf Process Landforms* 29:687–711. doi:[10.1002/esp.1064](https://doi.org/10.1002/esp.1064)
- Marcelino EV, Formaggio AR, Maeda EE (2009) Landslide inventory using image fusion techniques in Brazil. *Appl Earth Obs Geoinf* 11:181–191. doi:[10.1016/j.jag.2009.01.003](https://doi.org/10.1016/j.jag.2009.01.003)
- Marfai MA, King L, Singh LP, Mardiatno D, Sartohadi J, Hadmoko DS, Dewi A (2008) Natural hazards in Central Java Province, Indonesia: an overview. *Environ Geol* 56:335–351. doi:[10.1007/s00254-007-1169-9](https://doi.org/10.1007/s00254-007-1169-9)
- Martha TR, Kerle N, Jetten V, van Westen CJ, Kumar KV (2010) Characterising spectral, spatial and morphometric properties of landslides for semi-automatic detection using object-oriented methods. *Geomorphology* 116:24–36. doi:[10.1016/j.geomorph.2009.10.004](https://doi.org/10.1016/j.geomorph.2009.10.004)
- McKeena J, Roering J (2004) Objective landslide detection and surface morphology mapping using high-resolution airborne laser altimetry. *Geomorphology* 57:331–351. doi: [10.1016/S0169-555X\(03\)00164-8](https://doi.org/10.1016/S0169-555X(03)00164-8)
- Muraoka H, Nasution A, Simanjuntak J, Dwipa S, Takahashi M, Takahashi H, Matsuda K, Sueyoshi Y (2004) Geology and geothermal systems in the Bajawa volcanic rift zone, Flores, Eastern Indonesia. In: proceedings world geothermal congress 2005 Antalya, Turkey, 24–29 Apr 2005
- Nandi A, Shakoor A (2009) A GIS-based landslide susceptibility evaluation using bivariate and multivariate statistical analyses. *Eng Geol* 110:11–20. doi:[10.1016/j.enggeo.2009.10.001](https://doi.org/10.1016/j.enggeo.2009.10.001)
- Önöz B, Bayazit M (2001) Effect of the occurrence process of the peaks over threshold on the flood estimates. *J Hydrol* 24:86–96. PII: S0022-1694(01)00330-4

- Parise M (2001) Landslide mapping techniques and their USA in the assessment of the landslide hazard. *Phys Chem Earth (C)* 26(9):697–703. doi:[10.1016/j.pce.2001.01.014](https://doi.org/10.1016/j.pce.2001.01.014)
- Pradhan B (2010) Remote sensing and GIS-based landslide hazard analysis and cross-validation using multivariate logistic regression model on three test areas in Malaysia. *Adv Space Res* 45:1244–1256. doi:[10.1016/j.asr.2010.01.006](https://doi.org/10.1016/j.asr.2010.01.006)
- Razak KA, Straatsma MW, van Westen CJ, Malet J-P, de Jong SM (2011) Airborne laser scanning of forested landslides characterization: terrain model quality and visualization. *Geomorphology* 126:186–200. doi:[10.1016/j.geomorph.2010.11.003](https://doi.org/10.1016/j.geomorph.2010.11.003)
- Reichenbach P, Guzzetti F, Cardinali M (1998) Map of sites historically affected by landslides and floods in Italy, 2nd ed. CNR Gruppo Nazionale per la Difesa dalle Catastrofi Idrogeologiche Publication n. 1786
- Reichenbach P, Galli M, Cardinali M, Guzzetti F, Ardizzone F (2005) Geomorphological mapping to assess landslide risk: concepts, methods and applications in the Umbria Region of central Italy. *Landslide risk assessment*. In: Anderson MG, Crozier MJ (eds) Glade T. Wiley, West Sussex
- Salvati P, Guzzetti F, Reichenbach P, Cardinali M, Stark CP (2003) Map of landslides and floods with human consequences in Italy, CNR Gruppo Nazionale per la Difesa dalle Catastrofi Idrogeologiche Publication n. 2822
- Salvati P, Balducci V, Bianchi C, Guzzetti F, Tonelli G (2009) A WebGIS for the dissemination of information on historical landslides and floods in Umbria, Italy. *GeoInformatica* 13:305–322
- Soeters R, Van Westen CJ (1996) Slope instability recognition, analysis, and zonation. In: Piancentini D, Troiani F, Soldati M, Notarnicola C, Savelli D, Schneiderbauer S, Strada C (2012) Statistical analysis for assessing shallow-landslide susceptibility in South Tyrol (South-eastern Alps, Italy). *Geomorphology* 151–152:196–206. doi:[10.1016/j.geomorph.2012.02.003](https://doi.org/10.1016/j.geomorph.2012.02.003)
- Stark CP, Hovius N (2001) The characterization of landslide size distributions. *Geophys Res Lett* 28(6):1091–1094. doi:[10.1029/2000GL008527](https://doi.org/10.1029/2000GL008527)
- Van Den Eeckhaut M, Poesen J, Verstraeten G, Vanacker V, Moeyersons J, Nyssen J, Van Beek LPH (2005) The effectiveness of hillshade maps and expert knowledge in mapping old deep-seated landslides. *Geomorphology* 67:351–363. doi:[10.1016/j.geomorph.2004.11.001](https://doi.org/10.1016/j.geomorph.2004.11.001)
- Van Den Eeckhaut M, Poesen J, Verstraeten G, Vanacker V, Nyssen J, Moeyersons J, van Beek LPH, Vandekerckhove L (2007) Use of LIDAR-derived images for mapping old landslides under forest. *Earth Surf Process Landforms* 32:754–769. doi:[10.1002/esp.1417](https://doi.org/10.1002/esp.1417)
- van Westen CJ, Van Asch TWJ, Soeters R (2005) Landslide hazard and risk zonation; why is it still so difficult? *Bull Eng Geol Env* 65(2):167–184. doi:[10.1007/s10064-005-0023-0](https://doi.org/10.1007/s10064-005-0023-0)
- van Westen CJ, Castellanos E, Kuriakose SL (2008) Spatial data for landslide susceptibility, hazard, and vulnerability assessment: an overview. *Eng Geol* 102:112–131. doi:[10.1016/j.engeo.2008.03.010](https://doi.org/10.1016/j.engeo.2008.03.010)
- Varnes DJ (1978) Slope movement types and processes. In: Guzzetti F, Mondini AC, Cardinali M, Fiorucci F, Santangelo M, Chang K-T (2012) *Landslide inventory maps: new tools for an old problem*. *Earth-Sci Rev* 112:42–66. doi:[10.1016/j.earscirev.2012.02.001](https://doi.org/10.1016/j.earscirev.2012.02.001)
- Varnes DJ (1984) *Landslide hazard zonation: a review of principles and practice*. UNESCO Press, Paris
- Yalcin A, Reis S, Aydinoglu AC, Yomralioglu T (2011) A-GIS based comparative study of frequency ratio, analytical hierarchy process, bivariate statistics and logistic regression for landslide susceptibility mapping in Trabzon, NE Turkey. *CATENA* 85:274–287. doi:[10.1016/j.catena.2011.01.014](https://doi.org/10.1016/j.catena.2011.01.014)

Part IV
Application and Case Studies

Chapter 9

Landslide Susceptibility Mapping Based on Aerial Photograph Interpretation Inventory for Tegucigalpa, Honduras: An Application of the Matrix Method

Elias Garcia-Urquia and Hiromitsu Yamagishi

Abstract Tegucigalpa, the capital city of Honduras, is being affected by landslides every year during the rainy season. Although intense rainfall events are likely to be the main trigger of these landslides, anthropogenic disturbances significantly contribute to predispose the populated slopes to failures. Unfortunately, the lack of geotechnical, hydrological and geomorphological data for the study area limits the range of methods available for landslide susceptibility mapping. However, this study summarizes the employment of the matrix method for the development of a landslide susceptibility map; this method was chosen due to its successful application in other data-scarce regions. A landslide inventory based on an aerial photograph interpretation carried out in 2013 by the Japan International Cooperation Agency was used. The study area was divided into cells, and for each cell, the relationship between landslide occurrence and three variables—slope angle, geology and distance to rivers—was determined. For each of the variables, different classes were established. Cells having the same combination of classes were grouped into Unique Condition Units. The Landslide Susceptibility Index, which relates the number of landslide cells to the total number of cells in each Unique Condition Unit, was determined. Based on this index, the landslide susceptibility map was developed and five susceptibility classes were established. Two measures were determined to evaluate the map's performance in depicting landslide-prone areas. On the one hand, the success rate curve shows that the map has an efficiency

E. Garcia-Urquia (✉)

Department of Civil Engineering, National Autonomous University of Honduras Ciudad Universitaria, Tegucigalpa, Honduras
e-mail: elias.urquia82@gmail.com

H. Yamagishi

Shin Engineering Consultant Co. Ltd., 2-8-30, Sakaedori, Shiroishi-ku, Sapporo 003-0021, Japan

© Springer Japan KK 2017

H. Yamagishi and N.P. Bhandary (eds.), *GIS Landslide*,
DOI 10.1007/978-4-431-54391-6_9

of 80%. On the other hand, the Degree of Fit reveals that 73% of the landslide cells are successfully classified as having “very high” and “high” susceptibility classes, while 8% of the landslide cells belong to the “low” and “very low” susceptibility classes. Some important observations about the applicability and limitations of this landslide susceptibility map are also provided.

Keywords Landslide susceptibility index · Matrix method · GIS · Tegucigalpa · Urban landslides

9.1 Introduction

Landslide susceptibility maps are constructed to indicate the areas prone to landslide occurrence in a given area. The reliability of these maps depends on the accuracy of the input data as well as the applicability of the method chosen to process the input data. The input data consist of a landslide inventory and the explanatory variables that are associated with landslide occurrence. Event-based landslide inventory maps are usually compiled after an anomalous triggering event and provide valuable landslide data (Ghosh et al. 2012). However, some authors have suggested that multi-temporal landslide information provides a better basis for the analysis of landslide occurrence (van Westen et al. 2008), since different triggers may induce different types of landslides. Regarding the explanatory variables, there is a wide range of geological, hydrological, geomorphological, geotechnical and even social variables that have been analyzed by different research groups. Each study area is unique, so the connection of the chosen variables to landslide occurrence must be evaluated; for this purpose, several methods have been proposed in the scientific literature to produce landslide susceptibility maps (Pardeshi et al. 2013). These methods include logistic regression (Ayalew and Yamagishi 2005), artificial neural networks (ANN; Pradhan and Lee 2010), frequency ratio (Lee and Sambath 2006), the matrix method (Irigaray et al. 2007), analytical hierarchy process (AHP) (Ayalew et al. 2005; Yagi et al. 2009), the weighted linear combination method (Ayalew et al. 2004) and the weights of evidence method (Dahal et al. 2008).

This study summarizes the use of the matrix method for the construction of a landslide susceptibility map for Tegucigalpa, the capital city of Honduras. The matrix method was chosen due to its successful application in several regions in Spain (Costanzo et al. 2012; Irigaray et al. 2007; Fernández et al. 2003; Jiménez-Perálvarez et al. 2009), UK (Cross 1998), Dominica and Jamaica (De Graff et al. 2012). In addition, because it calls for fewer variables than other statistical methods, this method is ideal for data-scarce regions (De Graff et al. 2012) such as

Tegucigalpa. The landslide susceptibility map was constructed upon a landslide inventory developed after an aerial photograph interpretation carried out in 2013 by the Japan International Cooperation Agency (JICA) and three environmental variables—slope angle, geology and distance to drainage—due to their strong connection to landslide occurrence in the study area.

9.2 Study Area

Tegucigalpa is located in a mountainous basin in the southern central part of Honduras (Fig. 9.1a, b). To date, it occupies an area of 150 km² and is inhabited by approximately 1.3 million people. For the past 40 years, Tegucigalpa has suffered from frequent landslide events due to its drastic urbanization toward the slopes and the social and economic vulnerability of its residents. During the rainy season (from May to October with sporadic rainfall events during April and November), there is an average annual rainfall of approximately 870 mm. Most of the landslides take place during the months of September and October, especially during the occurrence of hurricanes, such as Hurricane Mitch in 1998, and tropical storms (Garcia-Urquia and Axelsson 2014). In addition to the numerous intense rainfall events, the warm year-round temperatures (on average, between 19 and 23 °C) also contribute to the weathering of the different rock facies. The altitude of Tegucigalpa ranges between 900 and 1400 m above sea level. The city is particularly susceptible to landslides along the unvegetated margins of the surrounding flattened volcanic rocks and along the Choluteca River (which crosses Tegucigalpa from south to north and divides the city), its tributaries and the abundant creeks. Landslides are frequently occurring due to the erosion of slopes and artificial excavations and are being triggered by small rainfall events.

In recent years, the population increase pressure has led Tegucigalpa to an uncontrolled urban growth, and as a result, a big portion of its population has been residing on landslide-prone slopes and flood-prone areas (Angel et al. 2004). The lack of a proper urban plan with corresponding enforcement policies has allowed the rise of an illegal land market that offers low-cost housing options to the poorest in areas not suitable for construction (Pearce-Oroz 2005). The low income of many families living in Tegucigalpa has forced them to make use of inappropriate building techniques to construct their own households, sometimes employing low-quality materials or scraps from construction sites. Despite the constant warning evacuation calls during periods of intense rain, many families have to accept high levels of landslide risk, putting their lives and their few belongings in danger, rather than migrating to a more stable place. Figure 9.1 shows the precarious situation of four neighborhoods that have recently been affected by landslides.



◀**Fig. 9.1** **a** Location of Tegucigalpa, Honduras, in the Central American region. **b** Locations of the landslide-prone neighborhoods of Tegucigalpa. **c** C in Fig. 9.1b: In the Izaguirre neighborhood, to the northeast of the city, a total of 20 houses suffered damages due to a landslide episode in 2013. **d** D in Fig. 9.1b: The Los Pinos neighborhood, located in the southeastern part of the city, is constantly exposed to landslides in recent years due to the unfavorable physical conditions and the lack of a proper urban plan. **e** E in Fig. 9.1b: The social vulnerability of the residents of the Villanueva neighborhood, also located to the southeast of the city, has forced them to improvise retaining walls built from scrap in an attempt to reduce the damages produced by landslides. **f** F in Fig. 9.1b: The residents of the José Angel Ulloa neighborhood, to the northwest of the city, are in danger due to the continuous slope failures that threaten to destroy their fragile households. All photos were taken from El Heraldo newspaper: Fig. 9.1c was published on September 19, 2013, Fig. 9.1d and Fig. 9.1e were published on October 23, 2014, and Fig. 9.1f was published on June 30, 2015

9.3 Data

9.3.1 JICA-JSPS Aerial Photograph Interpretation Landslide Inventory Map

In 2011, JICA and the Japanese Society for the Promotion of Science (JSPS) began a project in Tegucigalpa focused on the capacity building for landslide hazard mapping based on aerial photograph interpretation. During the latter half of 2013, JICA experts trained students and staff members of two Honduran universities on aerial photograph interpretation using the color aerial photos that had been taken by JICA Honduras in March of the same year. The two Honduran universities are the Polytechnical University of Engineering (UPI, in its Spanish acronym) and the National Autonomous University of Honduras (UNAH, in its Spanish acronym). In 2014, an updated landslide inventory map containing recent landslide episodes occurring in 2008, 2011 and 2013 was provided to the local authorities (Yamagishi et al. 2014; UPI-JICA 2014). This map (Fig. 9.2) revealed that approximately 500,000 inhabitants living in 176 neighborhoods were at risk of landslides (El Heraldo 2014). Although the photograph interpretation yielded a total of 1528 landslide polygons, only 847 landslide polygons were considered in this analysis. These chosen polygons occupy an area of 8.95 km² and are plotted within the data extent of the explanatory variables (i.e., the urban area of Tegucigalpa in 2001).

9.3.2 Explanatory Variables

For this study, three natural factors have been chosen: slope angle, geology and distance to drainage. Slope angle is the most important factor in any landslide analysis, as it provides the potential energy that drives the downward movement of rock, soil or debris material, while the slope reaches a more stable position (Cross 1998). Concerning geology, despite the fact that very few physical tests have been

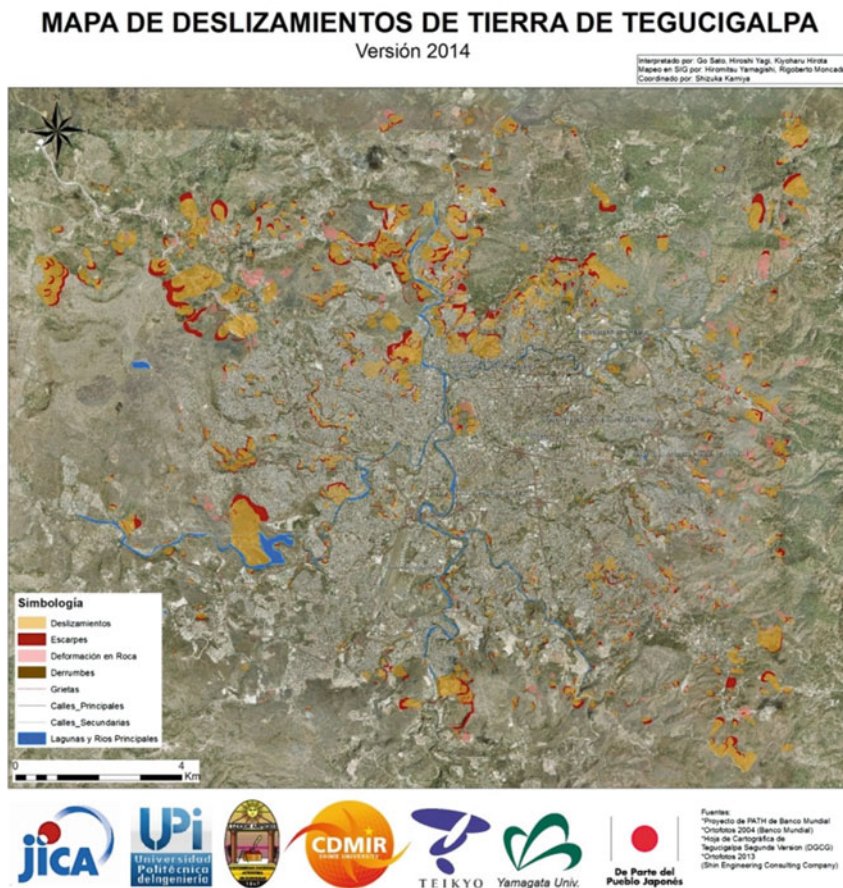


Fig. 9.2 Landslide inventory map based on the aerial photograph interpretation (UPI-JICA 2014)

performed to characterize the geological units in the study area, previous studies have shown that some geological units exhibit a higher propensity to slope failures than others (Harp et al. 2009; JICA 2002; Yamagishi et al. 2014). Meanwhile, the distance to drainage has been considered as an important factor in other landslide study areas (Akgun et al. 2008; Lee and Sambath 2006; Sützen and Doyuran 2004), and in the case of Tegucigalpa, it has been demonstrated that the undercutting of river banks has triggered several landslides in the past (e.g., during the passage of Hurricane Mitch (Harp et al. 2002)). In addition, although the distance to drainage appears to be a natural factor, it indirectly accounts for the anthropogenic actions carried out by the poorest sector in an attempt to build their weak households along the riverbanks. During the settlement, the slopes are affected by the removal of vegetation that contributes to its stability and by the uncontrolled loading.

Table 9.1 Slope angle classes

Class	Range (°)
1	0–5
2	5–10
3	10–15
4	15–20
5	20–25
6	25–30
7	>30

The data for the selected variables are based on a thorough and detailed field study carried out by JICA experts in 2001 after the passage of Hurricane Mitch in 1998 (JICA 2002):

- a. Slope angle: JICA’s topographic map, with contour lines at 2.5 m intervals, was used to construct a triangulated irregular network (TIN). This allowed the computation of the slope angle for every cell in the study area using ArcGIS. The fact that only 8% of the study area had slopes greater than 30° served as a guideline for the creation of seven subclasses; the last subclass particularly covers these steep slopes (see Table 9.1).
- b. Geology: JICA’s geologic map of the city, at a scale of 1:10,000, shows that Tegucigalpa is composed of Valle de Angeles formations in the Cretaceous period, the Matagalpa formations in the Paleogene period, the Padre Miguel group in the Tertiary period and Quaternary volcanic deposits. This map contains 21 different geologic units (see Table 9.2).
- c. Distance to drainage: As part of the flood analysis, JICA conducted a detailed survey that allowed the generation of spatial data for the four major rivers and streams of the city. Buffers of 50, 100, 150 and 200 m on either side of the drainage were created (see Table 9.3 and Fig. 9.3).

9.4 Method

To be able to employ the matrix method for the landslide susceptibility assessment of the study area, the landslide inventory and the data for the three environmental factors were converted into raster images in ArcGIS for the easiness in spatial data management. The study area was divided into a grid composed of 50 × 50 m cells, and a total of 40,000 cells were created. Each cell stored information regarding the presence or absence of landslides as well as information concerning the explanatory variables. Unique Condition Units (UCUs; Clerici et al. 2002) were then created to group those cells that share the same explanatory variables. The UCUs were divided into landslide cells and non-landslide cells. The Landslide Susceptibility Index (LSI) was calculated as:

Table 9.2 Geology classes (after JICA 2002)

Class	Unit	Description
1	Tcg	Ignimbrite and rhyolite lava equipped with the matrix of crystals of the glassy quartz and crystal feldspar of a violet color. The rock itself is very hard, it is strong in weathering and tends to form a steep cliff. Logic progresses and it is very easy to dissociate. When this rock is distributed on a layer with weak intensity, this rock serves as cap rock and it is easy to generate a landslide. The deterioration action is received locally, and in the portion, intensity is falling remarkably and it is easy to generate a slope failure
2	TM	It consists of tuff, tuff breccia and the andesite lava which presents a green color as its base. It is easy to weather and changes in the shape of clay easily near the surface of the earth. For this reason, it is easy to become the cause of a landslide
3	Qal	The latest alluvial sediment. It consists of clay, sand and boulders
4	River bank	Not available
5	Qe3	Lower terrace sediment: fan of sand and cobbles
6	Qan1	It is distributed over the low rank of Qan2. It consists of andesitic and rhyolitic tuff. Banded structure progresses. It is weak in weathering and easy to deteriorate in it. It becomes the cause of a landslide rarely
7	Qan2	It consists of andesite lava. Although the rock itself is precise hard, joint progresses and it is easy to dissociate massively. In the border part of a range, this stratum serves as cap rock and tends to cause a landslide
8	Tpm3	Ignimbritic sequence, upside member. Tuff of rhyolite of many colors. Some sedimentary rocks equipped with volcanic debris, tuff of quartz, andesite nature and andesitic tuff. This rock itself is massive and it is solid. When a stratum with weak intensity is distributed over the low rank of this stratum, it is easy to generate a landslide
9	Qe1	Higher terrace sediment. It mainly consists of sand and stones, and tuff layer is inserted. By oldest terrace deposits, the matrix is consolidated weakly
10	Krc	It consists of mudstone, siltstone, sandstone, thin conglomerate layer and thin limestone layer. Stratified structure is made. Its color is blackish brown. It is easy to weather and changes simply to earth and sand. It is the stratum which is easy to generate a landslide and a slope failure
11	Qe2b	Terrace sediment of middle rank. It consists of sand and stones. A matrix is not solid. An old fan or the sediment on the bottom of a river. It mainly consists of volcanic rock after the Tertiary. The color is from dark gray to gray
12	Qb	Lava of basalt (olivine slanting feldspar and scoria)
13	Tpm1	Member of an ignimbritic sequence low rank: tuff of rhyolite of many colors. Some sedimentary rocks equipped with volcanic debris, tuff of quartz, andesite nature and andesitic tuff
14	Qe2a	Terrace sediment of middle rank: It consists of sand, stones and silt. Tightness is good although a matrix is not solid. An old fan or bottom of river and the sediment of a lake. It mainly consists of rock of Valle de Angeles group and volcanic rock after the Tertiary. The color is from dark brown to blackish brown

(continued)

Table 9.2 (continued)

Class	Unit	Description
15	Kvn	Conglomeratic siliciclastic layers (with clast of metamorphic and volcanic rock and limestone). Brown to light red sandstone and some volcanic tuff. Stratified structure progresses partially. Its colors are thin red to dark purple. Although it is strong compared to Krc, the landslide is generated locally
16	Tpm2	Ignimbritic sequence middle member: tuff by which quartz andesite nature was divided by class by style rhyolite. Banded structure progresses and it becomes the cause of a layer slide
17	Tpml	Lahars (debris flow tuff) with clast of tertiary volcanic rocks and cretaceous sediments. It consists of debris and consolidated sandstone. It is hardly the cause of a landslide by massive and hard ones
18	Tep	It consists of rhyolitic tuff and conglomerate, sandstone and siltstone. It deposits in underwater environments, such as a river. Stratified structure progresses almost horizontally. It is easy to dissociate from a stratum side and may become the cause of a landslide in the part where the stratum inclines
19	Reservoir	Not available
20	Odt	It consists of debris of the stones which made the subject rhyolite with a diameter of 20 cm–3 m. It becomes the cause of a landslide rarely
21	Ti	Rhyolitic intrusive rock. Generally along with a dislocation, it is distributed, deterioration is given to the Valle de Angeles group, and it is easy to become the cause of a slope failure

Table 9.3 Distance to drainage classes

Class	Range (m)
1	0–50
2	50–100
3	100–150
4	150–200
5	>200

$$LSI_{UCU} = \frac{\text{number of landslide cells in the UCU}}{\text{total number of cells in the UCU}} * 100 \tag{9.1}$$

Figure 9.4 summarizes the employed methodology. A higher value of Landslide Susceptibility Index (LSI) indicates a higher susceptibility to landslides. To complete the susceptibility map, five susceptibility classes were created using the natural breaks classification method built in ArcGIS.

Two means of performance evaluation were used in this analysis. The first one is the area under the success rate curve, and it is used to evaluate how well the UCUs with the higher LSI values account for the landslide cells in the study area

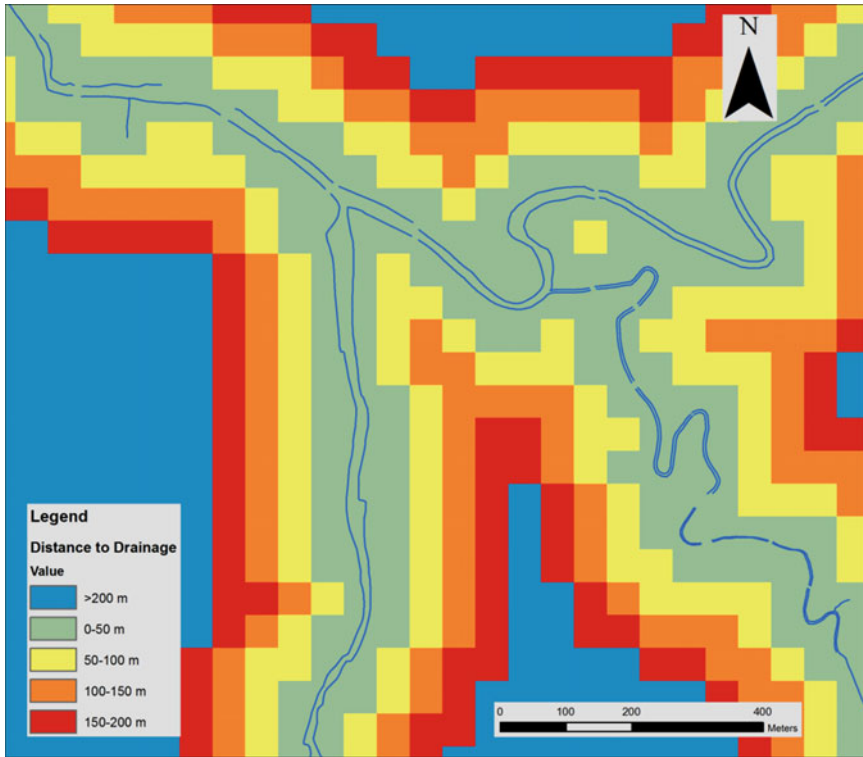


Fig. 9.3 Raster image for the distance to drainage variable. The legend shows the five classes created

(Bui et al. 2013; Zêzere et al. 2004). This curve, which is shown in Fig. 9.6, is obtained by cumulating both the number of landslide cells (shown in the y-axis) and total number of cells (shown in the x-axis) of the UCUs ordered by decreasing LSI value. Ideally, most of the landslide cells should be contained in some UCUs with the higher LSI values. The second measure is used to evaluate the relative proportion of landslide cells to the total number of cells in each susceptibility class. Ideally, a landslide susceptibility map should exclusively group all the landslide cells in the higher susceptibility classes, while all the non-landslide cells should be contained in the lower susceptibility classes. This measure is called the Degree of Fit (DoF) and has been employed by Fernández et al. (2003) and Jiménez-Perálvarez et al. (2009) as follows:

$$\text{DoF} = \frac{\sum \frac{z_i}{s_i}}{\sum \frac{z_i}{s_i}} \quad (9.2)$$

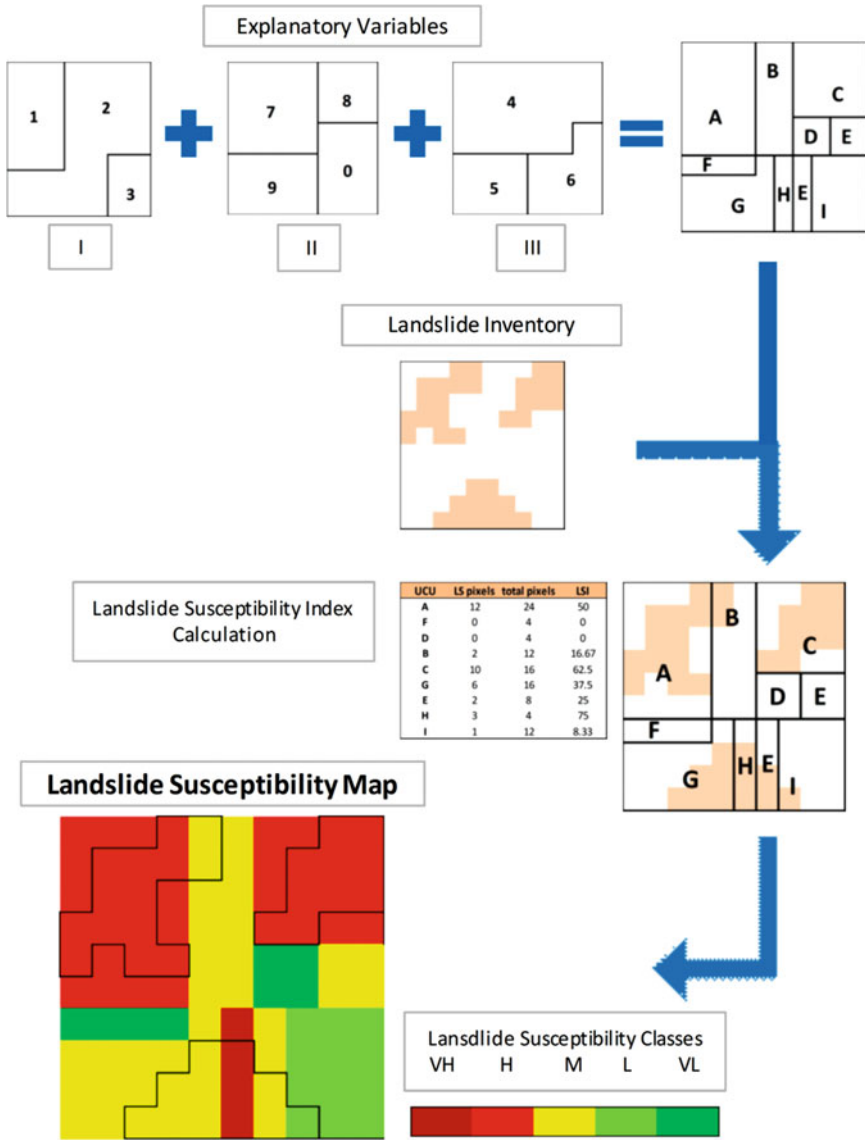


Fig. 9.4 Summary scheme of the employed methodology

where z_i is the number of landslide cells in the i th susceptibility class and s is the total number of cells belonging to the i th class. A good susceptibility map would have low values of DoF for the low and very low susceptibility classes (considered as the error) and high values of DoF for the high and very high susceptibility classes (considered as accuracy).

9.5 Results

The results of the LSI value calculation for some UCUs are shown in Table 9.4. Of the total 735 possible UCUs (i.e., $21 \times 7 \times 5$ combinations), only 525 UCUs were represented in the study area. A total of 286 UCUs contained at least one landslide

Table 9.4 Partial summary of the LSI value calculation

N° UCU	UCU			Number of landslide cells	Total number of cells	LSI
	Geology	Slope	Distance to drainage			
217	4	3	2	2	3	66.67
218	2	7	1	6	11	54.55
219	15	5	5	9	17	52.94
220	9	6	5	1	2	50
221	10	7	5	1	2	50
222	9	3	1	4	8	50
223	5	4	1	1	2	50
224	12	5	1	3	6	50
225	5	5	2	2	4	50
226	12	6	2	2	4	50
227	10	7	2	1	2	50
228	11	4	3	1	2	50
229	11	5	3	1	2	50
230	10	4	4	47	98	47.47
231	10	5	4	14	30	46.67
:	:	:	:	:	:	:
:	:	:	:	:	:	:
465	19	1	2	1	34	2.94
466	12	3	3	4	139	2.88
467	1	2	3	8	278	2.88
468	4	2	2	1	36	2.78
469	18	2	3	2	73	2.74
470	9	2	5	3	123	2.44
471	1	2	4	5	220	2.27
472	7	3	4	1	45	2.22
473	10	1	1	14	631	2.22
474	18	2	3	1	54	1.85

Table 9.4 summarizes the results of 25 of the 525 UCUs found in the study area. A total of 210 combinations were not found. An additional six units exclusively only had landslide cells, while 239 UCUs only had non-landslide cells. The numbers for each of the classes correspond to the ones shown in Table 9.1. For example, UCU No. 231 refers to those cells having a Krc geological formation (10), slope angles ranging between 20 and 25° (5) and buffers between 150 and 200 m on both sides of the drainage (4)

cell (including six UCUs that contained only landslide cells), while 239 UCUs contained only non-landslide cells. For the selected UCUs in Table 9.4, the number of landslide cells, the total number of cells and the corresponding LSI value are shown.

Figure 9.5 shows the landslide susceptibility map with five susceptibility classes: very low (dark green), low (light green), moderate (yellow), high (orange) and very high (red). The landslide bodies derived from the aerial photograph interpretation are marked by dark lines. This allows a visual overview of the consistency between the color associated with the different susceptibility classes and the absence/presence of landslides in the cells. The areas more likely affected by landslides are located in the northern sector and toward the southeast of the study area. The central and eastern sectors of the city seem to be very stable. In general,

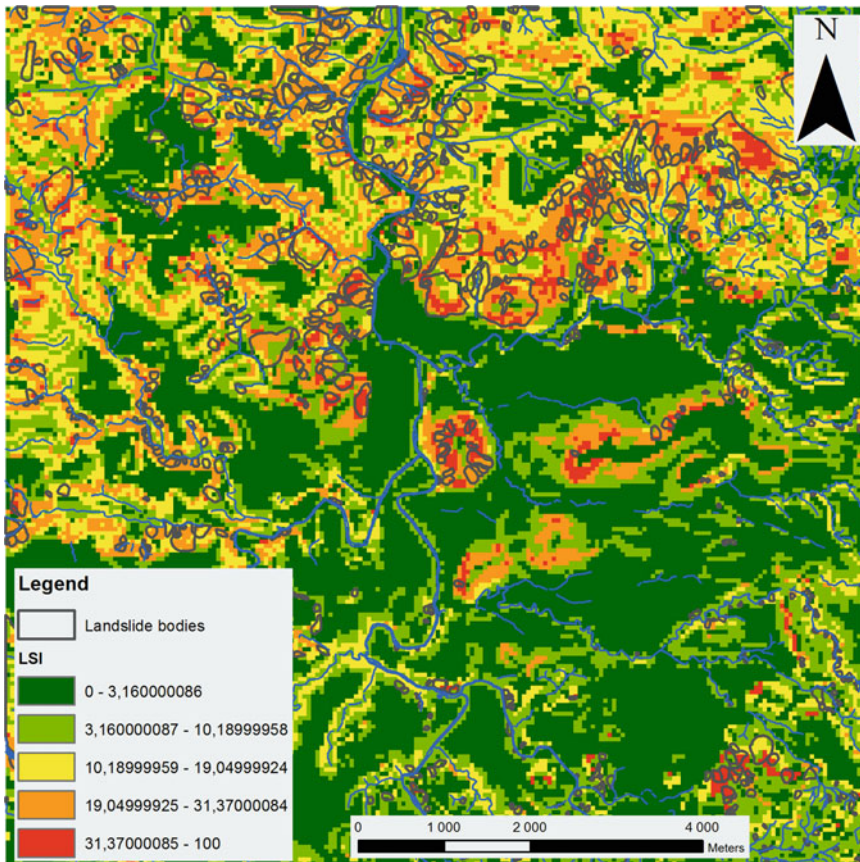


Fig. 9.5 Landslide susceptibility map constructed upon the aerial photograph interpretation landslide inventory. The five susceptibility classes shown are very low (*dark green*), low (*light green*), moderate (*yellow*), high (*orange*) and very high (*red*). The landslide bodies are shown by the *polygons with gray borders*

the landslide susceptibility map is able to capture most of the landslide bodies within the high (orange) and very high (red) susceptibility classes. This is supported by Fig. 9.6, which shows that the area under the success rate curve for the landslide susceptibility map is 79.78%. This high score is a clear indication that the selected environmental factors are closely related to the occurrence of past landslide events in the study area.

The accuracy and the error in assigning landslide cells to the different susceptibility classes were determined by the value of the DoF (Eq. 9.2). Table 9.5 shows the number of landslide cells, the total number of cells and the ratio of landslide cells to total number of cells in each susceptibility class. It can be seen that the accuracy (i.e., the sum of the DoF values in the “very high” and “high” susceptibility classes) is 73.8%. Meanwhile, the error (i.e., the sum of the DoF values in the “low” and “very low” susceptibility classes) barely reaches 8.4%. The high accuracy and the low error of the landslide susceptibility map show that the matrix method has been employed with success for the susceptibility assessment of the study area.

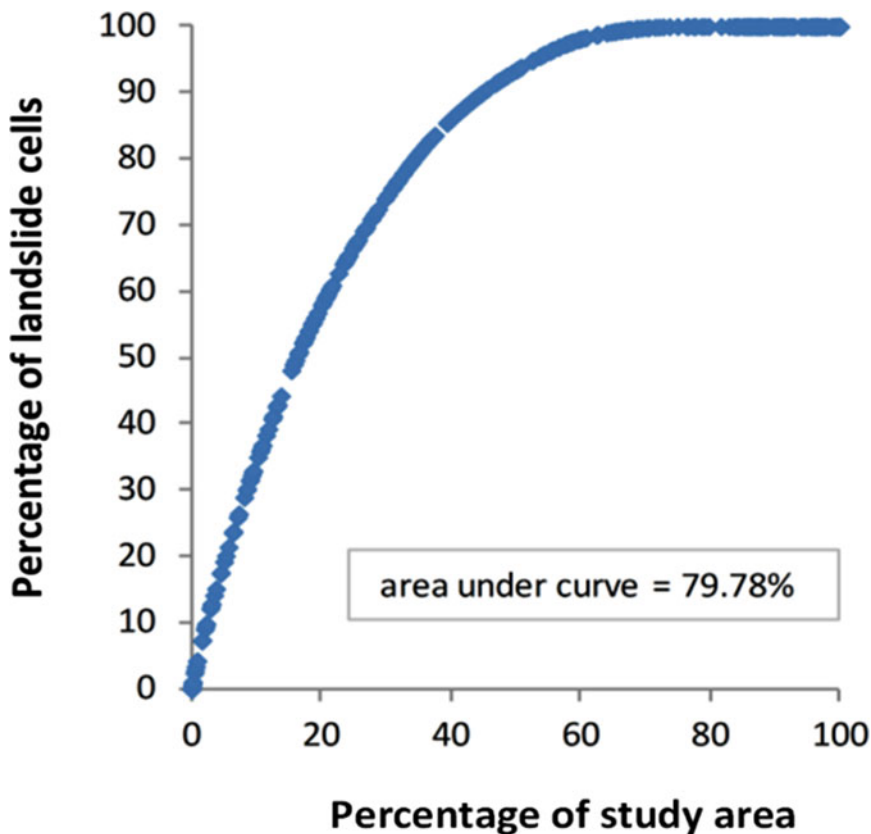


Fig. 9.6 Success rate curve for the landslide susceptibility map based upon the 2014 landslide bodies

Table 9.5 Calculation of the degree of fit for the landslide susceptibility map

Class	Area in class (%)	Number of landslide pixels per class (z_i)	Total number of pixels per class (s_i)	$\frac{s_i}{z_i}$	DoF = $\frac{z_i}{\sum \frac{s_i}{z_i}}$
Very high	12.69	453	1201	0.377	0.477 ^a
High	39.61	1414	5678	0.206	0.261 ^a
Moderate	29.66	1059	7514	0.141	0.178
Low	15.66	559	8988	0.062	0.078 ^b
Very low	2.38	85	16,617	0.005	0.006 ^b
Total	100	3570	40,000	0.791	1.0

^aThe sum of DoF (Eq. 9.2) for the very high and high classes represents the accuracy of the method

^bThe sum of DoF for the low and very low classes represents the error of the method

9.6 Discussion

There is no doubt that aerial photograph interpretation is an important source of information commonly used for the creation of landslide inventories for a given study area. Although the 2013 aerial photographs were not taken to analyze a particular massive landslide-triggering event (as was the case for Hurricane Mitch in 1998 (JICA 2002)), some landslides that had been triggered in 2008 and 2011 were successfully captured in the photographs. However, it is important to point out that the population growth of Tegucigalpa has driven many important urbanization works in recent years. The construction of new residential projects, buildings and roads as well as the maintenance works of existing infrastructure has brought about significant terrain modifications that may have altered the evidence of past landslides. Therefore, the detection of past landslides from aerial photographs becomes more challenging. Furthermore, the tropical environment of the city promotes a fast growth of vegetation, which also helps obscure the signs of past landslide events (Vranken et al. 2015). For these reasons, efforts should be carried out to analyze the landslides as soon as they take place and also to keep a thorough record of landslides in time. A more reliable landslide susceptibility map for Tegucigalpa can be constructed if it is based upon these historical records as well as event-based inventories (Van Westen et al. 2008).

So far, the most important landslide susceptibility investigations carried out for Tegucigalpa have dealt with the massive destruction caused by Hurricane Mitch in 1998 (JICA 2002; Harp et al. 2002, 2009; Pineda 2004). From these studies, no strong conclusions about Tegucigalpa’s landslide susceptibility under ordinary rainfall events can be drawn due to the anomalous nature of Hurricane Mitch. However, studies focusing on the temporal aspect of landslides in Tegucigalpa (Garcia-Urquia and Axelsson 2015; Garcia-Urquia 2016) have revealed that between 1980 and 2005, many landslide episodes took place under low rainfall conditions. This suggests that the social vulnerability of the residents may have significantly contributed to landslide occurrence. Furthermore, while it is true that

several old landslide sites that were active during Hurricane Mitch suffered reactivations, many other landslides have been triggered in new places. This supports the fact that the city lacks a proper urban development plan and the disorganized growth of the city has contributed to the occurrence of landslides. Some major efforts to reduce the danger in historical landslide sites like El Berrinche Hill have been carried out in recent years by JICA (see Fig. 9.7). Yet, as long as the



Fig. 9.7 Countermeasures carried out by JICA to reduce the landslide risk in El Berrinche Hill. **a** Channels that transport surface water are shown. **b** One of the drainage wells with intake pipes at different depths to collect groundwater is shown. Both figures were taken from El Heraldo newspaper and were published on April 7, 2014

destabilization of the slopes of the city is driven without control, Tegucigalpa's overall landslide susceptibility will remain critical and the identification of all the susceptibility factors that bring about landslides will continue to be difficult.

9.7 Conclusion

This study presents the application of the matrix method for the construction of a landslide susceptibility map for Tegucigalpa, the capital city of Honduras. This method has been considered ideal for the study area because it requires fewer explanatory variables than any other statistical methods. Landslide data were derived from an aerial photograph interpretation carried out by JICA in 2013, and three variables were analyzed: slope angle, geology and distance to drainage. The performance of the map was evaluated by means of the area under the success rate curve and the Degree of Fit (DoF) value. The high scores of both measures indicate that the map successfully identifies the areas where past landslides have occurred and the chosen variables exhibit a strong connection to landslide occurrence. Although it is likely that many past landslide events may have not been identified by the aerial photograph interpretation due to the major urbanization works in the city and the rapid growth of vegetation, the map constitutes an important tool for the urban development plan of the city. Yet, efforts must be made by research teams and local authorities to keep records of the landslide activity of the city. This will allow the development of historical landslide inventories and the construction of more reliable landslide susceptibility maps in the future.

Acknowledgements This study was carried out within the Centre for Natural Disaster Science (CNDS) research school, supported by the Swedish International Development Cooperation Agency (SIDA) through their contract with the International Science Programme (ISP) at Uppsala University (contract number: 54100006). We are grateful to JICA Honduras, UPI and UNAH for providing us the landslide inventory map based upon the aerial photograph interpretation. In addition, we would like to thank Dr. Hiroshi Yagi, Dr. Go Sato, Dr. Kiyoharu Hirota and Rigoberto Moncada Lopez, M.Sc., for instructing the interpretation on making the landslide inventory map. We are also grateful to El Heraldo newspaper for sharing the photographs showing Tegucigalpa's vulnerability to landslides.

References

- Akgun A, Dag S, Bulut F (2008) Landslide susceptibility mapping for a landslide-prone area (Findikli, NE of Turkey) by likelihood-frequency ratio and weighted linear combination models. *Environ Geol* 54(6):1127–1143. doi:[10.1007/s00254-007-0882-8](https://doi.org/10.1007/s00254-007-0882-8)
- Angel S, Bartley K, Derr M (2004) Rapid urbanization in Tegucigalpa, Honduras: preparing for the doubling of the city's population in the next twenty-five years
- Ayalew L, Yamagishi H (2005) The application of GIS-based logistic regression for landslide susceptibility mapping in the Kakuda-Yahiko Mountains, central Japan. *Geomorphology* 65(1–2):15–31. doi:[10.1016/j.geomorph.2004.06.010](https://doi.org/10.1016/j.geomorph.2004.06.010)

- Ayalew L, Yamagishi H, Ugawa N (2004) Landslide susceptibility mapping using GIS-based weighted linear combinations, the case in Tsugawa are of Agano river, Niigata prefecture, Japan. *Landslides* 1(1):73–81. doi:10.1007/s10346-003-0006-9
- Ayalew L, Yamagishi H, Marui H, Kanno T (2005) Landslides in Sado Island of Japan: part II. GIS-based susceptibility mapping with comparisons of results from two methods and verifications. *Eng Geol* 81(4):432–445. doi:10.1016/j.enggeo.2005.08.004
- Bui DT, Pradhan B, Lofman O, Revhaug I, Dick ØB (2013) Regional prediction of landslide hazard using probability analysis of intense rainfall in the Hoa Binh province, Vietnam. *Nat Hazards* 66(2):707–730. doi:10.1007/s11069-012-0510-0
- Clerici A, Perego S, Tellini C, Vescovi P (2002) A procedure for landslide susceptibility zonation by the conditional analysis method. *Geomorphology* 48(4):349–364. doi:10.1016/S0169-555X(02)00079-X
- Costanzo D, Rotigliano E, Irigaray Fernandez C, Jimenez-Peralvarez JD, Chacon Montero J (2012) Factors selection in landslide susceptibility modelling on large scale following the GIS matrix method: application to the river Biero basin (Spain)
- Cross M (1998) Landslide susceptibility mapping using the matrix assessment approach: a Derbyshire case study. In: Maund J, Eddleston M (eds) *Geohazards in engineering geology*, vol 15. The Geological Society, London, UK, pp 247–261
- Dahal RK, Hasegawa S, Nonomura A, Yamanaka M, Dhakal S, Paudyal P (2008) Predictive modelling of rainfall-induced landslide hazard in the Lesser Himalaya of Nepal based on weights-of-evidence. *Geomorphology* 102(3–4):496–510. doi:10.1016/j.geomorph.2008.05.041
- De Graff J, Romesburg H, Ahmad R, McCalpin J (2012) Producing landslide susceptibility maps for regional planning in data scarce regions. *Nat Hazards* 64(1):729–749. doi:10.1007/s11069-012-0267-5
- El Heraldo (2014) Identifican 1,500 áreas de deslizamiento en la capital. *El Heraldo*. Retrieved from <http://www.elheraldo.hn/csp/mediapool/sites/ElHeraldo/Metro/story.csp?cid=588018&sid=298&fid=213>
- Fernández T, Irigaray C, El Hamdouni R, Chacón J (2003) Methodology for landslide susceptibility mapping by means of a GIS. Application to the Contraviesa area (Granada, Spain). *Nat Hazards* 30(3):297–308. doi:10.1023/B:NHAZ.0000007092.51910.3f
- Garcia-Urquia E (2016) Establishing rainfall frequency contour lines as thresholds for rainfall-induced landslides based on the graphical assessment of the frequency of occurrence of rainfall events in Tegucigalpa, Honduras, 1980–2005. *Nat Hazards* 82(3):2107–2132
- Garcia-Urquia E, Axelsson K (2014) The use of press data in the development of a database for rainfall-induced landslides in Tegucigalpa, Honduras, 1980–2005. *Nat Hazards* 73(2):237–258. doi:10.1007/s11069-014-1043-5
- Garcia-Urquia E, Axelsson K (2015) Rainfall thresholds for the initiation of urban landslides in Tegucigalpa, Honduras: an application of the critical rainfall intensity. *Geogr Ann Ser A Phys Geogr* 97(1):61–83. doi:10.1111/geoa.12092
- Ghosh S, van Westen CJ, Carranza EJM, Jetten VG, Cardinali M, Rossi M, Guzzetti F (2012) Generating event-based landslide maps in a data-scarce Himalayan environment for estimating temporal and magnitude probabilities. *Eng Geol* 128:49–62. doi:10.1016/j.enggeo.2011.03.016
- Harp EL, Castañeda M, Held MD (2002) Landslides triggered by Hurricane Mitch in Tegucigalpa. U.S. Geologic Survey Open File Report, Honduras, pp 02–0033
- Harp EL, Reid ME, McKenna JP, Michael JA (2009) Mapping of hazard from rainfall-triggered landslides in developing countries: examples from Honduras and micronesia. *Eng Geol* 104(3–4):295–311. doi:10.1016/j.enggeo.2008.11.010
- Irigaray C, Fernández T, El Hamdouni R, Chacón J (2007) Evaluation and validation of landslide susceptibility maps obtained by a GIS matrix method: examples from the Betic Cordillera (southern Spain). *Nat Hazards* 41(1):61–79. doi:10.1007/s11069-006-9027-8
- JICA (2002) The study on flood control and landslide prevention in Tegucigalpa metropolitan area of the Republic of Honduras. Retrieved from Tegucigalpa, Honduras

- Jiménez-Perálvarez JD, Irigaray C, El Hamdouni R, Chacón J (2009) Building models for automatic landslide susceptibility analysis, mapping and validation in ArcGIS. *Nat Hazards* 50(3):571–590. doi:[10.1007/s11069-008-9305-8](https://doi.org/10.1007/s11069-008-9305-8)
- Lee S, Sambath T (2006) Landslide susceptibility mapping in the Damrei Romel area, Cambodia using frequency ratio and logistic regression models. *Environ Geol* 50(6):847–855. doi:[10.1007/s00254-006-0256-7](https://doi.org/10.1007/s00254-006-0256-7)
- Pardeshi SD, Autade SE, Pardeshi SS (2013) Landslide hazard assessment: recent trends and techniques. *SpringerPlus* 2(1):523. doi:[10.1186/2193-1801-2-523](https://doi.org/10.1186/2193-1801-2-523)
- Pearce-Oroz G (2005) Causes and consequences of rapid urban spatial segregation. In: Varady D (ed) *Desegregating the city: Ghettos, enclaves and inequality*. Suny Press, pp 108–124
- Pineda MA (2004) Identificación y análisis de las áreas susceptibles de los procesos de remoción en masa, en la cuenca alta del río Grande o Choluteca, en Tegucigalpa, Honduras. CA. Masters degree thesis. Universidad de Costa Rica
- Pradhan B, Lee S (2010) Delineation of landslide hazard areas on Penang Island, Malaysia, by using frequency ratio, logistic regression, and artificial neural network models. *Environ Earth Sci* 60(5):1037–1054. doi:[10.1007/s12665-009-0245-8](https://doi.org/10.1007/s12665-009-0245-8)
- Süzen ML, Doyuran V (2004) A comparison of the GIS based landslide susceptibility assessment methods: multivariate versus bivariate. *Environ Geol* 45(5):665–679. doi:[10.1007/s00254-003-0917-8](https://doi.org/10.1007/s00254-003-0917-8)
- UPI-JICA (2014) Manual para elaboración de mapa de inventario de deslizamientos de tierra. Caso de aplicación: Ciudad de Tegucigalpa. JICA Honduras y UPI, p 76
- van Westen CJ, Castellanos E, Kuriakose SL (2008) Spatial data for landslide susceptibility, hazard, and vulnerability assessment: an overview. *Eng Geol* 102(3–4):112–131. doi:[10.1016/j.enggeo.2008.03.010](https://doi.org/10.1016/j.enggeo.2008.03.010)
- Vranken L, Vantilt G, Van Den Eeckhaut M, Vandekerckhove L, Poesen J (2015) Landslide risk assessment in a densely populated hilly area. *Landslides* 12(4):787–798. doi:[10.1007/s10346-014-0506-9](https://doi.org/10.1007/s10346-014-0506-9)
- Yagi H, Higaki D, Japan Landslide Society (2009) Methodological study on landslide hazard assessment by interpretation of aerial photographs combined with AHP in the middle course area Agano River, Central Japan. *Jpn Landslide Soc* 45(5):8–16 (in Japanese and English abstract)
- Yamagishi H, Yagi H, Sato G (2014) Landslide hazard mapping of Tegucigalpa, Honduras—capacity building by JICA-JSPS Project (2012 to 2014). In: *Proceedings of world landslide forum*, vol 3. Beijing, 2–6 June 2014, pp 712–715
- Zêzere JL, Reis E, Garcia R, Oliveira S, Rodrigues ML, Vieira G, Ferreira AB (2004) Integration of spatial and temporal data for the definition of different landslide hazard scenarios in the area north of Lisbon (Portugal). *Nat Hazards Earth Syst Sci* 4:133–146

Chapter 10

An Assessment of the Effective Geofactors of Landslide Susceptibility: Case Study Cibeber, Cianjur, Indonesia

Yukni Arifianti and Fitriani Agustin

Abstract Landslides in Indonesia cause severe disasters, significantly in populated areas and their vicinities. Landslide susceptibility assessment (LSA) is a vital tool for its mitigation. In this study, a bivariate statistical method called the Weights of Evidence (WoE) was applied to characterize landslide-prone areas on a landslide susceptibility map. The objective of this study was to estimate the spatial relationships between effective geofactors and landslide inventory data, and their relationship with landslide susceptibility. The three geofactors: slope gradient, lithology, and the landuse, together with a landslide inventory were found effective in LSA at Cibeber Sub-District, Cianjur Regency. After that a geographic information system (GIS) was applied to analyze and produce geofactor maps. The validation of the generated maps was carried out using areas under the curve (AUC). The results of modeling indicated a positive relationship between slope gradient, lithology, and land use with the occurrence of landslides, with the success rate of 81.69, 80.1 and 81.39%, respectively. Finally, the success and prediction accuracy of the WoE model for the landslide susceptibility map was 82 and 80.4%, respectively. Following this, the study area was classified into four levels of landslide susceptibility: very low, low, moderate, and high. According to the validation results, the landslide susceptibility map produced by the WoE model exhibited satisfactory properties. This landslide susceptibility map can be used for preliminary landslide hazard prevention and mitigation, as well as for proper planning of landuse and infrastructure development.

Keywords Landslide susceptibility assessment · Weights of evidence · Geofactor · Areas under the curve (AUC)

Y. Arifianti (✉) · F. Agustin
Geological Agency of Indonesia, Jl. Diponegoro 57,
Bandung 40122, Indonesia
e-mail: yukni.a@gmail.com

F. Agustin
e-mail: afitchan@gmail.com

10.1 Introduction

An accelerated population growth towards landslide-prone areas has caused an increase in casualties through human-induced landslide hazards each year. A significant effort to reduce the number of losses is attempted using landslide disaster mitigation. One such activities is to conduct a landslide susceptibility assessment (LSA) as the basis for producing a landslide susceptibility map. In this study the spatial relationships between effective geofactors and landslide inventory data is investigated to estimate landslide susceptibility in an area.

The selected area was Cibeber Sub-District, Cianjur Regency in West Java, Indonesia (Fig. 10.1). It is located in Java Island and covers an area of approximately 124.5 km². According to the Landslide Inventory Database of Indonesia, between 2011 and 2015, almost 40% of the landslide in Indonesia occurred in West Java. Cianjur, with its prominent factors affecting landslides, i.e., highly weathered material (lithology) and the steep morphology, is a hotspot for landslides in West Java. The Cibeber Sub-District was selected for the study because it is considered to have the main link road, and land connected, to the southern and northern parts of Cianjur. Frequent landslide disasters in Cibeber directly influence, or even isolated, the southern part of Cianjur. The research in the study area was conducted between May, 2013 and April, 2014.

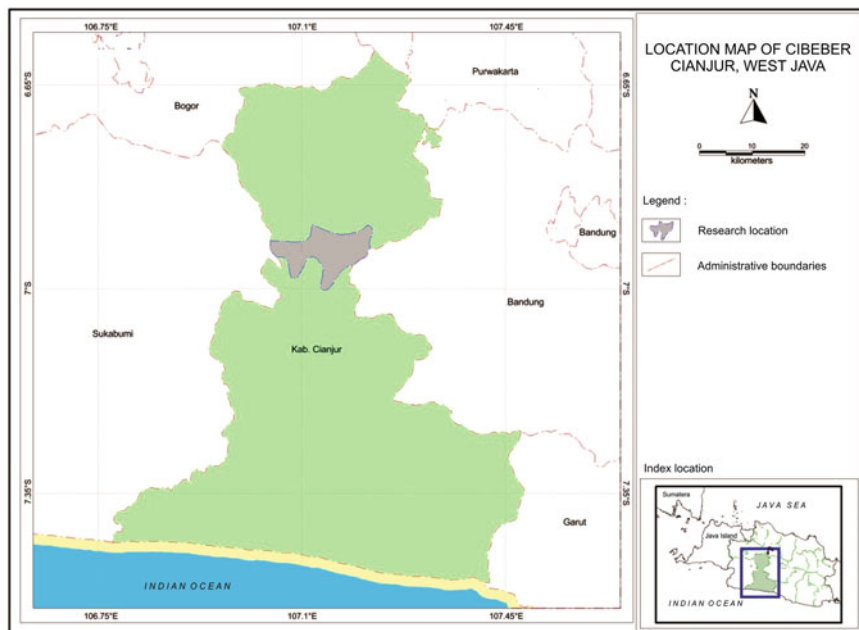


Fig. 10.1 The selected study area of the Cibeber Sub-District, Cianjur Regency, Indonesia

10.2 Landslide Inventory and Geofactor Data

Landslides are represented as geo-referenced points, in order to create a homogeneous database, with point positions identified near the scar of the landslide body (Neuhäuser et al. 2011). A total of 57 recent landslides in Cibeber area were mapped into the landslide inventory map, shown in Fig. 10.2. They were commonly identified as rotational and translational types of landslide. A landslide inventory was the initial step made and represented a fundamental part in the LSA. It provided a framework and tools for displaying and analyzing landslide information collected in a spatially aware digital format and as the basis for all the zoning creation of susceptibility, hazard, and risk maps (Balzer and Kuhn 2011).

The inventory of landslides represented indispensable input information for the statistical analysis of susceptibility or hazardous areas prone to landslides. The statistical approach optimally processes the data series of geofactors in order to produce landslide susceptibility zoning (Arifianti et al. 2015). Geofactors are landslide conditioning factors—a stack of parameter layers containing the input parameters for a statistical approach—which provide information which may control the occurrence of areas prone to landslides. The following geofactors were supported and derived through a geographical information system (GIS) processing and interpreting satellite remote sensing data (Arifianti et al. 2013, 2014).

Researchers used and different geofactors to produce landslide susceptibility maps (LSM) (Neuhäuser et al. 2011). In this study, three basic geofactors, all

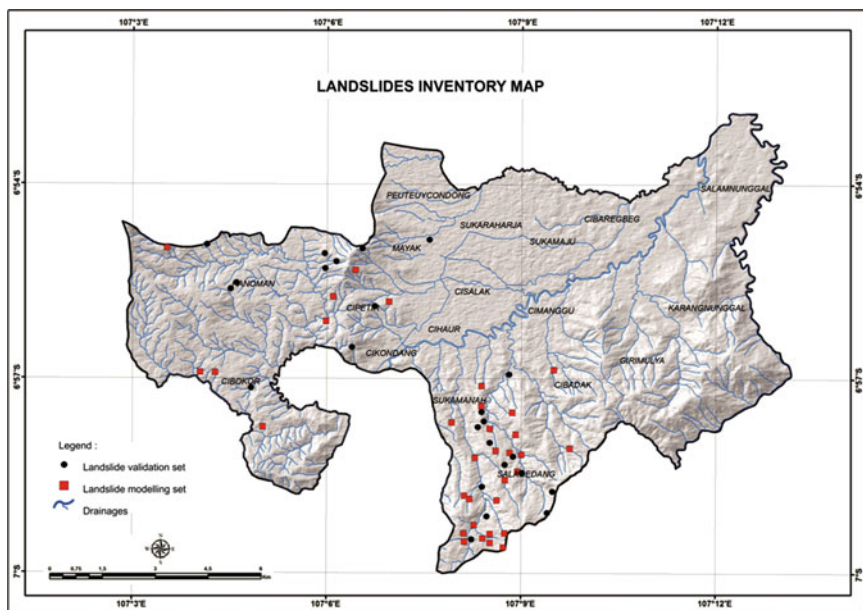


Fig. 10.2 Landslide inventory map in the Cibeber area

considered effective factors, were chosen to produce LSM, i.e., lithology, slope gradient, and landuse. There are many studies on LSA using the spatial distribution of the three geofactors in order to determine zones of landslide prone areas without any temporal implication (Van Westen et al. 2003; Magliulo et al. 2009; Barbieri and Cambuli 2009; Nefeslioglu et al. 2011).

Lithology represents different geological units or rock formations (Torizin 2011). Each unit has different susceptibilities to slope stability. The lithological units were identified by the integration and fusion of Landsat 7 ETM+ and TerraSAR X satellite data. This process created a geological map (Agustin 2013). There are 17 units defined in the study area (Table 10.1), which is mainly covered by volcanic breccia. The map is shown in Fig. 10.3.

Slope gradient is one of the main parameters of geomorphology, representing elevation points which influence the slide susceptibility—since the driving force of the mass movement is gravity (Torizin 2011). This was extracted from the digital elevation model (DEM) of TerraSAR X satellite data as the first derivative of the slope. The data was interpolated to a grid cell size of 9 m, and classified into seven slope gradient classes: flat, undulating, moderately sloping, hilly, moderately steep, steep, and very steep (see Fig. 10.4 and Table 10.2). The study area was dominated by moderately sloping areas and hilly areas.

Landuse is the impact of humans on the environment, it provides a significant factor for slope instability which is responsible for the initiation and reactivation of landslides (Torizin 2011; Dahal et al. 2008; Bruschi et al. 2013). Landuse data is

Table 10.1 Lithology units (Agustin 2013)

Unit symbol	Lithology unit
a	Andesitic intrusive
Oml	Limestone member, impermeable limestone, interbedded limestone
Md	Limy tuffaceous sandstone, claystone
Qot1	Andesitic breccia
Qyc	Basalt boulder
Pl	Andesitic lava
Qot	Old volcanic products, breccia
Pbb	Tuffaceous breccia, tuffaceous sandstone
Qvf	Undifferentiated old volcanic products
Omc	Clay member, marl, quartz sandstone, marl clay, conglomerate, cobble, quartz
Pb	Tuffaceous breccia
Pbtk	Tuffaceous breccia, conglomerate
Qot11	Old volcanic eruptive material, andesitic breccia intercalated with andesitic lava
Mts	Sandstone member, siltstone, claystone, breccia
Pbl	Tuffaceous breccia, lava
Qaf	Alluvium, clay, sand, gravel
Qyg	Breccia, mount, Gede laharic

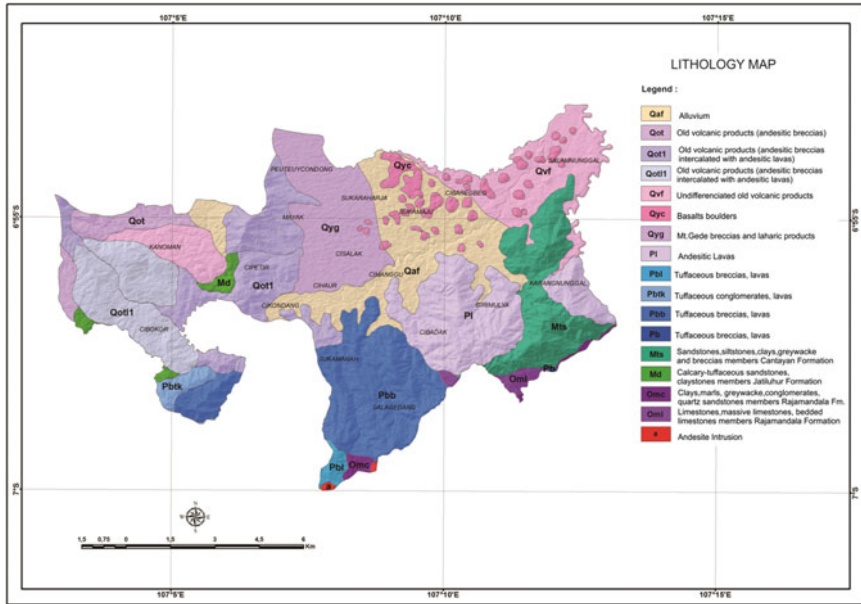


Fig. 10.3 Lithology map of the Cibeber area

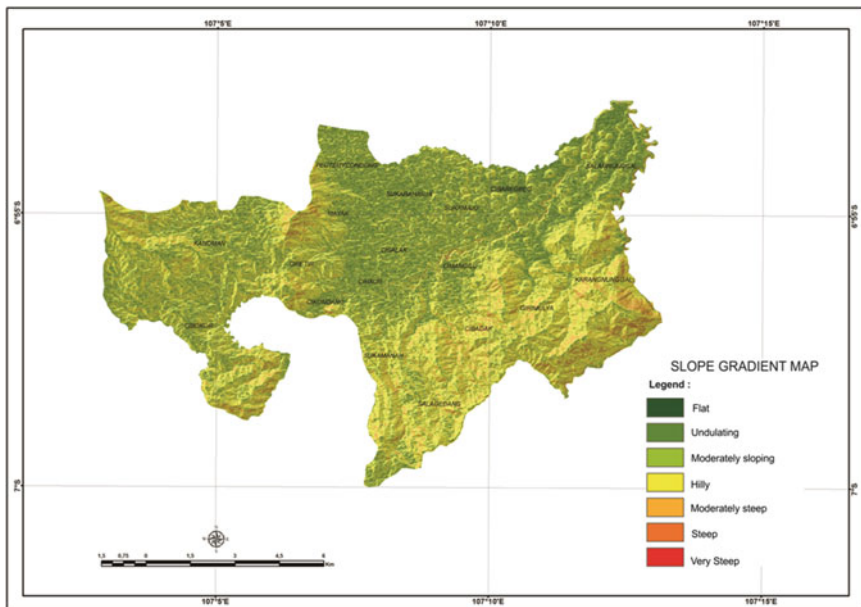


Fig. 10.4 Slope gradient map of the Cibeber area

Table 10.2 Slope gradient classes based on USDA (*United States Department of Agriculture*) classification (2009; in 12) (Wahono 2010)

Description	Slope gradient classes	
	Percentage	Degree
Flat	0–3	<2
Undulating	3–8	2–5
Moderately sloping	8–15	5–8
Hilly	15–30	8–17
Moderately steep	30–45	17–24
Steep	45–65	24–33
Very steep	>65	>33

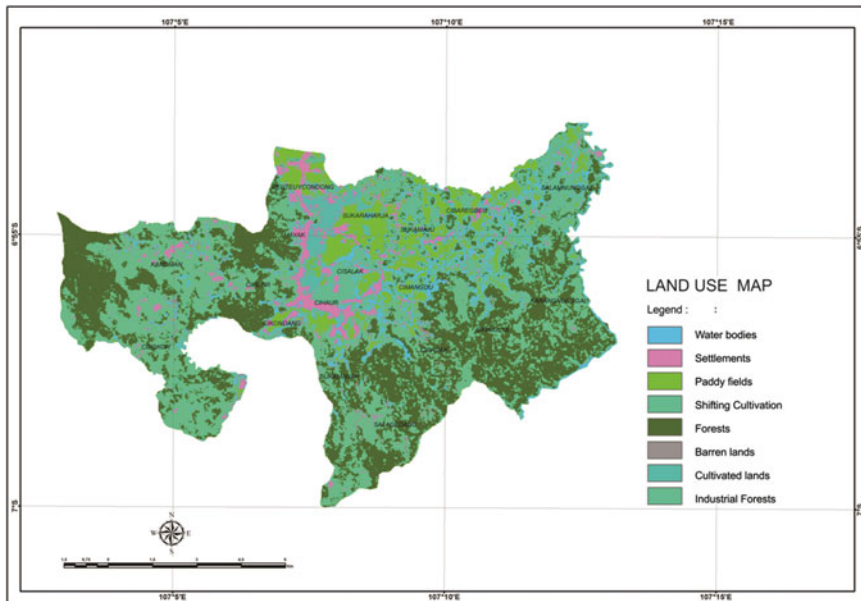


Fig. 10.5 Landuse map of the Cibeber area

based on Landsat 8 *Operational Land Imager* (OLI) satellite data. The supervised classification (expert guided) was calculated using a series of Landsat images, taken on a nearly cloud-free day, with path/row 116/066, taken February 11, 2014. The Cibeber area was classified into eight landuse classes: settlements, paddy fields, shifting cultivation, forest, industrial forests, cultivated land, barren land, water bodies (Fig. 10.5).

10.3 Methodology

Three effective geofactors were extracted from remotely sensed dataset (satellite data). These data sources represented the initial base for the derivation of geofactors and subsequent modeling (Neuhäuser et al. 2011). The procedure was to convert all data layers, geofactors, and landslide inventory data, into a grid raster dataset with similar resolutions (Table 10.3). The probabilities were calculated on the basis of so-called unit areas, measured in square kilometres, which represented a constant parameter set at the beginning of the modeling process (Neuhäuser et al. 2011). This was all processed and added to a geo-database using ArcGIS software.

The LSA in the study area was assessed using a bivariate statistical approach, referred to as weights of evidence (WoE) modeling. This method has been applied to landslide susceptibility mapping by many researchers (Neuhäuser et al. 2011; Van Westen et al. 2003; Barbieri and Cambuli 2009; Dahal et al. 2008; Lee and Choi 2004; Poli and Sterlacchini 2007; Mezughi et al. 2011; Kayastha et al. 2012; Chen et al. 2016). The WoE calculates the relationship between the effective geofactor classes and the distribution of landslides, in the form of positive weights (W^+) and negative weights (W^-). Apart from the calculation of (W^+) and (W^-), the contrast of the weight (C) is added to define how significant the overall spatial association is between the effective geofactors and landslide distribution (Torizin 2011; Dahal et al. 2008).

The WoE model comprises the following processing steps: (I) the landslide inventory was randomly subdivided into a modeling set (60%) and validation set (40%); (II) calculations were made for the weights of each effective geofactor using the modeling set of the landslides; (III) a multiclass generalization was made of the continuous evidence based on cumulative weighting; (IV) calculation of the posterior probability map was generated (i.e., a combination of the geofactors in order to predict potential landslide occurrences) (Neuhäuser et al. 2011).

The next crucial step was to evaluate the performance of WoE model using success rate and prediction rate curve approaches. The success rate used the modeling set of landslides and the prediction rate used the validation set of the inventory (Chung and Fabbri 2003).

Table 10.3 Dataset based on a GIS system

Data	Type	Format	Scale/resolution (m)
Landslide	Points	Vector	9 × 9
Lithology	Polygon	Raster	1:50.000/9 × 9
Slope gradient	Grid	Raster	9 × 9
Landuse	Polygon	Raster	9 × 9

10.4 Results

The strongest positive relation between landslides and lithology was found in tuffaceous breccia and tuffaceous sandstone (Pbb). The weighting of the slope gradient classes showed that a slope gradient of >65% (>33°) was the most susceptible to landslides. The weighting of landuse indicated that industrial forest has the highest positive relationship with landslides (Table 10.4).

Table 10.4 Computed WoE for geofactor layers based on landslide occurrences

Geofactor layers	Area Total (pixel)	Landslide points (n)	W^+	W^-	C
<i>Slope gradient</i>					
0–3%	485,308	0	-3.52638	0.371922	-3.8983
3–8%	187,677	2	-0.67486	0.066324	-0.74118
8–15%	361,806	3	-0.90944	0.169609	-1.07905
15–30%	76,175	7	1.427267	-0.18133	1.608599
30–45%	248,263	7	0.261567	-0.05961	0.321176
45–65%	158,164	7	0.704188	-0.12531	0.829497
>65%	13,485	7	3.153324	-0.22201	3.37533
<i>Lithology</i>					
a	74,878	0	-3.52638	0.04871	-3.57509
Oml	76,745	0	-3.52638	0.049957	-3.57634
Md	77,616	2	0.173648	-0.01018	0.183828
Qot1	105,086	2	-0.12065	0.008342	-0.12899
Qyc	82,148	0	-3.52638	0.053576	-3.57996
Pl	107,643	1	-0.80364	0.040924	-0.84457
Qot	83,195	1	-0.56104	0.024377	-0.58542
Pbb	112,402	18	1.979736	-0.68212	2.66186
Qvf	97,603	0	-3.52638	0.064004	-3.59039
Omc	76,314	4	0.87109	-0.07569	0.946783
Pb	74,664	0	-3.52638	0.048567	-3.57495
Pbtk	77,669	0	-3.52638	0.050575	-3.57696
Qot11	99,700	3	0.325168	-0.02713	0.352301
Mts	98,412	0	-3.52638	0.064553	-3.59094
Pbl	76,368	2	0.189461	-0.01101	0.200473
Qaf	111,091	0	-3.52638	0.0732	-3.59958
Qyg	99,344	0	-3.52638	0.065186	-3.59157

(continued)

Table 10.4 (continued)

Geofactor layers	Area Total (pixel)	Landslide points (n)	W^+	W^-	C
<i>Landuse</i>					
Water body	150,080	0	-3.52638	0.121683	-3.64807
Paddy field	184,375	0	-3.52638	0.124785	-3.65117
Cultivated land	190,092	1	-1.32324	0.098965	-1.42221
Forest	226,804	9	0.59672	-0.15308	0.749803
Barren land	171,375	1	-1.23052	0.085473	-1.316
Shifting cultivation	173,009	0	-3.52638	0.116598	-3.64298
Settlement	207,330	0	-3.52638	0.119702	-3.64608
Industrial forest	227,813	22	1.47657	-0.89282	2.369393

The area under curve (AUC) of success rate of lithology, slope gradient, and landuse are 0.80101, 0.8169, and 0.8139, respectively, shown in Fig. 10.6. The nearer the AUC is to the value 1 the better the quality of the model (Pourghasemi et al. 2013). According to validation results of the AUC evaluation, slope gradient had the highest factor controlling landslides in the area. Overall, the AUC for effective geofactors in the study area showed a good correlation between geofactor and landslide distribution data.

The WoE modeling which was applied to the three effective geofactors, was then used to generate a total WoE of landslide susceptibility. The calculated success rate for the WoE model was 0.82 with the prediction rate being 0.804. The curve provided a basis for distinguishing different susceptibility levels (Fig. 10.7). There were four levels of relative landslide occurrence defined on the landslide susceptibility map: (1) very low; (2) low; (3) moderate; and (4) high susceptibility to landslides (Fig. 10.8).

The Red areas on the map show high susceptibility to landslides, with the potential for landslides being approximately 70% of the landslide predictions in the study area, representing an area of approximately 22% of the total study area. The yellow area shows moderate susceptibility to landslides, with the potential for landslides being approximately 15% of the landslide predictions in the study area, with an area of approximately 34% of the total study area. The green and blue areas show low and very susceptibility to landslides, the potential for landslide being approximately 10 and 5% of the landslide predictions in the study area, representing approximately 16 and 28% of the total study area, respectively.

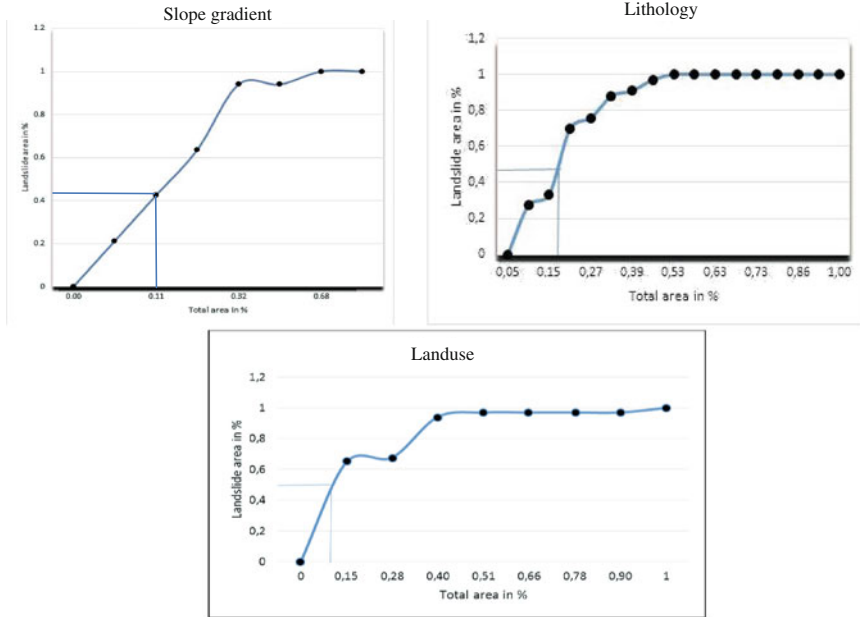


Fig. 10.6 Success rate curves for lithology, slope gradient, and landuse

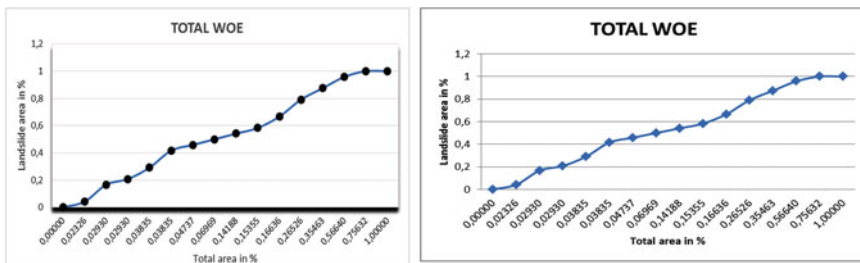


Fig. 10.7 Graphs showing AUC WoE total success rate (left) and AUC WoE total prediction rate (right)

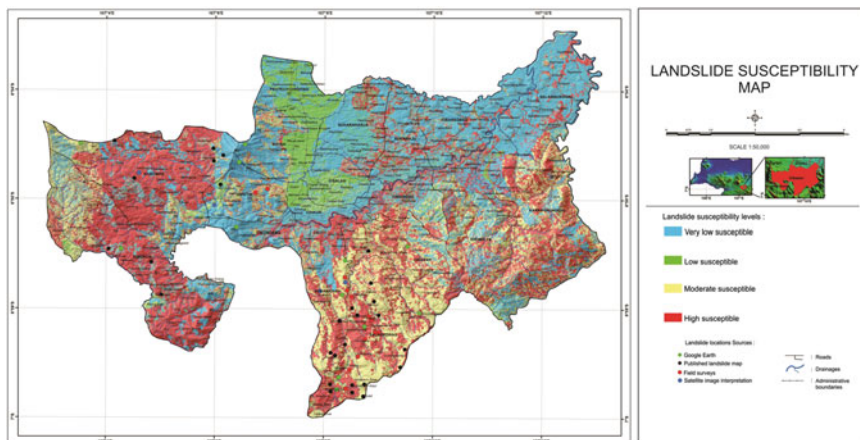


Fig. 10.8 Landslide susceptibility map of the Cibeber area

10.5 Conclusions and Suggestions

The existing geofactor data applied to the WoE model showed the suitability of the model is very good regarding the incidence of landslides. Likewise, the prediction value rate showed the model used was very good at predicting new events. The selection of causal geofactors and landslide data was good and acceptable because its AUC value (validity) exceeded the recommended limit, being 0.6. Analysis showed how effective the relationships are between geofactors (slope, landuse, and lithology) and landslide distribution along with determining susceptibility levels across the study area and creating landslide susceptibility maps.

The present landslide susceptibility map of the Cibeber area can be used for preliminary landslide hazard prevention and mitigation, along with proper planning for landuse and infrastructure development. Due to the dynamic nature of precipitation, rapid urbanization, deforestation, and anthropogenic activities, the presented landslide susceptibility map is subjected to change (Kayastha et al. 2012). Hence, the map should be verified and modified by added other landslide conditioning factors in the analysis.

Based on a literature review and analysis, it can be stated that other geofactors are considered influential in our study area. In the rainy season, rainfall is the major trigger of landslide disasters in Indonesia, including in our study area. Distance to roads also is a factor (the proximity to the road), with the discovery that many

landslide events occur along the main road running through the Cibeber area. The results show that the most influential class in the landuse factor is industrial forest. Therefore, the density of vegetation index (NDVI—normalized difference vegetation index) should be considered a significant influence in the advanced analysis of the Cibeber area. Since slope gradient has highest factor controlling landslides in the area, other derivatives of DEM, slope curvature, and slope aspect are thought to be influential too.

References

- Agustin F (2013) Peta geologi lembar Cianjur berbasis penginderaan jauh skala 1:50.000. Bandung. Pusat Survei Geologi publication, Bandung, Indonesia
- Arifianti Y, Kusnadi, Torizin J, Fuchs M (2013) Remote sensing based geo-factor maps in landslide susceptibility analysis on Lombok Island. In: Proceedings of HAGI-IAGI joint convention, Medan, Indonesia
- Arifianti Y, Teerarungsigul S, Cita A, Kuehn F, Fuchs M (2014) Landslide susceptibility assessment based on remote sensing and GIS in Lombok Island of Indonesia. In: Sassa K, Canuti P, Yuenping Y (eds) Landslide science for a safer geoenvironment, vol 2: methods of landslide studies. Springer International Publishing, pp 305–311
- Arifianti Y, Torizin J, Balzer D, Kuhn D, Cita A (2015) Geospatial tools for landslide susceptibility assessment: a case study in Lombok, Indonesia. In: Proceedings of the 36th Asian conference on remote sensing, Manila, Philippines
- Balzer D, Kuhn D (2011) Manual landslide inventory database indonesia (LIDIA)—Instruksi Singkat—. Project of technical cooperation ‘mitigation of georisks’. BGR-Report publication, Hannover
- Barbieri G, Cambuli P (2009) The weight of evidence statistical method in landslide susceptibility mapping of the Rio Pardu Valley (Sardinia, Italy). In: Proceedings of 18th world IMACS/MODSIM congress, Cairns, Australia
- Bruschi VM, Bonachea J, Remondo J, Gómez-Arozamena J, Rivas V, Barbieri M, Capocchi S, Soldati M, Cendrero A (2013) Land management versus natural factors in land instability: some examples in northern Spain. *Environ Manage* 52(2):398–416
- Chen W, Ding X, Zhao R (2016) Application of frequency ratio and weights of evidence models in landslide susceptibility mapping for the Shangzhou District of Shangluo City, China. *Envi Earth Sci* 75:64
- Chung CJF, Fabbri AG (2003) Validation of spatial prediction models for landslide hazard mapping. *Nat Haz* 30(3):451–472
- Dahal RK, Hasegawa S, Nonomura A, Yamanaka M, Masuda T, Nishino K (2008) GIS-based weights-of-evidence modelling of rainfall-induced landslides in small catchments for landslide susceptibility mapping. *Environ Geol* 54(2):311–324
- Kayastha P, Dhital M, Smedt FD (2012) Landslide susceptibility mapping using the weight of evidence method in the Tinau Watershed, Nepal. *Nat Haz* 63:479–498
- Lee S, Choi J (2004) Landslide susceptibility mapping using GIS and the weight-of-evidence model. *Int J Geogr Inf Sci* 18:789–814
- Magliulo P, Di Lisio A, Russo F (2009) Comparison of GIS-based methodologies for the landslide susceptibility assessment. *Geoinformatica* 13(3):253–265
- Mezoghi T, Akhir JM, Rafek AG, Abdullah I (2011) A multi-class weight of evidence approach for landslide susceptibility mapping applied to an area along the E–W highway (Gerik–Jeli), Malaysia. *EJGE* 16:1259–1273

- Nefeslioglu HA, Gokceoglu C, Sonmez H, Gorum T (2011) Medium-Scale hazard mapping for shallow landslide initiation: the Buyukkoy catchment area (Cayeli, Rize, Turkey). *Landslides* 8 (4):459–483
- Neuhäuser B, Damm B, Terhorst B (2011) GIS-based assessment of landslide susceptibility on the base of the weights-of evidence model. *Landslides* 9:511–528
- Poli S, Sterlacchini S (2007) Landslide representation strategies in susceptibility studies using weights-of-evidence modeling technique. *Nat Resour Res* 16(2):121–134
- Pourghasemi HR, Moradi HR, Aghda FSM (2013) Landslide susceptibility mapping by binary logistic regression, analytical hierarchy process, and statistical index models and assessment of their performances. *Nat Haz* 69:749–779
- Torizin J (2011) Bivariate statistical method for landslide susceptibility analysis using ArcGis. Project of technical cooperation 'mitigation of georisks'. BGR-Report publication, Hannover
- Van Westen CJ, Rengers N, Soeters R (2003) Use of geomorphological information in indirect landslide susceptibility assessment. *Nat Haz* 30:399–419
- Wahono BFD (2010) Applications of statistical and heuristic methods for landslide susceptibility assessments, a case study in Wadas Lintang Sub District, Wonosobo Regency, Central Java Province, Indonesia. ITC Publication. Thesis

Chapter 11

GIS Approach to Landslide Hazard Mapping: A Case Study of Syangja District in Western Nepal

Vishnu Dangol

Abstract Landslides are one of the main natural disasters in Nepal. The annual loss of lives and property due to landslides and floods is significantly high in Nepal. The landslide hazard mapping is essential for delineating hazard-prone areas. The landslide hazard maps are very useful for planning, development, and disaster management. For mitigation and management of landslide disaster, hazard maps provide important information on landslide susceptibility condition of certain region. On the other hand, the landslide hazard maps are prepared using different methods. This paper discusses some of the hazard mapping used in Nepal. It also attempts to present the GIS approaches for hazard mapping using statistical method and describes in brief a case study from Syangja District located in western Nepal.

Keywords GIS · Landslide · Hazard map · Syangja District · Western Nepal

11.1 Introduction

The inherently unstable nature of mountain areas of Nepal is well recognized. The steep slopes, unstable geology, and intense monsoon rains combine to make it one of the most hazard-prone areas in the world. Moreover, there has been an increase in human settlement of hazard-prone areas as a result of population pressure, as well as improvements in accessibility by the road and the onset of other infrastructural developments. Consequently, natural and man-made disasters are increasing, which are often resulting in substantial economic and environmental losses and causing a great suffering to many people.

Landslides are one of the main natural disasters in Nepal, responsible for huge social and economic losses for mountain populations. Landslide hazard mapping is an important tool that provides the basic knowledge of landslide susceptibility

V. Dangol (✉)

Department of Geology, Tri-Chandra Campus, Tribhuvan University, Kathmandu, Nepal
e-mail: vdangol@yahoo.com

condition of certain region, which is essential for prevention and control works of landslides as well as for development works in hill and mountain areas of Nepal.

11.1.1 Definition and Classification of Landslide and Hazard in Nepal

The term 'landslide' is used variously by specialists. It is the most overused and loosely defined term employed in slope studies. The term 'landslide' is used to denote the downward and outward movements of slope-forming material along surfaces of separation (Varnes 1978). Among the various classifications of landslides, Varnes' classification (Varnes 1978) is widely used in Nepal.

'Hazard' and 'risk' are used interchangeably in most reports on geological processes, but they must be clearly differentiated. Varnes (1984) has defined 'hazard' as the probability of occurrence of a potentially dangerous phenomenon within a specific period of time within a given area. Whereas 'risk' signifies the expected number of lives lost, persons injured, damage to property, or disruption of economic activity due to the phenomenon (Einstein 1988).

11.1.2 Major Factors Causing Landslides in Nepal Himalaya

11.1.2.1 Geology

It is one of the primary factors causing landslides. Most of the landslides are observed in the following rock types: fractured slate, interbedded quartzite/sandstone and shale, interbedded limestone/dolomite and slate, massive limestone, dolomite, marble or quartzite, interbedded soft sandstone and mudstone, massive, granite, gneiss, crystalline rocks, and phyllite/quartzite alteration. The most common types of landslides are rockslides, rockfalls, rock toppling, and wedge failure.

11.1.2.2 Rock Structure

Along the major geological structures, there are numerous small and large landslides since these zones are weak and crushed. Similarly, the orientation of folds, bedding, foliation, and joints in the rocks also plays a vital role in landsliding. On the other hand, active faults are also common in Nepal Himalaya along which also many landslides are aligned.

11.1.2.3 Weathering

In Nepal Himalaya due to the warm temperate and subtropical climate, the rocks are usually deeply weathered. Chemical weathering of rocks reaches tens of meters below the surface along the discontinuities. Due to such conditions, the strength parameters of the rock and soil are reduced considerably. In many landslide events, chemical alterations, such as hydration and ion exchange in clay, are thought to have contributed to triggering of landslides.

11.1.2.4 Soil Type

Genetically, the soils on the hillslopes of Nepal can be classified as alluvium, colluvium, and residual soils. Along the major river valleys, alluvial soils are present on the hillslopes—much higher than the present river levels due to the upliftment of the Himalayas. Often, in the old terraces, vertical joints develop which facilitates toppling and fall. All types of soils are often silty gravel and occasionally clayey silt. Deep gully erosion and translational and rotational slides occur in these soils.

11.1.2.5 Groundwater

Flowing groundwater exerts pressure on soil particles thus impairing slope stability. Abrupt rise of the water level increases the pore water pressure on slopes, which may lead to the liquefaction of sandy soils. Groundwater also reduces the mechanical strength of the ground by dissolving soluble cementing material. Also, the flowing groundwater flushes out fine particles, and the strength of the slope is reduced by the cavities formed in the process.

11.1.2.6 Precipitation

Rainfall is one of the main factors controlling the frequency of landslides. Generally, the direct relationship between the amount of rainfall and frequency of landslides is found in Nepal Himalaya too.

11.1.2.7 Change in Natural Slope

Change in slope gradient is one of the principal factors causing landslides. The change may be either natural or man-made. The change in slope gradient produces an internal change in the internal stress of the rock or soil mass, and equilibrium conditions are disturbed by an increase in shear stress.

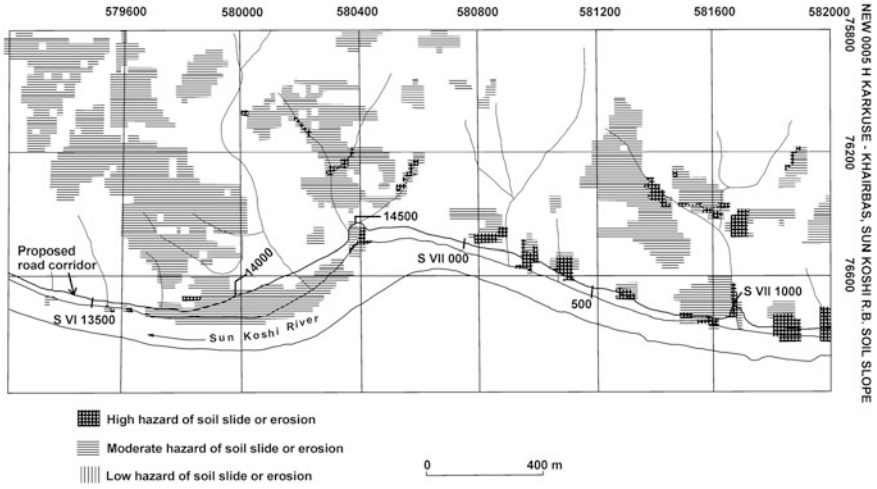


Fig. 11.1 Soil hazard map of a part of the proposed Sagarmatha road alignment, eastern Nepal (Dangol et al. 1993)

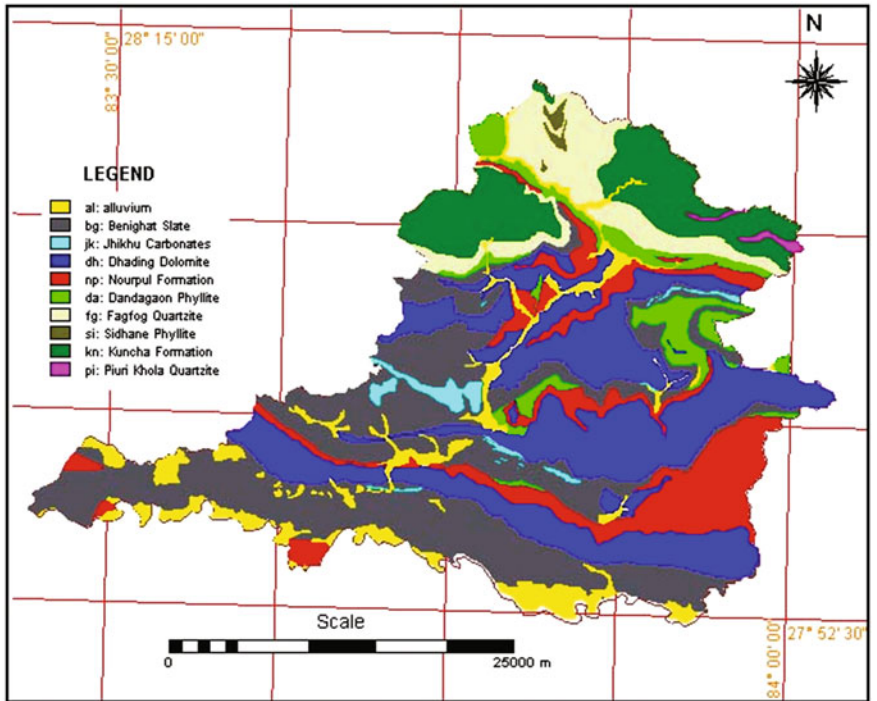


Fig. 11.2 Geological map of the Syangja District, western Nepal

11.2 Landslide Hazard Mapping in Nepal

Landslide hazard mapping is essential for delineating landslide-prone areas. Landslide hazard maps generally depict the probability of occurrence of landslide (its frequency, extent, and/or level of landslide hazard). Such maps are useful for carrying out detail investigation and monitoring of landslide-prone slopes as well as for decision-making and planning purposes.

The landslide hazard mapping in Nepal was first carried out along the road corridors and then found its application in watersheds and particular sites. Initially, the maps were prepared manually by superimposing all of the concerned maps and other relevant data. Among the several methods available for landslide hazard mapping, the method proposed by Deoja et al. (1991) has been widely applied in several landslide hazard mapping in Nepal, especially along the road corridors.

Computer-assisted landslide hazard mapping has been used from early nineties in Nepal. Based on the experiences from studies in Nepal, Wagner et al. (1990) developed the computer program ‘SHIVA’ to make soil and rock hazard maps. This method takes into account the slope angle, lithology, rock structure, soil type, soil depth, hydrology, hydrogeology, and tectonics. The maps are digitized and various ratings are assigned. The program superimposes different maps and data and

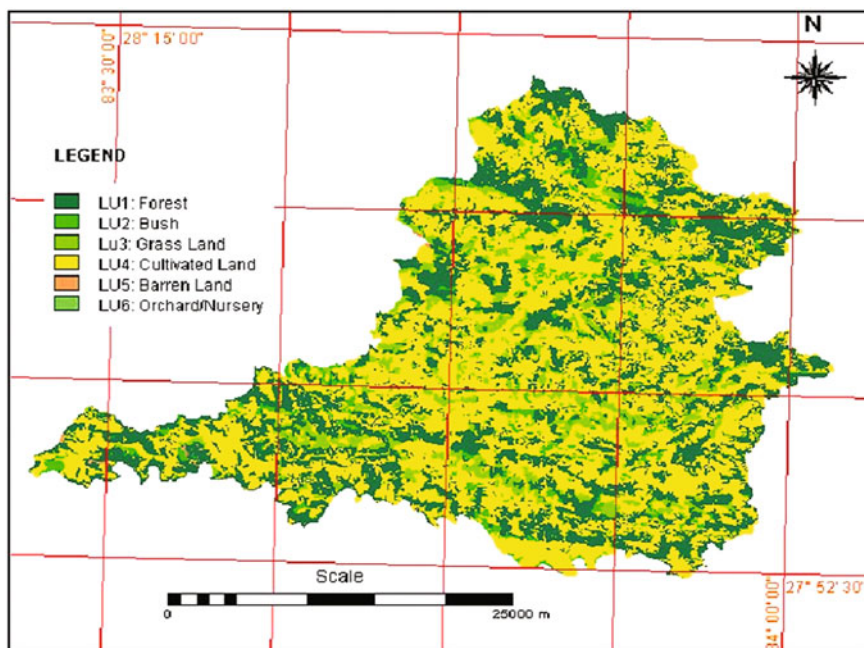


Fig. 11.3 Land use map of the Syangja District, western Nepal

produces the hazard maps (Fig. 11.1). Hazard maps of a few areas in Nepal were prepared using the software ‘SHIVA’ (Dangol et al. 1993).

With the advent of Geographic Information System (GIS), their use for landslide hazard assessment has been increasing constantly in recent years. GIS is a powerful tool for data storage, analysis, modeling, and cartography. Many GIS softwares have a capability of satellite image processing. Various methods of GIS hazard assessment have been proposed and demonstrated (Carrara et al. 1991; Chacón et al. 1993; Dangol et al. 1993; Brabb 1995; Chung et al. 1995; Terlien et al. 1995; van Westen 1997; Jibson et al. 1998; Ayalew and Yamagishi 2005; Wang et al. 2005; Safei et al. 2010).

11.3 Application of GIS in Landslide Hazard Mapping of Syangja District, Western Nepal

As the landslides are the results of various causative factors affecting slope instability at a specific location, the first step was to map individual landslides and subsequently digitize them for the purpose of a landslide inventory. The

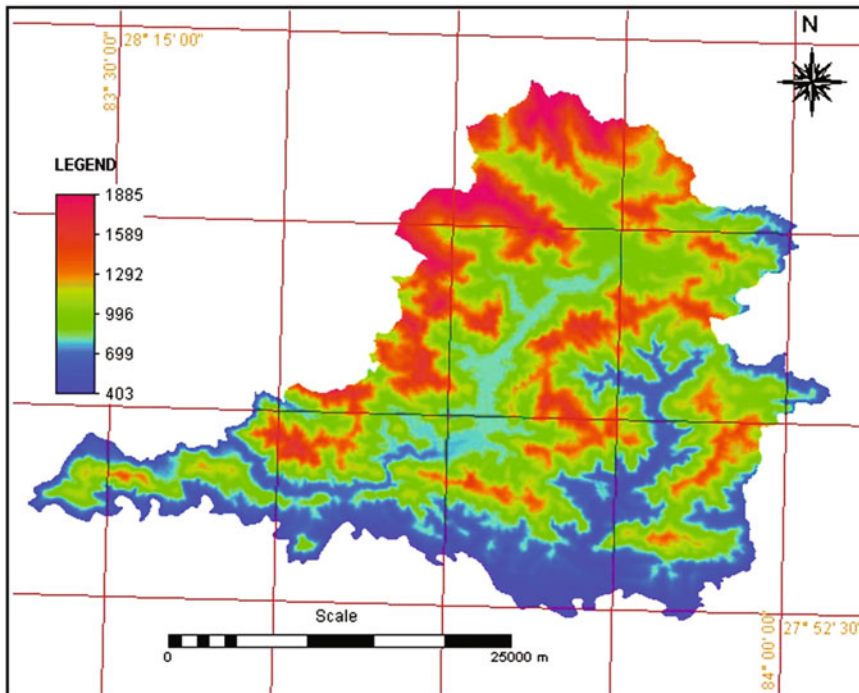


Fig. 11.4 Digital elevation model of the Syangja District, western Nepal

information on landslides was extracted from the aerial photographs and fieldwork. More than 550 instabilities were observed in the Syangja District (Dangol et al. 2001).

The presumed causative factors are either mapped in the field or gathered information on them from secondary data sources and transferred to GIS data layers and analysed. In practice, there are several methods of landslide hazard mapping: landslide distribution, qualitative hazard, statistical hazard, deterministic hazard, landslide frequency, etc. Among them, this paper discusses only the bivariate statistical landslide hazard mapping.

The landslide hazard map of the Syangja District was prepared by using various maps such as geological (Fig. 11.2), land use (Fig. 11.3), DEM (Fig. 11.4), slope (Fig. 11.5), aspect (Fig. 11.6), river distance, path distance, proximity of geological structure, and rainfall. Data source of the geology of the study area was the maps prepared by the Department of Mining and Geology, Government of Nepal.

The DEM was created using contour layers digitized from topographic maps, which were prepared by the Department of Survey, Government of Nepal. Slope maps and aspect maps were derived from the DEM. River distances were calculated from the drainage map (Fig. 11.7) and buffered according to the order of rivers. Path distances were calculated from the topographical map. Rainfall data source for

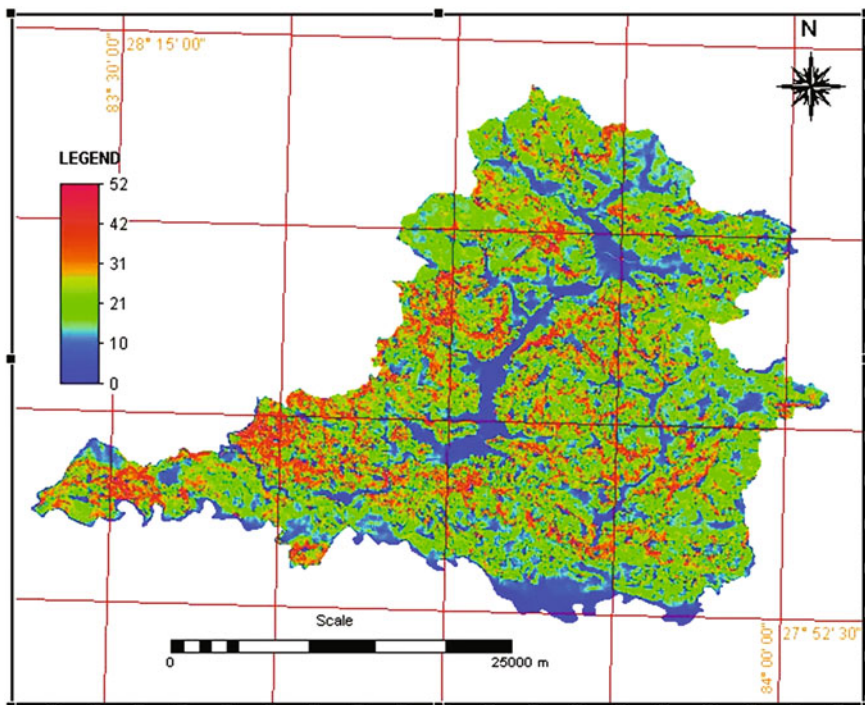


Fig. 11.5 Slope map of the Syangja District, western Nepal

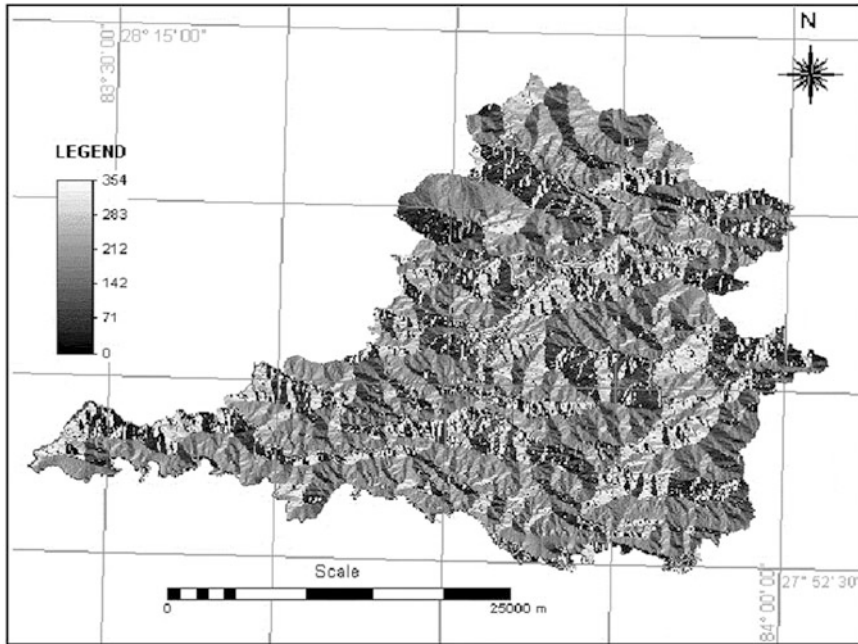


Fig. 11.6 Aspect map of the Syangja District, western Nepal

the hazard assessment was the Department of Hydrology and Meteorology, Government of Nepal.

For preparing statistical hazard map, various parameters of individual maps are classified by using the slicing operations. Then the factor maps were overlaid with landslide activity map, and landslide density for each class and the overall landslide density for each class were calculated.

The first step in the statistical hazard analysis is to calculate a weight value for each parameter. In the present study, the landslide index method was used. A weight value for a parameter class is defined as the natural logarithm of the landslide density in the class divided by the landslide density on the entire map.

The method is based on the following formula:

$$\begin{aligned} \ln W_i &= \ln [\text{Densclas} / \text{Densmap}] \\ &= \ln \left[\frac{\sum \text{Npix} (S_i)}{\sum \text{Npix} (N_i)} \right] / \left[\frac{\sum \text{Npix} (S_i)}{\sum \text{Npix} (N_i)} \right] \end{aligned}$$

where,

- W_i weight given to a certain parameter class (e.g., rock type or slope class)
- Densclas landslide density within the parameter class
- Densmap landslide density within the entire map

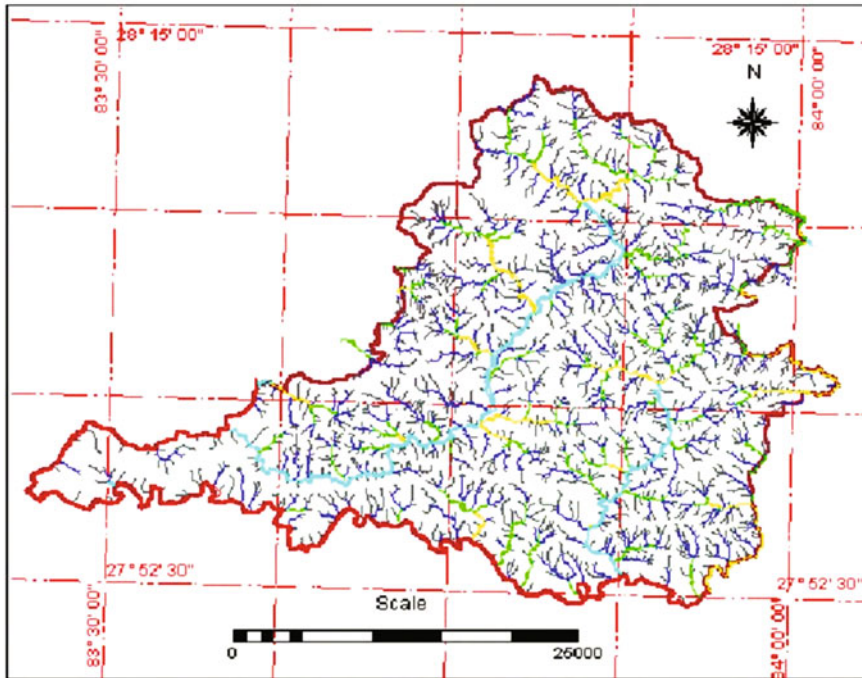


Fig. 11.7 Drainage map of the Syangja District, western Nepal

$N_{pix}(S_i)$ = number of pixels, which contain landslide in a certain parameter class
 $N_{pix}(N_i)$ total number of pixels in a certain parameter class

This method is based on the crossing of a landslide map with certain parameter map. The map crossing results in a cross-table, which can be used to calculate the density of landslide per parameter class. A standardization of these density values can be obtained by relating them to the overall density in the entire area.

All these calculations have been carried out in cross-table, by creating an attribute table with the respective domain. The procedure was repeated for all the parameter maps (Geology, Land use, altitude (Demclas), slope (Slopeclas), slope aspect (Aspclas), distance from stream (Rivdist), distance from geological structures (Strucdis), distance from paved road (Roaddist), distance from the main trail (Pathdist), and classified mean annual rainfall (Rainclas).

All the weight maps were combined together into a single map using certain combination rules:

$$\text{Weight} = W_{\text{slope}} + W_{\text{geol_Wland}} + W_{\text{dem}} + W_{\text{asp}} + W_{\text{riv}} + W_{\text{stru}} + W_{\text{road}} + W_{\text{path}} + W_{\text{rain}}$$

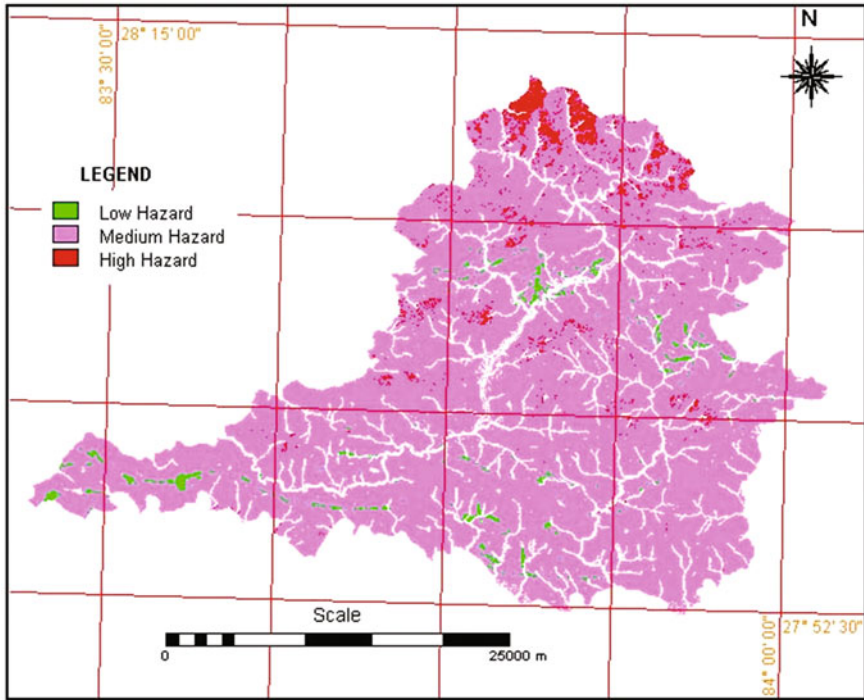


Fig. 11.8 Hazard map of the Syangja District, western Nepal

The resulted map was reclassified into three classes: low, medium, and high hazards (Fig. 11.8).

11.4 Validation of the Hazard Map

The best way to validate landslide hazard map is physical validation in the field, which, however, is a difficult job. Among the existing validation methods, the success rate curve is utilized in the present study. The success rate curve is obtained by plotting the cumulative percentage of observed landslide occurrence against the areal percentage in decreasing LHI values as shown in Fig. 11.9. The area under a curve can be used to assess the prediction accuracy. The overall success rate of the landslide hazard map is 88.01%.

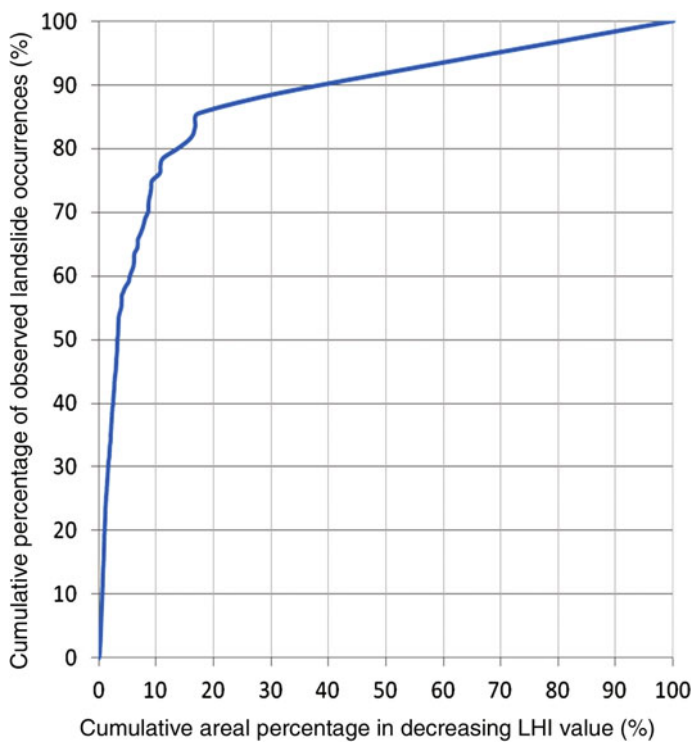


Fig. 11.9 Success rate curve (cumulative percentage of observed landslide occurrence vs cumulative percentage of decreasing LHI value)

11.5 Conclusions

The mountains of Nepal are highly susceptible to various natural disasters, landslide being the major one, which causes huge social and economic losses. The major natural factors of landslides are steep slopes, unstable geology, and intense monsoon rains.

The landslide hazard mapping is essential for delineating hazard-prone areas. Further, the landslide hazard maps are very useful for planning, development, and disaster management.

In Nepal, initially, the landslide hazard mapping was carried out manually for selection of better road alignments and then applied to watersheds and individual landslide sites. The first computer-assisted landslide hazard mapping in Nepal was carried out by using 'SHIVA' software.

The GIS is easy, useful, and powerful tool for data capture, management, and analysis for hazard map preparation. Among a numerous GIS methods of landslide hazard mapping, a bivariate statistical method was applied to prepare the hazard map of Syangja District, western Nepal.

The presumed causative factors of the landslides were mapped and other relevant data were gathered from secondary sources and transferred to GIS layers. By slicing method, various parameters of maps were reclassified, from which then weight values were calculated. All the weight maps were combined together, and the resulted map was reclassified to prepare the hazard map of the area.

The analysis of the success rate curve shows that the rate of the landslide hazard map is 88.01%, which shows that the predicted hazard levels are found to be good agreement with the past landslides.

References

- Ayalew L, Yamagashi H (2005) The application of GIS based logistic regression for 361 landslide susceptibility mapping in Kakuda-Yahiko Mountains, Central Japan. *Geomorphology* 65(1–2):15–31
- Brabb EE (1995) The San Mateo County GIS project for predicting the consequences of hazardous geologic processes. In: Carrara A, Guzzetti F (eds) *Geographical information systems in assessing natural hazards*. Kluwer Pub., Dordrecht, The Netherlands
- Carrara A, Cardinali M, Detti R, Guzzetti F, Pasqui V, Reichenbach P (1991) GIS techniques and statistical models in evaluating landslide hazard. *Earth Surf Proc Land* 16:427–445 (John Wiley & Sons, New York)
- Chacón J, Irigaray C, Fernández T (1993) Methodology for large scale landslide hazard mapping in a G.I.S. In: Novosad S, Wagner P (eds) *Proceedings of the 7th international conference and field workshop on landslides in Czech and Slovak republics*, 28 Aug–15 Sept 1993, Balkema, Rotterdam, the Netherlands, pp 77–82
- Chung CHF, Fabbri AG, van Westen CJ (1995) Multivariate regression analysis for landslide hazard zonation. In: Carrara A, Guzzetti F (eds) *Geographical information systems in assessing natural hazards*. Kluwer Pub., Dordrecht, the Netherlands
- Dangol V, Ulak PD, Mali R (2001) Application of remote sensing and geographic information system in landslide hazard evaluation: an example from Syangja district, W. Nepal. In: *International symposium on geotechnical and environmental challenges in Mountain Terrain*, 6–7 Nov 2001, Katmandu, Nepal
- Dangol V, Upreti BN, Dhital MR, Wagner A, Bhattarai TN, Bhandari AN, Pant SR, Sharma MP (1993) Engineering geological study of a proposed road corridor in eastern Nepal. *Bull Dept Geol* 3(1):91–107 (Tribhuvan University)
- Deoja B, Dhital MR, Thapa B, Wagner A (principal editors) (1991) *Mountain risk engineering handbook*. ICIMOD, Kathmandu, p 857
- Einstein HH (1988) Landslide risk assessment procedure. In: *Proceedings of the 5th international symposium on landslides*, 10–15 Jul 1988, Lausanne, Switzerland
- Jibson RW, Harp EL, Michael JA (1998) A method for producing digital probabilistic seismic landslide hazard maps: an example from the Los Angeles, California, area. *Open-file report 98–113*, USGS
- Safei M, Omar H, Yousuf ZBM, Ghiasi V (2010) Applying geospatial technology to landslide susceptibility assessment. *Electron J Geotech Eng* 15(G):677–696
- Terlien MTJ, van Westen CJ, van Asch THWJ (1995) The use of deterministic models in landslide hazard assessment. In: Carrara A, Guzzetti F (eds) *Geographical information systems in assessing natural hazards*. Kluwer Pub., Dordrecht, the Netherlands
- van Westen CJ (1997) *Statistical landslide hazard analysis*. ILWIS Application Guide, ITC, Netherlands, pp 73–84

- Varnes DJ (1978) Slope movements, types and processes. In: Schuster RI, Krizek RJ (eds) Landslides, analysis and control. Sp Rep 176, National Academy of Sciences, Washington
- Varnes DJ (1984) Landslide hazard zonation: a review of principles and practice. Highway Res Board Sp Rep 29:20–47
- Wagner A, Leite E, Oliver R (1990) A landslide hazard mapping software (version 1.0), 2 volumes. ITECO CH and University of Lausanne, Switzerland
- Wang H, Liu G, Xu W, Wang G (2005) GIS-based landslide hazard assessment: an overview. *Prog Phys Geogr* 112:190–204

Chapter 12

GIS Application in Landslide Susceptibility Mapping of Indian Himalayas

Shantanu Sarkar and Debi Prasanna Kanungo

Abstract The landslide susceptibility zonation maps provide an assessment of the safety of existing habitations and infrastructural elements. This in turn helps to plan further developmental activities in mountainous regions. GIS has been proved to be an integral part of landslide studies in recent times. Besides mapping landslides based on field investigation and remote sensing image interpretation to create a landslide database, GIS has been established as an indispensable tool for preparing various thematic data layers pertaining to landslide causative factors by using field-based data, digitally interpreted remote sensing data and through spatial and 3D analysis of terrain data. These thematic data layers are spatially integrated using arithmetic and weighted overlay statistical techniques on GIS platform to prepare landslide susceptibility maps. CSIR-CBRI has carried out landslide susceptibility mapping of different parts of the Himalayas by employing different techniques such as expert opinion-based approach, field-based rating criteria, statistical approach, and ANN and fuzzy concept-based approaches, in which GIS and remote sensing has extensively been used. The present paper illustrates a broad methodology employed for mapping of landslide susceptibility in GIS environment.

Keywords Landslide susceptibility · GIS · Remote sensing · Himalayas

12.1 Introduction

Landslide occurrences have been a regular feature in the Himalayan region. Loss of lives, properties and functional activities due to landslides are immense and apparently are growing as urbanisation expands into hill areas under the pressure of expanding populations. A greater awareness of landslide problems has led to significant research in the subject. The Himalayan mountain-building process is still

S. Sarkar (✉) · D.P. Kanungo
CSIR-Central Building Research Institute, 247667 Roorkee, India
e-mail: shantanu_cbri@yahoo.co.in

continuing and as a result, it is frequently subjected to several natural disasters such as earthquakes, landslides, avalanches, glacial lake outburst floods, and flooding. Further, intensified regional precipitation caused by changing climatic pattern is also responsible for increase in frequency of landslide events. Landslides, rock fall, and avalanches are posing serious problems in the regions of mountainous areas, where the means of mitigation and corrective measures are scarce. Hence, it is imperative to assess the hazard and risk of hilly regions.

There has been a drastic increase in magnitude and frequency of natural disasters but at the similar time there is a dramatic increase in the technical capabilities to mitigate them. A considerable amount of work has been carried out worldwide to assess the landslide susceptible zones in the form of landslide hazard zonation mapping. Application of GIS for landslide hazard zonation has been well documented by van Westen (1994). Now, we have remote sensing technology coupled with geographical information system (GIS) which has proven their usefulness in disaster mitigation and management. In this direction, an integrated approach using remote sensing and GIS has been increasingly used in India for landslide hazard mapping (Nagarajan et al. 1998; Gupta et al. 1999; NRSA 2001; Sarkar and Kanungo 2004). The paper illustrates the GIS-based methodology used for landslide susceptibility mapping in Indian Himalayas by the authors.

12.2 Landslide Mapping on Satellite Image

Mapping of existing landslides is essential to understand the relationships between the landslide distribution and the causative factors. As it is just not possible to map each and every landslide via field surveys in a rugged hilly terrain, a comprehensive mapping of landslide in GIS through remote sensing image interpretation, aided by field verifications at sampled locations is an wise alternative. Landslide information extracted from satellite images with high spatial resolution is successful in mapping the existing landslides. Landslide detection on satellite imagery largely depends on the spectral characteristics, size, shape, contrast and morphological expression. In general, there is a distinct spectral contrast between landslides and the background area. With the recent advancement in remote sensing, landslides can be well identified, mapped and transferred to the real world to produce a landslide inventory map, which serves as a crucial information for preparing landslide susceptibility maps. A landslide inventory map shows the landslide distribution in the area. Such maps are very useful for determining the weights of the factors in most of the statistical and soft computing techniques. Further a landslide inventory map can be used for the validation of the landslide susceptibility map. To prepare such maps, landslides are usually detected on satellite image (Fig. 12.1) and through field investigation and finally transferred in GIS. A landslide map prepared in GIS platform provides the area coverage of the individual landslides which is one of the valuable parameters while carrying out the susceptibility analysis.

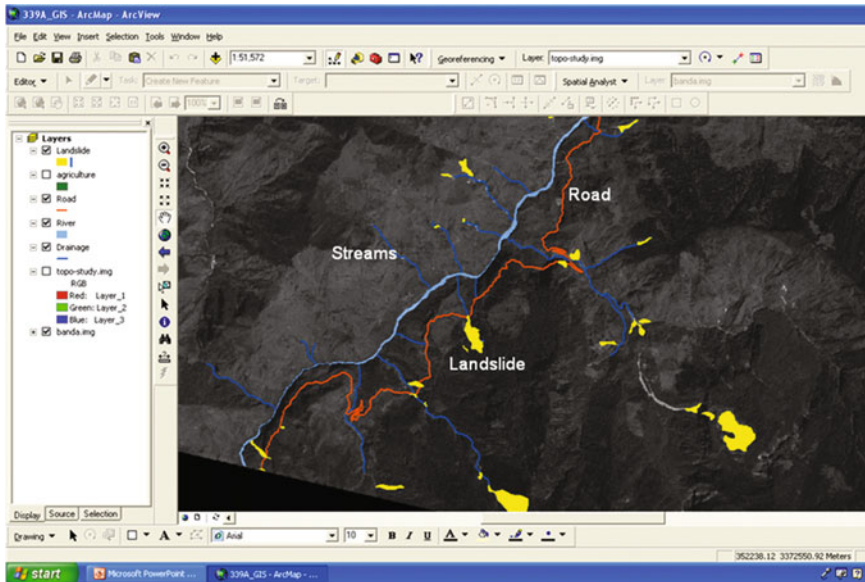


Fig. 12.1 Landslide identified in CARTOSAT 1 satellite image

12.3 Thematic Data Layers in GIS

Landslide occurrences are governed by several factors and broadly these come under geology, geotechnical engineering, hydrology, land use and climate. However, it is not always possible to obtain all the data. In most of the landslide susceptibility studies, the triggering factors such as rainfall and earthquakes are not considered. The factors considered are essentially the preparatory factors which can be collected from the field and available information. Various thematic data layers corresponding to the causative parameters are necessary to be prepared which are the input parameters for any landslide susceptibility mapping. These data layers should be prepared by collecting data from satellite image, published maps, field investigation and also through spatial and 3D analysis of terrain data in GIS. In our study, we have mostly considered slope, aspect, lithology, soil type, drainage density, lineament density, presence of faults and land use parameters for landslide susceptibility mapping. The selection of these factors and their classes depends on the nature of terrain and existing landslides based on the field investigation. To establish relationship between the factors and the landslide, a landslide distribution map also needs to be prepared. A few of the data layers where GIS has been extensively used by the authors are described below.

12.3.1 Digital Elevation Model and Its Derivatives

A digital elevation model (DEM) can be used to obtain data related to two important parameters i.e. slope and aspect. To prepare DEM, Survey of India topographic map sheets of the area at 1:25,000 and 1:50,000 scales are generally employed. The contour data are digitised for generating the DEM using the TIN module of Arc View 3D Analyst. Slope angle which is one of the key factors in inducing slope instability is then derived from the DEM and the slope map with required cell size is generated. Slope can be designated as the first derivative of DEM. A slope map is a raster map in which the attribute of each pixel denotes the maximum slope at a particular location. The map represents the spatial distribution of slope values in the range from 0° to 90° in the area. These are then suitably classified into various classes as desired for the analysis (Fig. 12.2a). Aspect is defined as the direction of maximum slope of any location on surface of the earth. Aspect can be designated as the second derivative of DEM. The aspect map generated from the DEM shows slope directions from 0° to 360° with respect to the north. A slope aspect map is also generated from the DEM with a desired cell size (Fig. 12.2b).

12.3.2 Lithology

Rock types play an important role in slope stability. The lithological constituents, their texture and degree of weathering are the basic elements which differentiate various rock types in influencing slope instability in a region. For example, it has been found that phyllites, schists are more prone to landslides than quartzites. Hence, a geological map which contains different lithologies of the area is an

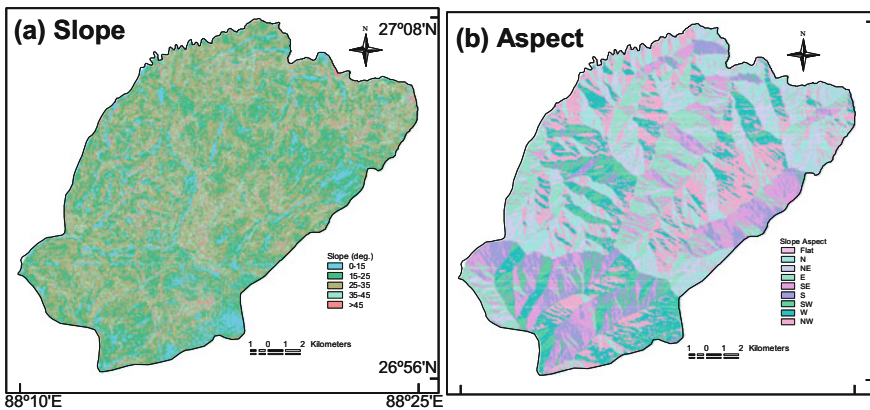


Fig. 12.2 Slope and aspect maps of Darjeeling Himalaya, India (Kanungo et al. 2009a, b)

essential component. The lithological map is mostly prepared from the available geological maps and field investigation and finally transferred into GIS.

12.3.3 Lineament

The lineaments represent the fractures, discontinuities and shear zones which can be interpreted from the satellite image. Faults also could be considered as mega lineaments. After preparing the lineament map, the lineament density for the desired cell size is obtained and a lineament density map is prepared by classifying the density into desired classes. It has been observed that thrust/faults have an effect on landslide occurrence. Some times to incorporate the effect of thrust/major faults/lineaments, a fault/lineament buffer map is also generated in GIS with a desired buffer width which could vary from a few metres to a few kilometres.

12.3.4 Drainage

The drainage map can be prepared from the topographic map with additional inputs from the satellite images. From the drainage map, the drainage density for the desired cell size is obtained. From this data, a drainage density map is prepared which classify the area into various drainage density classes. From the drainage map, sometimes the drainage order map is also prepared as it has been observed that the first order drainages are mostly associated with landslides as compared to the higher drainage orders. A drainage buffer map (Fig. 12.3a) is sometimes also generated in GIS with a desired buffer width for some particular orders of drainages.

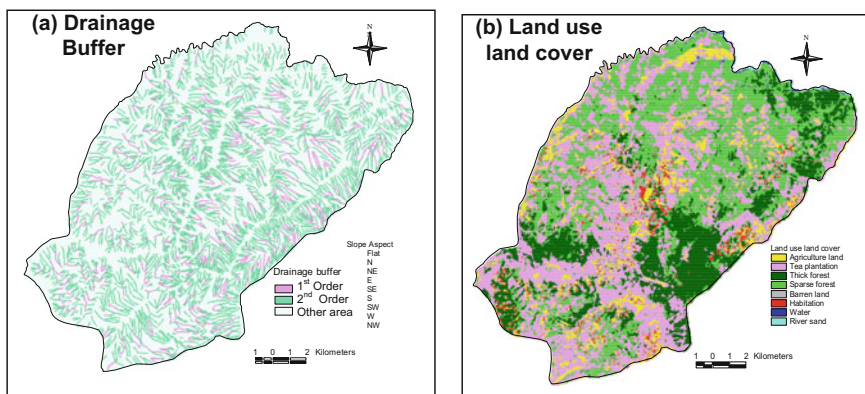


Fig. 12.3 Drainage buffer and land use and land cover maps of Darjeeling Himalaya (Kanungo et al. 2009a, b)

12.3.5 Land Use

Land use is one of the very important factors in landslide susceptibility studies. Land use map in hilly areas generally shows the distribution of forest cover, water bodies and habitats. This map can be prepared by satellite data interpretation using unsupervised and supervised classification techniques using remote sensing software such as ERDAS Imagine. An unsupervised classification is the natural grouping of pixels in the input image data. The classes obtained in the unsupervised classification are checked in the field. These classes are considered as training samples for the supervised classification process. Finally, the land use map is prepared using the supervised classification technique with the maximum-likelihood parametric rule. The land use map is finally prepared in the GIS (Fig. 12.3b).

12.4 Landslide Susceptibility Mapping in GIS Environment

In recent years, assessment of landslide susceptibility in the form of hazard zonation maps has been widely attempted in almost all the countries where landslides are considered to be one of the recurrent disasters. The methodology for preparing such maps has diverse approaches. In India, an integrated approach combining remote sensing and spatial data analysis using GIS has been greatly used for landslide susceptibility mapping. GIS is a powerful tool in modelling the landslide hazards by evaluating the combined effect of the factors which are responsible for landslide occurrence.

12.4.1 Methodology

Landslide susceptibility mapping of different parts of Himalaya has been attempted by many research workers by applying different techniques. The most commonly used techniques are qualitative map combination, statistical approach, analytic hierarchy process, and fuzzy- and ANN-based methods. The selection of suitable techniques depends on nature and availability of data, expertise and mapping scale. In India, mostly the landslide susceptibility maps are on 1:50,000 and 1:25,000 scale. Now, it is being felt that we need such maps on larger scale preferably on 1:10,000 scales. Different LSZ approaches are given in details from time to time in the review articles by Hansen (1984), Varnes (1984), van Westen (1994), Carrara and Guzzetti (1995), Hutchinson (1996), Mantovani, et al. (1996), Aleotti and Chowdhury (1999), Guzzetti et al. (1999) and Kanungo et al. (2009a, b). The different methods with different input data and thematic data layers used by the authors is summarised in the flow diagram (Fig. 12.4).

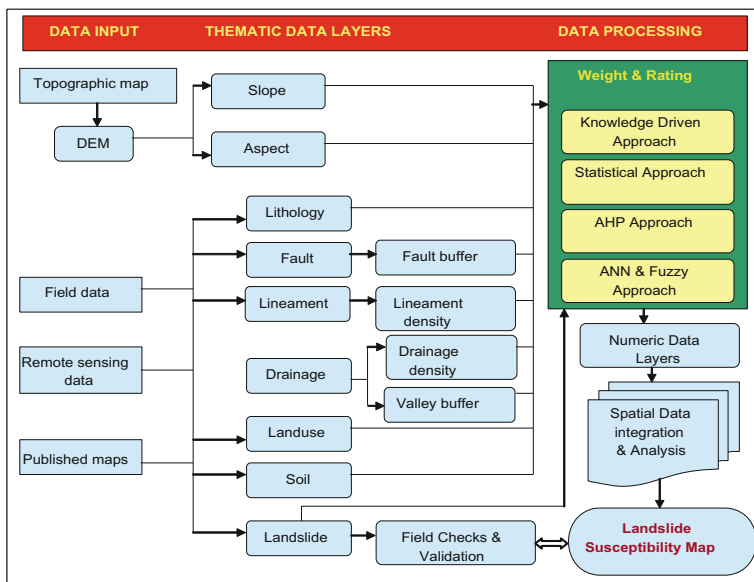


Fig. 12.4 Flow diagram showing the methodology for landslide susceptibility mapping

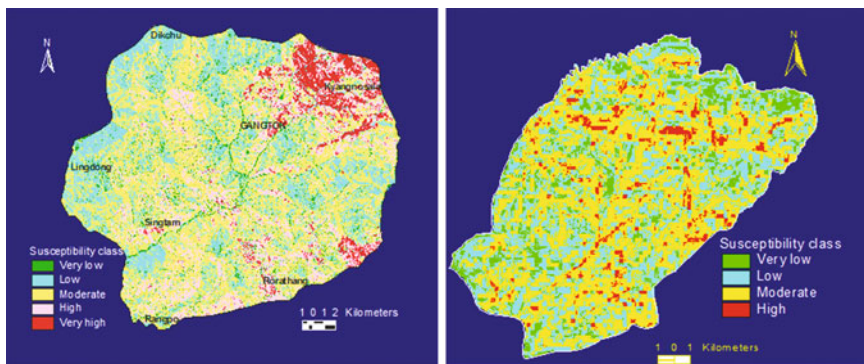


Fig. 12.5 Examples of landslide susceptibility maps from Sikkim and Darjeeling Himalayas (Sarkar et al. 2008; Sarkar and Kanungo 2004)

The input data used are mostly collected from the field, remote sensing data, topographic maps and published literature. These data are converted into digital form to generate the thematic layers in GIS. The desired parameters are taken for the spatial analysis in GIS depending on the techniques employed. After assigning or deriving the weights to different factors and their categories using different techniques, the thematic layers are integrated and classified into various classes of susceptibility in GIS to produce the landslide susceptibility maps (Fig. 12.5).

Further a comparative analysis of landslide susceptibility maps of an area obtained through different techniques can be done using GIS. A comparative study of landslide susceptibility maps of parts of Darjeeling Himalaya using ANN and fuzzy approaches has been carried out by Kanungo et al. (2006).

12.5 Conclusion

The collection of information through remote sensing and spatial data analysis using GIS has proved the capabilities of geoinformatics in the field of landslide disaster mitigation and management. Landslide susceptibility mapping is one of the crucial aspects for any regional landslide hazard study. Analysis of landslide hazard is a complex task, as many factors play a crucial role and with the help of GIS these different kinds of spatial data can be easily integrated. It is observed that analysis of all the factors leading to instability in the region may be accomplished more systematically and scientifically using GIS.

In general, the landslide susceptibility map shows four to five relative classes of landslide susceptible zones as documented. Such maps can be validated by determining the landslide density using the landslide inventory map and also using success rate curve method for different susceptible classes. These landslide susceptibility maps are very useful for planners for selecting suitable locations for any infrastructural developmental projects. However, the area under very high and high landslide susceptible zones should be investigated in detail to pinpoint the potentially unstable slopes so that suitable protection measures can be designed and implemented for a safe built space.

Acknowledgements Authors are grateful to the Director, CSIR-CBRI for his kind permission to publish the work.

References

- Aleotti P, Chowdhury R (1999) Landslide hazard assessment: summary, review and new perspectives. *Bull Eng Geol Environ* 58:21–44
- Carrara A, Guzzetti F (eds) (1995) Geographical information systems in assessing natural hazards. Kluwer Academic Publisher, Dordrecht, The Netherlands, p 353
- Gupta RP, Joshi BC (1990) Landslide hazard zonation using the GIS approach—a case study from the Ramganga catchment, Himalayas. *Eng Geol* 28:119–131
- Guzzetti F, Carrara A, Cardinali M, Reichenbach P (1999) Landslide hazard evaluation: a review of current techniques and their application in a multi-scale study, Central Italy. *Geomorphology* 31:181–216
- Hansen A (1984) Landslide hazard analysis. In: Brundsen D, Prior DB (eds) *Slope instability*. Wiley, New York, pp 523–602
- Hutchinson JN (1996) Keynote paper: landslide hazard assessment. In: Bell DH (ed) *Landslides*, vol 3. Balkema, Rotterdam, The Netherlands, pp 1805–1841

- Kanungo DP, Arora MK, Sarkar S, Gupta RP (2006) A comparative study of conventional, ANN Black Box, Fuzzy and Combined Neural and Fuzzy Weighting Procedures for Landslide Susceptibility Zonation in Darjeeling Himalayas. *Eng Geol* 85:347–366
- Kanungo DP, Arora MK, Sarkar S, Gupta RP (2009a) A fuzzy set based approach for integration of thematic maps for landslide susceptibility zonation. *Georisk* 3(1):30–43
- Kanungo DP, Arora MK, Sarkar S, Gupta RP (2009b) Landslide susceptibility zonation (LSZ) mapping—a review. *J S Asia Disaster Stud* 2(1):81–105
- Mantovani F, Soeters R, Van Westen CJ (1996) Remote sensing techniques for landslide studies and hazard zonation in Europe. *Geomorphology* 15:213–225
- Nagarajan R, Mukherjee RA, Roy A, Khire MV (1998) Temporal remote sensing data and GIS application in landslide hazard zonation of part of Western Ghat, India. *Int J Remote Sens* 19:573–585
- NRSA (2001) Atlas on landslide hazard zonation mapping in the himalayas of Uttaranchal and Himachal Pradesh States using remote sensing and GIS. National Remote Sensing Agency, Hyderabad, India
- Sarkar S, Kanungo DP (2004) An integrated approach for landslide susceptibility mapping using remote sensing and GIS. *Photogram Eng Remote Sens* 70:617–625
- Sarkar S, Kanungo DP, Patra AK, Kumar P (2008) GIS based spatial data analysis for landslide susceptibility mapping. *J Mt Sci* 85(5):52–62
- Varnes DJ (1984) Landslide hazard zonation: a review of principles and practice. UNESCO, Paris, pp 1–63
- van Westen CJ (1994) GIS in landslide hazard zonation: a review, with examples from the Andes of Colombia. In: Price M, Heywood I (eds) *Mountain environments and geographic information system*. Taylor & Francis, Basingstoke, UK, pp 135–165

Chapter 13

Characteristics of the Torrential Rainfall-Induced Shallow Landslides by Typhoon Bilis, in July 2006, Using Remote Sensing and GIS

Jie Dou, Hiromitsu Yamagishi, Yueren Xu, Zhongfan Zhu and Ali P. Yunus

Abstract During July 14–16, 2006 Typhoon Bilis swept over the southern China. The typhoon brought torrential downpour, resulting in many shallow landslides in the region. This study describes the characteristics of the landslides in an area around the Dongjiang Reservoir, Hunan Province, which was seriously affected by the event. We sketch the landslide occurrences and extreme rainfall event in the study area based on the high-resolution QuickBird images, medium-scale China-Brazil Earth Resources Satellite (CBERS) images, rain gauge data, a digital elevation model, and field surveys. All the satellite images, rain gauge points, geological maps, and field notes were processed and constructed into a spatial database in a GIS platform.

J. Dou (✉)
Public Works Research Institute, Tsukuba, Japan
e-mail: douj888@gmail.com

J. Dou
Center for Spatial Information Science, The University of Tokyo, Chiba, Japan

H. Yamagishi
Shin Engineering Consultant Co. Ltd. Japan, Hakodate, Japan
e-mail: hiromitsuyamagishi88@gmail.com

H. Yamagishi
Ehime University, Matsuyama, Japan

Y. Xu
Institute of Earthquake Science, China Earthquake Administration,
Fuxing Rd. 36, Beijing, China
e-mail: yuefei189@gmail.com

Z. Zhu
College of Water Sciences, Beijing Normal University,
Xinjiekouwai Street 19, Beijing 100875, China
e-mail: zhuzhongfan1985@gmail.com

A.P. Yunus
Department of Geology, Aligarh Muslim University, Aligarh 202 002, India
e-mail: yunusp@csis.u-tokyo.ac.jp

The landslide occurrences in the study area before the event was low, and significantly increased during and after Typhoon Bilis of 2006. The short duration, high-intensity rainfall was the major triggering factor. In addition, topographical factors such as slope and aspect also contributed to landslide occurrence. The combined influence of rainfall and the topographic factors. The paper attempts to provide a better understanding of the rainfall and causative factors of landslides in the wake of typhoon Bilis.

Keywords Torrential rainfall · Shallow landslide · Typhoon Bilis · GIS · Reservoir

13.1 Introduction

Landslides are one of the most frequent natural disasters in China (Fig. 13.1a), because 75% of the country falls under mountainous terrain, and the landslides are caused by earthquakes, torrential rainfalls, highway construction and rapid urbanization, and hillslope erosion during a flood event. The landslide often causes a substantial damage to human property as well as severe loss of lives. As indicated

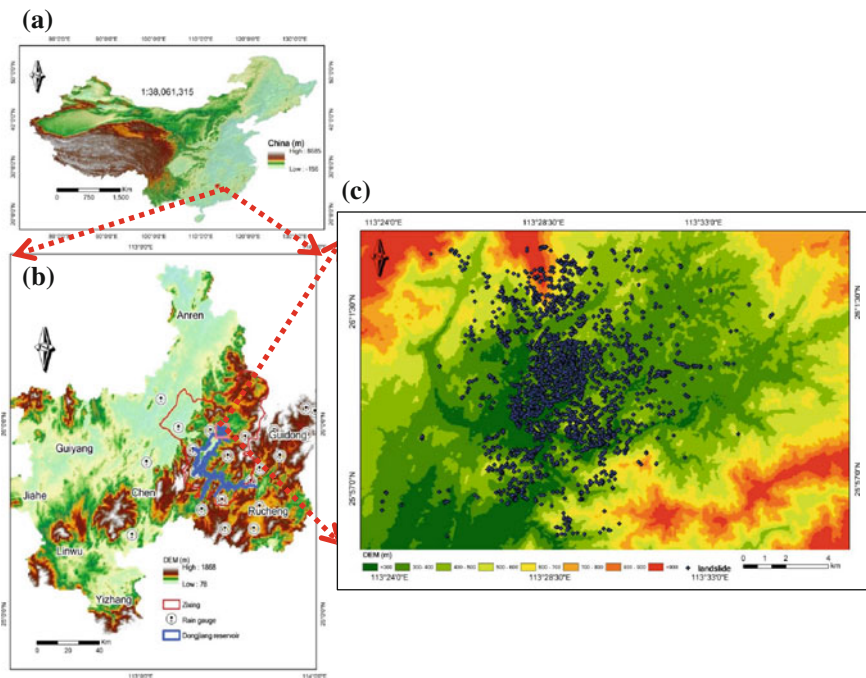


Fig. 13.1 Study area: **a** location map of China, **b** inset showing study area and rain gauge distribution, and **c** the spatial distribution of shallow landslides on the elevation map derived from ASTER GDEM

in Turner and Schuster (1996) studies, this trend will be aggravating in the future with the rapid development of urbanization and economies and increase in regional precipitation because of global earth warming (Zhu et al. 2015; Dou et al. 2015a, c).

This research focused on a rainfall-induced landslide event caused by tropical cyclones (TCs)—Typhoon Bilis. TCs are one of the most devastating weather phenomena all over the world as they trigger numerous hazards such as flooding, debris flows, and landslides. Researchers have thus paid close attention to the topic of heavy rainfall-induced landslides in various parts of the world (Dai and Lee 2002; Yamagishi and Iwahashi 2007; Yamagishi et al. 2013; Zou et al. 2013; Dou et al. 2014, 2015b).

Bilis is one of the severe tropical storms in the western North Pacific Ocean, in July 2006, which made landfall in the southeastern coast of Fujian Province, China. Bilis was not especially intense at landfall and then gradually weakened. Its trail was well forecasted by the China National Meteorological Center (CNMC), but the real-time prediction greatly underestimated the intensity of the heavy precipitation that induced drastic flooding over a large area after the storm proceeded inland. The torrential downpour during typhoon Bilis (July 14–16, 2006) brought about many shallow landslides with a maximum rainfall intensity of 466 mm in 36 h in the southern China. More than half of the precipitation (826 mm) of the total area, in July, triggered many landslides and other related mass movements. The torrential precipitation in Fujian and Zhejiang provinces was directly caused by the inner-core storm circulation during its landfall. The interaction between the typhoon and the South China Sea Monsoon also caused the increased precipitation around the area between Jiangxi and Hunan provinces, leading to the catastrophic flooding and mass movements.

Understanding of rainfall characteristics concerning the reservoir watershed is useful for disaster forecasting and warning systems. Several investigations have tried to explore the influences of TCs on hydrologic processes in reservoir watershed (Chien-Yuan et al. 2008; Lin et al. 2010; Xu et al. 2011; Shen 2013; Zou et al. 2013), but only a few have paid attention to the relationship between the characteristics of typhoon and landslide occurrences. The lack of observations with adequate spatial and temporal resolution substantially obstructed the study on major storms associated with landslide data over a reservoir watershed. However, this paper is one of the few reports of the typhoon and landslide events in China.

13.2 Geographical Setting of the Study Area

The study area is located in the southeast of Hunan Province, China (Fig. 13.1a, b), and the Dongjiang Reservoir is susceptible to heavy precipitation during tropical cyclone seasons. In the studied area, the elevation ranges from 78 to 1868 m with a mean of 540 m. As far as geomorphology is considered, the study area mainly composed of three distinct parts, namely the hilly plain, the hilly valley, and the Luoxiao Mountains near the eastern and southern boundaries. Geologically, the

area is composed mostly of metamorphic rocks and sedimentary rocks of Paleozoic age, such as sandstone, sandy slate, and limestone, which were intruded by granitic rocks in places. The granitic rocks are deeply weathered, additionally the weathering of soils in the studied area leads to laterite materials due to high oxidation, and prone to serious erosion. Land use in the study area is characterized by settlements and small-scale agro-industrial activities, such as paddy farming and plantation. The zone including the study area belongs to the humid subtropical monsoon climate. Usually, annual precipitation is approximately 1538 mm, mostly affected by typhoons.

The Dongjiang Reservoir is the largest one in the south of Hunan Province, covering the water area of 160 km², and has the capacity of 8.12×10^9 m³. Due to this heavy rainfall caused by the Typhoon Bilis in 2006, thousands of sediment-related disasters, including numerous slope failures (shallow landslides), debris flow, and shallow landslides occurred, which were inventoried through the QuickBird images (0.6 m), CBERS images (20 m), and field work (Fig. 13.2). The torrential precipitation event associated with Typhoon Bilis caused 246 deaths, 95 missing, and more than 300 million US dollars in damage around the Zixing City. Damages of destroyed or buried buildings by debris flows were serious around the study area. There were also considerable slope failure disasters in the strong precipitation intensity areas; moreover, they induced flash floods inundated the short and steep rivers in the hilly areas.

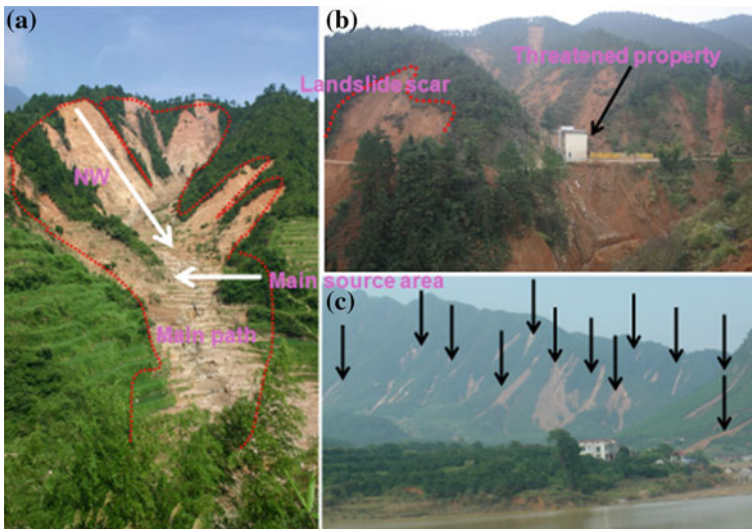


Fig. 13.2 Rainfall-induced landslides by the typhoon Bilis: **a** example of shallow landslide (*dots* on the scar indicate vector points for Fig. 13.1c) and associated with debris flows, **b** landslide scar and threatened property, and **c** many shallow landslides (the *black arrows*)

13.3 Data Collection

Rainfall data from the records of 21 rain gauges (Fig. 13.1b) in and along the study area were used to analyze the rainfall characteristics of the major storm. Analyzing the pre and post event images of QuickBird (0.6 m in resolution) and CBERS (20 m in resolution), we inventoried a total of 2407 landslide sites (dots) as shown in Fig. 13.1c. The landslide points shown in Fig. 13.1c indicate the center of the scar as shown in Fig. 13.2a. The landslide density is counted as approximately 8.2/km². Topographic data for analyses were collected and derived from the 30 m ASTER GDEM (version 2).

13.4 Analysis of the Rainstorm Caused by the Typhoon Bilis

Typhoon Bilis was a strong tropical storm with severe precipitation in a short duration, whose trail was shown in Fig. 13.3a, on July 9, and it landed on the coast of Fujian Province, China, on July 14, 2006, with the maximum wind speed of 108 km/h. And then, it shortly weakened into a tropical storm and moved westward and north-westward at the speed of 10–15 km/h until July 16, 2006, when it disappeared in Hunan Province.

The rainfall data obtained from the rain gauge networks around the reservoir observed during 14th and 15th July, 2006, are displayed in Fig. 13.3b. As shown in the 36-h and total month rainfall curves of Dongjiang Reservoir, Longxi region rain gauge shows the maximum rainfall with 507 mm/36 h, and 826 mm/month, respectively. We also select two rain gauges around the reservoir, namely Xingnin and Lianping (Fig. 13.4). From the graphs, in 48 h, the cumulative rainfall in

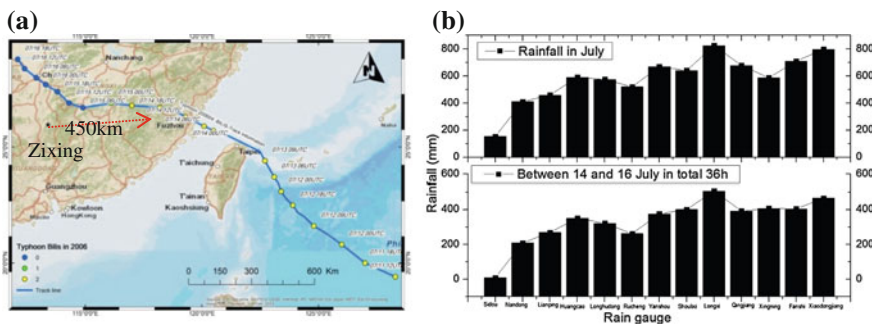


Fig. 13.3 **a** Trail of the Typhoon Bilis (data from Japan National Institute of Informatics), **b** graphs showing rain gauge precipitation in the Dongjiang Reservoir for the month of July 2006 (*top*), and during 14–16th, July 2006 (36 h) rainfall (*bottom*). It is noted that the depth of water of the reservoir increased 7.73 m from 14 to 19 July, 2006

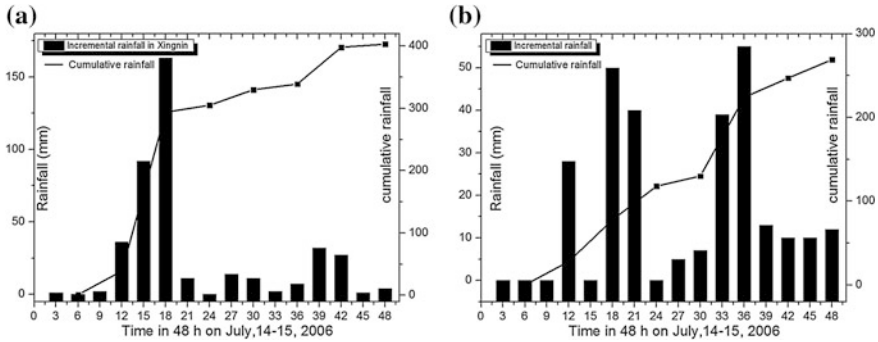


Fig. 13.4 Incremental and cumulative rainfall rain gauges in Xingnin (a) and Lianping around the Dongjiang Reservoir (b)

Xingnin and Lianping is more than 400 mm and 285 mm, respectively. In particular, the incremental rainfall of Xingnin at 15–18 UTC was approximately 180 mm/3 h. This indicates that the reservoir region was severely suffered from the heavy rainfall in a short time.

13.5 Statistical Analysis of the Landslides and Geographical Factors

To analyze the relationship between the landslides and topographic factors, we prepared the landslide data of vector of points and the topographic factors derived from 30 m ASTER GDEM. We employed the raster calculation function to investigate the relationship between the landslide frequency and precipitation (vector point), also elevation, and slope gradient, which were then reclassified into an interval of 100 m and 5° respectively. The calculation of topographic factors was implemented by the software ArcGIS v. 10.2.

The relationship between the spatial location of the landslides (Fig. 13.1c) and conditioning factors of precipitation and slope factors were analyzed in GIS environment (Fig. 13.5). In the case of the cumulative rainfall, it shows that most of the landslides occurred in areas of 340–360 mm in precipitation (Fig. 13.5a). In general, rainfall leads to increase in moisture content that can raise pore water pressure above the critical value necessary to trigger slope instability. In the case of highly permeable soils in the most part of tropical areas, the failure surface of the landslide is usually shallow. In addition, high cumulative rainfalls causes more shallow and deep landslides occurring due to the increase in pore water pressure.

With respect to incremental rainfall, the landslides mostly occurred when rainfall exceeded 152 mm (Fig. 13.5b). The landslide frequency related to the incremental rainfall revealed that these two days of heavy precipitation composed of antecedent rainfall, and hourly precipitation intensity, induced a huge number of debris flows and shallow landslides. Due to the torrential rainfall, the high permeability of the

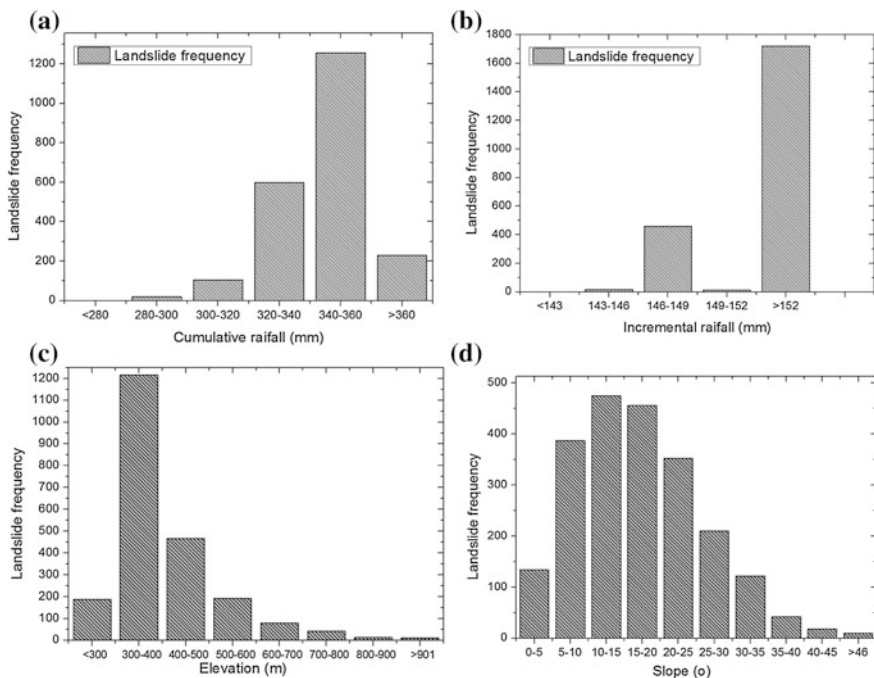


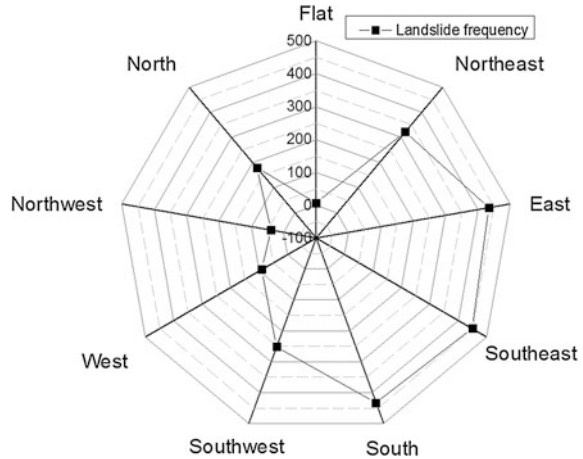
Fig. 13.5 Relationship between landslide frequency and geographical factors (climate and topographic factors): **a** cumulative rainfall, **b** incremental rainfall, **c** elevation, and **d** slope gradient

colluvium deposits allowed the development of a transient water table above the interface between the colluvium and less permeable underlying soil material, resulting in direct surface infiltration and subsurface seepage.

In terms of elevation, most landslides occurred from 300 to 600 m, which are not so high mountainous region (Figs. 13.1c and 13.5c). The results reveal that landslides are frequent in the middle altitudes, because the ratio of the study area in the middle altitudes is larger than that of the higher, and the lower areas are more gentle and not prone to landslide occurrence.

In the case of slope gradient, landslide frequency is concentrated at the 10°–30° zone (Fig. 13.5d). The results show that the occurrence of landslides gradually increases with an increasing slope angle until it drops after a 46° slope angle. Gentler slopes have a relatively low frequency of landslide occurrences because of the lower shear stress corresponding to the low gradient, whereas very steep slope angles lead to outcropped bedrock, which is less susceptible to landslides. However, recently in Japan, Yamagishi et al. (2013) emphasized that the frequency of heavy rainfall-induced landslides occurred mostly concentrated at the slope of the 25°–30° at maximum, while, at Hong Kong Island, Dai and Lee (2002) reported that most of the heavy rainfall-induced landslides occurred on the slope of 35°–40°. These three studies including our's show different results in terms of

Fig. 13.6 Relationship between landslide frequency and slope aspect



relationship between landslide frequency and slope gradient. Such differences probably depends on GIS analysis methods and various conditions of topography including soil moisture content and geology etc.

With respect to the slope aspect, most of landslides occurred at the south-east facing slope direction (Fig. 13.6). Slope aspect strongly influences hydrologic process via evapotranspiration and hence impacts weathering processes, vegetation, and root development. In this case, we expect that the wind direction of Typhoon Bilis was from southeast to northwest. It is probably due to the direction of the typhoon. Thus, it would be expected that southeast-facing slopes were strongly affected by rainfall-induced landslides compared to the north-facing slopes.

13.6 Conclusions

The objective of this study was to identify the characteristics of typhoon associated torrential rainfall and to reveal the relationship between the rainfall characteristics, topographic factors, and landslide occurrences in and around the Dongjiang Reservoir, Hunan Province, China. We discuss the triggering mechanisms of the landslides by rainfall that caused by the wind shear, warm-air advection (Gao et al. 2009), and also the topographic features for generation of the landslides. Simultaneously, owing to the orographic effects, the areas around the reservoir are likely to have received extremely high rainfall totals.

This paper also exposes that an extreme rainfall event triggered numerous shallow landslides around the reservoir. In particular, the accumulated rainfall over the Dongjiang Reservoir watershed was considerably more than the surrounding areas in a 6-h period with unprecedented rainfall rate and accounted for the severe flash floods in the reservoir watershed on July 14, 2006. And then, we inventoried more than 2000 landslide sites through QuickBird images with 0.6 m in resolution.

And finally, we analyzed the landslides related to precipitation and topographic factors using GIS, based on the rain gauges at the reservoirs and topographic data of 30 m ASTER GDEM.

The results revealed that shallow landslide frequency was caused by and/or intimately related to cumulative rainfall, incremental rainfall, elevation, slope gradient, and slope aspect. As Yamagishi et al. (2013) mentioned, shallow landslides are mainly dependent on topography rather than bedrock geology. Nevertheless, in the future, we have to analyze also the relationship between the land use, vegetation, geology, and landslide occurrence.

Acknowledgements We would like to express our gratitude to Professor Dr. Li Tiefeng of China Geological Survey (CGS) for providing the image data. Dou also thanks Dr. Zou Yi, Uttam, and Hagar for their constructive suggestions and help.

References

- Chien-Yuan C, Lien-Kuang C, Fan-Chieh Y et al (2008) Characteristics analysis for the flash flood-induced debris flows. *Nat Hazards* 47:245–261. doi:[10.1007/s11069-008-9217-7](https://doi.org/10.1007/s11069-008-9217-7)
- Dai FC, Lee CF (2002) Landslide characteristics and slope instability modeling using GIS, Lantau Island, Hong Kong. *Geomorphology* 42:213–228
- Dou J, Oguchi T, Hayakawa YSS et al (2014) Susceptibility mapping using a certainty factor model and its validation in the Chuetsu Area, Central Japan. *Landslide Sci Safer Geoenviron* 2:483–489. doi:[10.1007/978-3-319-05050-8_65](https://doi.org/10.1007/978-3-319-05050-8_65)
- Dou J, Chang K, Chen S, et al (2015a) Automatic case-based reasoning approach for landslide detection: integration of object-oriented image analysis and a genetic algorithm 4318–4342. doi:[10.3390/rs70404318](https://doi.org/10.3390/rs70404318)
- Dou J, Paudel U, Oguchi T, et al (2015b) Shallow and deep-seated landslide differentiation Using support vector machines : a case study of the Chuetsu area, Japan. 26:227–239. doi:[10.3319/TAO.2014.12.02.07\(EOS\)1](https://doi.org/10.3319/TAO.2014.12.02.07(EOS)1)
- Dou J, Yamagishi H, Pourghasemi HR, et al (2015c) An integrated artificial neural network model for the landslide susceptibility assessment of Osado Island, Japan. *Nat Hazards* 78:1749–1776. doi:[10.1007/s11069-015-1799-2](https://doi.org/10.1007/s11069-015-1799-2)
- Gao S, Meng Z, Zhang F, Bosart LF (2009) Observational analysis of heavy rainfall mechanisms associated with severe tropical storm bilis (2006) after its landfall. *Mon Weather Rev* 137:1881–1897. doi:[10.1175/2008MWR2669.1](https://doi.org/10.1175/2008MWR2669.1)
- Lin G-F, Chen G-R, Huang P-Y (2010) Effective typhoon characteristics and their effects on hourly reservoir inflow forecasting. *Adv Water Resour* 33:887–898. doi:[10.1016/j.advwatres.2010.04.016](https://doi.org/10.1016/j.advwatres.2010.04.016)
- Shen P-SS (2013) Nonparametric estimation of the bivariate distribution function with doubly truncated data
- Turner AK, Schuster R (1996) Landslides: investigation and mitigation
- Xu Y, He H, Shen X (2011) Case study on dynamic survey of group geological disasters in Dongjiang reservoir Region, Zixing City using CBERS images. *Acta Sci Nat Univ Pekin* 47:689–697
- Yamagishi H, Doshida S, Pimiento E (2013) GIS analysis of heavy-rainfall induced shallow landslides in Japan. In: *Landslide science and practice*, pp 601–607
- Yamagishi H, Iwahashi J (2007) Comparison between the two triggered landslides in Mid-Niigata, Japan by July 13 heavy rainfall and October 23 intensive earthquakes in 2004. *Landslides* 4:389–397. doi:[10.1007/s10346-007-0093-0](https://doi.org/10.1007/s10346-007-0093-0)

- Zhu Z, Yu J, Wang H, et al (2015) Fractal dimension of cohesive sediment flocs at steady state under Seven shear flow conditions. 4385–4408. doi:[10.3390/w7084385](https://doi.org/10.3390/w7084385)
- Zou Y, Qiu S, Kuang Y, Huang N (2013) Analysis of a major storm over the Dongjiang reservoir basin associated with Typhoon Bilis (2006). *Nat Hazards* 69:201–218. doi:[10.1007/s11069-013-0696-9](https://doi.org/10.1007/s11069-013-0696-9)